Meshless numerical formulation for analysis of shell-like structures

Jarak, Tomislav

Doctoral thesis / Disertacija

2010

Degree Grantor / Ustanova koja je dodijelila akademski / stručni stupanj: **University of Zagreb, Faculty of Mechanical Engineering and Naval Architecture / Sveučilište u Zagrebu, Fakultet strojarstva i brodogradnje**

Permanent link / Trajna poveznica: https://urn.nsk.hr/urn:nbn:hr:235:047021

Rights / Prava: In copyright/Zaštićeno autorskim pravom.

Download date / Datum preuzimanja: **2025-01-26**

UNIVERSITY OF ZAGREB
FACULTY OF MECHANICAL ENGINEERING
AND NAVAL ARCHITECTURE

MESHLESS NUMERICAL FORMULATION FOR ANALYSIS OF SHELL-LIKE STRUCTURES

DOCTORAL THESIS

TOMISLAV JARAK

ZAGREB, 2010

UNIVERSITY OF ZAGREB
FACULTY OF MECHANICAL ENGINEERING
AND NAVAL ARCHITECTURE

MESHLESS NUMERICAL FORMULATION FOR ANALYSIS OF SHELL-LIKE STRUCTURES

DOCTORAL THESIS

Supervisor:
Dr.sc. Jurica Sorić, prof.   Tomislav Jarak, dipl.ing.

ZAGREB, 2010

BIBLIOGRAPHY DATA

Acknowledgments

First, I would like to express my gratitude to my supervisor Professor Jurica Sorić (FMENA, University of Zagreb) for his guidance and the constant support that he gave me throughout the research that resulted in this thesis. I am also very thankful to the jury members, Professors Jan Sladek (Slovak Academy of Sciences) and Zdenko Tonković (FMENA, University of Zagreb), for finding time to review my thesis, and for giving valuable comments and encouragement needed for completing this work.

Personal thanks are due to Professor Satya Atluri (University of California, Irvine) for introducing me to the fascinating world of the state-of-the-art numerical techniques called meshless methods.

I would like to thank my colleagues from the Department of Technical Mechanics, Faculty of Mechanical Engineering and Naval Architecture, University of Zagreb, for the help and advice given during the period I have spent at the Department. Among them, my special appreciation goes to all those great people working at the Laboratory of Numerical Mechanics, for their personal support and friendly attitude.

A very special thank goes to my closest friends, who have always been there for me to cheer me up when the things went badly, and whose jokes always managed to brighten the day.

Finally, I am deeply grateful to my family and to my girlfriend for their immense patience and understanding, which proved essential for completion of this work.

<div align="right">
Tomislav Jarak

Zagreb, May 2010
</div>

Contents

III

Preface

In the last couple of decades, numerical engineering computations have become indispensable for the analysis of complex engineering problems, due to their potential in solving large systems of partial differential equations. By properly using various numerical methods, it is possible to cut the costs and time needed for the development of new efficient products or to simulate the behaviour of already existing products realistically. The Finite Element Method (FEM) is currently the most popular and widely used numerical method in the simulation of deformation responses of solid structures. The method is robust, well developed, and has made an enormous impact over the last couple of decades. Nevertheless, it still suffers from some drawbacks associated with the use of the meshes consisting of geometrically adjacent elements.

Currently, shell structures are perhaps the most widely used structural components in modern engineering due to their optimal ratio of weight and load-carrying capabilities. Classic examples of shell structures include ship hulls, aircrafts, space vehicles, cars, tanks, and pipelines in mechanical engineering, as well as reinforced shell roofs and membranes in civil engineering, etc. The problem of the numerical modelling of shell structures has been intensively researched in the frame of FEM, and a great variety of different efficient formulations have been developed. Nevertheless, the development of an optimal FEM model for shells has remained an opened question even today; in a great measure because of the various problems appearing due to the thinness of such structures.

Recently, a new class of numerical methods known commonly as meshless methods have gained a considerable attention from the academic community, due to their flexibility and capacity to solve the systems of partial differential equations without the use of predefined meshes. So far, they have shown a potential in solving various engineering problems, in which the use of the global geometrical meshes has a negative effect on the performance of FEM. These new numerical approaches have also opened further possibilities in tackling some critical issues concerning the numerical modelling of shells, such as the elimination of various locking effects. However, as meshless methods still represent a relatively new concept in computational mechanics, there are few meshless formulations for shell-like structures available in the literature, as compared to FEM technology. Because of the afore-mentioned reasons, a

considerable interest exists for developing new numerical shell models based on the meshless and other closely related methods.

Abstract

Meshless computational methods for the analysis of plate and shell structures are proposed in this thesis. The developed algorithms are based on the local Petrov-Galerkin approach. A shell is considered as a three dimensional (3-D) solid continuum, and the solid-shell concept, which allows the implementation of complete 3-D material models, is employed. Geometry of the shell is described by employing a mapping technique, whereby the shell middle surface is defined mathematically exactly. Discretization is carried out by the couples of nodes located on the upper and lower surfaces of the structure. The governing equations are the local weak forms (LWF) of the 3-D equilibrium equations, which are written over the local sub-domains surrounding the node couples. The approximation of all unknown field variables is carried out by using the Moving Least Squares (MLS) approximation scheme in the in-plane directions, while simple polynomials are applied in the thickness direction. Both the purely displacement-based (primal) and mixed formulations are proposed and special attention is given to the elimination of locking effects.

Two different primal formulations are presented where only the displacement field is approximated. In both cases, the Poisson's thickness locking effect is circumvented by adopting the hierarchical quadratic interpolation for the transversal displacement component. The transversal shear locking phenomenon is alleviated by applying a sufficiently high order of the in-plane MLS functions.

In the mixed approach, appropriate strain and stress components are approximated separately from the displacement field. The nodal strain and stress values are then expressed in terms of the approximated displacements, and a global system of equations containing only the unknown nodal displacement variables is obtained. In the formulation for plates, thickness locking is eliminated by modifying the nodal values of the normal transversal strain component, while the transversal normal stress is approximated instead of the transversal normal strain in the algorithm for curved shells. In the thin structural limit, transversal shear locking is efficiently suppressed by means of the separate strains approximation. It is theoretically proved that the mixed approach is numerically more efficient than the proposed primal meshless formulations.

The numerical efficiency of the derived algorithms is demonstrated by numerical examples.

Sažetak

Predloženi su novi bezmrežni algoritmi za numeričku simulaciju procesa deformiranja ploča i ljusaka u linearno-elastičnom području. Prikazane formulacije temelje se na bezmrežnoj lokalnoj Petrov-Galerkinovoj (MLPG) metodi. Ljuske su razmatrane kao deformabilna trodimenzijska tijela primjenom tzv. *solid-shell* koncepta koji omogućava ugradnju potpunih trodimenzijskih materijalnih modela. Geometrija ljusaka opisana je parametrizacijom srednje plohe, pri čemu je srednja ploha opisana matematički egzaktno. Diskretizacija je provedena pomoću parova čvorova, koji se nalaze na gornjoj, odnosno donjoj plohi ljuske. Jednadžbe ravnoteže zadovoljene su u obliku lokalnih slabih formi uz primjenu Petrov-Galerkinovog principa. Testne funkcije su opisane jednostavnim polinomima u smjeru normale na srednju plohu, dok se u ravnini tangentnoj na srednju plohu koriste Heavisideove step funkcije. Nepoznate veličine polja u svim predloženim algoritmima aproksimirane su primjenom metode pomičnih najmanjih kvadrata (MLS funkcije) u tangentnoj ravnini, a u smjeru normale jednostavnim polinomima.

Predložene su dvije formulacije temeljene na metodi pomaka. Poissonov *locking* eliminiran je primjenom hijerarhijske kvadratne interpolacije za komponentu pomaka u smjeru normale na srednju plohu. Poprečni posmični *locking* ublažen je primjenom dovoljno visokog stupnja baze MLS funkcija.

U mješovitim formulacijama su uz polje pomaka direktno aproksimirane i neke od komponenata tenzora deformacija i naprezanja. Nepoznate čvorne vrijednosti deformacija i naprezanja izračunavaju se iz aproksimiranih pomaka pomoću odgovarajućih kolokacijskih postupaka. Na taj način dobiva se zatvoreni globalni sustav jednadžbi u kojem su nepoznanice samo čvorni pomaci. Poissonov *locking* je eliminiran modificiranjem čvornih vrijednosti za poprečnu normalnu komponentu deformacije u formulaciji za ploče, dok je u algoritmu za ljuske to postignuto direktnim aproksimiranjem poprečne normalne komponente naprezanja. Poprečni posmični *locking* učinkovito je otklonjen direktnim aproksimiranjem komponenata tenzora deformacije koje djeluju u tangentnoj ravnini na srednju plohu. Pokazano je teorijski i eksperimentalno da je mješoviti MLPG pristup superioran u odnosu na formulacije koje su temeljene na metodi pomaka. Točnost i učinkovitost predloženih algoritama pokazani su odgovarajućim numeričkim primjerima.

Prošireni sažetak

Uvod

Usporedno s razvojem računala došlo je do intenzivnog razvoja učinkovitih numeričkih metoda namijenjenih izvođenju računalnih simulacija ponašanja realnih konstrukcija. Njihovom pravilnom primjenom moguće je smanjiti troškove i vrijeme potrebno za razvoj novih ili za analizu već postojećih proizvoda. Pri tome se u nekim granama privrede, kao što su zrakoplovna industrija, brodograđevna industrija, građevinarstvo, automobilska industrija ili procesna tehnika, vrlo intenzivno primjenjuju tankostjene konstrukcije zbog povoljnog omjera nosivosti i težine. Zbog toga numeričko modeliranje procesa deformiranja ljuskastih konstrukcijskih elemenata pobuđuje posebni interes istraživača već dugi niz godina, pri čemu se danas najčešće koristi metoda konačnih elemenata (MKE).

Iako je razvijeno mnoštvo različitih formulacija konačnih elemenata koji služe rješavanju čitavog niza složenih fizikalnih problema, njihova je učinkovitost ponekad ograničena zbog problema čija je pojava povezana s topologijom geometrijske mreže konačnih elemenata. Poželjno je da elementi u mreži imaju što je moguće pravilniji geometrijski oblik jer jako distordirani elementi mogu biti uzrok značajnih numeričkih grešaka. Stvaranje takve mreže u praktičnim je slučajevima nerijetko mukotrpan i dugotrajan zadatak. Čak i ako su mreže na početku proračuna u zadovoljavajućoj mjeri strukturirane, tijekom simulacije može doći od velikih distorzija konačnih elemenata što u konačnici može uzrokovati značajni gubitak točnosti rješenja ili čak i prijevremeni prekid numeričkog proračuna. Posebno su osjetljive simulacije koje uključuju rješavanje nelinearnih problema kod kojih se javljaju velike deformacije, kao što su simulacije sudara u automobilskoj industriji (*chrash anal*ysis)*, procesa dubokog vučenja ili propagacija pukotina u mehanici loma. Da bi se izbjegli navedeni problemi, koriste se automatske metode za izradu mreža kao i adaptivne metode ponovne izrade mreža na mjestima na kojima tijekom numeričkog proračuna dolazi do velike distorzije elemenata (remeshing). Nažalost, do sada razvijeni postupci učinkoviti su samo za geometrijski najjednostavnije trokutne ili tetraedarske elemente koji posjeduju relativno loša numerička svojstva. Stoga problem stvaranja kvalitetne mreže konačnih elemenata i danas predstavlja jedno od ključnih pitanja u MKE.

U numeričkoj analizi ljuskastih konstrukcija pomoću MKE posebni problem predstavlja pojava tzv. *locking* fenomena, koji u pravilu uzrokuju prekruti odaziv konstrukcije. U svrhu otklanjanja tih nepoželjnih efekata, u MKE razvijeno je mnoštvo postupaka koji uključuju metode reducirane integracije ili primjenu mješovitih varijacijskih principa kao što su Heillinger-Reissner ili Hu-Washizu princip. Iako su ti postupci više ili manje učinkoviti, njihova primjena može dovesti do novih poteškoća. Upotreba reducirane integracije može kod nekih elemenata prouzročiti pojavu tzv. modova nulte energije ili do *hourgla*ss efekta, koji se javljaju zbog smanjenog ranga matrice krutosti elementa. Te pojave također mogu izazvati pogrešan odziv konstrukcije. S druge strane, primjena mješovitih varijacijskih principa rezultira relativno složenim formulacijama konačnih elemenata koje ponekad imaju veliki broj stupnjeva, a postavlja se i pitanje određivanja optimalnih funkcija za aproksimaciju nepoznatih varijabli polja.

Iz gore navedenih razloga, u posljednjem desetljeću sve veću pažnju znanstvenika zaokuplja nova grupa numeričkih metoda koje se skupnim imenom nazivaju bezmrežne metode (*meshless methods*). Pomoću tih metoda moguće je numerički riješiti sustave parcijalnih diferencijalnih jednadžbi bez upotrebe geometrijskih mreža sastavljenih od elemenata koji su međusobno povezani čvorovima. Kod bezmrežnih metoda čvorovi nisu međusobno povezani u elemente prije početka numeričkog postupka. Štoviše, veze među čvorovima često se uspostavljaju automatskim postupcima koji se izvršavaju nakon pokretanja numeričkog proračuna. Na taj način moguće je postići znatnu uštedu vremena koje je potrebno utrošiti za izradu pogodne mreže konačnih elemenata. Također, upotrebom bezmrežnih metoda teoretski se mogu izbjeći problemi do kojih dolazi zbog velike distorzije elemenata tijekom numeričkih proračuna. Aproksimacijske sheme koje se koriste u bezmrežnim metodama omogućavaju izvođenje adaptivne diskretizacije jednostavnim dodavanjem, odnosno brisanjem čvorova iz modela. Obrada rezultata jednostavnija je kod bezmrežnih metoda nego u MKE kod problema kod kojih je naprezanje doista kontinuirano raspodijeljeno jer aproksimacijske funkcije koje se upotrebljavaju u bezmrežnim metodama u pravilu imaju visoki stupanj globalnog kontinuiteta. To u mnogim slučajevima rezultira globalno kontinuiranom i glatkom raspodjelom polja naprezanja. Nadalje, pokazalo se da je kod nekih bezmrežnih metoda moguće ublažiti neke od *locking* fenomena na principijelno jednostavniji način nego kod konačnih elemenata. Pri tome se često primjenjuju novi numerički postupci koje nije moguće primijeniti u MKE.

S obzirom da bezmrežne metode predstavljaju relativno novi koncept u numeričkoj mehanici u usporedbi s MKE, u dostupnoj literaturi trenutno je moguće naći relativno mali broj bezmrežnih formulacija namijenjenih analizi ljuskastih konstrukcija. Potrebno je također naglasiti da neki teorijski aspekti bezmrežnih metoda nisu ni približno tako dobro istraženi kao u MKE. Osjetljivost tih metoda na *locking* fenomene kao i otkrivanje procedura za njihovo uspješno otklanjanje trenutno je još uvijek jedno od otvorenih pitanja u istraživanju vezanom za bezmrežne metode. Ozbiljnu prepreku u upotrebi tih metoda u komercijalnoj primjeni predstavlja nezadovoljavajuća numerička neučinkovitost u pogledu potrošnje računalnog vremena i resursa. Zbog gore navedenih razloga kao motivacija za ovaj rad nametnula se potreba za razvijanjem nove bezmrežne numeričke strategije za analizu ljusaka kod koje će na efikasan način biti otklonjeni nepoželjni *locking* fenomeni.

BEZMREŽNE METODE

Intenzivan razvoj bezmrežnih metoda započeo je sredinom 90-tih godina prošlog stoljeća. Do sada je predložen veći broj metoda koje su uspješno primijenjene za rješavanje različitih fizikalnih problema. Neke od najzastupljenijih su bezmrežna Galerkinova metoda (*Element Free Galerkin (EFG) method*), metoda reprodukcije osnovnih djelića (*Reproducing Kernel Particle method, RKPM*), metoda glatkih hidrodinamičkih djelića (*Smoothed Particle Hydrodynamics (SPH) method*), bezmrežna lokalna Petrov-Galerkin metoda (*Meshless Local Petrov-Galerkin (MLPG) method*), metoda prirodnih elemenata (*Natural Element method, NEM*), lokalna metoda graničnih integrala (*Local Boundary Integral (LBIE) method*), metoda konačnih točaka (*Finite Point method, FPM*) i tako dalje.

Osnovna karakteristika svih bezmrežnih metoda je aproksimiranje nepoznatih veličina polja putem funkcija pomoću kojih se može provesti interpolacija razasutih podataka (*scattered dana interpolation*) bez podjele globalne domene u manje elemente, odnosno ćelije. Funkcije koje se trenutno najčešće koriste su metoda pomičnih najmanjih kvadrata (*Moving Least Squares, MLS*), funkcije radijalne baze (*Radial Basis Functions, RBF*), metoda reprodukcije osnovnih djelića (*Reproducing Kernel Particle method, RKPM*), metoda interpolacije u točkama (*Point Interpolation Method, PIM*) itd. Važno je naglasiti da su bezmrežne funkcije u pravilu znatno složenije od polinoma koji se koriste u MKE te da njihovo računanje iziskuje veći utrošak računalnog vremena. Također, složeni algebarski oblik tih aproksimacijskih funkcija doprinosi netočnosti i

nestabilnosti u numeričkoj integraciji jednadžbi pa je stoga razvoj učinkovitih algoritama za numeričku integraciju kod bezmrežnih metoda trenutno jedno od gorućih područja istraživanja.

Do danas nije napravljena jedinstvena sistematizacija bezmrežnih metoda, ali jedan od kriterija prema kojem se one mogu podijeliti je način na koji su zadovoljene jednadžbe problema. Tako se mogu razlikovati metode koje se temelje na jakim formama parcijalnih diferencijalnih jednadžbi (kolokacijske metode), metode koje koriste globalne slabe forme parcijalnih diferencijalnih jednadžbi (metode temeljene na EFG metodi, itd.) te metode kod kojih su parcijalne diferencijalne jednadžbe zadovoljene u tzv. lokalnim slabim formama (MLPG metoda, LBIE metoda, itd.). Da bi se provela numerička integracija slabih formi kod metoda koje se temelje na globalnim slabim formama, potrebno je koristiti neku vrstu globalne mreže sastavljene od geometrijskih elemenata koji se međusobno dodiruju duž svojih granica. Za razliku od tih metoda, kod tzv. pravih bezmrežnih metoda (*trully meshless methods*) teoretski je moguće provesti numeričku integraciju bez upotrebe bilo kakve globalne geometrijske mreže. U grupu pravih bezmrežnih metoda ubrajaju se bezmrežne metode koje se temelje na lokalnim slabim formama ili jakim formama jednadžbi sustava. Među njima posebni položaj zauzima MLPG metoda koja zbog svoje teorijske općenitosti i fleksibilnosti pruža široke mogućnosti u razvoju novih numeričkih strategija. Štoviše, može se pokazati da se gotovo sve preostale bezmrežne metode mogu izvesti kao posebni slučajevi MLPG metode.

Većina dostupnih bezmrežnih formulacija namijenjenih analizi ploča i ljusaka temelji se na nekoj od klasičnih teorija ljusaka. Pri izvodu takvih modela najčešće se koriste teorije ljusaka koje koriste Reissner-Mindlinove ili Kirchhoff-Loveove kinematičke pretpostavke. Pogodnost bezmrežnih metoda u takvim slučajevima proizlazi prije svega iz činjenice da neke bezmrežne funkcije inherentno posjeduju globalni kontinuitet visokog reda. U bezmrežnim metodama koje koriste takve funkcije zadovoljavanje C^1 kontinuiteta funkcija pomaka predstavlja trivijalan zadatak. Izvrstan ilustrativni primjer predstavljaju MLS funkcije kod kojih se C^1 kontinuitet lako postiže odabirom odgovarajuće težinske funkcije. Kao i kod MKE, u slučaju kad je debljina stjenke mala u odnosu na raspon konstrukcije, dolazi do pojave nenormalnog povećanja posmične ili/i membranske krutosti konstrukcije. Takvi fenomeni se u literaturi nazivaju poprečni posmični *locking* (*transversal shear locking*), odnosno membranski *locking* (*membrane locking*). Te pojave se često očituju kao prekruti odziv konstrukcije do

kojeg dolazi uslijed pogrešno proračunatih poprečnih posmičnih, odnosno membranskih komponenti deformacija. Ukoliko se ispravno ne otklone, *locking* pojave mogu dovesti do iznimno loših rezultata, posebice kod numeričkih formulacija temeljenih na metodi pomaka. Daljnji nedostatak bezmrežnih metoda temeljenih na klasičnim teorijama predstavlja nepotpunost tenzora deformacije, odnosno naprezanja, do čega dolazi zbog usvojenih pretpostavki o stanju deformacija, odnosno naprezanja. Iz tog razloga u te formulacije nije moguće ugraditi potpune trodimenzijske (3-D) materijalne modele. U numeričkim modelima koji se temelje na klasičnim teorijama ljusaka kao stupnjevi slobode numeričkog proračunskog modela se uz pomake javljaju i rotacije, što otežava spajanje takvih algoritama s općenitim 3-D numeričkim modelima.

Osim klasičnih teorija ljusaka u kojima je pretpostavljena linearna raspodjela pomaka u smjeru normale na srednju plohu, često se koriste i više teorije ljusaka (*higher shell theories*), gdje je raspodjela pomaka u smjeru normale opisana polinomom višeg reda. Takav pristup posebno je pogodan za razvoj bezmrežnih formulacija namijenjenih analizi ploča i ljusaka načinjenih od kompozitnih ili ortotropnih materijala. U te je algoritme moguće ugraditi potpune 3-D materijalne modele. Osjetljivost na *locking* efekte manja je nego kod modela temeljenih na klasičnim teorijama ljusaka zbog toga što su pomaci u smjeru normale aproksimirani polinomima visokog stupnja. Načelni nedostatak tih formulacija predstavlja veliki broj stupnjeva slobode neophodan za opisivanje kinematike ljuskastih konstrukcija, što dovodi do velikog utroška vremena i računalnih resursa potrebnih za provođenje numeričkih proračuna. Zbog toga upotreba viših teorija ljusaka nije prikladan pristup za razvoj bezmrežnih formulacija namijenjenih analizi ljusaka načinjenih od homogenih materijala. Slični zaključci vrijede i za direktnu primjenu 3-D bezmrežnih formulacija u numeričkim simulacijama procesa deformiranja u ljuskastim konstrukcijama.

Ploče i ljuske mogu se razmatrati kao 3-D deformabilna tijela primjenom tzv. *solid-shell* koncepta. U toj strategiji ljuskasta konstrukcija opisuje se kao 3-D deformabilno tijelo uz pretpostavku o linearnoj raspodjeli pomaka u smjeru normale na srednju plohu ljuske. Usvojene su Reissner-Mindlinove kinematičke pretpostavke prema kojima materijalna vlakna koja su u početnom stanju okomita na srednju plohu nakon deformiranja ostaju ravna, ali ne nužno i okomita na srednju plohu. Ipak, dopuštena je promjena duljine tog vlakna. Drugim riječima, normalna komponenta tenzora naprezanja u smjeru navedenih materijalnih vlakana uključena je u numerički model. Na taj način omogućena je ugradnja cjelovitih 3-D konstitutivnih jednadžbi u

solid-shell modele, pri čemu je kinematika ljuskastog kontinuuma opisana na relativno jednostavan način. Slično numeričkim formulacijama temeljenima na klasičnim teorijama ljusaka u kojima se primjenjuju Reissner-Mindlinove pretpostavke, i kod *solid-shell* algoritama mogu se javiti značajni poprečni posmični i membranski *locking* fenomeni ako se u njima aproksimira samo polje pomaka. Uz to, dolazi i do pojave tzv. Poissonovog *locking* efekta (*Poisson's thickness locking effect*). Taj *locking* fenomen javlja se u algoritmima kod kojih je poprečna normalna komponenta tenzora deformacije (normalna komponenta tenzora deformacije u smjeru normale na srednju plohu) konstantna po debljini (smjer normale na srednju plohu). Do njegove pojave dolazi kod materijala kod kojih je Poissonov koeficijent različit od nule, a očituje se u prekrutom odzivu konstrukcije. Intenzitet tog fenomena ne ovisi o dimenzijama konstrukcije pa se javlja i kod debelih i kod tankih ploča i ljusaka. Mehanizam nastajanja tog *lockinga* objašnjen je detaljno u odjeljku 5.3.1.

Slično kao i kod MKE, i kod bezmrežnih metoda su do sada predloženi razni postupci za otklanjanje raznih *locking* pojava. Nažalost, metode koje su se pokazale uspješnima u MKE u pravilu nisu direktno primjenjive u bezmrežnim metodama. Stoga danas postoji iznimna potreba za razvijanjem novih učinkovitih postupaka za otklanjanje *locking* efekata u bezmrežnim metodama. Pri tome trenutno veliki potencijal pokazuje primjena mješovitih formulacija. Detaljni pregled postojećih postupaka za otklanjanje locking fenomena u bezmrežnim metodama dan je u odjeljku 1.4.2 ovoga rada.

Kako učinkovitost numeričkih proračuna ljuskastih konstrukcija ovisi o točnosti opisivanja geometrije ljusaka i rubnih uvjeta pomaka, i kod bezmrežnih metoda je potrebno obratiti pažnju na te detalje. Za razliku od MKE gdje je geometrija promatrane konstrukcije opisana lokalno pomoću geometrije elemenata, kod bezmrežnih metoda potrebno je na neki način eksplicitno definirati geometriju cijele promatrane konstrukcije. U bezmrežnim metodama to je do sada izvedeno pomoću različitih aproksimacijskih shema (MLS funkcije, Lagrangeovi polinomi, itd.), preuzimanjem informacija o geometriji iz CAD modela ili matematički egzaktno u slučaju jednostavnih geometrijskih oblika. Pri tome se većina bezmrežnih metoda koristi nekim oblikom parametrizacije srednje plohe pomoću prikladnog skupa krivocrtnih koordinata.

Problem točnog zadovoljavanja rubnih uvjeta pomaka predstavlja još jedno od otvorenih pitanja u istraživanju bezmrežnih metoda. Za razliku od polinoma koji se

koriste u MKE, mnoge od bezmrežnih aproksimacijskih shema ne posjeduju interpolacijska svojstva u čvorovima. Zbog toga prilikom primjene takvih funkcija geometrijski rubni uvjeti nisu zadovoljeni *a priori*. Do sada je predloženo više postupaka za zadovoljavanje geometrijskih rubnih uvjeta. Neki poznatiji su metoda Lagrangeovih multiplikatora, modificirana kolokacijska metoda, kaznena metoda, povezivanje bezmrežnih metoda s konačnim ili rubnim elementima, transformacijska metoda, itd. Nijedna od tih metoda nije bez nedostataka. Njihova djelotvornost između ostalog značajno ovisi i o bezmrežnoj metodi koja se koristi u numeričkom proračunu. Kod MLPG metode od navedenih procedura za primjenu su najpogodnije modificirana kolokacijska metoda, kaznena metoda i transformacijska metoda.

HIPOTEZA RADA

Cilj ovog rada je razvijanje novih učinkovitih numeričkih formulacija namijenjenih analizi pločastih i ljuskastih konstrukcija u linearno-elastičnom području. Nove formulacije moraju biti fleksibilne. Stoga je poželjno da pripadaju grupi pravih bezmrežnih metoda kod kojih teorijski nije potrebno generirati nikakvu globalnu geometrijsku mrežu međusobno spojenih elemenata da bi se aproksimirale nepoznate veličine polja i provela numerička integracija. Navedene ciljeve moguće je ostvariti primjenom bezmrežne lokalne Petrov-Galerkinove (MLPG) metode za izvođenje diskretiziranog sustava jednadžbi, kao i primjenom *solid-shell* koncepta za opisivanje ljuskastog kontinuuma.

Predložene bezmrežne formulacije moraju biti numerički podjednako učinkovite pri analizi tankih i debelih ljuskastih konstrukcija, odnosno ne smiju biti osjetljive na pojavu *locking* efekata. Kod MLPG formulacija temeljenih na metodi pomaka, *locking* fenomene je moguće ublažiti ili čak u potpunosti eliminirati upotrebom i modifikacijom postupaka poznatih iz MKE. Neki od tih postupaka su hijerarhijska kvadratna interpolacija ili podizanje stupnja aproksimacijskih funkcija. Aproksimacijom deformacija ili naprezanja neovisno o pomacima moguće je razviti nove mješovite bezmrežne formulacije koje su neosjetljive na pojavu nekih od *locking* fenomena kao što su Poissonov i poprečni posmični *locking*.

MLPG *SOLID-SHELL* KONCEPT

U skladu sa *solid-shell* konceptom ljuska se razmatra kao 3-D deformabilno tijelo smješteno u globalnom Kartezijevom koordinatnom sustavu. Tijelo zauzima volumen

Ω koji je omeđen plohom Γ. U radu se razmatra samo statički slučaj opterećenja pa polaznu jaku formu diferencijalnih jednadžbi za sve izvedene formulacije predstavljaju standardne 3-D jednadžbe ravnoteže. Te jednadžbe moraju biti zadovoljene u svim točkama unutar Ω, a njihovo rješenje mora zadovoljiti pripadne geometrijske i prirodne rubne uvjete koji su propisani na globalnoj plohi Γ. U okviru ovoga rada geometrija ljusaka je opisana definiranjem geometrije srednje plohe i normale na srednju plohu. Pri tome je srednja ploha parametrizirana pomoću prikladnih krivocrtnih koordinata te je opisana matematički egzaktno. Pomoću metričkih vektora parametrizirani kontinuum se preslikava u parametarski prostor gdje se vrši diskretizacija kontinuuma pomoću parova čvorova. Čvorovi koji čine jedan par nalaze se na gornjoj, odnosno donjoj plohi ljuske i leže na istom materijalnom vlaknu koje je u početnom stanju okomito na srednju plohu ljuske.

Slabe forme 3-D jednadžbi ravnoteže izvedene su pomoću metode težinskog reziduala. Oko svakog para čvorova definira se područje koje se naziva lokalna sub-domena. Nakon toga se za svaku lokalnu sub-domenu formira tzv. lokalna slaba forma (*local weak form*, LWF) 3-D jednadžbi ravnoteže primjenom prihvatljive testne, odnosno težinske funkcije (*test functions*). Nepoznate funkcije polja aproksimiraju se pomoću odabranih aproksimacijskih funkcija koje se nazivaju probne funkcije (*trial functions*). U skladu s MLPG metodom, lokalne slabe forme izvedene su primjenom Petrov-Galerkinovog postupka kod kojeg testne i probne funkcije ne moraju pripadati istom prostoru funkcija. U ovom radu testne funkcije su opisane jednostavnim polinomima u smjeru normale na srednju plohu, dok se u ravnini koja je tangentna na srednju plohu koriste Heavisideove step funkcije. S druge strane, nepoznate veličine polja u svim predloženim algoritmima aproksimirane su primjenom MLS funkcija u tangentnoj ravnini, dok se u smjeru normale također koriste jednostavni polinomi.

Lokalne sub-domene koje pripadaju različitim parovima čvorova mogu biti različitih oblika i veličina i mogu se međusobno preklapati. Obično se koriste lokalne sub-domene jednostavnih geometrijskih oblika. U ovom radu lokalne sub-domene imaju oblik kvadra ili kružnog cilindra u parametarskom prostoru pri čemu se njihove vertikalne osi poklapaju sa smjerom normale na srednju plohu. Također, zbog jednostavnosti se lokalna sub-domena poklapa s domenom pripadne testne funkcije. Teoretski, lokalne sub-domene trebale bi u potpunosti prekrivati čitavu globalnu domenu Ω da bi rješenje lokalnih slabih formi ujedno bilo i rješenje jake forme 3-D jednadžbi ravnoteže za cijelo tijelo. Međutim, pokazalo se da se zadovoljavajući

rezultati ponekad mogu dobiti i ako unija lokalnih sub-domena ne pokriva Ω u potpunosti. Nakon što se izvrši aproksimiranje nepoznatih veličina polja, diskretizirani kontinuum se preslikava natrag u globalni Kartezijev sustav.

Interesantno je spomenuti da, za razliku od MKE, u MLPG metodi nije potrebno provoditi „klasično" *asembliranje* globalne matrice krutosti. Naime, ako su testne funkcije neke potpuno poznate funkcije, onda se iz diskretiziranih lokalnih slabih formi direktno dobivaju diskretizirane jednadžbe na globalnom nivou. Globalna matrica krutosti popunjava se po redcima sukcesivnim raspisivanjem lokalnih slabih formi jednadžbi ravnoteže za sve parove čvorova u modelu.

Izvodi lokalnih slabih formi koje služe kao polazišna točka za izvođenje formulacija predloženih u ovom radu, prikazani su u odjeljku 5.2. Osnovne ideje i terminologija vezana za MLPG metodu ukratko su objašnjeni u poglavlju 4 dok je u poglavlju 3 detaljno izložena MLS aproksimacijska shema.

Kao što je poznato iz MKE, *solid-shell* konačni elementi kod kojih se aproksimira samo polje pomaka osjetljivi su na razne *locking* efekte. U odjeljku 5.3 pokazano je na ilustrativnom primjeru, u kojem se razmatra ploča opterećena na čisto savijanje, da se kod *solid-shell* MLPG formulacija javlja Poissonov *locking* ako je komponenta pomaka u smjeru normale aproksimirana linearno duž normale. Na sličan način dokazana je i prisutnost poprečnog posmičnog *lockinga* u slučaju tankih ploča. Iz navedenih razmatranja može se zaključiti da je i kod bezmrežnih formulacija potrebno zadovoljiti slične uvjete kao i u MKE da bi se izbjegli navedeni *locking* efekti.

SOLID-SHELL MLPG FORMULACIJE KOJE SE TEMELJE SAMO NA APROKSIMACIJI POMAKA

Kao što je već spomenuto, kod MLPG formulacija temeljenih na metodi pomaka neovisna veličina polja je samo vektor pomaka. Poissonov *locking* izbjegnut je primjenom tzv. hijerarhijske kvadratne interpolacije (*hierarchical quadratic interpolation*) za komponentu pomaka u smjeru normale. Hijerarhijska kvadratna interpolacija objašnjena je u odjeljku 6.1, a rezultirajući diskretizirani oblik svih veličina polja izveden je u odjeljku 6.2.

Primjena hijerarhijske kvadratne interpolacije zahtijeva izračunavanje sedam nepoznatih veličina povezanih sa nekim parom čvorova. Te nepoznanice uključuju komponente pomaka u čvorovima i skalarni parametar povezan s hijerarhijskim kvadratnim članom. S druge pak strane, lokalne slabe forme dobivene primjenom

linearnih testnih funkcija predstavljaju skup od šest jednadžbi po svakom paru čvorova. Stoga je potrebno formirati dodatne jednadžbe kako bi se dobio zatvoreni sustav jednadžbi na globalnoj razini. U okviru ovoga rada predložena su dva različita *solid-shell* MLPG algoritma koja koriste hijerarhijsku kvadratnu interpolaciju za poprečnu komponentu pomaka.

U prvoj formulaciji opisanoj u odjeljku 6.3 dodatne jednadžbe za svaki par čvorova dobivene su postavljanjem dodatnog uvjeta ravnoteže u točkama koje leže na srednjoj plohi točno između čvorova koji tvore jedan par. Tako dobivene tri 3-D jednadžbe ravnoteže su zatim zbrojene kako bi se dobila jedna potrebna dodatna jednadžba po paru čvorova. Potrebno je naglasiti da dodavanje spomenutih kolokacijskih izraza ne zahtijeva dodatnu numeričku integraciju koja je u bezmrežnim metodama numerički zahtjevna i može biti izvor numeričke netočnosti rješenja. S druge strane, potrebno je računati drugu derivaciju MLS funkcija u kolokacijskim točkama što komplicira cijeli postupak u slučaju zakrivljenih ljusaka. Stoga je predloženi algoritam pogodniji za primjenu kod pločastih konstrukcija.

U drugoj formulaciji temeljenoj na metodi pomaka zatvoreni sustav jednadžbi na globalnoj razini dobiva se direktno iz lokalnih slabih formi primjenom testnih funkcija koje su kvadratne u smjeru normale. Kvadratni član testne funkcije rezultira trima novim jednadžbama u lokalnoj slaboj formi. Te su jednadžbe zatim zbrojene kako bi se dobila jedna dodatna jednadžba za svaku lokalnu sub-domenu, odnosno za svaki pojedini par čvorova. Izvod lokalne slabe forme za ovu formulaciju, kao i pripadne diskretizirane jednadžbe, dane su u odjeljku 6.4 ove doktorske teze. Za razliku od prethodne formulacije, ovdje je potrebno provesti numeričko integriranje dodatnih jednadžbi, ali s druge strane ne treba računati druge derivacije MLS funkcija. Zbog veće jednostavnosti, ovaj algoritam pogodniji je za proračun ljuskastih konstrukcija.

Rezultati provedenih numeričkih proračuna pokazali su da oba algoritma daju praktički istovjetne rezultate pri analizi debelih ploča i ljusaka te da upotreba hijerarhijske kvadratne interpolacije učinkovito otklanja Poissonov *locking*. Dobivene brzine konvergencije usporedive su s vrijednostima dobivenima upotrebom 3-D heksaedarskih konačnih elemenata iz programskog paketa MSC.Nastran. Potrebno je naglasiti da je zbog primjene hijerarhijske interpolacije potrebno definirati dodatne nepoznate skalarne parametre uz nepoznate čvorne komponente pomaka. Za razliku od MKE, te nepoznanice u prikazanim MLPG formulacijama nije moguće eliminirati iz sustava jednadžbi na lokalnoj razini pa je stoga broj jednadžbi u diskretiziranom

globalnom sustavu jednadžbi veći nego kod analognih formulacija konačnih elemenata. Rezultati proračuna vezanih za tanke ljuske također su jasno potvrdili postojanje poprečnog posmičnog *lockinga*, koji se u predloženim formulacijama manifestira usporenom konvergencijom te povećanom numeričkom nestabilnosti i netočnosti. Ta je nepoželjna numerička pojava ublažena povećanjem reda p-baze MLS funkcija, analogno postupku podizanja reda aproksimacijskih polinoma koji se ponekad koristi u MKE. Za razliku od MKE, kod bezmrežnih funkcija taj je postupak moguće provesti bez povećanja ukupnog broja čvorova, odnosno ukupnog broja globalnih stupnjeva slobode u proračunskom modelu. S druge strane, na taj način nije moguće u potpunosti otkloniti poprečni posmični *locking*, a proračunavanje MLS funkcija višeg reda zahtijeva značajan utrošak računalnog vremena. Nadalje, potrebno je definirati velike domene čvornih MLS funkcija oblika, što povećava širinu pojasa u matrici koeficijenata globalnog sustava jednadžbi zbog čega rješavanje globalnog sustava jednadžbi postaje numerički previše zahtjevno. Primijećeno je i da je stabilnost numeričke integracije smanjena u slučaju kad se primjenjuju MLS funkcije višeg reda.

MJEŠOVITE *SOLID-SHELL* MLPG FORMULACIJE

U sklopu ovog rada predložene su dvije nove mješovite MLPG formulacije za analizu ploča i ljusaka. Obje se formulacije temelje na 2-D mješovitom MLPG pristupu. U okviru tog pristupa, ovisno o potrebi, u slabim formama jednadžbi ravnoteže uz polje pomaka aproksimiraju se i komponente ostalih fizikalnih veličina kao što su tenzori deformacija, naprezanja ili gradijenta pomaka. Nakon toga se nepoznate čvorne vrijednosti tih dodatnih veličina izračunavaju preko aproksimiranih pomaka te se eliminiraju iz globalnog sustava jednadžbi. Predložena koncepcija otvara široke mogućnosti za izvođenje novih učinkovitih bezmrežnih metoda u numeričkoj mehanici.

Predložen je novi bezmrežni numerički postupak za rješavanje problema savijanja tankih ploča koji se temelji na mješovitoj MLPG metodi, gdje je uz polje pomaka neovisno aproksimirano i polje deformacija. Matematički opis modela dan je odjeljku 7.1 ovog rada. Oba polja aproksimirana su pomoću istih MLS funkcija u ravnini srednje plohe, dok su u smjeru normale primijenjeni jednostavni interpolacijski polinomi. Diskretizacija je provedena pomoću parova čvorova koji se nalaze na gornjoj i donjoj plohi ploče. Za svaki par čvorova definirane su cilindrične lokalne sub-domene za koje se pomoću Petrov-Galerkinova postupka izvode lokalne slabe forme 3-D uvjeta ravnoteže. Pri tome su testne funkcije opisane linearnim polinomima u smjeru normale

na srednju plohu, dok su u srednjoj ravninu primijenjene jednostavne Heavisideove step funkcije. Budući da se u ovoj formulaciji za aproksimaciju nepoznatih varijabli korištene MLS funkcije koje ne posjeduju Kronecker delta svojstvo, geometrijski rubni uvjeti zadovoljeni su pomoću kaznene metode. U ovako dobivenim lokalnim slabim formama kao neovisne varijable pojavljuju se komponente pomaka i deformacija. Za svaki par čvorova vezano je ukupno 18 nepoznatih čvornih veličina koje uključuju komponente vektora pomaka i 3-D tenzora deformacije u svakom čvoru. S druge strane, lokalne slabe forme predstavljaju skup od ukupno šest jednadžbi za svaki par čvorova. Može se lako zaključiti da je sustav jednadžbi na globalnoj razini otvoren. Zatvoreni globalni sustav jednadžbi dobiva se postavljanjem dodatnih 3-D kinematičkih relacija u čvorovima. Te se jednadžbe mogu dobiti primjenom kolokacijskog postupka koji je detaljno opisan u odjeljku 7.1.1. Pomoću tih dodatnih izraza izračunavaju se čvorne vrijednosti komponente deformacije pomoću neovisno aproksimiranih pomaka. Uvrštavanjem tako dobivenih dodatnih jednadžbi u lokalne slabe forme, eliminiraju se nepoznate čvorne vrijednosti deformacija iz diskretiziranih lokalnih slabih formi. Iz tako transformiranih jednadžbi izvodi se globalni sustav jednadžbi u kojem se kao nepoznati parametri javljaju samo čvorne komponente pomaka.

U odjeljku 7.1.3 prvo je teorijski dokazano pojavljivanje Poissonovog *lockinga* te je predložena nova procedura za njegovo otklanjanje. U tom postupku čvorne vrijednosti poprečne normalne komponente deformacije koje se dobivaju direktno iz aproksimiranih pomaka proširene su dodavanjem člana koji je linearan u smjeru normale na srednju plohu. Ti se članovi određuju postavljanjem dodatnih uvjeta ravnoteže u točkama koje se nalaze na srednjoj plohi ljuske točno između čvorova koji tvore parove. Odgovarajućim transformacijama čvornih veličina dobiva se konačna veza između modificiranih čvornih vrijednosti poprečnih normalnih komponenata tenzora deformacije i čvornih vrijednosti komponenata pomaka.

Učinkovitost predložene formulacije pokazana je numeričkim primjerima u kojima se razmatraju kvadratne ploče. U primjeru čiji su rezultati dani u odjeljku 7.3.1 pokazano je da je primijenjeni mješoviti MLPG superiorniji od MLPG formulacija temeljenih na metodi pomaka u pogledu točnosti i stabilnosti numeričke integracije. Rezultati jasno pokazuju da je kod mješovite metode potrebno primijeniti znatno manje točaka integracije po lokalnoj sub-domeni da bi se postigla ista točnost rješenja. Također je potvrđena učinkovitost predložene procedure za otklanjanje Poissonovog *lockinga*, a promatrana konvergencija je čak i bolja od rješenja dobivenih primjenom 3-

D heksagonalnih konačnih elemenata iz programskog paketa MSC.Nastran. Izvrsne konvergencije postignute su i za tanke ploče čak i u slučajevima kad su primijenjene MLS funkcije drugog reda, što ukazuje da izvedena mješovita formulacija nije osjetljiva na poprečni posmični *locking*. Takvo se ponašanje može pripisati direktnoj aproksimaciji komponenata deformacija. Ipak, procedura za otklanjanje Poissonovog *lockinga* zbog svoje je složenosti neprikladna za primjenu u numeričkoj simulaciji ljusaka.

Zbog toga je za analizu ljuskastih konstrukcija predložena nova mješovita formulacija gdje su uz polje pomaka direktno aproksimirane i određene komponente tenzora deformacija i naprezanja. Matematički model detaljno je prikazan u odjeljku 7.2. U ovoj formulaciji, jednadžbe modela izvedene su postavljanjem lokalnih slabih formi za lokalne sub-domene koje imaju oblik kružnog cilindra i kvadra u parametarskom prostoru. Testne funkcije su linearne u smjeru debljine ljuske, a u tangentnoj ravnini korištene su Heavisideove step funkcije. Za razliku od prethodno opisanih algoritama, komponente deformacija i naprezanja aproksimirane su u krivocrtnom koordinatnom sustavu. Pojava Poissonovog *locking* efekta eliminirana je postupkom zamjene neovisnih varijabli. Umjesto poprečne normalne komponente deformacije neovisna varijabla je poprečna normalna komponenta naprezanja. Zamjena varijabli provedena je pomoću konstitutivne jednadžbe za poprečnu normalnu komponentu naprezanja prema postupku koji je detaljno opisan u odjeljku 7.2.2. Poprečni posmični *locking* je odstranjen direktnom aproksimacijom komponenata tenzora deformacije, slično kao i kod formulacije za ploče. Sve veličine polja aproksimirane su pomoću istih MLS funkcija u tangentnoj ravnini. U smjeru normale na srednju plohu pretpostavljena je linearna raspodjela za sve komponente pomaka i tangentne komponente deformacije, a poprečne posmične komponente deformacije i poprečna normalna komponenta naprezanja su konstantni po debljini. U ovako dobivenom modelu svaki par čvorova posjeduje ukupno 15 neovisnih stupnjeva slobode dok lokalne slabe forme uključuju ukupno šest neovisnih jednadžbi. U svrhu dobivanja zatvorenog globalnog sustava jednadžbi za svaki par čvorova, odnosno za svaku lokalnu sub-domenu, postavljene su odgovarajuće dodatne ograničavajuće relacije za aproksimirane komponente deformacije i naprezanja. Ti su izrazi u ovom radu nametnuti primjenom odgovarajućih kolokacijskih postupaka objašnjenih u odjeljku 7.2.3. Iz tih je izraza nakon aproksimiranja neovisnih varijabli moguće izračunati nepoznate čvorne vrijednosti deformacija i naprezanja pomoću aproksimiranih pomaka.

Uvrštavanjem tako dobivenih izraza u diskretizirane lokalne slabe forme dobiva se sustav diskretiziranih jednadžbi na način opisan u odjeljku 7.2.4. U tako dobivenom sustavu jednadžbi pojavljuju se samo čvorni pomaci kao neovisne varijable.

U odjeljku 7.2.5 provedeno je teoretsko razmatranje računalnih troškova mješovite formulacije te je dokazano da je predložena formulacija mnogo učinkovitija od MLPG formulacije temeljene na metodi pomaka koja je prikazana u odjeljku 6.4. Jedan od razloga za takav ishod je činjenica da u mješovitom pristupu nije potrebno računati derivacije MLS funkcija u svakoj integracijskoj točki, nego samo u čvorovima. Odsutnost derivacija u sub-integralnim funkcijama povećava učinkovitost numeričke integracije jer je potrebno upotrijebiti manje točaka za postizanje iste točnosti, a smanjuje se i ovisnost rješenja o izboru veličina domena testnih (test functions) i probnih funkcija (trial functions). Nadalje, zahtijevani stupanj kontinuiteta aproksimacijskih funkcija je za jedan red niži nego kod formulacija temeljenih na metodi pomaka. Vrlo je važno naglasiti da mješovita formulacija nije toliko osjetljiva na poprečni posmični *locking* pa je stoga moguće primijeniti niži red p-baze MLS funkcije pri proračunu tankih ploča i ljusaka za postizanje iste točnosti. Gore navedeni zaključci potvrđeni su rezultatima provedenih numeričkih eksperimenata.

Rezultati provedenih numeričkih eksperimenata prikazani su u odjeljku 7.3. Utvrđeno je da predložene mješovite formulacije daju gotovo istovjetne rezultate pri analizi ploča. Pri tome je važno primijetiti da je Poissonov *locking* kod formulacije za ljuske uspješno otklonjen na principijelno jednostavniji način. To potvrđuje da je metoda zamjene neovisnih varijabli pogodan način za otklanjanje raznih *locking* fenomena u MLPG metodi. Provedene su i detaljne analize ponašanja predloženog numeričkog modela u slučajevima kada se za numeričku integraciju koriste cilindrične i heksagonalne lokalne sub-domene, kao i usporedba rezultata dobivenih primjenom interpolacijskih i „klasičnih" MLS funkcija. Interpolacijske MLS (IMLS) funkcije posjeduju Kronecker delta svojstvo u čvorovima pa su u tom slučaju geometrijski rubni uvjeti zadovoljeni na direktan način kao u MKE. Iz dobivenih rezultata jasno je da je ovisnost točnosti rješenja o veličini domene čvornih MLS funkcija oblika manja kad se upotrebljavaju IMLS funkcije. Kod ploča ta ovisnost ne ovisi značajnije o obliku lokalne sub-domene. Međutim, tijekom istraživanja utvrđeno je da je točnost i stabilnost rješenja pri analizi dvostruko zakrivljenih ljuskastih konstrukcija veća ako se upotrebljavaju heksagonalne lokalne sub-domene. Takvi rezultati vjerojatno su posljedica činjenice da Gaussove formule nisu prikladne za numeričku integraciju

trigonometrijskih funkcija koje je potrebno upotrijebiti da bi se opisala geometrija cilindričnih lokalnih sub-domena. Rezultati numeričkih testova provedenih za zakrivljene ljuskaste konstrukcije potvrdili su da mješoviti MLPG pristup nije osjetljiv na pojavu poprečnog posmičnog *lockinga*. Iako su korištene MLS baze drugog i trećeg reda, postignuta je veća točnost nego kod MLPG formulacija temeljenih na metodi pomaka kod kojih su korištene baze četvrtog ili višeg reda. Interesantno je spomenuti da su dobivene brzine konvergencije i postignuta točnost za momente savijanja usporedivi s brzinama konvergencije i razinama točnosti pomaka. Dobivene konvergencije pomaka u nekim primjerima su čak i bolje od rezultata dobivenih primjenom 3-D heksagonalnih konačnih elemenata. Važno je napomenuti da su kod predložene MLPG formulacije sve neovisne varijable aproksimirane istim aproksimacijskim funkcijama što nije slučaj kod *solid-shell* konačnih elemenata, gdje su aproksimacijske funkcije pojedinih neovisnih varijabli u pravilu različite. Ipak, rezultati primjera u kojem je razmatrana sferna ljuska opterećena koncentriranim silama ukazuju na moguću pojavu membranskog *lockinga* što je potrebno uzeti u obzir u budućem istraživanju.

ZAKLJUČAK I DOPRINOS RADA

Izvedene su nove bezmrežne formulacije za analizu ljuskastih konstrukcija koje se temelje na MLPG metodi. U svim predloženim algoritmima korišten je *solid-shell* koncept za opisivanje ljuskastog kontinuuma pri čemu su ljuske promatrane kao 3-D deformabilna tijela. Time je omogućena ugradnja potpunih 3-D materijalnih modela.

U formulacijama temeljenima na metodi pomaka Poissonov *locking* je otklonjen primjenom hijerarhijske kvadratne interpolacije za poprečnu komponentu pomaka, dok je poprečni posmični *locking* ublažen upotrebom visokog reda p-baze MLS funkcija. Zbog osjetljivosti na poprečni posmični *locking*, prikazane formulacije prikladne su za numeričke simulacije debelih ploča i ljusaka.

Mješoviti MLPG pristup je primijenjen za izvođenje dviju učinkovitih mješovitih *solid-shell* formulacija namijenjenih numeričkim simulacijama tankih ploča i ljusaka. Pri tome su razvijene dvije nove metode za eliminiranje Poissonovog *locking* efekta. Izvedeni mješoviti algoritmi nisu osjetljivi na poprečni posmični *locking* što je ostvareno direktnim aproksimiranjem komponenata deformacije.

Teoretski je utvrđeno postojanje Poissonovog i poprečnog posmičnog *locking*a u predloženim formulacijama te su objašnjeni uzroci njihova nastajanja. Također je provedena procjena računalnih troškova mješovitog MLPG *solid-shell* koncepta te je

teoretskim razmatranjima pokazano da je mješoviti MLPG *solid-shell* pristup numerički mnogo učinkovitiji od MLPG *solid-shell* pristupa u kojem se aproksimiraju samo pomaci. Rezultati numeričkih testova jasno potvrđuju teoretske pretpostavke.

U mješovitoj formulaciji za analizu ljusaka Poissonov i poprečni posmični *locking* eliminirani su na jednostavan i učinkovit način pa je taj algoritam posebno pogodan za primjenu u numeričkoj analizi tankih ljusaka. Pravilnim izborom parametara kao što su veličina domena testnih i probnih funkcija, njenom primjenom moguće je ostvariti konvergenciju i točnost koje su usporedive s onima koje se dobivaju primjenom komercijalnih 3-D heksagonalnih konačnih elemenata.

Kako bi razvijeni algoritmi postali prihvatljiva alternativa MKE u praktičnoj primjeni, nužno je u budućem istraživanju posvetiti značajnu pažnju unapređivanju njihove numeričke učinkovitosti. Očekuje se da će razvijeni mješoviti MLPG pristup poslužiti kao polazišna točka za razvijanje novih učinkovitih bezmrežnih algoritama koji će služiti rješavanju raznih nelinearnih problema vezanih za ljuskaste konstrukcije.

Keywords

Meshless methods, Meshless Local Petrov-Galerkin method, Moving Least Squares approximation, plates, shells, Poisson's thickness locking, transversal shear locking

Ključne riječi

bezmrežne metode, bezmrežna lokalna Petrov-Galerkinova metoda, metoda pomičnih najmanjih kvadrata, ploče, ljuske, Poissonov *locking*, poprečni posmični *locking*

Symbols and Abbreviations

Symbols

$\mathbf{A}_a$	metric vectors of middle surface of shell
$\mathbf{A}_3$	unit normal vector to middle surface of shell
$\mathbf{A}$	moment matrix of MLS approximation
$\mathbf{a}$	vector of coefficients of MLS approximation
$\mathbf{B}$	matrix used for evaluation of MLS shape functions
$\mathbf{B}_I$, $\tilde{\mathbf{B}}_I$	strain-displacement or strain/stress-displacement matrix related to node I
$\boldsymbol{\mathcal{B}}_J$	matrix that contains derivatives of strain-displacement matrix
$\mathcal{B}$	3-D continuum body
$\mathbf{b}$	body force vector
$\mathbf{C}$	material tensor
$\tilde{\mathbf{C}}$	modified 3-D elastic material matrix
c_0, c_1, c_2	arbitrary real constants
$\mathbf{D}$	3-D elastic material matrix
$\mathbf{D}_K$	3-D kinematic differential operator
$\mathbf{D}_\Omega$, $\mathbf{D}_\Gamma$	partial differential operators
$\boldsymbol{\mathcal{D}}$	vector that contains rows of 3-D elasticity matrix
d	distance
d_t	half-length of square in-plane base side of parallelepipedic local sub-domains
E	Young's modulus
$\mathbf{e}_i$, $\mathbf{e}^i$	unit vector of global Cartesian coordinate system
f	function
f_1, f_2	in-plane test functions
$\mathbf{G}$	metric tensor of a shell continuum
G	elastic shear modulus
$\mathbf{G}_i, \underline{\mathbf{G}}_i, \widehat{\mathbf{G}}_i$	covariant metric vectors

$\mathbf{G}^i$	contravariant metric vectors
$\sqrt{G}$	determinant of metric tensor
g_1, g_2	test functions that are linear in θ^3
h	structure thickness, distance
h_m	characteristic nodal distance
$\mathbf{I}_3$, $\mathbf{I}_6$	3x3 and 6x6 identity matrices, respectively
$\mathbf{J}$	Jacobian matrix
J^i_j, J_{ij}	terms of Jacobian matrix
J^{-1}_{ij}	terms of inverse Jacobian matrix
L_S	part of local boundary $\partial\Omega_S$ that is completely inside Ω
L^I_{s0}	intersection between local boundary $\partial\Omega^I_s$ and plate middle surface
$\mathbf{N}$	matrix containing components of unit normal vector to boundary
N	total number of nodes used for discretization, total number of nodes in domain of influence
$\mathbf{n}$	unit normal vector to boundary
n, $\tilde{n}$	total number of nodes influencing approximation at given point
n_c, n_r	numbers of integration points in circular and radial direction of cylindrical local sub-domain, respectively
n_g	total number of Gaussian points per local sub-domain
M	total number of nodes in domain of influence
m	number of terms in MLS basis
$M_{\alpha\beta}$	bending or twisting moments
O	upper bound of a given functions
$\mathbf{p}$	basis vector of MLS approximation
p	order of spline-type MLS weight function
R	convergence rate
$\mathbf{R}_A$, $\mathbf{R}_B$	residuals of strong form of differential equations
R_t	radius of local sub-domain, i.e., of support domain of test function
R_{tr}	radius of support domain of nodal shape trial function
$R_{\max}$	normalization parameter for local MLS coordinates

r	relative error of L_2 norm
r_s	radius of support domain of a MLS weight function
$\mathbf{T}$	transformation matrix for displacements in primal MLPG method
$\mathbf{T}^\sigma$	transformation matrix for stress tensor
T_e	computational time required for calculation of single term in global stiffness matrix
T_h	computational time needed for evaluation of MLS shape function at given point
T_K	computational time needed for assembling of global stiffness matrix
$T_{K\varepsilon}$	computational cost needed for integration of non-zero terms in discretized LWF
T_{mlt}	computational cost of matrix multiplication needed for replacing nodal strain and stress values by nodal displacement components
T_ω	computational cost of evaluating the nodal stress and strain values
$\mathbf{t}$	surface traction vector
t	time
t_w	computational time needed for calculation of MLS weight function at given evaluation point
$\mathbf{u}$	displacement vector
$\mathbf{u}_{(1)}$	displacement parameter that describes rotations
$\tilde{u}$	vector or matrix or trial functions
$\mathbf{u}'$	displacement vector in local curvilinear coordinates
$\mathbf{v}, \breve{\mathbf{v}}$	vector or matrix of test functions
v	test function for LWF
v_i	test function, components of velocity field
$v_{(ij\varepsilon)}, v_{(\varepsilon\alpha\beta)},$ $v_{(\varepsilon\alpha3)}, v_{(\sigma33)}$	test functions for additional kinematic constraints
W	weight function of MLS approximation
W_R	regularized weight function of MLS approximation
w	plate deflection
$\tilde{w}_R$	regularized function

$\mathbf{X}$	position vector
$\mathbf{X}_{(1)}$	shell director
α	penalty parameter
Γ	boundary of global domain, global boundary
Γ_{su}	part of local boundary $\partial\Omega_S$ with prescribed essential BC
Γ_{st}	part of local boundary $\partial\Omega_S$ with prescribed natural BC
Γ_t	part of global boundary Γ with prescribed natural BC
Γ_u	part of global boundary Γ with prescribed essential BC
γ	function that describes quadratic hierarchical interpolation
$\nabla\mathbf{d}^\mathrm{T}$, $\nabla\mathbf{d}_2^{\ T}$	matrix describing gradients of sets of test functions
δ_j^i, δ_{ij}, δ^{ij}	Kronecker-delta symbol
$\mathbf{\Phi}$, $\mathbf{\Phi}_u$	matrix of 3-D nodal shape functions for displacements
$\mathbf{\Phi}_\varepsilon$, $\mathbf{\Phi}_\omega$	matrix of strain and strain/stress 3-D shape functions for mixed formulations, respectively
ϕ	shape function of a trial function
$\mathbf{\varepsilon}$	strain tensor, strain vector
ε	regularization parameter
$\varepsilon_{\alpha\beta}^{(b)}$	covariant bending strain components
θ^k	parametric coordinates
λ	Lame's elastic constant, scalar parameter associated with hierarchical quadratic term
μ	Lame's elastic constant
ν	Poisson's coefficient
ξ^k	unit parametric coordinates
ρ	mass density
ρ_s	scaling factor for r_s
$\mathbf{\sigma}$	stress tensor, stress vector
$\mathbf{\Psi}$	matrix that describes displacement interpolation in shell thickness direction
ψ^1, ψ^2	functions that describe linear approximation of variables in

	thickness direction of structure
Ω	volume representing global domain, global domain
Ω_{inf}	domain of influence
Ω_s	volume representing local sub-domain, local sub-domain
Ω_{s0}	intersection between Ω_s and the X^1, X^2-plane for plate
Ω_t	support domain of test function
Ω_{tr}	support domain of trial function
Ω_X	definition of definition MLS at point $\mathbf{X}$
$\partial\Omega_s$	boundary of local sub-domain, local boundary
$\partial\Omega_s^{I+}$, $\partial\Omega_s^{I-}$	parts of $\partial\Omega_s^I$ that coincide with upper and lower plate surface, respectively
$\boldsymbol{\omega}$	vector of nodal strains and stress values
$(\ )_{(0)}, (\ )_{(1)}$	variable associated with middle surface of shell-like structure
$(\ )_{(u)}$	variable associated with upper surface of shell-like structure
$(\ )_{(l)}$	variable associated with lower surface of shell-like structure
$(\ )_i$	covariant components of first-order tensor, components of a vector
$(\ )_{ij}$	covariant components of second-order tensor
$(\ )_{ijkl}$	covariant components of fourth-order tensor
$(\ )^i$	contravariant components of first-order tensor
$(\ )^{ij}$	contravariant components of second-order tensor
$(\ )^{ijkl}$	contravariant components of fourth-order tensor
$(\ )^{-1}$	inverted matrix
$\overline{(\ )}$	prescribed value
$\hat{(\ )}$	nodal value
$(\ )^{(h)}$	approximated variable
$(\ )_I, (\ )^I$	variable associated with node I

$(\ )_{,X^i}$	first derivative with respect to Cartesian coordinate X^i
$(\ )_{,X^iX^j}$	second derivative respect to Cartesian coordinates X^i and X^j
$(\ )_{,\theta^i}$	first derivative with respect to curvilinear coordinate θ^i
d	distance
$(\ )_g$	variable associated with sample point
$(\ )^T$	transposed vector or matrix
$(\ )^{(c)}$	field variables that are compatible with displacements
$(\ )^d$	parameters associated with purely displacement-based algorithms
$(\ )^m$	parameters associated with mixed algorithms
$\|\ \|$	L_2 norm for given field variable

Abbreviations

2-D, 3-D	two-dimensional, three-dimensional
BC	boundary conditions
FEM	Finite Element Method
IMLS	interpolation MLS function
LWF	Local weak form
LSWF	Local symmetric weak form
MLS	Moving Least Squares, non-interpolation MLS function
MLPG	Meshless Local Petrov-Galerkin method

List of Figures

List of Tables

1 Introduction

1.1 Background and motivation

In the last couple of decades, numerical engineering computations have become indispensable for the analysis of complex engineering problems, due to their potential in solving large systems of partial differential equations. By properly using various numerical methods, it is possible to cut the costs and time needed for the development of new efficient products or to simulate the behaviour of already existing products realistically. Shell structures are perhaps the most widely used structural components in modern engineering due to their optimal ratio of weight and load-carrying capabilities. Classic examples of shell structures include ship hulls, aircrafts, space vehicles, cars, tanks, and pipelines in mechanical engineering, as well as reinforced shell roofs and membranes in civil engineering, etc.

The Finite Element Method (FEM) is the most popular and widely used numerical method in the simulation of shell structures. Although the method is robust, well developed, and has made an enormous impact over the past decades, it still suffers from some drawbacks. One of the prerequisites in using FEM is the existence of meshes consisting of congruent finite elements (FE), which may cause serious obstacles in the successful application of FEM. The creation of well-defined meshes can consume much of the analyst's available time. In general, it is preferable that the shapes of the finite elements are as ideal as possible, since their distorted geometry may negatively affect the solution accuracy. This is especially important in highly nonlinear problems involving large deformations, e.g., the crash analysis, metal forming, etc. In such cases, mesh distortion may cause the severe loss of accuracy or even the complete failure of computations.

Another challenging application of FEM is the crack propagation, where the crack growth normally does not coincide with the element boundaries. Remeshing procedures are usually applied to alleviate such problems. However, these procedures may lead to the further loss of accuracy, due to problems associated with the mapping of state variables from the old mesh to the new mesh, and also tend to increase the total computational costs (CPU time). Furthermore, from the mathematical point of view, the remeshing procedures are not simple problems, and so far, reliable adaptive mesh

generators that are capable of handling the 3-D hexahedral meshes in a satisfactory way do not exist. The stresses calculated by FEM are typically discontinuous along the elements boundaries, and the post-processing of stresses demands additional computational effort.

The appearance of the so-called locking phenomena, which may result in a completely erroneous deformation response of the computational model, poses an additional obstacle in the numerical analysis of shell-like structures. In order to alleviate these problems, different procedures exist in FEM, such as the reduced integration methods, the Assumed Natural Strains (ANS) method, the Discrete Strain Gap (DSG) method, the Enhanced Assumed Strain (EAS) method and various hybrid methods, among others. The FEM formulations may employ a combination of the aforementioned methods in order to successfully deal with various locking phenomena. Although such approaches may result in very efficient locking-free algorithms, their application may cause further unwanted problems, including "zero energy" modes, problems with passing various "patch" tests, a large number of internal degrees of freedom (DOF), etc. These problems must be treated properly through additional numerical techniques, further complicating the element formulations and possibly reducing computational efficiency. In order to gain better insight into the numerical modelling of shell-like structures by using FEM, one can refer to the review works [1],[2],[3], and the references therein, as well as many books dealing with the general application of FEM, such as [4],[5],[6],[7], to mention just a few from the vast pool of available literature.

Recently, a new class of numerical methods known commonly as meshless methods have attracted considerable attention from the academic community, due to their flexibility and capacity to solve boundary-value problems without the use of predefined meshes. Using these new numerical procedures, a computational model is represented simply by a set of nodes scattered within the global domain and on the global boundary. These nodes do not have to be connected into any kind of explicitly defined elements. Theoretically, information about the connectivity between the nodes is not required prior to the solving process. Thus, some issues associated with the meshes in FEM, such as the time-consuming mesh generation or element distortion problems, may be efficiently overcome. The connectivity between nodes may be established during the computation process itself, reducing the need for human labour, which is required for creating the element mesh. The problem of remeshing may also be alleviated simply by adding or removing the nodes as needed during the computation,

and by redefining the nodal connectivity in these local regions. In some meshless formulations, the resulting stress field is globally continuous, which simplifies the post-processing.

One of the more attractive fields for the application of meshless methods is the analysis of shell-like structures due to the flexibility of meshless algorithms, and the ability of meshless approximation functions to produce the interpolation field of a high order of continuity in a simple manner. Furthermore, it is supposedly possible to alleviate or circumvent some of the locking phenomena in a simpler manner than with FEM. However, since the meshless methods still represent a relatively new concept in computational mechanics, there are relatively few meshless formulations for shell-like structures available in the literature, as compared to FEM technology. Furthermore, meshless methods have not been investigated as thoroughly as FEM formulations. In that context, it has been concluded that there exists the need for further research on developing the general meshless formulation capable of successfully dealing with the various locking effects.

1.2 Meshless approximation functions

An essential component of all meshless methods is the use of functions that are able to approximate the data defined on randomly scattered points without employing the predefined mesh of elements. A number of different functions suitable for the application in meshless methods have been proposed, e.g., the Moving Least Squares (MLS) interpolation scheme [8], the Radial Basis Functions (RBF) [9],[10], the Reproducing Kernel Particle Methods (RKPM) [11], the Partition of Unity Methods (PUM) [12], the Point Interpolation Methods (PIM) [13], and the Natural Neighbour Interpolations [14].

In general, most of the functions currently employed in meshless methods are able to approximate data on randomly scattered nodes in a non cell-like manner. In FEM, only the nodes belonging to the same element influence the approximation values in each point inside that element. Conversely, in meshless functions usually only a finite number of nodes, positioned in the immediate neighbourhood of the point of interest, affect the approximation values at that point. An exception is the Natural Neighbour Interpolation scheme, where the approximants are constructed by employing the Voronoi tessellation and the Delaunay triangulation of a set of nodes. Although this approach results in well-defined and robust approximations and circumvents the need to

define various user-defined parameters, the tessellation procedure is similar to the creation of meshes in-based numerical methods.

In order to cut the computational costs needed for the calculation of trial functions, it is favourable to keep the total number of nodes influencing the approximation at the point of interest as small as possible. This concept of locality may be established in different ways, depending on the approximation scheme used. Two approaches currently dominate [13]:

- **The concept of the nodal domain of influence.** This approach is "static", as the influencing domains are associated with the predefined points, i.e., nodes that carry the data to be approximated. These regions are defined prior to the calculation. One of the criteria can be that some sufficient, yet minimal number of the nodal influencing domains covers each point in the computation domain.

- **The concept of the support domain associated with the sample point.** This is a "dynamic" approach in that the support domain is associated with the point of interest, i.e., the sample point, in which the approximation is calculated. The size of the support domain may vary for different points inside the computation domain. It may be defined by prescribing the minimal number of nodes influencing the approximation in the sample point. It is possible to find these nodes during the calculation by inspecting only the local neighbourhood of the current sample point.

It has been reported that the nodal influence domains is more efficient than the concept of support domain in the case of the arbitrary non-uniform distribution of nodes [13].

The calculation of meshless functions generally demand greater computational costs than the polynomial approximants used in FEM. Their analytical shape is also more complicated. The meshless approximants are usually non-polynomial rational functions. In contrast to FEM, the support domains of trial functions and the integration domains generally do not coincide, which may cause serious problems associated with numerical integration. Many meshless functions do not possess the Kronecker delta property at the nodes. In those cases, the imposition of the essential boundary conditions in meshless methods demands special attention. A detailed overview of certain approximation functions currently used in the meshless methods is available in [9], [10], [13], [15], [16].

1.3 Overview of meshless methods

Meshless methods have drawn the attention of the scientific community mainly because of their flexibility and the absence of the element meshes whose creation sometimes demands intensive human labour and whose topology may be the cause of various numerical problems. A number of different meshless methods have been proposed in literature. The most popular include the Element Free Galerkin (EFG) method [17], the Reproducing Kernel Particle Method (RKPM) [11], the Smoothed Particle Hydrodynamics (SPH) [18], the Meshless Local Petrov-Galerkin (MLPG) Method [19], the Local Boundary Integral Equation (LBIE) [20], the Method of finite Spheres [21], the Finite Point Method (FPM) [22], and the Natural Element Method (NEM) [14],[23].

The feature common to most of these approaches is that the existence of predefined mesh of congruent elements or cells is not necessary for the approximation of field variables. In some cases, it is even possible to perform the numerical integration of discretized equations in a non-cell manner. However, differences arise from the way in which the governing equations are satisfied, from the types of functions used for the approximation of test and trail functions, or from the techniques used for numerical integration.

1.3.1 Classification of meshless methods

So far, no unique systematic classification or even terminology has been adopted for meshless methods. Nevertheless, there are a couple of ways to categorize these methods. One is to classify the methods depending on the form of partial differential equations used during the solution procedure. According to this criterion, meshless methods may be divided into three distinct groups:

- **Methods based on the strong forms of governing equations.** Obtaining an exact solution of a practical engineering problem from a system of equations written in their strong forms is in general an exceptionally difficult task. Various collocation methods, such as the Finite Points Method [22],[24], as well as the formulations based on the finite difference method [25], employ the strong forms of equations. Although they are fast and simple to implement because numerical integration is completely avoided, such methods are notorious for their numerical instability and inaccuracy, especially in cases of non-uniform nodal distribution and irregular

computation domains. A special case is the Smooth Hydrodynamics (SPH) method, where improved stability and accuracy are obtained by an integral representation of approximation functions [13],[15],[18]. Another problem is how to satisfy the natural boundary conditions in the purely displacement collocation methods. Various procedures have been proposed to avoid this difficulty, such as the employment of local weak forms around the nodes positioned on the boundary with the prescribed essential boundary conditions [13], or the implementation of various mixed approaches [25],[26]. Furthermore, in those methods the unknown field variables have to posses a high order of continuity, which has to be equal to the degree of differential equations involved. Unfortunately, the meshless approximation function sometimes generates considerable inaccuracies in approximating the derivatives of higher order, which may severely affect the overall accuracy of the method.

▫ **Methods based on the global weak forms.** Due to the reasons mentioned above, many meshless methods are based on the global weak forms of governing equations. Such methods are in general more stable and produce more accurate results than the methods based on the strong forms. For the differential equations of the $2k^{th}$ order, in the global weak forms the continuity of a kth order for the field variables is required, which is a lower order than those required in the strong-form based methods. There exist various global weak forms of the partial differential equations. The global variational weak forms are a popular choice, like in the EFG methods that employ the Galerkin principle. The more general approach, called the Weighted Residual Method (WRM) is used in the Least-Squares Meshfree Method (LSMFM) [27].

Although very efficient in solving many different engineering problems, the methods based on the global weak forms still require certain meshes of contiguous background cells or elements. For instance, in the EFG and similar formulations, the congruent background cells are necessary to integrate the global weak forms. In some cases, the finite elements created by the existing FEM mesh generators serve as the integration cells [13]. If a nodal integration is employed, as in [28],[29],[30],[31], a solution domain has to be discretized by means of the Voronoi tessellation and Delaunay triangulation in order to define the node-dependant congruent integration cells. Furthermore, in the Natural Neighbour Galerkin methods [14],[23],[32], the Voronoi tessellation is required in order to create the

natural neighbour-based approximants, such as Sibson or Laplace interpolations. Although the use of various FEM mesh generators and the Voronoi tessellation brings significant advantages because they have been well developed within the framework of FEM technology, some of the drawbacks associated with meshes may be inherited, such as the time-consuming cell generation or the problems associated with mesh topology.

▫ **Methods based on the local weak forms.** These meshless methods are based on the concept of local weak forms [19],[20]. Instead of trying to satisfy the weighted residual form over the entire global domain, the governing equations are satisfied locally over the sub-domains positioned inside the global domain and defined around each node, i.e., the point that is used for the discretization of a global domain. Numerical integration is then performed over these local sub-domains. Since it is possible to define the local sub-domains and to approximate unknown variables without having to create any kind of mesh over the entire global domain, the numerical methods belonging to this group are sometimes called the truly meshless methods. The MLPG method [19], where the Petrov-Galerkin principle is employed to derive the local weak forms, is the origin of such numerical stratagem.

A good overview of the meshless methods and their applications, as well as of the weak or strong forms used in the meshless methods, can be found in [13],[15],[18],[33],[34], and the references contained therein.

1.3.2 The MLPG approach and the truly meshless methods

Atluri and Zhu developed the Meshless Local Petrov-Galerkin (MLPG) method [19] by introducing a local weak formulation of a considered physical problem. In this approach, the global set of equations is derived by writing the weak forms of governing equations over the small sub-domains defined around the nodes used for the discretization of a continuum. These nodaly-based local sub-domains also serve as the quadrature cells for the numerical integration of the weak forms. The size and shape of the local sub-domains may vary from node to node, and they may overlap each other. The desirable, but not necessary, condition is that the local sub-domains form a union set that completely covers the global computation domain.

For each node, it is theoretically possible to define the required size of the local sub-domain by taking into account only the layout of the nodes positioned in the immediate neighbourhood of the node. Furthermore, as in all meshless methods, various

meshless functions are used for trail and test functions. Consequently, the use of the global mesh of background cells or elements is avoided throughout the solution procedure; the MLPG method therefore represents a truly meshless concept.

The MLPG is a general platform for deriving other truly meshless methods. It employs the Petrov-Galerkin principle, so that the test and trail functions may come from different functional spaces. This means that their corresponding support domains may also differ in shape and size. It is important to note that a differential equation of a higher order possesses more than just one local weak form, and any one of these may be used for deriving various MLPG formulations [35],[36]. All of these features provide the MLPG method with great flexibility in solving various engineering problems. It is possible to devise many different variants of the MLPG method by choosing an appropriate combination of the test functions and trial functions, as well as the different shapes and sizes of their support domains. Accordingly, many other prominent truly meshless methods, such as the Local Boundary Integral Equation (LBIE) Method [20], the Method of Finite Spheres (MFS) [21], the Local Point Interpolation (LPIM) Method [37],[38], or the Local Radial Point Interpolation (LR-PIM) Method [38],[39], may be perceived as variants of the MLPG method. It is also possible to derive various collocation methods from the MLPG method by employing the Dirac delta function as the test function in the local weak forms.

Recently, Atluri et al. [40], developed a new mixed MLPG method, called the Meshless Finite Volume Method (MFVM). In this approach, both the displacements and strains are interpolated by means of the same meshless functions. For each node, the equilibrium equations are written in a local weak form in terms of the strain components. The nodal values of strain components are then eliminated from the equations by enforcing the strain-displacement relations directly at the nodes. In this way, in the closed global system of equations only the nodal displacements appear as unknown variables. The proposed mixed formulation is computationally superior to the purely-displacement meshless approaches because it avoids the differentiation of the shape functions at each integration point. Additionally, the continuity requirements for the trial functions are lower by one order. This approach has since then shown great potential in efficiently solving engineering problems. In [35], various formulations for solving the 4th order ordinary differential equations were presented. Analogous mixed collocation and finite difference schemes were presented in [25],[26], where the stresses are approximated in order to impose the traction boundary conditions directly, while the

employment of the mixed concept decreases the continuity requirements for the approximation functions.

Due to its generality and flexibility, the MLPG method has so far been successfully applied to solve a variety of engineering problems involving deformable solids. In [41], [42],[43], the MLPG method was applied for solving the 2-D elasto-static problems by employing different meshless functions, while Wang et al. [44], derived the natural neighbour Petrov-Galerkin method for elasto-statics. The 2-D MLPG approach was extended to the 3-D elasto-static problems in [45], where various MLPG formulations are presented. The MLPG algorithm for 3-D elastic problems involving material discontinuities was developed in [46]. Various 2-D elasto-dynamic problems were solved using the MLPG and LBIE method in [47],[48],[49], while a general 3-D MLPG formulation was introduced in [50].

The MLPG and LBIE approaches for solving geometrically nonlinear boundary value problems were presented in [51],[52],[53], and 2-D large deformation problems involving material nonlinearities were considered in [54],[55],[56]. Han and co-workers used a 3-D mixed MLPG in [57],[58] for solving complicated nonlinear dynamic problems, including high-speed impact, contact and penetration. Using the sub-domain variational inequalities, the contact problems have been successfully resolved [59],[60]. Heat conduction problems and thermo-elastic deformations have also been analyzed by the MLPG method [61], [62]. Information about the application of the MLPG method in the fluid mechanics, nanotechnology and multi-scale modelling may be found in [13],[15].

The MLPG method has been applied for the bending problems of thin beams [63], [64],[65], where the generalized moving least squares (GMLS) interpolation scheme [15] is especially suitable for approximation of deflections and rotations. Moreover, the MLS functions are especially suitable for the use in the MLPG formulations for solving the bending problems of thin plates, because the MLS approximations of a high continuity order may be obtained in a simple manner by choosing the suitable weight function, as shown in [66]. The LBIE method has been extensively used to solve various problems involving thin plates, e.g., the elasto-statics of thin plates [67], [68], thin elastic plates resting on elastic foundations [69], the elasto-dynamics of thin plates [70], and the large deflection of thin plates [71]. In [72] and [73], J. Sladek and co-workers presented the MLPG methods based on the Reissner-Mindlin theory to solve static and dynamic problems of shear-deformable thick plates. Recently, they have also

developed the MLPG formulations for the analysis of shallow shear-deformable shells [74], [75]. Thick homogeneous or composite laminated plates have been analyzed [76],[77],[78], where the higher-order plate theories are usually employed to describe the kinematics.

1.4 Meshless methods in the numerical analysis of shell-like structures

1.4.1 Numerical meshless shell models

There exist several different ways to obtain numerical shell modes in computational mechanics. They may be roughly divided in the following groups:

▫ **Numerical formulations that implement classical plate and shell theories directly.** Such models employ the classical shell theories directly to obtain the discretized systems of equations. In shell theories, a shell kinematics is associated with the middle surface of the structure by means of differential geometry. It is usually assumed that the displacements are distributed linearly across the thickness direction of the shell. Consequently, various kinematic constraints are introduced, such as the Kirchhoff-Love or Reissner-Mindlin assumptions. Furthermore, the models based on the shell theories that employ the linear displacement distribution across the shell thickness in general require a reduction of general 3-D material laws, because of the adopted assumptions about the state of the stresses in the shell continuum, such as plane stress tangent to the middle surface of the shell. The unknown kinematic variables in the resulting numerical models include both displacement and rotational degrees of freedom (DOF). For interpretation of the stresses over the thickness, the energetically adjoining dynamic variables associated with the middle surface are introduced, including the in-plane stress resultants, the bending and twisting moments and the transversal shear stress resultants. In some cases, the use of the higher-order shell theories that employ the higher-order polynomials to approximate the displacements in the thickness direction, is favourable.

▫ **Degenerated shell concept.** Such numerical shell models are obtained by direct degeneration of a 3-D continuum to the shell-like kinematics by assuming that the displacements are approximated linearly in the thickness direction. In the

degenerated shell concept, the mid-surface description, similar to those used in the classical shell theories, is implemented. This approach adopts the Reissner-Mindlin kinematic assumptions, including the straightness of the material line that is normal to the structure mid-surface, the unchanged structure thickness, and the non-existence of the transversal normal stress component.

▫ **Solid-shell concept.** Another approach, considered by some authors as an extension of the degenerated shell concept, is the solid-shell concept [3]. As in the degenerated shell concept, it is assumed that the material fibres that are initially normal to the shell middle surface remain straight, but not necessarily normal to the mid-surface, and the distribution of all displacement components is linear in the thickness direction in standard solid-shell formulations. However, the stretching of the fibre in the thickness direction is allowed, which enables the more realistic description of shell deformation response. Consequently, the normal stress component in the thickness direction is included in the solid-shell formulations, which allows the implementation of complete 3-D material models. The solid-shell concept is also more straightforward to implement than the models based on the shell theories. The kinematics is described by using only the displacement parameters, and the use of rotational degrees of freedom is avoided. Consequently, the connection of solid-shell numerical formulations with general 3-D solid models may be achieved directly without having to resort to the application of additional numerical procedures, such as the solid-to-shell transition elements. However, the FEM literature [93],[94],[95] makes clear that the purely-displacement solid-shell numerical models are prone to the appearance of a variety of locking effects.

▫ **Direct three-dimensional (3-D) continuum approach.** The concept of a general 3-D continuum is employed directly to shells without any further limitations.

More details about the numerical shell models, including their comparative advantages and disadvantages, can be found in [2],[79] and in the references therein.

Many available meshless formulations are based on the classical plate and shell theories. For example, the Kirchhoff-Love theory has often been employed for the thin plate formulations [66],[67],[80], as well as for the analysis of thin shells [81],[82],[83]. The MLS approximation scheme is used in these models to produce a C^1 continuous function in a simple and straightforward manner. Such formulations are not suitable for the application in the numerical simulations of thick structures. Therefore, most of the

meshless algorithms for plate/shell analysis employ the Reissner-Mindlin kinematical assumptions [28], [72], [74], [75], [84], [85], [29], [30], [86]. Therein, the effects of the transversal shear strains are taken into account and the assumption that the unit director vector remains straight - but not always normal to the mid-surface during deformation - is satisfied. Although the aforementioned algorithms are capable of achieving excellent convergences in solving a variety of different problems, they all possess the rotational DOF, which may lead to difficulties in properly describing the boundary conditions (BC). In geometrically nonlinear problems, complicated update procedures for the rotations are needed. In addition, special care should be taken if such formulations have to be connected with numerical 3-D solid algorithms where only the displacements appear as unknown nodal parameters. In FEM, algebraic constraints between the appropriate DOF of the solid and shell finite elements to be connected must be defined [87],[88]. Moreover, neither of the above-mentioned stratagems allows the implementation of a general 3-D material model due to the introduced reduction of a material law. This restriction may become problematic in numerical simulations involving material nonlinearities. Perhaps the most challenging problem in the displacement-based algorithms is the appearance of the membrane and shear locking in the thin structural limit.

One way to allow the implementation of complete 3-D material laws into meshless methods is to utilize the higher-order shell theories. The Higher-Order Shear and Normal Deformable Plate Theory (HOSNDPT) was used in [76] for the elasto-static simulation of homogenous thick plates. Similar to FEM, the higher-order theories are applied in meshless methods for the numerical computations involving composite shell-like structures. For example, HOSNDPT has been successfully implemented in the MLPG method for the elasto-static and elasto-dynamic analysis of functionally graded plates [77],[78], while the third-order Reddy theory, using multiquadric RBF, has been employed to model the mechanical behaviour of laminate composite plates and shells [89]-[91]. However, a large number of DOF over the thickness is needed for the description of shell kinematics, which is time-consuming and demands great computational effort if employed for modelling homogenous plates.

In [92], Li et al. used a direct 3-D continuum approach for the large deformations of thin shells. The proposed algorithm is simple to implement. Allegedly, it is free of shear and volumetric locking. However, it seems that at least three layers of nodes are

necessary in the thickness direction to capture the displacement gradients accurately, rendering it inefficient in the numerical simulations of homogeneous shells.

1.4.2 Locking effects in meshless methods

Efficient numerical formulations for the modelling of thin plates and shells should be free from locking phenomena. Unfortunately, these unwanted numerical effects have not been investigated in the context of meshless methods theoretically as thoroughly as they have with FEM. In early publications, it was even claimed that some of the meshless methods might be free from some locking effects [17],[96],[97]. However, in those cases the shape functions were calculated by using large support domains, which may have blurred the true behaviour of the proposed formulations with respect to locking [97]. Since then a deeper insight into the behaviour of meshless methods has been gained and a number of approaches have been proposed to solve these numerical anomalies.

The solid-shell finite elements based only on the approximation of displacements are plagued by the Poisson's thickness locking effect if the transversal displacement component is linear through the structure thickness. In such cases, the normal transversal strain component computed directly from displacements does not vary through the thickness, and locking arises if the Poisson's coefficient is different from zero. In meshless methods, the thickness locking effect has so far been avoided by employing the formulations based either on the higher-order shell theories [76], or on the 3-D direct continuum approach [92]. As detailed above, such formulations are computationally costly and time-consuming.

The appearance of the shear and membrane locking effects in the structural thin limit still presents a serious obstacle in the successful development and application of meshless methods. The shear locking phenomenon appears in the plate and shell formulations if they are unable to satisfy the zero transversal shear strain condition in the bending mode. As a result, parasitic transversal shear strains occur even in the pure bending state. On the other hand, membrane locking occurs only in curved structures if a numerical model is unable to represent the membrane forces in the bending state correctly. In that case, substantial parasitic membrane forces may appear during inextensional bending. Because of these parasitic forces, the deformation response of the numerical models may be completely erroneous. In both cases, the errors depend on

the structure length-to-thickness ratio, and become more severe as the thickness approaches zero.

Krysl and Belytschko detected the membrane locking effect by numerical experiments in their EFG formulation for thin shells based on the Kirchhoff-Love theory [81], and alleviated it by employing the MLS functions of a sufficiently high order. Since then, the analogous technique has been used in various plate and shell meshless formulations. In the formulation for thick plates presented in [85] the hp-cloud approximation of a high order was used to deal with the shear locking phenomenon. Similarly, Noguchi et al. used the EFG method for the geometrically nonlinear analysis of shear deformable shells in [86] and treated shear locking by employing the bi-cubic and quartic MLS functions. In [98] and [99], the shell theory based on the Cosserat continuum was employed for the static and dynamic analysis of spatial shell structures. The membrane and shear locking were detected in numerical experiments by evaluating the membrane and shear deformation energies as the fractions of the total deformation energy, and the error of calculated energies was decreased by raising the order of trial functions. The increase of the degree of interpolation functions in some meshless approximations, like the MLS functions, can be performed without adding new nodes or DOF to the discretized model, and consequently, the total number of DOF on the global level does not increase. However, such p-refinement only alleviates locking, while the calculation of the higher-order meshless shape functions demands significantly higher computational costs. In addition, further problems may appear because of the deteriorated stability of the numerical integration due to more complicated sub-integral functions.

Donning and Liu used cardinal splines as approximation functions in [84] and proposed the use of the so-called consistency paradigm to circumvent locking effects, wherein the rotation field shape functions were constructed by differentiating the displacements shape functions. Kanok-Nukulchai et al. implemented the analogous concept in [100] for the MLS functions in their EFG formulation for beams and plates, and obtained satisfying results even for the second-order MLS functions. However, it has been proved by Tiago and Leitão [101],[102] that such an approach may yield a rank deficient global system of equations within the Galerkin method, because the approximation functions for the rotation field are linearly dependent.

A formulation free of shear locking may also be obtained by applying a simple change of independent field variables, as proposed by Cho and Atluri [63] in their

MLPG method for the analysis of shear deformable beams, where they substituted the total rotations by transversal shear strains as independent variables. The analogous strategy was later employed in the EFG formulation for Timoshenko beam analysis in [101], and in the MLPG formulation for shear-deformable plate analysis [103]. Since in such an approach strains or rotations are approximated directly and separately from displacements, it may be considered a type of mixed formulation. It is important to note that the switch of independent variables does not increase the total number of DOF. It is furthermore possible to approximate all independent variables by using the same functions. On the other hand, the calculation and integration of the second-order shape functions derivatives are necessary, which increases computational costs.

Another form of mixed concept is adopted in the Stabilized Nodal Conforming Integration (SNCI) method [104], based on the nodal integration of the Galerkin meshless methods. Therein, the strain smoothing stabilization procedure for the integration of the bending energy is applied to eliminate shear locking in the thin structure limit [28]-[31]. Such an approach is numerically quite efficient due to the nature of the nodal integration. Nevertheless, the employed approximation functions have to satisfy some special requirements, such as the Kirchhoff conditions under pure bending and the integration constraints needed for achieving the bending exactness. In addition, SCNI works exceptionally well with the linear MLS basis, but its convergence degrades if the higher-order polynomial bases are used [105].

In meshless formulations, the mixed approaches usually used in FEM were first employed for the elimination of volumetric locking, which is accomplished by approximating the pressure and displacement fields separately, as in [97],[106], and the references therein. In addition, in [97] the selective reduced integration procedure was employed in the nodal integration. In the mixed formulations, the so-called inf-sup tests are often applied to test the stability and optimality of such approaches. For instance, the mixed MFS plate formulations that pass the inf-sub tests are locking-free and exhibit optimal or near-optimal convergence properties [107]. The classical B-bar method and the EAS procedures have also been adapted for the 2-D continuum EFG method [108]. Both methods perform equally well for uniform discretizations. The definition of congruent integration cell is obligatory, though, and the cell sizes are restricted by the layout of the nodes used for discretization, limiting the flexibility of the proposed formulations. Furthermore, a stabilization technique has to be employed in the B-bar approach in order to avoid "hourglassing," while the additional variables used in the

EAS formulation have to be condensed on the level of integration cells, which increases computational costs.

1.4.3 Description of shell geometry

In FEM, the geometry of a model is represented locally by the shapes of the finite elements. The same functions often approximate both the geometry and displacements in order to satisfy the zero-strain rigid body modes. In contrast, in meshless methods a set of nodes, positioned inside the global domain and on the global boundary, represents the entire geometry. In many cases the surface geometry is approximated between the nodes by employing the same meshless functions as for displacements [81],[82],[83],[98],[99].

If a finite element discretization is readily available, it can be used to obtain the positions of the nodes and the integration background cells [81],[98],[99]. Those background elements are then used for surface parameterization, enabling the description of arbitrary shapes. Belytschko and Krysl considered the effects of such surface approximations on the quality of solutions in [81], where they established certain surface approximation criteria for the MLS functions, e.g., the overall shape similarity, the preservation of symmetry, and the curvature and boundary representation. It has been found that MLS approximations in general cannot represent the symmetry and the boundary correctly, which may have a significant effect on the solution accuracy. One reason for this is that the approximated surface does not pass through the prescribed points if the applied functions do not posses the Kronecker delta property.

For relatively simple shapes, it is also possible to describe a 3-D geometry of the shell middle surface by mapping it from the global Cartesian coordinate system to the parametric curvilinear coordinate system. For example, Noguchi et al. employed the Lagrange polynomial functions for the representation of the smooth surfaces possessing C^1 continuity in [86]. For general shapes, the CAD parametric modelling technology may also be employed, as proposed in [30],[31]. In order to avoid problems associated with surface parameterization, in [29] Chan and Wang used the global Cartesian coordinates for the approximation of shell kinematics in arbitrary shell geometry. They propose two methods for eliminating the singularities in the Cartesian RKPM approximations of shell surface, which appear if the trial basis functions and shell surface functions are linearly dependant. For the simple geometrical surface shapes which can be described mathematically exactly, analytical equations are often used for

the geometry description, as in [74],[75]. Although straightforward, such an approach is not applicable for arbitrary shapes.

1.4.4 Enforcement of essential boundary conditions

One of the key issues in meshless formulations for plates and shells is the enforcement of the essential boundary conditions (BC). For the trial functions with the Kronecker delta property, such as the RBF or PIM approximation schemes, the essential BC are imposed directly, exactly as in FEM. However, as most of meshless approximation functions do not possess the Kronecker delta property, special techniques are necessary to impose the essential BC. A variety of procedures have been proposed, including the Lagrange multipliers [17], the use of the finite or boundary elements in regions with the prescribed essential BC [109], the collocation methods [96],[110], the penalty method [96], and the direct transformation method [111],[112].

Using the Lagrange multipliers is a well-known technique in FEM and is usually efficient. However, it introduces new unknowns into the governing equations and demands special solvers because the use of the Lagrange multipliers destroys the positive definiteness and bandedness of the resulting algebraic equations system. The direct collocation method is easy to implement, but Atluri and Zhu have shown [96] that it is not appropriate, since the meshless approximants lack the Kronecker Delta property and have thus proposed the modified collocation method.

Another numerically efficient method is the penalty method, which generally produces the same accuracy as the Lagrange multipliers, but only if the penalty parameter is appropriately selected [112]. Employing the finite or boundary elements at the global boundary with the prescribed essential BC is useful because it decreases the total computational costs. However, special techniques are needed to couple a finite or boundary element mesh with a region where a meshless method is applied, because of the non-compatible displacement distribution on the interface between the regions [109],[113],[114],[115],[116]. In the direct transformation method, a meshless function is reinterpreted as an interpolation, which passes through the actual nodal values. After performing such transformation, the essential BC are enforced in a straightforward manner, as in FEM. Nevertheless, the transformation procedure complicates the numerical implementation and demands additional computational costs for the calculation of the meshless approximations. Theoretically, any of the procedures

described above may work well in practice, but their efficiency generally depends on the meshless method employed, as well on the considered engineering problem.

1.5 Hypothesis, scope, and outline of the thesis

1.5.1 Hypothesis and aims of the thesis

The research presented in this thesis concerns the development of new meshless formulations for the elasto-static numerical analysis of shell-like structures. In order to achieve the full potential of meshless methods, the new algorithms should belong to the group of so-called truly meshless methods. Furthermore, the proposed meshless concepts should have as broad a theoretical scope as possible, and should not contain too many physical or mathematical restrictions. These goals can be reached by employing the Meshless Local Petrov-Galerkin (MLPG) method for deriving the discretized governing equations, as well as the solid-shell concept for describing the structure kinematics.

The new algorithms should be able to solve bending problems for both thick and thin shell-like structures without the loss of solution accuracy and stability due to the appearance of various locking phenomena. It is possible to eliminate, or at least alleviate, some of the locking phenomena in the displacement-based MLPG approach by borrowing suitable procedures from FEM, such as the hierarchical quadratic interpolation for the elimination of Poisson's thickness locking, or the raising of the trial function order for alleviating transversal shear locking. By approximating additional field variables separately from the displacement field, it is possible to derive a mixed concept free of the transversal shear and Poisson's thickness locking effect.

1.5.2 Research description and expected thesis contribution

This research deals with the development of novel meshless concepts suitable for the analysis of general shell-like structures. The new algorithms are based on the Meshless Local Petrov-Galerkin (MLPG) Method [15],[19], which is widely accepted as a general platform for all meshless methods. This approach is a truly meshless method, which does not require any kind of element mesh or background cells for either interpolation or integration. A computational model is discretized only by a set of nodes, which do not have to be connected into a mesh of elements. It is therefore

possible to avoid the human labour needed for the creation of a readily well-defined element mesh prior to the numerical analysis. Accordingly, it is expected that some of the numerical problems associated with the topology of the elements could be circumvented in the future applications of the proposed algorithms, such as the large deformation shell analysis.

In order to predict a deformation response for different problems accurately, it is desirable to impose as few restrictions on the stress state as possible. Accordingly, the solid-shell concept is adopted for the description of a shell-like continuum, according to [3],[93],[94],[95] and the references therein. In that case, the couples of nodes are used to discretize the shell structure, where the nodes are located on the upper and lower shell surfaces [93]. The solid-shell approach allows the implementation of complete 3-D material models and enables a simple connection of the proposed algorithms with 3-D solid models due to the absence of the rotational DOF.

The governing equations for the proposed formulations are the well-known equilibrium equations for a 3-D solid continuum, which obey the essential and natural BC on the global surface bounding the continuum. The discretized algebraic equations are derived by writing the equilibrium equations over the local sub-domains defined around each node couple. According to the solid-shell concept, the displacements are linear across the structure thickness, whereas the MLS functions are employed in the in-plane direction due to their good numerical features, such as a high order of the global continuity and of approximation consistency [15]. Since the MLPG method employs the Petrov-Galerkin principle, the test functions may be distinctively different from the trial functions. Here, the test functions that are linear in the structure thickness direction are chosen in order to obtain the closed system of equations, while the Heaviside step functions are applied in the in-plane directions.

As the MLS functions in general do not posses the Kronecker Delta property, special care should be devoted to the imposition of the essential BC. In this contribution they are enforced either in their local weak form by means of the penalty method [96], or by constructing the interpolating MLS procedure, similar to [117],[118].

This work analyzes only the shell geometry, which can be described exactly. Plate structures are considered as a special case of the shell geometry defined by zero value of the Gaussian curvature. Although such approach is not applicable for arbitrary shell geometries, in this way the negative effect of the inaccurate geometry description on the solution quality is avoided.

As the first step of the research, plates and shells are studied by approximating only the displacement field, leading to the so-called primal MLPG formulations. The aim is to develop efficient algorithms for the numerical analysis of thick shell-like structures. Since various numerical locking effects appear in the purely displacement-based approaches [4],[80],[81],[84],[86], some known techniques for the avoidance of those undesirable numerical phenomena are modified and implemented in the developed formulations. For example, the Poisson's thickness locking effect is eliminated by applying the hierarchical quadratic interpolation in the structure thickness direction [93], while the raising of the order of the MLS basis is expected to alleviate shear and membrane locking in the structure thin limit [80],[81],[84],[86].

In addition, some theoretical considerations are performed, with the aim of revealing the cause of the thickness and the transversal shear locking effect in the proposed meshless formulations. Furthermore, the influence of the certain parameters, characteristic for meshless methods, on the accuracy and stability of solutions is performed.

The second part of this research is devoted to the development of novel mixed MLPG formulations for the numerical analysis of general shell-like structures. Due to their theoretical straightforwardness and efficiency, they are based on the mixed MLPG approach proposed by Atluri and co-workers [35],[40]. The shear locking is eliminated by employing the approximation of both the strains and displacements. Two novel procedures for avoiding the Poisson's thickness phenomenon are proposed. The first is derived by modifying the nodal values for the normal strain component in the thickness direction, while the second one is based on an appropriate switch of independent field variables, analogous to [63],[103]. In all cases, the reduction of the total number of the unknown nodal variables is performed by means of appropriate collocation procedures.

Since the above-described mixed MLPG approach is numerically more efficient than the primal MLPG formulations [40], it is expected that the proposed novel formulations will show similar traits. Furthermore, the transversal shear locking effect should be efficiently alleviated even for the low-order MLS functions. Consequently, smaller support domains of the nodal shape functions may be used. In addition, the differentiation of the MLS functions over the local sub-domains is avoided, further increasing numerical efficiency and stability in comparison with the primal meshless methods. In addition, the continuity requirements for the trial functions are lower in the mixed MLPG approach.

It is expected that this work will contribute to the numerical analysis of shell-like structures by means of meshless methods, as well as to the further development of the MLPG method in general. The proposed MLPG formulations will represent a broad theoretical platform for developing new meshless formulations. Depending on the engineering problem, it should be possible to devise new and more efficient formulations by employing relatively few modifications to the proposed algorithms. By appropriately choosing the size and shape of the support domains of both the trial and test functions, as well as the size and shape of the local sub-domains, novel MLPG algorithms could be specially designed for solving specific engineering problems.

1.5.3 Outline of the thesis

This doctoral thesis is organized into eight chapters. In Chapter 2, the relations and methods of the continuum mechanics that are important for the solid-shell meshless formulations proposed in this work are given. A special attention is given to the weighted residual method (WRM), which is applied for deriving the weak forms of the governing equations. The MLS approximation scheme is described in detail in Chapter 3, together with some implementation details and findings gained during the research. Chapter 4 deals with the MLPG method, on which the developed formulations are based. Thereby the general idea of the MLPG is explained, the corresponding terminology used in the work is introduced, and some of the method's features, which are relevant for this contribution, are emphasized. In Chapter 5, the solid-shell MLPG concept is presented, and various corresponding local weak forms of governing equations are derived. Furthermore, the Poisson's and transversal shear locking effects that appear in the developed MLPG solid-shell approach are revealed from the theoretical point of view. Chapter 6 concerns with the purely displacement-based MLPG algorithms. Two different ways for deriving the discretized system of equations are explained in detail, and the numerical features of developed formulations are exposed by suitable numerical examples. The mixed MLPG solid-shell approach is presented in Chapter. 7. Two different formulations for the analysis of plates and shells are presented, and the claims about their numerical efficiency are corroborated by a set of numerical tests. The concluding remarks are given in Chapter 8.

2 Basic relations of Continuum Mechanics for MLPG solid-shell formulations

In this chapter, some important relations and methods of the continuum mechanics, which are necessary for developing the solid-shell meshless formulations proposed in this work, are given. The description of the geometry and kinematics used in the presented models are described in detail first. As herein only linear static problems are considered, the small-strains theory is adopted and the basic relations for linear elastic 3-D solids are presented. The 3-D constitutive relations for the linear isotropic Hookean materials are given next. The equilibrium equations and the corresponding boundary conditions for a 3-D static problem, which represent the strong form of the governing equations for the presented MLPG formulations, are explained. Finally, the weighted residual method (WRM) applied for deriving the weak forms of the governing equations is described in details. The reader is referred to the literature dealing with the continuum mechanics and shell theories, such as [120],[121],[122], for obtaining a deeper insight into the presented problematics.

2.1 Kinematics of the solid-shell approach

In the solid-shell concept, the kinematics of the shell structures is described by using only the displacements associated with the couples of material points. The points of the same couple are positioned on the upper and bottom structure surface and lie on the same material fibre that is initially oriented normally to the middle surface of the shell. During the deformation process, the fibre remains straight, but not necessarily normal to the middle surface.

2.1.1 Geometry Description and Mapping Techniques

A 3-D shell geometry is described by

$$\mathbf{X}\left(\theta^j\right) = X^i\left(\theta^j\right)\mathbf{e}_i = \psi^1\left(\theta^3\right)\mathbf{X}_{(u)}\left(\theta^\alpha\right) + \psi^2\left(\theta^3\right)\mathbf{X}_{(l)}\left(\theta^\alpha\right) \tag{2.1}$$

with the functions $\psi^1\left(\theta^3\right)$ and $\psi^2\left(\theta^3\right)$ defined as

$$\psi^1\left(\theta^3\right)=\frac{1}{2}+\frac{\theta^3}{h}, \qquad \psi^2\left(\theta^3\right)=\frac{1}{2}-\frac{\theta^3}{h}. \tag{2.2}$$

Herein $\mathbf{e}_i$ denotes the unit vectors in the global Cartesian coordinate system, while $\mathbf{X}_{(u)}\left(\theta^a\right)$ and $\mathbf{X}_{(l)}\left(\theta^a\right)$ are the position vectors associated with the upper and lower structure surface, respectively, as shown in Figure 2.1.
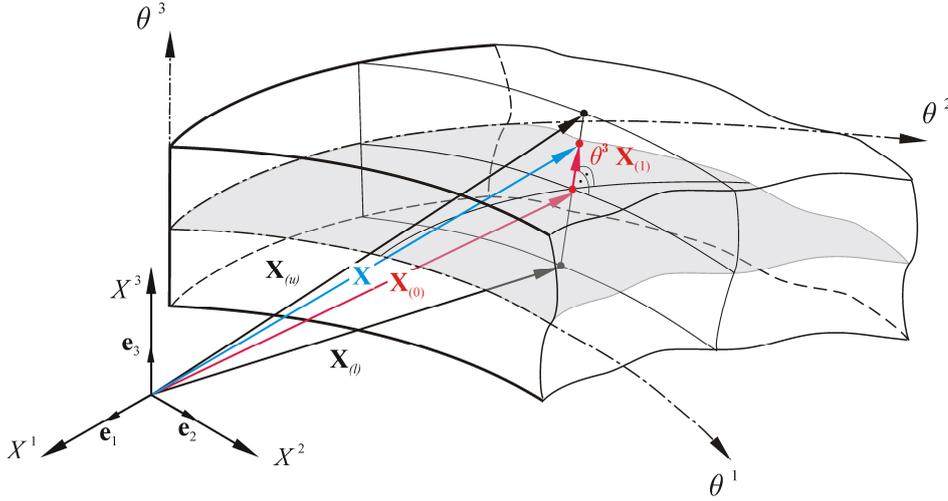
Figure 2.1 Geometry description of shell continuum. Position vectors.

The shell is parameterized by the curvilinear coordinates θ^j, where θ^α denotes the middle surface coordinates, while $\theta^3 \in \left[-h/2, h/2\right]$ is the local coordinate in the thickness direction, i.e., in the direction normal to the middle surface. h stands for the shell thickness.

In this work, the Greek indices take the values 1 or 2, and the Latin indices represent the numbers 1, 2 or 3, unless not specified otherwise. Furthermore, for the sake of clearness, from here on the arguments of the variables are omitted unless they are essential for the understanding of the presented subject.

Similarly to the approach taken in [119], instead of describing the geometries of both the upper and lower surfaces simultaneously, the relation (2.1) may be directly rewritten in the form used in the degenerated shell concept as

$$\mathbf{X}\left(\theta^j\right)=\mathbf{X}_{(0)}\left(\theta^\alpha\right)+\theta^3\,\mathbf{X}_{(1)}\left(\theta^\alpha\right) \tag{2.3}$$

with $\mathbf{X}_{(0)}$ as the middle surface position vector and $\mathbf{X}_{(1)}$ as the unit shell director, which are expressed by the relations

$$\mathbf{X}_{(0)}\left(\theta^{\alpha}\right)=\frac{1}{2}\left[\mathbf{X}_{(u)}\left(\theta^{\alpha}\right)+\mathbf{X}_{(l)}\left(\theta^{\alpha}\right)\right], \quad \mathbf{X}_{(1)}\left(\theta^{\alpha}\right)=\frac{1}{h}\left[\mathbf{X}_{(u)}\left(\theta^{\alpha}\right)-\mathbf{X}_{(l)}\left(\theta^{\alpha}\right)\right]. \quad (2.4)$$

Because in this contribution only the shell geometries that may be described mathematically exactly are considered, the expressions (2.3) and (2.4) are more convenient because the geometry of the shell continuum may now be described by defining only the shell middle surface and its shell director.

By inspecting the expression for $\mathbf{X}_{(1)}$ in equation (2.4), and taking into account the assumption about the position of the material point couples in the initial configuration, it can be easily concluded that $\mathbf{X}_{(1)}$ is actually identical with the unit normal vector to the shell middle surface. According to Basar and Krätzig [120], the normal vector may be easily calculated as

$$\mathbf{A}_{3}=\mathbf{X}_{(1)}=\frac{\mathbf{A}_{1}\times\mathbf{A}_{2}}{\left|\mathbf{A}_{1}\times\mathbf{A}_{2}\right|}, \quad (2.5)$$

with

$$\left|\mathbf{A}_{1}\times\mathbf{A}_{2}\right|=\sqrt{A}=\sqrt{A_{11}\,A_{22}-A_{12}}, \quad A_{\alpha\beta}=\mathbf{A}_{\alpha}\cdot\mathbf{A}_{\beta}. \quad (2.6)$$

Herein $\mathbf{A}_{\alpha}$ are the covariant metric vectors of the middle surface, shown in Figure 2.2,

$$\mathbf{A}_{\alpha}\left(\theta^{\delta}\right)=\left.\frac{\partial\mathbf{X}\left(\theta^{\delta}\right)}{\partial\theta^{\alpha}}\right|_{\theta^{3}=0}=\mathbf{X}_{(0)}\left(\theta^{\delta}\right),_{\theta^{\alpha}}. \quad (2.7)$$

The covariant basis vectors for each point in the shell continuum, illustrated in Figure 2.2, are calculated as

$$\mathbf{G}_{\alpha}\left(\theta^{j}\right)=\frac{\partial\mathbf{X}\left(\theta^{j}\right)}{\partial\theta^{\alpha}}=\mathbf{X}_{(0)}\left(\theta^{\delta}\right),_{\theta^{\alpha}}+\theta^{3}\,\mathbf{X}_{(1)}\left(\theta^{\delta}\right),_{\theta^{\alpha}}=\mathbf{A}_{\alpha}\left(\theta^{\delta}\right)+\theta^{3}\,\mathbf{A}_{3}\left(\theta^{\delta}\right),_{\theta^{\alpha}},$$

$$\mathbf{G}_{3}\left(\theta^{j}\right)=\frac{\partial\mathbf{X}\left(\theta^{j}\right)}{\partial\theta^{3}}=\mathbf{X}^{(1)}\left(\theta^{\delta}\right)=\mathbf{A}_{3}\left(\theta^{\delta}\right),$$

$$(2.8)$$

while the reciprocal or contravariant metric vectors are defined by means of the Kronecker-delta symbol δ_{j}^{i} as

$$\mathbf{G}^{i}=\delta_{j}^{i}\mathbf{G}_{i} \quad (2.9)$$

with δ^i_j defined as

$$\delta^i_j = \delta_{ij} = \delta^{ij} = \begin{cases} 1, & \text{if } i = j \\ 0, & \text{if } i \neq j \end{cases}. \tag{2.10}$$

Equation (2.9) yields the following expressions for the contravariant metric vectors

$$\mathbf{G}^1 = \frac{\mathbf{G}_2 \times \mathbf{G}_3}{\sqrt{G}}, \quad \mathbf{G}^2 = \frac{\mathbf{G}_3 \times \mathbf{G}_1}{\sqrt{G}}, \quad \mathbf{G}^3 = \frac{\mathbf{G}_1 \times \mathbf{G}_2}{\sqrt{G}}, \tag{2.11}$$

with

$$\sqrt{G} = \det(\mathbf{G}) = [\mathbf{G}_1, \mathbf{G}_2, \mathbf{G}_3] = \mathbf{G}_1 \cdot (\mathbf{G}_2 \times \mathbf{G}_3) \tag{2.12}$$

as the determinant of the metric tensor $\mathbf{G}$, which is defined as

$$\mathbf{G} = (\mathbf{G}_i \cdot \mathbf{G}_j)\mathbf{e}^i \otimes \mathbf{e}^j = G_{ij}\mathbf{e}^i \otimes \mathbf{e}^j. \tag{2.13}$$
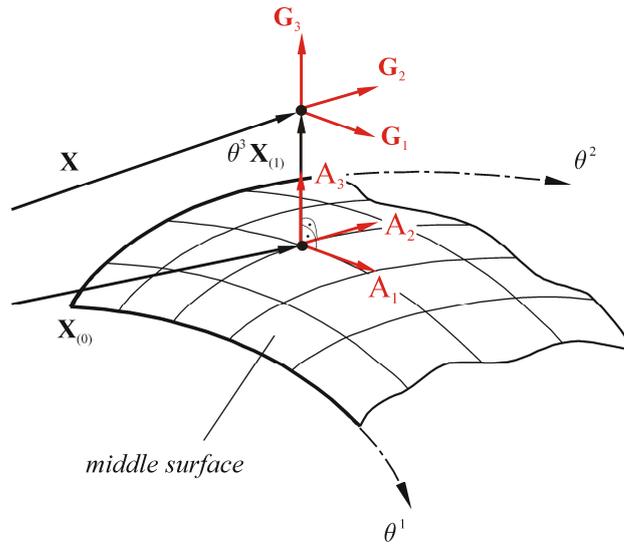
Figure 2.2 Metric covariant vectors

By employing relations (2.9)-(2.13) for the Cartesian coordinate system, it may be easily shown that $\mathbf{e}_i = \mathbf{e}^i$. Consequently, the covariant and contravariant tensor components defined in the Cartesian coordinate system are identical, e.g., $a_i = a^i$ and $a_{ij} = a^{ij}$. From now on, this fact is used through this work without any further referencing, and no distinction is made between such components.

The mapping of vectors and tensors from the curvilinear to the global Cartesian coordinate system is done by using the Jacobian matrix $\mathbf{J}$, defined as

$$\mathbf{J}\left(\theta^{k}\right)=\begin{bmatrix} \dfrac{\partial X^{1}}{\partial \theta^{1}} & \dfrac{\partial X^{1}}{\partial \theta^{2}} & \dfrac{\partial X^{1}}{\partial \theta^{3}} \\[2mm] \dfrac{\partial X^{2}}{\partial \theta^{1}} & \dfrac{\partial X^{2}}{\partial \theta^{2}} & \dfrac{\partial X^{2}}{\partial \theta^{3}} \\[2mm] \dfrac{\partial X^{3}}{\partial \theta^{1}} & \dfrac{\partial X^{3}}{\partial \theta^{2}} & \dfrac{\partial X^{3}}{\partial \theta^{3}} \end{bmatrix}=\begin{bmatrix} \mathbf{G}_{1} & \mathbf{G}_{2} & \mathbf{G}_{3} \end{bmatrix}, \tag{2.14}$$

as well as its inverse matrix $\mathbf{J}^{-1}$, which may be written as

$$\mathbf{J}^{-1}\left(\theta^{3}\right)=\begin{bmatrix} \dfrac{\partial \theta^{1}}{\partial X^{1}} & \dfrac{\partial \theta^{1}}{\partial X^{2}} & \dfrac{\partial \theta^{3}}{\partial X^{1}} \\[2mm] \dfrac{\partial \theta^{2}}{\partial X^{1}} & \dfrac{\partial \theta^{2}}{\partial X^{2}} & \dfrac{\partial \theta^{2}}{\partial X^{3}} \\[2mm] \dfrac{\partial \theta^{3}}{\partial X^{1}} & \dfrac{\partial \theta^{3}}{\partial X^{2}} & \dfrac{\partial \theta^{3}}{\partial X^{3}} \end{bmatrix}=\begin{bmatrix} \mathbf{G}^{1} \\ \mathbf{G}^{2} \\ \mathbf{G}^{3} \end{bmatrix}. \tag{2.15}$$

The contravariant components of a vector $\mathbf{v}=v^{i}\,\mathbf{e}_{i}=\underline{v}^{i}\underline{\mathbf{G}}_{i}$ are transformed from a curvilinear coordinate system $\left\{\underline{\theta}^{1},\underline{\theta}^{2},\underline{\theta}^{3}\right\}$ with the metric vectors $\underline{\mathbf{G}}_{i}$ to the global Cartesian system $\left\{X^{1},X^{2},X^{3}\right\}$ with the unit metric vectors $\mathbf{e}_{i}$ as follows

$$v^{i}=\mathbf{e}^{i}\left(\underline{v}^{j}\,\underline{\mathbf{G}}_{i}\right)=\left(\mathbf{e}^{i}\cdot\underline{\mathbf{G}}_{i}\right)\underline{v}^{j}=\frac{X^{i}}{\underline{\theta}^{j}}\underline{v}^{j}=J^{i}_{j}\underline{v}^{j}. \tag{2.16}$$

Herein v^{i} and $\underline{v}^{i}$ are the contravariant components in the global Cartesian and curvilinear coordinates, respectively, while J^{i}_{j} are the terms of the Jacobian matrix $\mathbf{J}$. Analogously, for the contravariant components of a second-order tensor $\mathbf{T}=T^{ij}\mathbf{e}_{i}\otimes\mathbf{e}_{j}=\underline{T}^{ij}\underline{\mathbf{G}}_{i}\otimes\underline{\mathbf{G}}_{j}$ the transformation rule is

$$T^{ij}=\mathbf{e}^{i}\left(\underline{T}^{kl}\,\underline{\mathbf{G}}_{k}\otimes\underline{\mathbf{G}}_{l}\right)\mathbf{e}^{j}=\left(\mathbf{e}^{i}\cdot\underline{\mathbf{G}}_{k}\right)\underline{T}^{kl}\left(\underline{\mathbf{G}}_{l}\cdot\mathbf{e}^{j}\right)=\frac{X^{i}}{\underline{\theta}^{k}}\frac{X^{j}}{\underline{\theta}^{l}}\underline{T}^{kl}=J^{i}_{k}J^{j}_{l}\underline{T}^{kl}. \tag{2.17}$$

Herein T^{ij} and $\underline{T}^{ij}$ are the contravariant components of the tensor $\mathbf{T}$ defined in the global Cartesian and curvilinear coordinate system, respectively. The covariant tensor components may be transformed by applying analogous formulas [121].
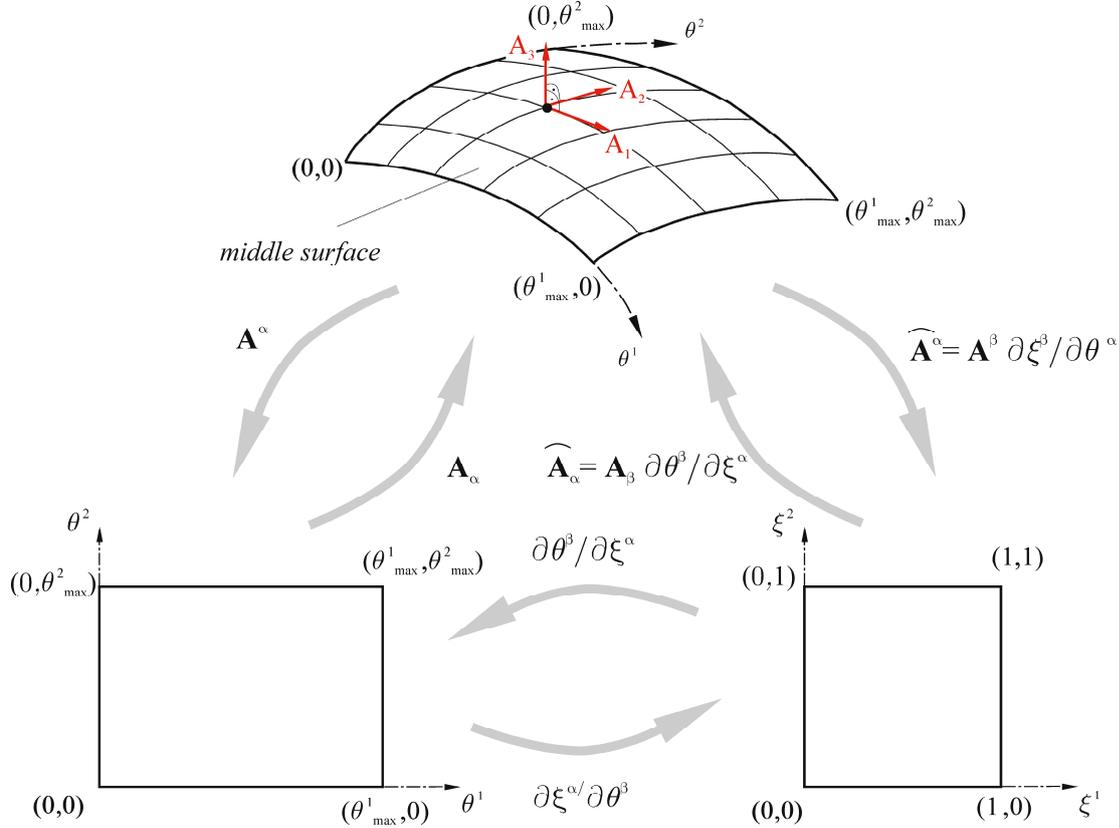
Figure 2.3 Parameterization and mapping of shell middle surface

It is possible to parameterize the curved surface in different ways. Here the curvilinear coordinates $\theta^\alpha \in \left[0, \theta^\alpha_{\text{max}} \right]$ are used, which map the middle surface to the rectangle in the θ^1, θ^2- parametric plane, according to Figure 2.3. Alternatively, the curved middle surface may be mapped by using the normalized parametric coordinates defined as $\xi^\alpha = \dfrac{\theta^\alpha}{\theta^{(\alpha)}_{\text{max}}}$, and thus their range is $0 \le \xi^\alpha \le 1$. Such an approach is convenient because it maps all quadrilateral surface patches to the unit square in the ξ^1, ξ^2- parametric plane, as shown in Figure 2.3. For the normal coordinate, it holds that $\xi^3 = \theta^3$. In that case, the covariant metric vectors may be computed by means of equations (2.8) as

$$\widehat{\mathbf{G}}_k \left(\xi^j \right) = \frac{\partial \mathbf{X} \left(\theta^j \left(\xi^i \right) \right)}{\partial \xi^k} = \frac{\partial \mathbf{X} \left(\theta^j \right)}{\partial \theta^l} \frac{\partial \theta^l}{\partial \xi^k} = \mathbf{G}_l \frac{\partial \theta^l}{\partial \xi^k} , \qquad (2.18)$$

$$\hat{\mathbf{A}}_\alpha\left(\xi^j\right) = \frac{\partial \mathbf{X}_{(0)}\left(\theta^\gamma\right)}{\partial \xi^\alpha} = \frac{\partial \mathbf{X}_{(0)}\left(\theta^\gamma\right)}{\partial \theta^\beta}\frac{\partial \theta^\beta}{\partial \xi^\alpha} = \mathbf{A}_\beta \frac{\partial \theta^\beta}{\partial \xi^\alpha} \ . \tag{2.19}$$

The mathematical description of the geometrical shapes used in the numerical experiments in this work is presented in Table 2.1. It should be noted that for a rectangular plate $\theta^i = X^i$, and consequently $\mathbf{G}_i = \mathbf{e}_i$.

Circular cylindrical surface in cylindrical coordinates	
	Position vector $$\mathbf{X}^{(0)}\left(\theta^\alpha\right) = R\cos\left(\frac{\theta^1}{R}\right)\mathbf{e}_1 + $$ $$R\sin\left(\frac{\theta^1}{R}\right)\mathbf{e}_2 + \theta^2\mathbf{e}_3$$
Spherical surface in spherical coordinates	
	Position vector $$\mathbf{X}^{(0)}\left(\theta^\alpha\right) = R\cos\left(\frac{\theta^1}{R}\right)\cos\left(\frac{\theta^2}{R}\right)\mathbf{e}_1 + $$ $$R\sin\left(\frac{\theta^1}{R}\right)\cos\left(\frac{\theta^2}{R}\right)\mathbf{e}_2 + R\sin\left(\frac{\theta^2}{R}\right)\mathbf{e}_3$$
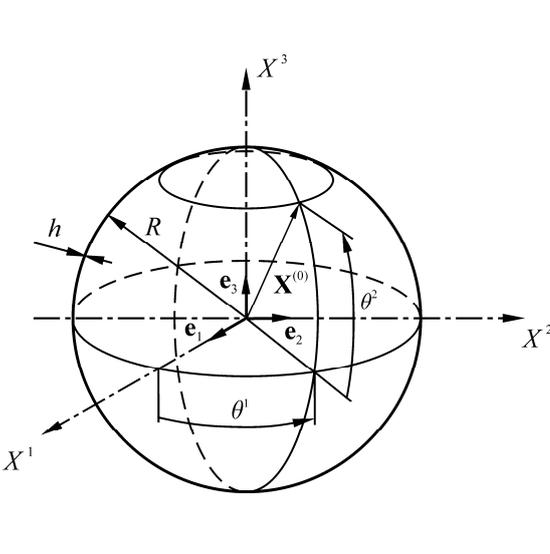
Table 2.1 Shell geometry. Middle surface position vectors for some simple shell geometries

2.1.2 Displacements

According to the solid-shell concept, the linear distribution over the thickness is assumed for the displacements in the directions of the global Cartesian axes as

$$\mathbf{u}\left(\theta^{j}\right)=u^{i}\left(\theta^{j}\right)\mathbf{e}_{i}=\psi^{1}\left(\theta^{3}\right)\mathbf{u}_{(u)}\left(\theta^{\alpha}\right)+\psi^{2}\left(\theta^{3}\right)\mathbf{u}_{(l)}\left(\theta^{\alpha}\right), \tag{2.20}$$

where $\mathbf{u}_{(u)}\left(\theta^{\alpha}\right)=u^{i}_{(u)}\left(\theta^{\alpha}\right)\mathbf{e}_{i}$ and $\mathbf{u}_{(l)}\left(\theta^{\alpha}\right)=u^{i}_{(l)}\left(\theta^{\alpha}\right)\mathbf{e}_{i}$ are the displacement vectors associated with the points on the upper and lower surfaces, respectively. The functions ψ^{1} and ψ^{2} describe their linear distribution over the structure thickness according to (2.2). Analogously to the position vector $\mathbf{X}$, the displacement vector $\mathbf{u}$ may be written in terms of the variables associated with the middle surface as

$$\mathbf{u}\left(\theta^{j}\right)=\mathbf{u}_{(0)}\left(\theta^{\alpha}\right)+\theta^{3}\,\mathbf{u}_{(1)}\left(\theta^{\alpha}\right). \tag{2.21}$$

The variables $\mathbf{u}_{(0)}$ and $\mathbf{u}_{(1)}$ are defined by

$$\mathbf{u}_{(0)}=\frac{\mathbf{u}_{(u)}+\mathbf{u}_{(l)}}{2},\qquad\mathbf{u}_{(1)}=\frac{\mathbf{u}_{(u)}-\mathbf{u}_{(l)}}{h}, \tag{2.22}$$

where $\mathbf{u}_{(0)}\left(\theta^{\delta}\right)=u^{i}_{(0)}\left(\theta^{\delta}\right)\mathbf{e}_{i}$ stands for the middle surface displacement vector, while $\mathbf{u}_{(1)}\left(\theta^{\delta}\right)=u^{i}_{(1)}\left(\theta^{\delta}\right)\mathbf{e}_{i}$ describes the total rotations.

2.1.3 Strains

Adopting the small strain theory, the strain tensor may be calculated from the displacements as follows [121]

$$\boldsymbol{\varepsilon}=\varepsilon_{ij}\mathbf{G}^{i}\otimes\mathbf{G}^{j}=\frac{1}{2}\left(\mathbf{G}_{i}\cdot\mathbf{u}_{,\theta^{j}}+\mathbf{G}_{j}\cdot\mathbf{u}_{,\theta^{i}}\right)\mathbf{G}^{i}\otimes\mathbf{G}^{j}. \tag{2.23}$$

The strain tensor $\boldsymbol{\varepsilon}$ may be written in the vector form as

$$\boldsymbol{\varepsilon}^{T}=\begin{bmatrix}\varepsilon_{11} & \varepsilon_{22} & \varepsilon_{33} & 2\varepsilon_{12} & 2\varepsilon_{23} & 2\varepsilon_{13}\end{bmatrix}, \tag{2.24}$$

which is suitable for the use in the discretized numerical models. Relation (2.23) may then be rewritten in a matrix form as

$$\boldsymbol{\varepsilon} = \mathbf{D}_K \mathbf{u} \tag{2.25}$$

with $\mathbf{D}_K$ as the 3-D kinematic differential operator

$$\mathbf{D}_K = \begin{bmatrix} \mathbf{G}_1 \cdot (\ )_{,\theta^1} \\ \mathbf{G}_2 \cdot (\ )_{,\theta^2} \\ \mathbf{G}_3 \cdot (\ )_{,\theta^3} \\ \mathbf{G}_1 \cdot (\ )_{,\theta^2} + \mathbf{G}_2 \cdot (\ )_{,\theta^1} \\ \mathbf{G}_2 \cdot (\ )_{,\theta^3} + \mathbf{G}_3 \cdot (\ )_{,\theta^2} \\ \mathbf{G}_1 \cdot (\ )_{,\theta^3} + \mathbf{G}_3 \cdot (\ )_{,\theta^1} \end{bmatrix}. \tag{2.26}$$

By employing (2.23), the strain components are defined in the global Cartesian coordinates by

$$\boldsymbol{\varepsilon} = \varepsilon_{ij} \mathbf{e}^i \otimes \mathbf{e}^j = \frac{1}{2} \left(\frac{\partial u^i(\theta^k)}{\partial X^j} + \frac{\partial u^j(\theta^k)}{\partial X^i} \right) \mathbf{e}^i \otimes \mathbf{e}^j. \tag{2.27}$$

Herein the derivatives are evaluated by employing the chain derivative rule as

$$\frac{\partial u^i(\theta^k)}{\partial X^j} = \frac{\partial u^i(\theta^k)}{\partial \theta^p} \frac{\partial \theta^p}{\partial X^j}, \tag{2.28}$$

where $\partial \theta^p / \partial X^j$ are the components of the contravariant metric vectors (2.9).

2.2 Constitutive Relations and Stresses

The 3-D constitutive equations, which give the relationship between the strain and stress tensors, may be written by employing the generalized Hook's law as

$$\sigma^{ij} = C^{ijkl} \varepsilon_{kl}, \tag{2.29}$$

where σ_{ij} represents the components of the stress tensor

$$\boldsymbol{\sigma} = \sigma^{ij} \mathbf{G}_i \otimes \mathbf{G}_j, \tag{2.30}$$

which, analogously to the strain tensor vector $\boldsymbol{\varepsilon}$ (2.24), may be written as a vector as

$$\boldsymbol{\sigma}^T = \begin{bmatrix} \sigma^{11} & \sigma^{22} & \sigma^{33} & \sigma^{12} & \sigma^{23} & \sigma^{13} \end{bmatrix}. \tag{2.31}$$

C^{ijkl} stands for the material tensor

$$\mathbf{C} = C^{ijkl}\mathbf{G}_i \otimes \mathbf{G}_j \otimes \mathbf{G}_k \otimes \mathbf{G}_l. \tag{2.32}$$

For the arbitrary curvilinear coordinates, the material tensor components for a linear isotropic Hookean material are

$$C^{ijkl} = \lambda G^{ij} G^{kl} + \mu(G^{ik} G^{jl} + G^{il} G^{jk}), \tag{2.33}$$

where λ and μ are the Lame's elastic constants

$$\lambda = \frac{E\nu}{(1+\nu)(1-2\nu)}, \qquad \mu = \frac{E}{2(1+\nu)}. \tag{2.34}$$

Herein E and ν are the Young's modulus and Poisson's coefficient, respectively, and $G^{ij} = \mathbf{G}^i \cdot \mathbf{G}^j$ are the contravariant components of the metric tensor $\mathbf{G}$. In the Cartesian coordinates, expression (2.33) assumes the form

$$C^{ijkl} = \lambda \delta^{ij} \delta^{kl} + \mu(\delta^{ik} \delta^{jl} + \delta^{il} \delta^{jk}). \tag{2.35}$$

By employing (2.33), and taking into account the orthogonality $\mathbf{G}^3 \perp \mathbf{G}^\alpha$ in the applied shell kinematics, the material tensor may be written in the matrix form as

$$
\mathbf{D} = \lambda
\begin{bmatrix}
G^{11}G^{11} & G^{11}G^{22} & G^{11}G^{33} & G^{11}G^{12} & 0 & 0 \\
G^{22}G^{11} & G^{22}G^{22} & G^{22}G^{33} & G^{22}G^{12} & 0 & 0 \\
G^{33}G^{11} & G^{33}G^{22} & G^{33}G^{33} & G^{33}G^{12} & 0 & 0 \\
G^{12}G^{11} & G^{12}G^{22} & G^{12}G^{33} & G^{12}G^{12} & 0 & 0 \\
0 & 0 & 0 & 0 & 0 & 0 \\
0 & 0 & 0 & 0 & 0 & 0
\end{bmatrix}
+
$$

$$
\mu
\begin{bmatrix}
2G^{11}G^{11} & 2G^{12}G^{12} & 0 & 2G^{11}G^{12} & 0 & 0 \\
2G^{12}G^{12} & 2G^{22}G^{22} & 0 & 2G^{22}G^{12} & 0 & 0 \\
0 & 0 & 2G^{33}G^{33} & 0 & 0 & 0 \\
2G^{11}G^{12} & 2G^{12}G^{22} & 0 & G^{11}G^{22}+G^{12}G^{12} & 0 & 0 \\
0 & 0 & 0 & 0 & G^{22}G^{33} & G^{12}G^{33} \\
0 & 0 & 0 & 0 & G^{12}G^{33} & G^{11}G11^{33}
\end{bmatrix}.
\tag{2.36}
$$

Note that similar form may be obtained from (2.35) for the elasticity matrix in the global Cartesian system. By employing (2.24), (2.31) and (2.36), constitutive relations (2.29) may be rewritten in the matrix form as

$$\boldsymbol{\sigma} = \mathbf{D}\boldsymbol{\varepsilon}. \tag{2.37}$$

The components of a stress vector $\mathbf{t} = t^i \mathbf{G}_i$ acting over a boundary surface $\partial\Omega$ may be calculated as

$$t^i = \sigma^{ij} n_j, \tag{2.38}$$

where n_j stands for the components of the outward unit normal vector to $\partial\Omega$. Employing (2.31), the matrix form of (2.38) reads as

$$\mathbf{t} = \mathbf{N}\boldsymbol{\sigma} \tag{2.39}$$

with $\mathbf{N}$ as the matrix describing the unit outward normal on $\partial\Omega_s$

$$\mathbf{N} = \begin{bmatrix} n_1 & 0 & 0 & n_2 & 0 & n_3 \\ 0 & n_2 & 0 & n_1 & n_3 & 0 \\ 0 & 0 & n_3 & 0 & n_2 & n_1 \end{bmatrix}. \tag{2.40}$$

2.3 Equation of equilibrium

Consider a body $\mathscr{B}$, occupying a volume Ω bounded by a surface Γ, as shown in Figure 2.4, at time t. The body is subjected to the traction $\mathbf{t}$, i.e., the force measured per unit surface area $\mathrm{d}\Gamma$, and to the body forces $\mathbf{b}$ defined per unit volume $\mathrm{d}\Omega$.
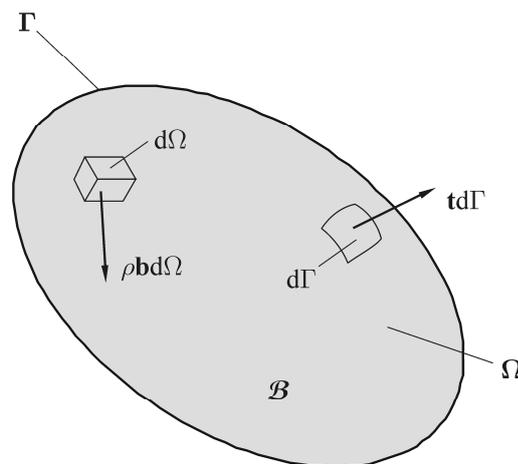
Figure 2.4 Balance of momentum

From the balance of linear momentum for such a body it follows for each point in the body the following statement, which is written here with respect to the global Cartesian coordinate system $\{X^1, X^2, X^3\}$, holds at all times t [122]

$$\sigma_{ij,X^j} + b_i = \rho \frac{Dv_i}{Dt}. \tag{2.41}$$

Herein b_i denotes the body force vector, ρ is a mass density, and v_i describes a velocity field. Relation (2.41) is referred to as the equations of motion. If the acceleration is zero for all points in Ω, then (2.41) becomes

$$\sigma_{ij,X^j} + b_i = 0, \tag{2.42}$$

usually called the equations of equilibrium in elastostatics. Furthermore, from the balance of angular momentum follows that for a non-polar continuum the stress tensor is symmetric in each point in $\mathcal{B}$, i.e. $\sigma_{ij} = \sigma_{ji}$ [122].

2.4 Weighted residual methods and weak forms of differential equations

The weighted residual methods (WRM) represent a family of the mathematical techniques that use the weak forms of differential equations to find the approximated solutions for a given problem. The method is applicable to many sets of partial differential equations appearing in usual engineering problems and gives a good approximated solution if certain requirements are met.

Let $\mathcal{A}(\mathbf{u}) = \mathbf{0}$ be the set of N governing equations for a steady-state problem defined over a domain Ω with $\mathbf{u}$ as a set of unknown solution functions. The domain is bounded by a surface Γ according to Figure 2.5, on which the boundary conditions are prescribed by another set of M equations $\mathcal{G}(\mathbf{u}) = \mathbf{0}$.

If the equations $\mathcal{A}(\mathbf{u})$ and $\mathcal{G}(\mathbf{u})$ are linear differential equations, they may be written in their strong forms as

$$\mathcal{A}(\mathbf{u}) = \mathbf{D}_\Omega(\mathbf{u}) - \mathbf{b} = \mathbf{0}, \ \text{in}\,\Omega, \tag{2.43}$$

$$\mathcal{G}(\mathbf{u}) = \mathbf{D}_\Gamma(\mathbf{u}) - \mathbf{t} = \mathbf{0}, \ \text{on}\,\Gamma, \tag{2.44}$$

with

$$\boldsymbol{u} = \begin{bmatrix} u_1 & u_2 & \cdots & u_i & \cdots \end{bmatrix}^{\mathrm{T}}. \tag{2.45}$$

Herein, D_Ω and D_Γ are differential operators, and **b** and **t** denote some prescribed known variables over Ω and Γ, respectively. If in D_Ω the highest-order member is of order m, then in D_Γ only the terms up to the order $m-1$ may appear.

sub-domains
Ω_s

Γ_{sC}

$\partial\Omega_s$

$\Omega, \mathcal{A}(\boldsymbol{u})=\boldsymbol{0}$

Γ_C

$\Gamma, \mathcal{G}(\boldsymbol{u})=\boldsymbol{0}$
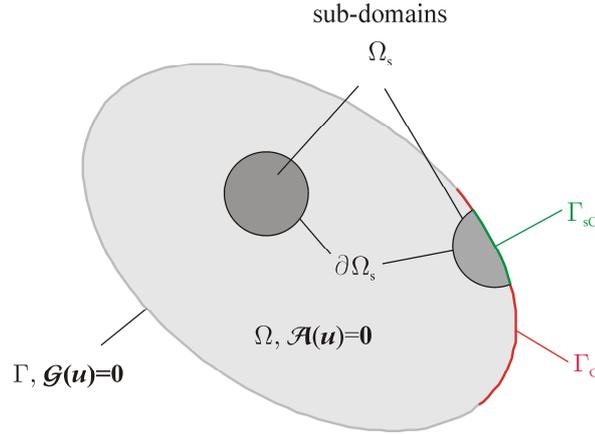
Figure 2.5 Global domain Ω with corresponding boundary Γ and local sub-domains Ω_s used for constructing local weak forms.

In WRM, a set of the trail or candidate functions $\tilde{\boldsymbol{u}}$, which is an approximation of the exact solution set (2.46), is assumed

$$\tilde{\boldsymbol{u}} = \begin{bmatrix} \tilde{u}_1 & \tilde{u}_2 & \cdots & \tilde{u}_i & \cdots \end{bmatrix}^{\mathrm{T}}, \tag{2.47}$$

where trial function $\tilde{u}_i$ are assumed as the linear combination of independent basis functions. The coefficients in these linear combinations have to be determined in the solution process. The residuals of the strong forms (2.43) and (2.44) are calculated as

$$\mathbf{R}_{\mathcal{A}} = \mathcal{A}(\tilde{\boldsymbol{u}}) = \mathbf{D}_\Omega(\tilde{\boldsymbol{u}}) - \mathbf{b}, \ \text{in}\,\Omega, \tag{2.48}$$

$$\mathbf{R}_{\mathcal{G}} = \mathcal{G}(\tilde{\boldsymbol{u}}) = \mathbf{D}_\Gamma(\tilde{\boldsymbol{u}}) - \mathbf{t}, \ \text{on}\,\Gamma. \tag{2.49}$$

It is generally difficult to assume the exact solution which produces the zero residuals in each point inside the solution domain, i.e., $\mathbf{R}_{\mathcal{A}} \neq \mathbf{0}$ and $\mathbf{R}_{\mathcal{G}} \neq \mathbf{0}$. Therefore, the solution is sought which satisfies equation sets (2.43) and (2.44) in a weighted integral form

$$\int_\Omega \mathbf{v}^\mathrm{T} \mathbf{R}_{\mathscr{A}} \, \mathrm{d}\Omega = 0 , \tag{2.50}$$

where $\mathbf{v}$ is the set of arbitrary weighting or test functions

$$\mathbf{v} = \begin{bmatrix} v_1 & v_2 & \cdots & v_i & \cdots & v_N \end{bmatrix}^\mathrm{T} . \tag{2.51}$$

The total number of test functions is equal to the total number of equations involved in (2.43). Since the relation (2.50) has to be satisfied for all possible admissible choices of functions in $\mathbf{v}$, it may be shown that it is equivalent to the strong form (2.43) and (2.44) [7],[123] if the essential BC are satisfied *a priori*.

Since the solution of (2.50) can be obtained only if it is possible to evaluate the integrals appearing in the weak form, certain restrictions are posed on the possible choice of the test and trial functions. It is obvious from (2.48)-(2.50) that, if the highest-order derivative which appears in D_Ω and acts on $\tilde{u}_i$ is of the order m, then $\tilde{u}_i$ has to be such that its derivatives up to the $(m-1)$-th order are continuous in order for $\tilde{u}_i$ to be admissible trial function [123]. In such a case $\tilde{u}_i$ is called a C^{m-1} continuous function. A function is a C^m continuous function if all its derivatives of order j for $0 \le j \le m$ exist and are continuous in the entire domain Ω. On the other hand, no continuity condition is posed on the derivatives of the test functions in the weak form (2.50), and they may be C^{-1} continuous functions.

Theoretically, all types of the functions that obey the continuity conditions may be used to approximate the solution. Nevertheless, the choice of the trial function affects the quality of the solution. Similarly to the trial functions, the choice of the test functions is completely arbitrary, as long as the functions are admissible. However, it also affects the quality of the solution and therefore only some suitable subset of all admissible functions is considered [7],[123]. Depending on the type of the test functions applied and on the subsequent solution procedure, different "classical" weighted residual methods may be discerned [15], such as the collocation method, the sub-domain method, the least-squares method, the Galerkin method, or the Petrov-Galerkin method.

By performing the integration by parts, it can be shown that some of the boundary conditions (BC) in (2.44) are implicitly included in the weak form (2.50) [7],[15],[123]. These BC are automatically satisfied *a posteriori* and are therefore called natural BC.

All the other BC, which are not included in the weak form, are called essential or forced BC because it is essential for the validity of solution that they are enforced either a priori, by the proper choice of the trial function, or *a posteriori*, by employing some additional numerical procedure.

In the case when the trial functions do not satisfy the essential BC, the so-called constrained WRM [13] has to be employed. For the penalty method, which is especially suitable for the use in the truly meshless methods, the weak form can be written as

$$\int_{\Omega} \mathbf{v}^{\mathrm{T}} \mathbf{R}_A \, \mathrm{d}\Omega + \int_{\Gamma_C} \check{\mathbf{v}}^{\mathrm{T}} \boldsymbol{\alpha} \mathbf{C}\left(\tilde{\boldsymbol{u}}, \bar{\boldsymbol{u}}\right) \mathrm{d}\Gamma = 0, \tag{2.52}$$

where $\boldsymbol{\alpha}$ is a diagonal matrix of penalty parameters, the vector $\mathbf{C}$ contains the essential boundary conditions that have to be enforced and Γ_C is the part of the global boundary Γ with some prescribed values $\bar{\boldsymbol{u}}$. $\check{\mathbf{v}}$ is a vector of the test functions corresponding to the equations in $\mathbf{C}$. For simplicity, it is usually chosen to be $\check{\mathbf{v}} = \mathbf{v}$. The penalty parameters are some user-defined positive constant numbers, which must be large enough to enforce the essential BC contained in $\mathbf{C}$ successfully. However, too large values may cause the numerical problems associated with the numerical stability of the solution process. The penalty method is very simple to implement and does not increase the total number of unknown parameters in the final algebraic equation system, in contrast to the Lagrange multipliers method [13], which is often used in the EFG method [13],[17].

The well-known principle of virtual displacements, which is often applied in FEM, may be derived from the generalized weighted residual method by the proper choice of the test functions [7],[15],[123]. However, in contrast to the variational methods, in WRM the strong form of equations needs to be known, but on the other hand, it is not important whether a functional for the problem exists. Many meshless methods are based on the global weak forms, such as the EFG methods [17], which employ the Galerkin method.

2.4.1 Local weak forms for the 3-D solids

Instead of trying to satisfy the relation (2.50) over the entire global domain Ω, the WRM may be applied only over small regions which cover Ω and its boundary $\partial\Omega$. Such approach is called the local WRM, which is used for developing various truly meshless methods [15]. Accordingly, in order to obtain the solutions, a generalized

weighted residual form is written over a set of sub-domains Ω_s for the equation set (2.43) in the following form

$$\int_{\Omega_s} \mathbf{v}^{\mathrm{T}} \mathbf{R}_A \, \mathrm{d}\Omega + \int_{\Gamma_{sC}} \check{\mathbf{v}}^{\mathrm{T}} \boldsymbol{\alpha} \mathbf{C}(\tilde{\mathbf{u}}, \bar{\mathbf{u}}) \, \mathrm{d}\Gamma = 0 \,, \qquad (2.53)$$

wherein Γ_{sC} is the part of the local boundary $\partial\Omega_s$ that coincides with Γ_C, i.e., Γ_{sC} is the part of $\partial\Omega_s$ with the prescribed BC according to Figure 2.5, , i.e., $\Gamma_{sC} = \partial\Omega_s \cap \Gamma_C$. The sub-domains are positioned completely inside the computation domain Ω, $\Omega_s \subset \Omega \cup \partial\Omega$. Theoretically, as long as they cover the computation domain completely, the relation (2.53) should be equivalent to the global weak form (2.50).

3 MLS approximation scheme

The Moving Least Squares (MLS) method is a variant of the well-known method of the least squares, introduced for the multivariate surface construction from a set of scattered points [8]. The MLS functions are now a popular tool used for the interpolation of field variables in meshless methods. In this chapter the procedure for calculating the MLS functions and their derivatives is given. This is followed by the description of the applied MLS weight functions. Thereafter the relevant features of the MLS approximants are disclosed, and at the end, some details about the numerical implementation are presented.

3.1 MLS procedure

Consider the function $f(\mathbf{X})$ representing the distribution of a field variable f over a domain Ω. The MLS approximation strategy is based on the assumption that the approximation of $f(\mathbf{X})$, denoted here as $f^{(h)}(\mathbf{X})$, should be most strongly influenced by the values at the nodes positioned in the nearest neighbourhood of the point of interest $\mathbf{X}$. The nodes are the points that carry the values of $f(\mathbf{X})$. Furthermore, the concept of locality is introduced, i.e., the nodes that are positioned far away from $\mathbf{X}$ should not have any influence on $f^{(h)}(\mathbf{X})$. The MLS approximant $f^{(h)}(\mathbf{X})$, which approximates the function $f(\mathbf{X})$ in Ω for a set of randomly scattered points $\mathbf{X}_I = 1, 2, ..., N$, may be written as

$$f^{(h)}(\mathbf{X}) = \mathbf{p}^T(\mathbf{X})\mathbf{a}(\mathbf{X}), \tag{3.1}$$

where $\mathbf{p}(\mathbf{X})$ is a vector of a basis functions,

$$\mathbf{p}^T(\mathbf{X}) = \begin{bmatrix} p_1(\mathbf{X}) & p_2(\mathbf{X}) & \cdots & p_j(\mathbf{X}) & \cdots & p_m(\mathbf{X}) \end{bmatrix} \tag{3.2}$$

Herein m stands for the total number of terms in the basis. Usually the complete monomial basis is used in order to ensure the consistency of the approximations, whereby different types of the polynomials may be used [124]. Depending on the problem, other types of functions may also be employed in order to enhance the

solutions, as in the analysis of crack propagation [125],[126]. For a 2-D space, used in this work, the complete monomial bases are defined as

   □   Linear basis

$$\mathbf{p}^{\mathrm{T}}(\mathbf{X}) = \begin{bmatrix} 1 & X^1 & X^2 \end{bmatrix}, \tag{3.3}$$

   □   Quadratic basis

$$\mathbf{p}^{\mathrm{T}}(\mathbf{X}) = \begin{bmatrix} 1 & X^1 & X^2 & \left(X^1\right)^2 & X^1 X^2 & \left(X^2\right)^2 \end{bmatrix}, \tag{3.4}$$

   □   etc.

The terms of the complete 2-D basis may be obtained by employing the Pascal triangle. For the complete polynomial bases, the total number of terms is related to the order of the basis by the expression $m = (t+1)(t+2)/2$ with t as the order of the basis [15]. Vector $\mathbf{a}(\mathbf{X})$ contains the unknown coefficients

$$\mathbf{a}^{\mathrm{T}}(\mathbf{X}) = \begin{bmatrix} a_1(\mathbf{X}) & a_2(\mathbf{X}) & \cdots & a_j(\mathbf{X}) & \cdots & a_m(\mathbf{X}) \end{bmatrix} \tag{3.5}$$

which are the functions of $\mathbf{X}$, i.e. they have to be calculated for each point $\mathbf{X}$.

The values of the unknown coefficients $a_i(\mathbf{X}), i = 1, 2, ..., m$, at the point $\mathbf{X}$ should be influenced only by a finite, relatively small number of the nodes, positioned in some local neighbourhood of $\mathbf{X}$, to keep the computational costs acceptable. According to the terminology usually used in the MLPG methods [15], this local neighbourhood of $\mathbf{X}$, denoted as Ω_X, is called the domain of definition of the MLS approximation for the point $\mathbf{X}$. The vector $\mathbf{a}(\mathbf{X})$ is determined by means of the discrete weighted L_2 norm, defined as

$$J(\mathbf{a}(\mathbf{X})) = \sum_{J=1}^{n} W_J(\mathbf{X}) \left(\mathbf{p}(\mathbf{X}_J)\mathbf{a}(\mathbf{X}) - \hat{f}_J\right)^2, \tag{3.6}$$

where $f(\mathbf{X}_J) = \hat{f}_J$ are the function values at the nodes $\mathbf{X}_J, J = 1, 2, ..., n$, and $W_J(\mathbf{X})$ stands for the weight function associated with the node $\mathbf{X}_J$. n denotes the total number of nodes in Ω_X, which may now be defined as a region that covers all those nodes

$\mathbf{X}_J$, $J = 1, 2, ..., n$, whose weight functions do not vanish at $\mathbf{X}$, i.e., $W_J(\mathbf{X}) \neq 0$, see Figure 3.1.
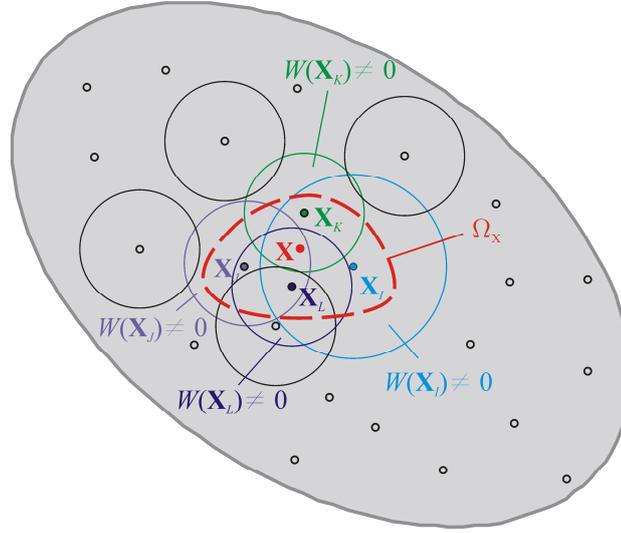
Figure 3.1 Domain of definition of MLS approximation at point $\mathbf{X}$

The minimization of $J(\mathbf{a}(\mathbf{X}))$ leads to the following system of equations

$$\mathbf{A}(\mathbf{X})\mathbf{a}(\mathbf{X}) = \mathbf{B}(\mathbf{X})\hat{\mathbf{f}}. \tag{3.7}$$

Herein the matrix $\mathbf{A}$ is the so-called moment matrix,

$$\mathbf{A} = \sum_{J=1}^{n} W_J(\mathbf{X})\mathbf{p}(\mathbf{X}_J)\mathbf{p}^T(\mathbf{X}_J), \tag{3.8}$$

the matrix $\mathbf{B}$ is defined as

$$\mathbf{B} = \begin{bmatrix} W_1(\mathbf{X})\mathbf{p}(\mathbf{X}_1) & W_2(\mathbf{X})\mathbf{p}(\mathbf{X}_2) & \cdots & W_J(\mathbf{X})\mathbf{p}(\mathbf{X}_J) & \cdots & W_n(\mathbf{X})\mathbf{p}(\mathbf{X}_n) \end{bmatrix}, \tag{3.9}$$

and the vector $\hat{\mathbf{f}}$ contains the fictitious nodal values

$$\hat{\mathbf{f}}^T = \begin{bmatrix} \hat{f}_1 & \hat{f}_2 & \cdots & \hat{f}_J & \cdots & \hat{f}_n \end{bmatrix}. \tag{3.10}$$

The coefficients $\mathbf{a}(\mathbf{X})$ are evaluated by solving the equation system (3.7), leading to

$$\mathbf{a}(\mathbf{X}) = \mathbf{A}^{-1}(\mathbf{X})\mathbf{B}(\mathbf{X})\hat{\mathbf{f}}. \tag{3.11}$$

Substituting (3.11) into equation (3.1), the MLS approximation is obtained, written here in the form similar to that usually used in FEM as

$$f^{(h)}(\mathbf{X}) = \sum_{J=1}^{n} \phi_J(\mathbf{X})\hat{f}_J. \qquad (3.12)$$

$\phi_J(\mathbf{X})$ is the shape function associated with the node $\mathbf{X}_J$, which is calculated as

$$\phi_J(\mathbf{X}) = \sum_{i=1}^{m} p_i(\mathbf{X})\Big[\mathbf{A}^{-1}(\mathbf{X})\mathbf{B}(\mathbf{X})\Big]_{iJ}. \qquad (3.13)$$

It should be noted that the MLS functions in general do not interpolate the given values at the nodes $\mathbf{X}_J$, $f^{(h)}(\mathbf{X}_J) \neq \hat{f}_J$, as shown in Figure 3.2. Therefore, the nodal parameters $\hat{f}_J$ are called the fictitious nodal values.
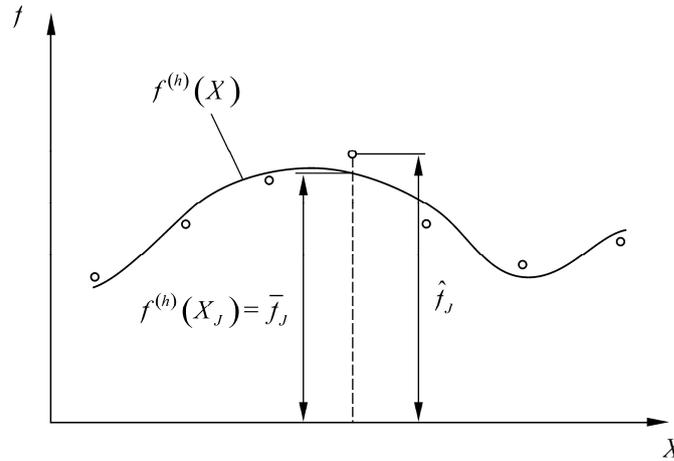
Figure 3.2 Non-interpolation character of MLS approximations: $f^{(h)}(\mathbf{X}_J)$ is calculated nodal function value and $\hat{u}_J$ is nodal "fictitious" value.

From (3.11) it is obvious that the crucial condition for the MLS approximation (3.13) to be well defined is the inversibility of the matrix $\mathbf{A}$, i.e., $\mathbf{A}$ must be a non-singular matrix. By more detailed inspection of equation (3.8), it follows that this condition is satisfied only if the number of nodes in Ω_X is greater or equal than the number of terms in the basis vector $\mathbf{p}(\mathbf{X})$, i.e., it must be $n \geq m$. Furthermore, the nodes inside Ω_X must not be arranged so that the vectors $\mathbf{p}(\mathbf{X}_J), J = 1, 2, ...n$ are linearly independent vectors. Fortunately, for a certain order of the MLS basis, only a finite small number of such problematic nodal arrangements may be identified. In most cases, $n \gg m$ ensures the inversibility of the matrix $\mathbf{A}$, although this increases the computational costs needed for the calculation of the MLS approximation.

The derivatives of the shape functions $\phi_J(\mathbf{X})$ may be obtained by direct differentiation of (3.13) as

$$\phi_{J,X^k} = \sum_{i=1}^{m} \left[p_{i,X^k} \left(\mathbf{A}^{-1}\mathbf{B} \right)_{iJ} + p_i \left(\mathbf{A}^{-1}\mathbf{B}_{,X^k} + \mathbf{A}^{-1}_{,X^k}\mathbf{B} \right)_{iJ} \right], \tag{3.14}$$

$$\begin{aligned}
\phi_{J,X^k X^l} = \sum_{i=1}^{m} \Big[&p_{i,X^k X^l} \left(\mathbf{A}^{-1}\mathbf{B} \right)_{iJ} + p_{i,X^k} \left(\mathbf{A}^{-1}\mathbf{B}_{,X^l} + \mathbf{A}^{-1}_{,X^l}\mathbf{B} \right)_{iJ} + \\
&+ p_{i,X^l} \left(\mathbf{A}^{-1}\mathbf{B}_{,X^k} + \mathbf{A}^{-1}_{,X^k}\mathbf{B} \right)_{iJ} + \\
&+ p_i \left(\mathbf{A}^{-1}_{,X^k X^l}\mathbf{B} + \mathbf{A}^{-1}_{,X^l}\mathbf{B}_{,X^k} + \mathbf{A}^{-1}_{,X^k}\mathbf{B}_{,X^l} + \mathbf{A}^{-1}\mathbf{B}_{,X^k X^l} \right)_{iJ} \Big],
\end{aligned} \tag{3.15}$$

where the derivatives of $\mathbf{A}^{-1}$ are evaluated as

$$\begin{aligned}
\mathbf{A}^{-1}_{,X^k} &= -\mathbf{A}^{-1}\mathbf{A}_{,X^k}\mathbf{A}^{-1}, \\
\mathbf{A}^{-1}_{,X^k X^l} &= \mathbf{A}^{-1}\mathbf{A}_{,X^l}\mathbf{A}^{-1}\mathbf{A}_{,X^k}\mathbf{A}^{-1} - \mathbf{A}^{-1}\mathbf{A}_{,X^k X^l}\mathbf{A}^{-1} + \mathbf{A}^{-1}\mathbf{A}_{,X^k}\mathbf{A}^{-1}\mathbf{A}_{,X^l}\mathbf{A}^{-1}.
\end{aligned} \tag{3.16}$$

3.2 MLS Weight functions

The choice of the weight functions is very important because some important properties of the MLS approximants are inherent to the properties of its weight function.

The chosen weight functions should posses the following properties [13]:

□ **Positivity.** $W_J(\mathbf{X}) > 0$ over its support domain. This ensures the existence of the minimum of the discrete L2 norm (3.6).

□ **Compact support.** $W_J(\mathbf{X}) = 0$ outside its support domain. The compact support domain of $W_J(\mathbf{X})$ ensures the locality of the MLS approximation, because the node influences $u^{(h)}(\mathbf{X})$ only in the points where $W_J(\mathbf{X}) \neq 0$, according to (3.6).

□ $W_J(\mathbf{X})$ **should be monotonically decreasing function.** This feature gives more weighting to the nodes inside Ω_X which are closer to the point $\mathbf{X}$, i.e., $W_J(\mathbf{X})$ determine the intensity of the influence of the corresponding node $\mathbf{X}_J$ on $f^{(h)}(\mathbf{X})$.

In addition, it is desirable for $W_J(\mathbf{X})$ to satisfy the Kronecker delta property because in that case the MLS approximant itself possesses the Kronecker delta property [117], which simplifies the enforcement of the essential BC. This feature is not

obligatory, because there are many methods for enforcing the essential BC in meshless methods *a posteriory*.

3.2.1 Choice of MLS weight functions

Any function that satisfies the necessary requirements mentioned in the previous section may be used as the MLS weight function. From relations (3.8), (3.9) and (3.13) it is easy to prove that the support domain of the nodal shape function $\phi_J(\mathbf{X})$ coincides with the support domain of the weight function $W_J(\mathbf{X})$. Usually the support domains have the simple shapes, such as circles or rectangles for 2-D cases. The choice of $W_J(\mathbf{X})$ is in most cases also responsible for the order of the continuity of $f^{(h)}(\mathbf{X})$.

Popular choices for the weight functions include the Gaussian- or the spline-type functions, some of which are presented in [13],[15], and the references therein. Although both types of functions may produce results of sufficient and comparable quality, the improper choice of those parameters destroys the accuracy and stability of results. Finding the optimal values of those parameters, which would be suitable for a general-purpose application, is still an open question [13].

3.2.2 Spline-type weight functions

In this work only the 2-D spline-type weight functions with the circular support domain are applied. They are defined as

$$W_I(\mathbf{X}) = \begin{cases} 1 - \sum_{k=1}^{p} a_k \left(\dfrac{d_I}{r_{sI}}\right)^k, & 0 \leq d_I \leq r_{sI} = \rho_{sI} h_{mI}, \\ 0, & d_I > r_{sI} h_{mI}, \end{cases} \tag{3.17}$$

where p denotes the order of the spline, a_k stands for the coefficients, $d_I = |\mathbf{X} - \mathbf{X}_I|$ is the distance from the node $\mathbf{X}_I$ to the point $\mathbf{X}$, while r_{sI} represents the radius of the circular support domain of $W_I(\mathbf{X})$. The size of r_{sI} is usually determined by scaling a characteristic nodal distance h_{mI} with some user-defined scaling factor ρ_{sI}. The accuracy and the stability of the MLS scheme may significantly depend on the value of r_{sI}. The coefficients a_k in (3.17) are determined by means of the boundary conditions for the centre

$$W_I(d_I = 0) = 1, \qquad m_0 \geq 1,$$

$$\frac{\partial^{m_0} W_I(d_I = 0)}{\partial(X^i)^{m_0}} = 0, \quad m_0 \geq 1, \tag{3.18}$$

and the outer edges of the support domain

$$W_I(d_I = 1) = 0, \qquad m_1 = 1,$$

$$\frac{\partial^{m_1} W_I(d_I = 1)}{\partial(X^i)^{m_1}} = 0, \quad m_1 \geq 1, \tag{3.19}$$

where $p = m_0 + m_1 + 1$. Figure 3.3 shows the shape of 4th-order spline function (3.20) and its derivatives.

$W(X^a)$ $\partial W(X^a)/\partial X^1$ $\partial W(X^a)/\partial X^2$

$\partial^2 W(X^a)/\partial(X^1)^2$ $\partial^2 W(X^a)/\partial(X^2)^2$ $\partial^2 W(X^a)/\partial(X^1 X^2)^2$
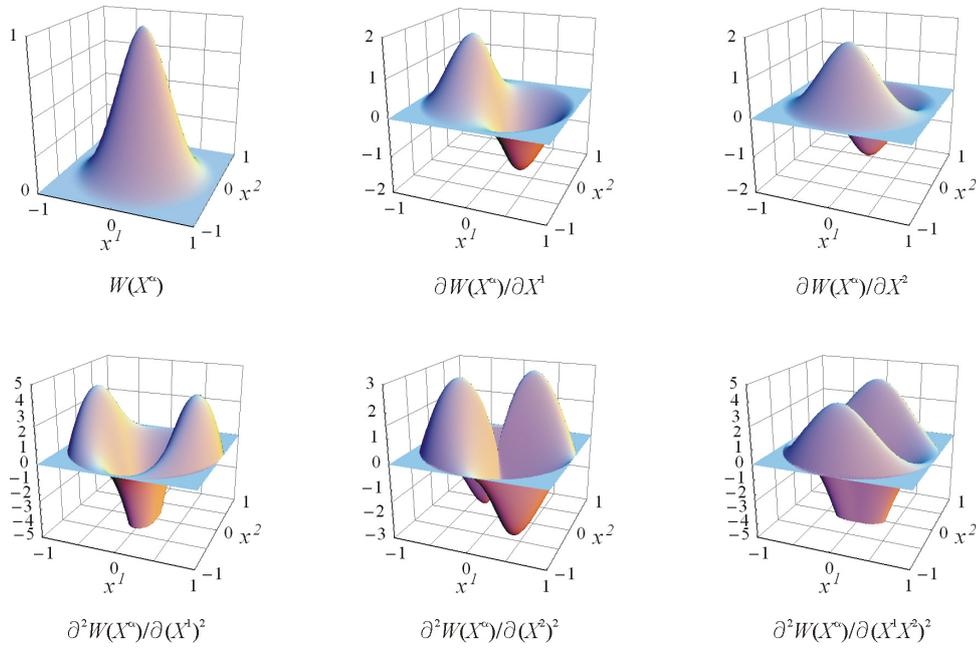
Figure 3.3 4th-order spline MLS weight function (3.20) and its derivatives

A very detailed analysis concerning the shapes of the nodal shape functions and their derivatives evaluated by employing such weight functions is available in [15]. Therein it is also suggested that the C^2 continuous 4th-order spline function, defined by

$$W_J(\mathbf{X}) = \begin{cases} 1 - 6\left(\dfrac{d_J}{r_{sJ}}\right)^2 + 8\left(\dfrac{d_J}{r_{sJ}}\right)^3 - 3\left(\dfrac{d_J}{r_{sJ}}\right)^4 & 0 \leq d_J \leq r_{sJ} \\ 0 & d_J > r_{sJ} \end{cases}, \tag{3.20}$$

is probably most suitable for the application in the MLPG methods.

3.2.3 Regularized weight functions and interpolating MLS (IMLS) functions

The MLS functions employing the "common" Gaussian- and spline-type weight functions do not possess the Kronecker delta property at the nodes. Furthermore, for such functions, the interpolation error in general depends significantly on the size of the support domain or the shape parameters of the weight functions. In [8] Lancaster and Salkauskas imposed the interpolating properties on the MLS functions by employing the weight functions that are singular at the corresponding interpolation points. However, such approach leads to the singularity of the matrices **A** and **B** at the nodes, and the special measures are needed in meshless methods to remove those singularities [127].

In order to avoid such complications, Most and Bucher have developed new types of regularized weight functions which satisfy the interpolation conditions at the nodes with a high accuracy [117], [128], or even mathematically exactly [129]. Analogously to their approach proposed in [117], [128], in this contribution the following normalized function

$$W_{RJ}(\mathbf{X}) = \frac{\tilde{w}_{RJ}(\mathbf{X})}{\sum_{I=1}^{n} \tilde{w}_{RI}(\mathbf{X})} \tag{3.21}$$

with

$$\tilde{w}_{RJ}(\mathbf{X}) = \frac{\left(\left(\frac{d_J}{r_J}\right)^4 + \varepsilon\right)^{-2} - (1+\varepsilon)^{-2}}{\varepsilon^{-2} - (1+\varepsilon)^{-2}}. \tag{3.22}$$

is used to construct the MLS weight functions. Herein n is the total number of nodes in Ω_X. The regularization parameter ε should be small enough to provide high accuracy, i.e., $\varepsilon \ll 1$, but at the same time large enough to avoid overflow error. Here it is assumed as $\varepsilon = 10^{-5}$. As proved in [117], because of the regularization strategy, the weight function (3.22) possesses the Kronecker delta property at the nodes with a high accuracy, which leads to the same condition for the MLS shape function, i.e.

$$\phi_J(\mathbf{X}_I) \approx \delta_{JI}. \tag{3.23}$$

It has also been shown that $\tilde{w}_{RJ}(\mathbf{X})$ may be used instead of $W_{RJ}(\mathbf{X})$ as the MLS weight function to reduce the computational effort, because both functions yield exactly the same nodal MLS shape functions [117]. On the other hand, the first and second derivatives of the function (3.22) are not exactly zero on the boundaries of the weight function support domain, i.e., $\partial\tilde{w}_{RJ}(d=r_{sJ})/\partial d \neq 0$ and $\partial^2\tilde{w}_{RJ}(d=r_{sJ})/\partial d^2 \neq 0$, and therefore $\tilde{w}_{RJ}(\mathbf{X})$ is only C^0 continuous. To obtain the MLS functions of a sufficiently high order of continuity, $\tilde{w}_{RJ}(\mathbf{X})$ may be multiplied with any common weight function that possesses the necessary order of continuity [128]. In this contribution this has been accomplished by multiplying function $\tilde{w}_{RJ}(\mathbf{X})$ with the spline-type function of the 4th order (3.20),

$$W_J(\mathbf{X}) = \begin{cases} w_{SJ}(\mathbf{X})\,\tilde{w}_{RJ}(\mathbf{X}), & 0 \leq d_J \leq r_{sJ}, \\ 0, & d_J > r_{sJ}, \end{cases} \tag{3.24}$$

where $w_{SJ}(\mathbf{X})$ is the fourth-order spline-type function (3.20). Figure 3.4 shows the shape of the regularized function (3.24) and of its derivatives

$$W(X^\alpha) \qquad \partial W(X^\alpha)/\partial X^1 \qquad \partial W(X^\alpha)/\partial X^2$$

$$\partial^2 W(X^\alpha)/\partial (X^1)^2 \qquad \partial^2 W(X^\alpha)/\partial (X^2)^2 \qquad \partial^2 W(X^\alpha)/\partial (X^1 X^2)^2$$
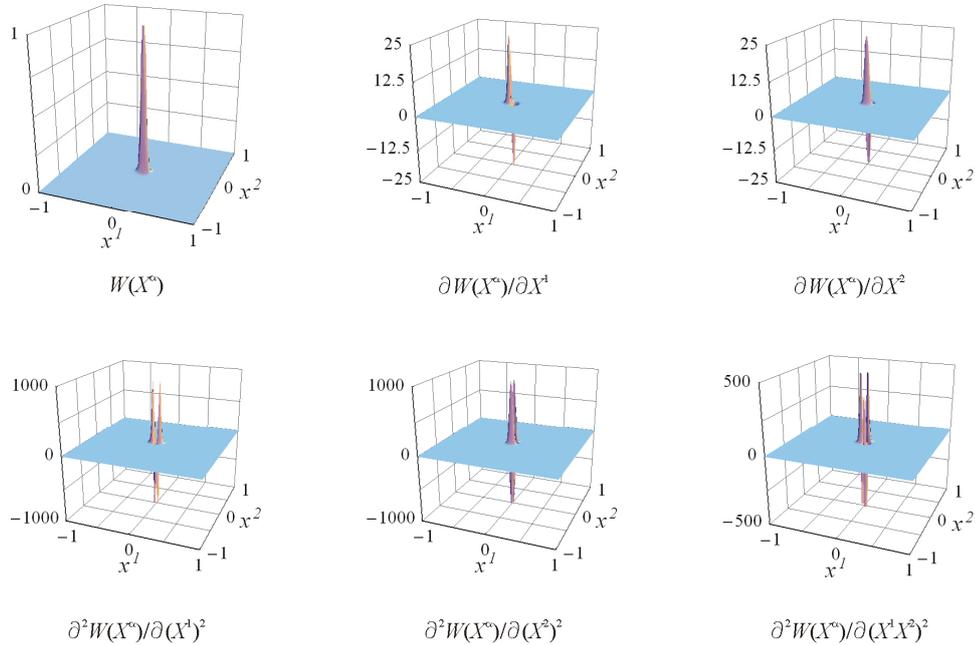
Figure 3.4 Regularized weight function (3.24) and its derivatives

It is also to note that the shapes of the MLS functions employing the regularized weight functions similar to (3.21),(3.22) or (3.24) are less dependant on the value of r_{sJ}

than it is the case when the "common" Gaussian- or spline-type weight functions are applied [117], [128], [129].

3.3 Properties of MLS approximations

The MLS approximation functions have the following features, which are very important for their applicability in meshless methods:

▫ **A high order of continuity.** The continuity and smoothness of the MLS functions theoretically depend on the orders of continuity of both the basis functions $p_i(\mathbf{X}), i = 1, 2, ..., m$, and the weight functions $W_J(\mathbf{X})$. However, since usually the continuity of $p_i(\mathbf{X}), i = 1, 2, ..., m$ is higher than that of $W_J(\mathbf{X})$, a MLS approximant inherits the continuity order of its weight function [15].

▫ **Reproducibility**. The MLS functions are reproductive, since they are able to reproduce the functions that are comprised in their basis vector $\mathbf{p}(\mathbf{X})$ [13].

▫ **A high order of the consistency of approximation function.** The consistency of approximation function is defined as the ability of an approximation function to reproduce the complete polynomials up to a given order [13],[131]. Since the MLS function is a reproductive function, it immediately follows that it is also consistent. It may be concluded that the order of consistency of the MLS functions is equal to the order of completeness of its base $\mathbf{p}(\mathbf{X})$. The consistency of the first order enables the passing of the standard patch tests where the linear polynomial reproduction is required.

▫ **Partition of Unity.** The MLS functions are the partitions of unity, because the support domains of the nodal shape functions are the overlapping sub-domains which cover the entire global domain, and $\sum_{J=1}^{n} \phi_J(\mathbf{X}) = 1$ in each point of the global domain. This property is identical to the consistency of the zeroth order and it allows the MLS functions to reproduce the rigid body movement.

▫ **Complex analytical form.** As may be seen from the procedure presented in Section 3.1, the evaluation of the MLS shape functions requires the inversion of the moment matrix $\mathbf{A}$. Therefore, computational costs are considerably higher than the ones needed to evaluate the polynomial shape functions in FEM. Furthermore, the MLS shape functions have the form of a rational polynomial function, which makes the numerical integration in meshless methods computationally more costly than in

FEM. This problem is even more aggravated by the fact that the derivatives of the MLS functions are often not smooth over the integration domains [15].

□ **Robustness.** The MLS scheme is able to approximate data over a set of randomly scattered points with a reasonable accuracy under the condition that all the influencing parameters, such as the size of the support domains of the MLS shape function and various shape parameters, are defined correctly. However, the efficiency of a meshless method employing the MLS functions may also significantly depend on other computational aspects, such as the accuracy of numerical integration or the imposition of the essential BC. Such details may also be influenced by the parameters of the MLS approximations and have to be taken into account during numerical analyses. In the literature, different approaches have been proposed for defining the optimal size of the support domains of the MLS weight function, such as those in [10],[34],[128],[130] and in the references therein. Often, some parametric analysis and benchmark tests are necessary prior to the numerical analysis of a problem to obtain information about the optimal values of the MLS parameters.

3.4 Numerical implementation

One of the mayor drawbacks in using the MLS scheme in meshless methods is the considerable computational time that is needed for the calculation of the MLS shape functions and their derivatives. The techniques described in this section are employed in order to cut these costs, and to increase the robustness of the MLS scheme.

3.4.1 Concept of local coordinate system and base shifting

Betytschko and co-workers [80],[131] introduced the concept of the so-called base-shifting, where the basis $\mathbf{p}(\mathbf{X})$ is calculated with respect to the locally defined coordinates

$$\tilde{\mathbf{X}} = \mathbf{X} - \mathbf{X}_g ,\qquad(3.25)$$

obtained by shifting the origin of the global coordinate system to the current sample point $\mathbf{X}_g$, which is usually an integration point or a node, leading to

$$\mathbf{p}^{\mathrm{T}}(\tilde{\mathbf{X}}) = \begin{bmatrix} p_1(\tilde{\mathbf{X}}) & p_2(\tilde{\mathbf{X}}) & \cdots & p_j(\tilde{\mathbf{X}}) & \cdots & p_m(\tilde{\mathbf{X}}) \end{bmatrix}.\qquad(3.26)$$

According to relations (3.8), (3.9) and (3.13), the shape functions may then be written as

$$\phi_J\left(\mathbf{X}_g\right) = \sum_{i=1}^{m} p_i(\tilde{\mathbf{X}}_g)\left[\mathbf{A}^{-1}\mathbf{B}\right]_{iJ},$$

$$\mathbf{A} = \sum_{J=1}^{n} W_J(\mathbf{X})\mathbf{p}(\tilde{\mathbf{X}}_J)\mathbf{p}^T(\tilde{\mathbf{X}}_J), \tag{3.27}$$

$$\mathbf{B} = \left[W_1(\mathbf{X})\mathbf{p}(\tilde{\mathbf{X}}_1) \quad W_2(\mathbf{X})\mathbf{p}(\tilde{\mathbf{X}}_2) \quad \cdots \quad W_J(\mathbf{X})\mathbf{p}(\tilde{\mathbf{X}}_J) \quad \cdots \quad W_n(\mathbf{X})\mathbf{p}(\bar{\mathbf{X}}_n)\right].$$

Note that for $\mathbf{X} = \mathbf{X}_g$ it follows that $\tilde{\mathbf{X}}_g = \mathbf{X}_g - \mathbf{X}_g = 0$, and therefore the following relations always hold

$$\mathbf{p}^T(\tilde{\mathbf{X}}_g) = \begin{bmatrix} 1 & 0 & 0 & \cdots & 0 & \cdots & 0 \end{bmatrix},$$

$$\mathbf{p}^T_{,\tilde{X}^1}(\tilde{\mathbf{X}}_g) = \begin{bmatrix} 0 & 1 & 0 & \cdots & 0 & \cdots & 0 \end{bmatrix}, \tag{3.28}$$

$$\mathbf{p}^T_{,\tilde{X}^2}(\tilde{\mathbf{X}}_g) = \begin{bmatrix} 0 & 0 & 1 & \cdots & 0 & \cdots & 0 \end{bmatrix},$$

which decreases the computational time needed to calculate the shape functions and their derivatives. Moreover, the use of the local coordinates improves the conditioning of the moment matrix $\mathbf{A}$, as well as the accuracy of the MLS approximation, as shown in details in [132] for a 1-D case involving beam analysis. In this work, the local coordinates are additionally normalized to avoid the problems associated with the ill-conditioning of $\mathbf{A}$ more efficiently, analogously to the approach used in [33],[133], as

$$\tilde{\mathbf{X}} = \frac{\mathbf{X} - \mathbf{X}_g}{R_{\max}}. \tag{3.29}$$

Herein $R_{\max}$ is a distance between a current sample point $\mathbf{X}_g$ and the farthest node in the domain of definition of MLS function Ω_{X_g}

$$R_{\max} = \max\left\{ d_J = \left|\mathbf{X}_g - \mathbf{X}_J\right| \middle| \mathbf{X}_J \in \Omega_{X_g} \right\}, \tag{3.30}$$

as illustrated in Figure 3.5. The derivatives with respect to the global coordinates X^α are obtained by employing the chain derivative rule

$$\frac{\partial(\ )}{\partial X^\alpha} = \frac{\partial(\ )}{\partial \tilde{X}^\beta}\frac{\partial \tilde{X}^\beta}{\partial X^\alpha} = \frac{\partial(\ )}{\partial \tilde{X}^\alpha}\frac{1}{R_{\max}}. \tag{3.31}$$
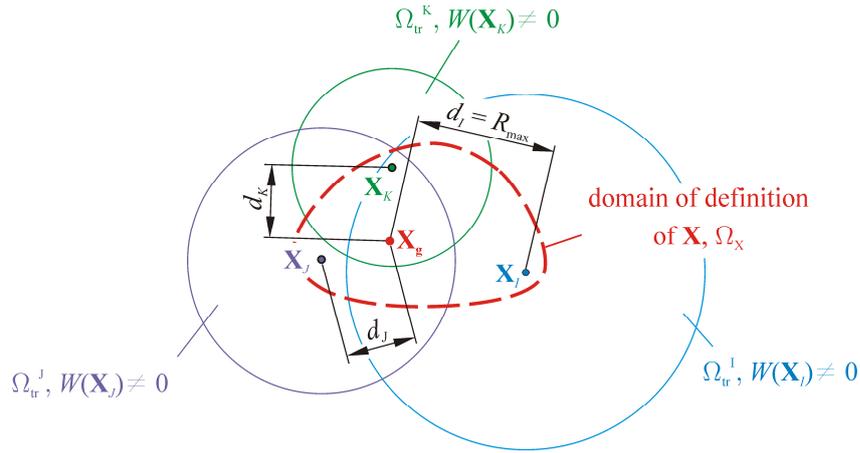
Figure 3.5 Normalization of coordinates

3.4.2 Fast derivative calculations

Belytschko and Fleming [125] proposed the following procedure for the faster computations of the MLS shape functions and their derivatives. The shape function in (3.13) may be rewritten as

$$\phi_J(\mathbf{X}) = \mathbf{p}(\mathbf{X})\mathbf{A}^{-1}(\mathbf{X})\mathbf{B}_J(\mathbf{X}) = \boldsymbol{\gamma}(\mathbf{X})\mathbf{B}_J(\mathbf{X}), \tag{3.32}$$

where $\mathbf{B}_J(\mathbf{X})$ is the Jth column of the matrix $\mathbf{B}(\mathbf{X})$, associated with the Jth node in Ω_X, and the vector $\boldsymbol{\gamma}(\mathbf{X})$ is determined by solving the following system of linear equations

$$\mathbf{A}(\mathbf{X})\boldsymbol{\gamma}(\mathbf{X}) = \mathbf{p}(\mathbf{X}). \tag{3.33}$$

The above system of equations may be solved by means of the LU-decomposition of the matrix $\mathbf{A}$ and by back substitution. This is computationally less expensive than performing the full inversion of the matrix $\mathbf{A}$ as in (3.13). The derivatives of ϕ_J may be obtained by differentiation of (3.32) as

$$\phi_{J,X^k}(\mathbf{X}) = \boldsymbol{\gamma}_{,X^k}(\mathbf{X})\mathbf{B}_J(\mathbf{X}) + \boldsymbol{\gamma}(\mathbf{X})\mathbf{B}_{J,X^k}(\mathbf{X}), \tag{3.34}$$

$$\begin{aligned}\phi_{J,X^kX^l}(\mathbf{X}) = {}&\boldsymbol{\gamma}_{,X^kX^l}(\mathbf{X})\mathbf{B}_J(\mathbf{X}) + \boldsymbol{\gamma}_{,X^k}(\mathbf{X})\mathbf{B}_{J,X^l}(\mathbf{X}) + \\ &\boldsymbol{\gamma}_{,X^l}(\mathbf{X})\mathbf{B}_{J,X^k}(\mathbf{X}) + \boldsymbol{\gamma}(\mathbf{X})\mathbf{B}_{J,X^kX^l}(\mathbf{X})\end{aligned}. \tag{3.35}$$

After $\boldsymbol{\gamma}(\mathbf{X})$ is evaluated from (3.33), the derivatives of $\boldsymbol{\gamma}(\mathbf{X})$ are computed by successively solving the following system of equations, obtained by differentiating (3.33)

$$\mathbf{A}(\mathbf{X})\boldsymbol{\gamma}_{,X^k}(\mathbf{X}) = \mathbf{p}(\mathbf{X}) - \mathbf{A}_{,X^k}(\mathbf{X})\boldsymbol{\gamma}(\mathbf{X}), \tag{3.36}$$

$$\mathbf{A}(\mathbf{X})\boldsymbol{\gamma}_{,X^k X^l}(\mathbf{X}) = \mathbf{p}_{,X^k X^l}(\mathbf{X}) - \mathbf{A}_{,X^k X^l}(\mathbf{X})\boldsymbol{\gamma}(\mathbf{X}) - \\ \mathbf{A}_{,X^k}(\mathbf{X})\boldsymbol{\gamma}_{,X^l}(\mathbf{X}) - \mathbf{A}_{,X^l}(\mathbf{X})\boldsymbol{\gamma}_{,X^k}(\mathbf{X}) \tag{3.37}$$

The values of ϕ_J, ϕ_{J,X^k} and $\phi_{J,X^{kl}}$ are obtained simply be inserting the solutions of (3.33), (3.36) and (3.37) into (3.32), (3.34) and (3.35), respectively. It is important to note that the LU-decomposition of the coefficient matrix $\mathbf{A}$ has to be calculated only while solving (3.33). After that it is memorized and only the back substitution is needed for solving the systems (3.36) and (3.37). The above procedure yields exactly the same results as the one presented in Section 3.1, but with lesser computational cost.

4 The MLPG method

Many popular meshless methods are based on global weak forms, such as the EFG method, which uses congruent background cells that completely cover the solution domain to integrate governing equations. In many cases, the procedure for defining such cells is similar to the mesh creation. These methods are therefore not truly meshless. In contrast, the MLPG method is based on the local concept where the integration is performed over local sub-domains that can be defined without having to employ a global mesh of congruent cells. Because the MLPG method does not necessarily apply the background cells or meshes for either approximation or integration, it is a truly meshless method.

4.1 The concept of the MLPG method

A global domain, defined by a volume Ω bounded by a surface Γ, is discretized only by a set of nodes that do not have to be connected into pre-defined elements. In order to develop the system of discretized equations, a local sub-domain Ω_s^I is defined around each node I with the position $\mathbf{X}_I$, $I = 1, 2, ... N$, as shown in Figure 4.1. N is the total number of nodes used for discretization. A weak form of governing differential equations is then imposed over each of these local sub-domains by applying the Petrov-Galerkin weighted residual method. These local sub-domains are allowed to overlap and may be of different shapes and sizes. As long as they completely cover the entire global domain, i.e., $\cup \Omega_s^I, I = 1, 2, ... N \supseteq \Omega \cup \partial\Omega$, the differential equations (2.43) and boundary conditions (2.44) should theoretically be satisfied *a posteriory* in their weak forms. Nevertheless, it has been discovered that even if the local domains do not completely cover the computational domain, a high quality solution may be obtained in some cases [15]. In contrast to the meshless formulations based on the global weak forms or FEM, the local weak forms and the corresponding discretized equations are formed in a node-by-node fashion, and no standard assembly of the global stiffness matrix is needed.

In the numerical implementation of the MLPG method, the following types of regions, illustrated in Figure 4.1, may be distinguished in the MLPG method:

▫ **Local sub-domain of the node** $\mathbf{X}_I$ **,** Ω_s^I **.** The local sub-domain Ω_s^I represents the integration domain over which numerical integration is performed to obtain the discretized algebraic equations associated with the node $\mathbf{X}_I$. It has been suggested [15],[18] that the concept of local integration over Ω_s^I actually acts as a relaxation of a strong form, and therefore, the size of Ω_s^I should be large enough to guarantee the stability and accuracy of a solution. However, too large a size of Ω_s^I may cause problems with the accuracy of the numerical integration, and generally lead to the increase of the total computational time.

▫ **The support of the test function for the node** $\mathbf{X}_I$ **,** Ω_t^I **.** In this region, a test function associated with the node $\mathbf{X}_I$ is non-zero. Ω_t^I may be completely different from Ω_s^I, but it is a common procedure to have $\Omega_s^I \equiv \Omega_t^I$. This is done in this work, and therefore from now on Ω_s^I will be synonymous with Ω_t^I.

▫ **The support of the nodal shape function of the node** $\mathbf{X}_I$ **(the support of the node** $\mathbf{X}_I$ **),** Ω_{tr}^I **.** In this region a nodal trial shape function $\phi_J(\mathbf{X})$, associated with the node $\mathbf{X}_I$ has non-zero values, $\phi_J(\mathbf{X}) \neq 0$. As meshless approximation functions are non-element functions, the connectivity between nodes is established by using the concept of Ω_{tr}^I, because the node $\mathbf{X}_I$ affects the approximation in all those points which are covered by its Ω_{tr}^I. For the MLS functions, Ω_{tr}^I coincides with the support domain of the MLS weight function $W_J(\mathbf{X})$, as explained in Section 3.2. The size of Ω_{tr}^I may have significant effects on the accuracy of the solution. Large sizes of Ω_{tr}^I increase the computational time needed for the evaluation of the shape functions. Furthermore, the non-zero band in the coefficient matrix of the global system of equations becomes wider, which demands more time for solving the system.

▫ **The domain of definition of the point X** This region includes all the nodes that influence the approximation at the point $\mathbf{X}$. For the MLS function, it is a region that includes all nodes whose MLS weight functions do not vanish at $\mathbf{X}$, as defined in Section 3.1.

- ▫ **The domain of influence of the node $\mathbf{X}_I$, Ω_{inf}^I.** This region covers all the nodes whose nodal shape functions have non-zero values over Ω_s^I associated with the node $\mathbf{X}_I$. Such nodes produce the non-zero couplings in the discretized equations stemming from the local weak form defined over Ω_s^I. Consequently, the domain of influence of the node $\mathbf{X}_I$ is identical to the union of the domains of definition Ω_x for all points $\mathbf{X}$ that belong to $\Omega_s^I \cup \partial\Omega_s^I$, i.e., $\cup\Omega_x \equiv \Omega_{\text{inf}}^I$, $\forall\mathbf{x} \in \Omega_s^I \cup \partial\Omega_s^I$.
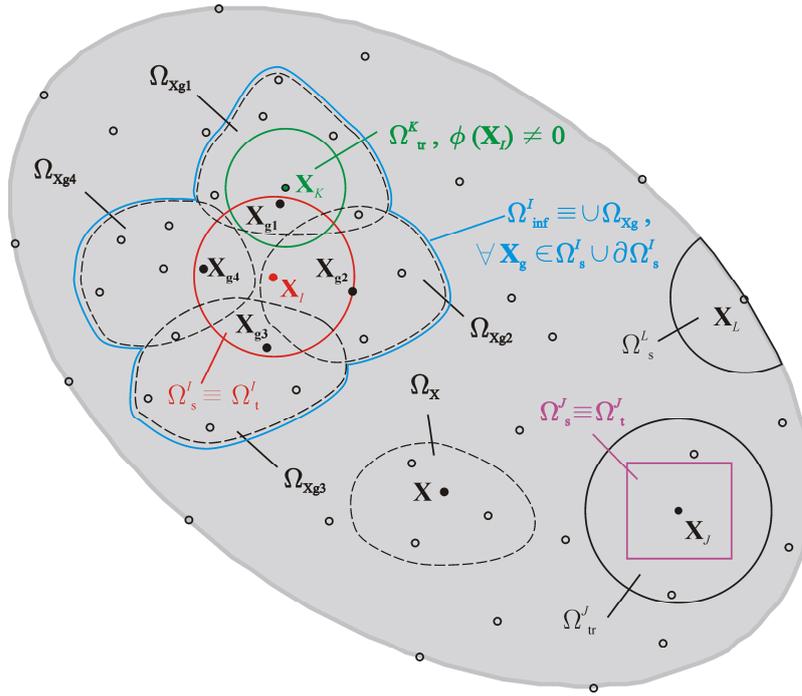
Figure 4.1Regions used in MLPG method

All above definitions are taken from [15] and have been designed mainly for the MLPG method. Consequently, they may be ambiguous to the terminology used in the literature dealing with other meshless approaches.

Theoretically, the choice of shapes for Ω_s^I, Ω_t^I and Ω_{tr}^I is arbitrary. However, in order to alleviate the numerical implementation, the simple geometrical shapes are usually used, such as spheres, parallelepipeds, or ellipsoids, with the corresponding nodes positioned at their centres.

4.2 Choice of trial and test functions

According to the Petrov-Galerkin principle, the test and trial functions may come from different functional spaces. This provides great flexibility to the MLPG method

because new formulations may be developed by choosing appropriate test and trial functions.

4.2.1 Trial functions

Any admissible non-element function that is able to approximate the set of data on randomly scattered nodes may be applied in the MLPG methods. The most popular meshless functions used in the frame of the MLPG method include:

▫ **Moving Least Squares (MLS) approximation functions.** These functions are often used in the MLPG formulations due to their good numerical features, such as the high order of continuity or consistency, as explained in Chapter 3. It should be noted that the identical functions for a given order of consistency may be derived by using the Reproducing Kernel Particle Method (RKPM) due to its equivalence with the MLS scheme in cases where the same weight or kernel functions are applied [15],[131].

▫ **The Shepard functions.** The Shepard functions are actually a special case of the MLS approximations, obtained if the zeroth-order monomial basis is employed [15], i.e., $\mathbf{p} = \begin{bmatrix} 1 \end{bmatrix}$. The shape functions are defined as

$$\phi_J(\mathbf{X}) = \frac{W_J(\mathbf{X})}{\displaystyle\sum_{I=1}^{N} W_I(\mathbf{X})}. \tag{4.1}$$

Herein $W_J(\mathbf{X})$ denotes the admissible chosen function associated with the J-th node [8],[15], and N stands for the total number of nodes used for discretization.

▫ **Compactly supported Radial Basis Functions (CS-RBF).** A vast number of various radial basis functions have been proposed in the literature [9],[10]. They are a popular approximation tool in meshless methods because they posses the Kronecker delta property and relatively simple derivatives. Among them, the CS-RBF functions are most suitable for the application in the MLPG method [15],[43],[45] due to their compact support, which ensures the locality. They lack consistency, but this can be overcome by adding polynomials into the approximation scheme.

▫ **Partition of Unity (PU).** This approximation scheme is used in the Method of Finite Sphere [21], which may be regarded as a special variant of the MLPG

approach. This scheme is actually an explicit generalization of the Shepard's method, in contrast to the MLS scheme, which generalizes Shepard's method implicitly. The PU approximations are not very suitable for use in the MPLG formulations because a relatively large number of unknown nodal parameters appear in the global system of equations [15].

▫ **Point Interpolation Method (PIM) and Radial Point Interpolation Method (RPIM).** The MLPG methods that employ the PIM or RPIM functions are often called the Local Point Interpolation Method (LPIM) or the Local Radial Point Interpolation Method (LRPIM), respectively. These techniques, developed by G.R. Liu and co-workers [13], is the local least-square approximation scheme, where, in contrast to the MLS method [15], no weighting is used. In PIM, the basis is composed of polynomials, while RPIM employs radial basis functions as the basis functions. PIM lacks a high order of continuity due to the restrictions posed on the choice of the nodes that are used for the construction of the approximations at the sample points. On the other hand, the RPIM functions lack consistency, unless the complete polynomials of the required order are added to the basis consisting of the radial basis functions. However, both schemes are able to produce convergent results [13], and therefore, are attractive choices due to their relative simplicity and computational efficiency.

4.2.2 Test functions

Depending on the type of test functions, six distinct MLPG methods have been identified in the literature [134],[135], labelled as MLPG1 to MLPG6. Although these types of test functions are predominantly used in the available MLPG formulations, any other admissible function can also be chosen as the test function. This fact has been used in the presented research. As revealed in Chapters 6 and 7, the proposed solid-shell formulations exploit some good sides of the following two "classical" six MLPG methods:

▫ **MLPG 2.** The Dirac delta functions at the nodes are applied as the test functions. The resulting formulations are actually collocation methods, and numerical integration is completely avoided.

▫ **MLPG 5.** The Heaviside step function is used as the test function in each Ω_s^I. In that case the domain integral over Ω_s^I is avoided and only the boundary integrals

over $\partial \Omega_s^I$ have to be calculated. Such an approach is very attractive because the resulting formulations are computationally very efficient [15], especially for 2-D and 3-D cases.

4.3 Imposition of the essential boundary conditions

Many of the meshless functions do not posses the Kronecker delta properties. Therefore, different numerical procedures have been developed to impose the essential BC *a posteriori*. In the MLPG method the following procedures are predominantly used:

▫ **The penalty method [96].** The penalty method, detailed in Section 2.4, is simple to employ and does not increase the total number of unknown parameters in the global system of equations. However, the quality of solution may be affected by the value of the penalty parameter. Currently the "optimal" values of the penalty parameter are often defined by applying various know-how formulas [15] or by performing parametric analyses.

▫ **The modified collocation method [96].** The modified collocation method enforces the essential boundary conditions only at the nodes and is simple to implement. For example, if the essential BC are prescribed at the node $\mathbf{X}_I$ for the displacements u, the given displacement value $\bar{u}_I$ is then enforced by setting the expression $u^{(h)}(\mathbf{X}_I) = \bar{u}_I$ instead of the corresponding equation in the local weak form associated with the node $\mathbf{X}_I$. Herein, $u^{(h)}$ is the value of the displacement approximation at the node $\mathbf{X}_I$.

▫ **The transformation method [33],[36].** In this approach, by imposing the interpolation conditions at the nodes, a standard non-interpolation meshless approximation is rewritten so that the true function values at the nodes become new nodal values. By employing such transformed approximations, after discretization the true nodal values appear as unknown parameters in the discretized equations and the essential BC may be satisfied directly, as in FEM. In order to reduce the computational costs, the transformation may be performed only at the nodes with the prescribed field values. This approach is efficient in imposing the essential BC, but it requires more computational effort than the previously mentioned procedures.

In cases where a meshless approximation possesses the Kronecker delta property, the above-described procedures may be avoided, and the essential BC may be imposed directly as in FEM. A more detailed description of the above-mentioned procedures, as well as their applications in the frame of the MLPG method, are available in [13],[15].

4.4 Numerical integration issues

In the MLPG method, numerical integration is performed over the local sub-domains Ω_s that are associated with the nodes used for discretization, and therefore may be regarded as a kind of nodal integration. However, in the MLPG method, integration domains are allowed to overlap. Finding an efficient general algorithm for the numerical integration in the MLPG method is still a critical issue. Meshless approximations, including relatively simple Shepard's functions, are complex non-polynomial functions that cannot be integrated exactly by employing simple Gaussian formulas, and therefore, a considerable numerical error may be generated.

Additional problems arising in the numerical integration of the local weak forms become more obvious by considering the local sub-domain Ω_s^I associated with the node $\mathbf{X}_I$, as shown in Figure 4.2.
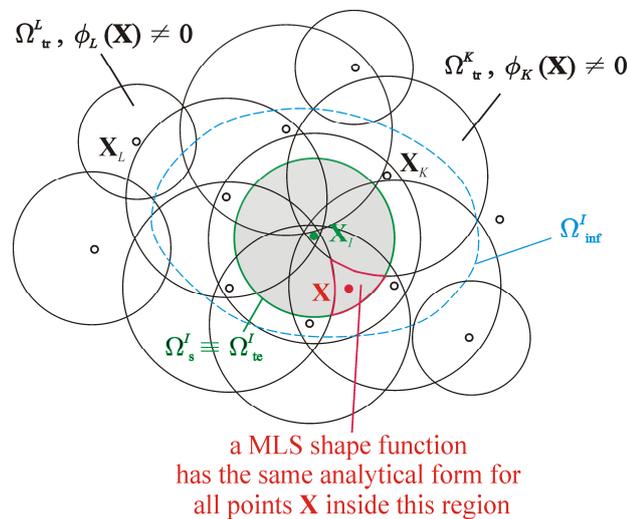
Figure 4.2 Local sub-domain Ω_s^I and its intersections with some Ω_{tr} associated with nodes belonging to domain of influence of node $\mathbf{X}_I$, labelled as Ω_{inf}^I.

As previously explained, only the nodes $\mathbf{X}_K$ that belong to the domain of influence of the node $\mathbf{X}_I$, labelled as Ω_{inf}^I, affect the approximation of the unknown field variables over Ω_s^I. In contrast to FEM, the support domains of their shape functions Ω_{tr}^K do not

coincide with each other or with Ω_s^I, and consequently, the MLS shape functions have different analytical expressions at different points $\mathbf{X}$ inside Ω_s^I, because the domains of definitions $\Omega_{\mathbf{X}}$ of the points $\mathbf{X}$ also differ. Because of this, the derivatives of the MLS shape functions have very complex forms over Ω_s^I, which may cause significant numerical errors during integration. In the above explanations, the definitions given in Section 4.1 are used. More detailed discussion about the problems encountered in the numerical integration in the MLPG method may be found in [15], and the references therein.

Generally, it is desirable to use smaller sizes of Ω_s^I to reduce the number of intersections of Ω_s^I with Ω_{tr}^J. In some formulations, integration is performed separately for each $\Omega_s^I \cap \Omega_{tr}^J$, but this is a tedious procedure, especially because the integration has to be performed over relatively complicated geometrical shapes such as lenses [15],[136]. On the other hand, the integrand can be made simpler by properly choosing the test functions. If the Heaviside test function is employed, as in the MLPG 5 method, the domain integral over Ω_s^I can by completely avoided. The shape of Ω_s^I may also affect the performance of the numerical integration. The Gaussian formulas are not suitable for integrating the trigonometric functions, which have to be employed to describe the geometries of the circular or spherical Ω_s^I. This problem may be circumvented by defining the quadratic or hexagonal shapes for Ω_s^I [13], albeit with the increase of computational costs. The spherical local sub-domains may be triangulated as in [45], and the obtained polyhedrons may then be used for numerical integration.

In this work, two approaches are used for the numerical integration over Ω_s^I:

▫ **A direct integration over the entire Ω_s^I by using Gaussian formulas.** This stratagem is popular due to its simplicity, especially where the integrands are relatively simple, as in the case of MLPG 1 and MLPG 5 methods. In the Method of Finite Spheres [21], the integration over a circular Ω_s^I is performed by means of the special cubature rule for annular sectors, where the Gauss-Legendre and Gauss-Chebyshev rules are applied in the circular and radial directions, respectively. Mazzia et al. [137] compared the performances of various Gaussian rules in the MLPG method and concluded that in all cases a relatively large number of

quadrature points is needed to obtain high accuracy. In this work, the integration over a circular Ω_s^I was performed by employing the 2-D Gauss-Legendre rule.

▫ **A partition of** Ω_s^I**.** Ω_s^I is partitioned into a sufficient number of smaller parts and the numerical integration is then performed over these parts by using a small number of quadrature points. It is shown in [15],[36] that such an approach yields more accurate results than by performing the integration over the entire Ω_s^I using a large number of Gaussian points. The partition of Ω_s^I is especially useful when integrands are complicated. Some special "engineering" solutions, developed for the circular Ω_s^I in the MFS method [21],[136], may also be regarded as a variant of such strategy. They employ the mid-point quadrature rules for the local sub-domains that intersect the global boundary. The rectangular sub-domains may also be partitioned for better accuracy, as in [13]. In this work, four parts were used for the integration over the rectangular Ω_s^I.

5 MLPG solid-shell concept

5.1 Strong formulation of problem and representation of shell-like continuum

The stationary state of a linear elastic shell is examined, considered here as a 3-D solid continuum represented by the global domain Ω, as illustrated in Figure 5.1. The well-known 3-D equilibrium equations for the static case, written here in the global Cartesian coordinate system as

$$\sigma_{ij,X^j} + b_i = 0, \quad \text{in } \Omega, \tag{2.42}$$

represent the strong form of the governing equations. In the above equation, σ_{ij} stands for the stress tensor and b_j denotes the body force vector, both defined in the global Cartesian coordinates. Ω is bounded by the global boundary Γ, $\Gamma = \Gamma_u \cup \Gamma_t$, on which the following boundary conditions (BC) are prescribed

$$u_i = \overline{u}_i, \quad \text{on } \Gamma_u, \tag{5.1}$$

$$t_i = \sigma_{ij} n_j = \overline{t}_i, \quad \text{on } \Gamma_t. \tag{5.2}$$

Herein Γ_u and Γ_t are the parts of Γ with the prescribed displacements $\overline{u}_i$ and surface tractions $\overline{t}_i$, respectively, while n_j denotes the direction cosines of the unit outward normal vector to Γ.

The geometry of the shell is defined by describing the geometry of its middle surface according to relations (2.3) and (2.4), given in Section 2.1.1. The middle surface is parameterized by employing the curvilinear coordinates θ^α, or by using the normalized curvilinear coordinates ξ^α. The covariant metric vectors $\mathbf{G}_i$ or $\widehat{\mathbf{G}}_i$ may then be calculated according to (2.8) or (2.18), respectively. In the following, the procedure for deriving the weak forms of the governing equations is described for the coordinate set $\left(\theta^1, \theta^2, \theta^3\right)$, but it is also directly applicable for the normalized coordinates $\left(\xi^1, \xi^2, \xi^3\right)$.
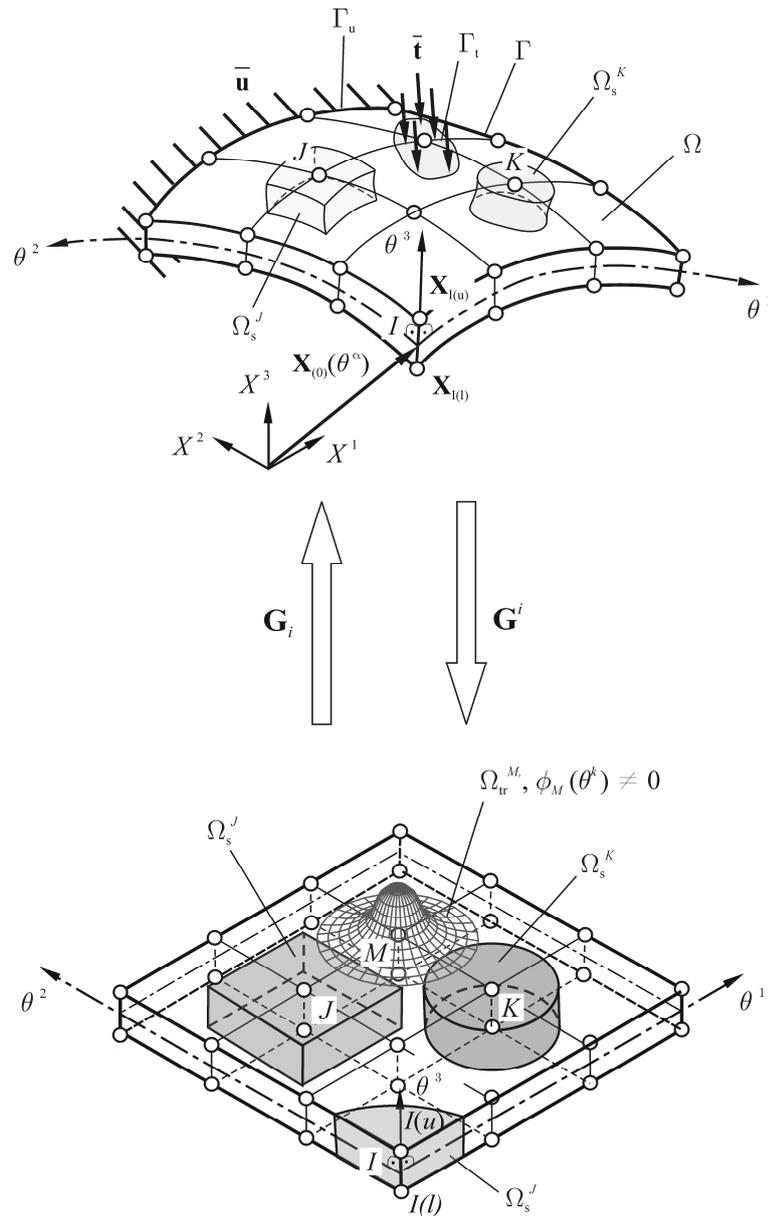
Figure 5.1 Parameterization and discretization of numerical model

By employing the above described parameterization technique, the continuum is mapped into the parametric space $\left(\theta^1, \theta^2, \theta^3\right)$. According to the solid-shell concept, the shell is then represented by a set of the node couples $I = 1, 2, ..., N$ in the parametric space. The nodes $I(u)$ and $I(l)$ which form one node couple are positioned on the upper and lower shell surface, respectively. These nodes lay on the same fibre in the direction of the normal vector to the shell middle surface, i.e., in the direction orthogonal to the θ^1, θ^2-plane, and their respective position vectors in the global Cartesian system are $\mathbf{X}_{I(u)}$ and $\mathbf{X}_{I(l)}$. N stands for the total number of the node couples used for discretization. All approximations are performed in the parametric space and

consequently, all approximated variables appearing in the governing equations are the functions of the parametric coordinates θ^k, i.e. $\sigma_{ij} = \sigma_{ij}(\theta^k)$. For simplicity, from this point on the arguments are omitted unless necessary for clear understanding.

In order to obtain the solutions of the equations (2.42), (5.1) and (5.2), the local weighted residual method (WRM) described in Section 2.4.1 is implemented. For that purpose, the local sub-domains represented by the volumes $\Omega_s^I, I = 1, 2, ..., N,$ are defined around each node couple $I, I = 1, 2, ..., N,$ in the parametric space. The local sub-domains are positioned inside the global domain, $\Omega_s^I \subset \Omega$. As explained in Chapter 4, they could be of any shape and size and they are allowed to overlap each other. For simplicity, the local sub-domains used in this work have the shapes of circular cylinders or parallelepipeds in the parametric space, and their vertical axes are parallel to the θ^3-direction, as shown in Figure 5.1. The node couples and their corresponding local sub-domains are mapped back to the global Cartesian coordinate system by means of the metric vectors $\mathbf{G}_i$, as explained in Section 2.1.1.

5.2 Local weak form of governing equations

According to the local WRM, a local weak form (LWF) of the equilibrium equations (2.42), defined over a local sub-domain $\Omega_s^I, I = 1, 2, ..., N$, has the following form

$$\int_{\Omega_s^I} v_i \left(\sigma_{ij,X^j} + b_i \right) \mathrm{d}\Omega - \alpha \int_{\Gamma_{su}^I} v_i (u_i - \overline{u}_i) \, \mathrm{d}\Gamma = 0. \tag{5.3}$$

Herein, v_i denotes a set of some admissible test functions, while the stresses σ_{ij} are the functions of the unknown field variables, which are approximated by employing meshless trial functions. Note that all variables in (5.3) are defined in the global Cartesian coordinate system. As many of the meshless approximation functions do not posses the Kronecker delta property, for generality a constrained local WRM employing the penalty method according to (2.52) is used in (5.3) to enforce the essential BC, with $\alpha \gg 1$ as the penalty parameter. The essential BC for the static problems considered here are the prescribed displacements (5.1). Γ_{su} is the part of the local boundary $\partial\Omega_s^I$, bounding Ω_s^I, which coincides with Γ_u, $\Gamma_{su}^I = \partial\Omega_s^I \cap \Gamma_u$. However, it is important to

note that if a trial function owns the Kronecker delta property, the penalty term may be omitted and the essential BC can be imposed directly like in FEM.

Employing the following identity for taking the derivative of a product

$$v_i \sigma_{ij,X^j} = \left(v_i \sigma_{ij} \right)_{,X^j} - v_{i,X^j} \sigma_{ij}, \tag{5.4}$$

the first integral term over Ω_s^I in LWF (5.3) is rewritten as follows

$$\int_{\Omega_s^I} v_i \left(\sigma_{ij,X^j} + b_i \right) \mathrm{d}\Omega = \int_{\Omega_s^I} \left(v_i \sigma_{ij} \right)_{,X^j} \mathrm{d}\Omega - \int_{\Omega_s^I} v_{i,X^j} \sigma_{ij} \mathrm{d}\Omega + \int_{\Omega_s^I} b_i \mathrm{d}\Omega . \tag{5.5}$$

Using the divergence theorem, the first term on the right-hand side in (5.5) may be transformed into the surface integral over $\partial\Omega_s^I$ as

$$\int_{\Omega_s^I} \left(v_i \sigma_{ij} \right)_{,X^j} \mathrm{d}\Omega = \int_{\partial\Omega_s^I} n_j v_i \sigma_{ij} \mathrm{d}\Gamma . \tag{5.6}$$

Inserting (5.5) and (5.6) into (5.3), LWF for the node couple I now reads as

$$\int_{\Omega_s^I} v_{i,X^j} \sigma_{ij} \mathrm{d}\Omega - \int_{\partial\Omega_s^I} n_j v_i \sigma_{ij} \mathrm{d}\Gamma - \int_{\Omega_s^I} v_i b_i \mathrm{d}\Omega + \alpha \int_{\Gamma_{su}^I} v_i (u_i - \overline{u}_i) \mathrm{d}\Gamma = 0 . \tag{5.7}$$

Note that in the last expression the continuity requirement for the test function is higher than in relation (5.3) so that now v_i have to be C^0 continuous. On the other hand, the condition for the continuity of the trial functions needed for the evaluation of σ_{ij} is lower by one degree. The local boundary $\partial\Omega_s^I$ can be split into three parts

$$\partial\Omega_s^I = L_s^I \cup \Gamma_{st}^I \cup \Gamma_{su}^I, \quad \Gamma_{st}^I = \Gamma_t \cap \partial\Omega_s^I, \quad \Gamma_{su}^I = \Gamma_u \cap \partial\Omega_s^I, \tag{5.8}$$

where L_s^I is the part of $\partial\Omega_s^I$ which is entirely inside Ω, while Γ_{st}^I is the part of $\partial\Omega_s^I$ which coincides with Γ_t, i.e., the part of Γ with the prescribed traction surface boundary conditions. Taking into account (2.38), it follows that $t_i = n_j \sigma_{ij}$ everywhere on $\partial\Omega_s^I$, and specifically $t_i = \overline{t}_i$ on Γ_{st}, according to (5.2) and (5.8). Consequently, LSW (5.7) may be transformed into

$$\int_{\Omega_s^I} v_{i,X^j} \, \sigma_{ij} \, \mathrm{d}\Omega - \int_{L_s^I} v_i \, n_j \sigma_{ij} \mathrm{d}\Gamma - \int_{\Gamma_{su}^I} v_i \, n_j \sigma_{ij} \mathrm{d}\Gamma + \alpha \int_{\Gamma_{su}^I} v_i u_i \, \mathrm{d}\Gamma -$$
$$\int_{\Omega_s^I} v_i \, b_i \, \mathrm{d}\Omega - \int_{\Gamma_{st}^I} v_i \, \overline{t}_i \mathrm{d}\Gamma - \alpha \int_{\Gamma_{su}^I} v_i \overline{u}_i \, \mathrm{d}\Gamma = 0. \tag{5.9}$$

As the traction surface BC (5.2) are included in LWF (5.9), they are the natural BC.

According to the Petrov-Galerkin approach, the test and trial functions may come from different functional spaces. It means that theoretically any of the functions satisfying the C^0 continuity may be employed as the test function. In the MLPG method, usually the known functions, such as the MLS weight functions given in the Section 3.2, or the MLS shape functions (3.13), are used. However, it is to note that if the test functions v_i are some known functions, then relation (5.9) yields only one equation per node couple.

As explained in [41],[42], in the systems of equations of the purely displacement 3-D solid formulations the unknown variables are three displacement components. Therefore, three linearly independent sets of the test functions have to be used to obtain the needed three discretized equations per each node. The analogous stratagem is employed here, leading to

$$\int_{\Omega_s^I} v_{ki,X^j} \, \sigma_{ij} \, \mathrm{d}\Omega - \int_{L_s^I} v_{ki} \, n_j \sigma_{ij} \mathrm{d}\Gamma - \int_{\Gamma_{su}^I} v_{ki} \, n_j \sigma_{ij} \mathrm{d}\Gamma + \alpha \int_{\Gamma_{su}^I} v_{ki} u_i \, \mathrm{d}\Gamma -$$
$$\int_{\Omega_s^I} v_{ki} \, b_i \, \mathrm{d}\Omega - \int_{\Gamma_{st}^I} v_{ki} \, \overline{t}_i \mathrm{d}\Gamma - \alpha \int_{\Gamma_{su}^I} v_{ki} \overline{u}_i \, \mathrm{d}\Gamma = 0. \tag{5.10}$$

Herein v_{ki} denotes the kth set of equations. For simplicity, they are formed by choosing the test functions sets such that

$$v_{ki} = \delta_{ki} v\left(\theta^j\right), \tag{5.11}$$

where δ_{ki} is the Kronecker delta symbol from (2.10) and $v(\theta^j)$ denotes an arbitrary admissible test function. Inserting the test function set (5.11) into (5.10), LWF yields the following expression

$$\int_{\Omega_s^I} v_{,X^j} \, \sigma_{kj} \, \mathrm{d}\Omega - \int_{L_s^I} v n_j \sigma_{kj} \mathrm{d}\Gamma - \int_{\Gamma_{su}^I} v n_j \sigma_{kj} \mathrm{d}\Gamma + \alpha \int_{\Gamma_{su}^I} v u_k \, \mathrm{d}\Gamma -$$
$$-\int_{\Omega_s^I} v b_k \, \mathrm{d}\Omega - \int_{\Gamma_{st}^I} v \overline{t}_k \mathrm{d}\Gamma - \alpha \int_{\Gamma_{su}^I} v \overline{u}_k \, \mathrm{d}\Gamma = 0. \tag{5.12}$$

It is important to note that in (5.12) the stresses σ_{ij} may actually be the functions of a set of unknown independent field variables, such as various displacement, strain or even stress components, which are then approximated by employing various meshless trial functions. Different approaches lead to different displacement-based or mixed meshless formulations. Accordingly, equation (5.12) serves as the starting point for developing all the MLPG formulations presented in this work, regardless on whether a mixed or purely displacement-based approach is adopted for their development.

5.2.1 Test functions that are linear in thickness direction and corresponding LWF

In the solid-shell formulations employing the linear displacement distribution across the thickness according to (2.20) or (2.21), each node possesses three unknown displacement variables. As in the proposed approach two nodes belonging to the same node couple share the same local sub-domain, six independent equations per each local sub-domain are needed to close the global system of equations. This may be easily achieved by assuming that the function $v\left(\theta^k\right)$ is a linear combination of two independent functions $v_1\left(\theta^k\right)$ and $v_2\left(\theta^k\right)$

$$v\left(\theta^k\right)=c_1 v_1\left(\theta^k\right)+c_2 v_2\left(\theta^k\right),\quad c_1,c_2\in\mathbb{R}, \tag{5.13}$$

where c_1 and c_2 are arbitrary chosen non-zero real constants. The functions $v_1\left(\theta^k\right)$ and $v_2\left(\theta^k\right)$ are defined as the products of two functions, analogously to the displacement trial functions, as

$$v_1\left(\theta^k\right)=f_1\left(\theta^\alpha\right)g_1\left(\theta^3\right),\quad v_2\left(\theta^k\right)=f_2\left(\theta^\alpha\right)g_2\left(\theta^3\right). \tag{5.14}$$

Herein, $f_\beta\left(\theta^\alpha\right)$ are some admissible arbitrary functions of in-plane coordinates θ^α. In order to cut the computational costs, in this work it is chosen as the Heaviside function

$$f_1\left(\theta^\alpha\right)=f_2\left(\theta^\alpha\right)=\begin{cases}1, & \theta^\alpha\in\Omega_s^I\cup\partial\Omega_s^I \\ 0, & \theta^\alpha\notin\Omega_s^I\cup\partial\Omega_s^I\end{cases}, \tag{5.15}$$

while $g_\beta\left(\theta^3\right)$ are linear polynomials in the thickness directions. Again, analogously to the displacement field, they may be chosen as

$$g_1\left(\theta^3\right)=1, \quad g_2\left(\theta^3\right)=\theta^3 \tag{5.16}$$

or as the linear functions from (2.2)

$$g_1\left(\theta^3\right)=\psi^1\left(\theta^3\right)=\frac{1}{2}+\frac{\theta^3}{h}, \quad g_2\left(\theta^3\right)=\psi^2\left(\theta^3\right)=\frac{1}{2}-\frac{\theta^3}{h}. \tag{5.17}$$

It should be noted that in most cases identical results are obtained for both (5.16) and (5.17). However, the functions defined by (5.17) are appropriate if the essential BC are to be enforced on the upper or lower structure surface by means of the penalty method, in which case the use of (5.16) may lead to the ill-conditioned global stiffness matrix and erroneous results. On the other hand, LWF are somewhat simpler and computationally less demanding if functions (5.16) are used. Therefore, LWF for the formulations presented in this contribution are derived by employing (5.16).

Inserting the test function set (5.13) and (5.14) into (5.12), the following form of LWF may be obtained

$$
\begin{aligned}
&c_1\left[\int_{\Omega_s^I} v_{1,X^j}\,\sigma_{kj}\,\mathrm{d}\Omega - \int_{L_s^I} v_1\,n_j\sigma_{kj}\,\mathrm{d}\Gamma - \int_{\Gamma_{su}^I} v_1\,n_j\sigma_{kj}\,\mathrm{d}\Gamma + \alpha\int_{\Gamma_{su}^I} v_1 u_k\,\mathrm{d}\Gamma - \right.\\
&\left.\quad -\int_{\Omega_s^I} v_1\,b_k\,\mathrm{d}\Omega - \int_{\Gamma_{st}^I} v_1\,\overline{t}_k\,\mathrm{d}\Gamma - \alpha\int_{\Gamma_{su}^I} v_1\overline{u}_k\,\mathrm{d}\Gamma\right]+\\
&c_2\left[\int_{\Omega_s^I} v_{2,X^j}\,\sigma_{kj}\,\mathrm{d}\Omega - \int_{L_s^I} v_2\,n_j\sigma_{kj}\,\mathrm{d}\Gamma - \int_{\Gamma_{su}^I} v_2\,n_j\sigma_{kj}\,\mathrm{d}\Gamma + \alpha\int_{\Gamma_{su}^I} v_2 u_k\,\mathrm{d}\Gamma - \right.\\
&\left.\quad -\int_{\Omega_s^I} v_2\,b_k\,\mathrm{d}\Omega - \int_{\Gamma_{st}^I} v_2\,\overline{t}_k\,\mathrm{d}\Gamma - \alpha\int_{\Gamma_{su}^I} v_2\overline{u}_k\,\mathrm{d}\Gamma\right]=0.
\end{aligned}
\tag{5.18}
$$

This expression has to hold for all choices of c_1 and c_2, which yields the following system of six governing equations for each Ω_s^I

$$
\begin{aligned}
&\int_{\Omega_s^I} v_{1,X^j}\,\sigma_{kj}\,\mathrm{d}\Omega - \int_{L_s^I} v_1\,n_j\sigma_{kj}\,\mathrm{d}\Gamma - \int_{\Gamma_{su}^I} v_1\,n_j\sigma_{kj}\,\mathrm{d}\Gamma + \alpha\int_{\Gamma_{su}^I} v_1 u_k\,\mathrm{d}\Gamma = \\
&\int_{\Omega_s^I} v_1\,b_k\,\mathrm{d}\Omega + \int_{\Gamma_{st}^I} v_1\,\overline{t}_k\,\mathrm{d}\Gamma + \alpha\int_{\Gamma_{su}^I} v_1\overline{u}_k\,\mathrm{d}\Gamma,
\end{aligned}
\tag{5.19}
$$

$$\int\limits_{\Omega_s^I} v_{2,X^j}\,\sigma_{kj}\,\mathrm{d}\Omega - \int\limits_{L_s^I} v_2\,n_j\sigma_{kj}\mathrm{d}\Gamma - \int\limits_{\Gamma_{su}^I} v_2\,n_j\sigma_{kj}\mathrm{d}\Gamma + \alpha \int\limits_{\Gamma_{su}^I} v_2 u_k\,\mathrm{d}\Gamma =$$

$$\int\limits_{\Omega_s^I} v_2\,b_k\,\mathrm{d}\Omega + \int\limits_{\Gamma_{st}^I} v_2\,\overline{t_k}\mathrm{d}\Gamma + \alpha \int\limits_{\Gamma_{su}^I} v_2\overline{u}_k\,\mathrm{d}\Gamma. \tag{5.20}$$

5.2.1.1 LWF for purely displacement-based solid-shell approach

In the purely displacement-based numerical formulations, the displacement field appears as the only unknown independent field. Such numerical methods are sometimes called the primal methods [40]. In the case of the small strain theory and for linear elastic materials, it is possible to calculate the stresses in the global Cartesian coordinate system by inserting the 3-D kinematic relations (2.27) into the constitutive relations (2.29) as

$$\sigma_{ij} = C_{ijkl}\varepsilon_{kl} = C_{ijkl}\frac{1}{2}\left(u_{k,X^l} + u_{l,X^k}\right). \tag{5.21}$$

After inserting (5.21) into relations (5.19) and (5.20), the following LWF for each Ω_s^I is obtained in terms of displacements as

$$\int\limits_{\Omega_s^I} v_{1,X^j}\,C_{ijkl}\frac{1}{2}\left(u_{k,X^l}+u_{l,X^k}\right)\mathrm{d}\Omega - \int\limits_{L_s^I} v_1\,n_j C_{ijkl}\frac{1}{2}\left(u_{k,X^l}+u_{l,X^k}\right)\mathrm{d}\Gamma -$$

$$-\int\limits_{\Gamma_{su}^I} v_1\,n_j C_{ijkl}\frac{1}{2}\left(u_{k,X^l}+u_{l,X^k}\right)\mathrm{d}\Gamma + \alpha \int\limits_{\Gamma_{su}^I} v_1 u_k\,\mathrm{d}\Gamma = \tag{5.22}$$

$$\int\limits_{\Omega_s^I} v_1\,b_k\,\mathrm{d}\Omega + \int\limits_{\Gamma_{st}^I} v_1\,\overline{t_k}\mathrm{d}\Gamma + \alpha \int\limits_{\Gamma_{su}^I} v_1\overline{u}_k\,\mathrm{d}\Gamma,$$

$$\int\limits_{\Omega_s^I} v_{2,X^j}\,C_{ijkl}\frac{1}{2}\left(u_{k,X^l}+u_{l,X^k}\right)\mathrm{d}\Omega - \int\limits_{L_s^I} v_2\,n_j C_{ijkl}\frac{1}{2}\left(u_{k,X^l}+u_{l,X^k}\right)\mathrm{d}\Gamma -$$

$$-\int\limits_{\Gamma_{su}^I} v_2\,n_j C_{ijkl}\frac{1}{2}\left(u_{k,X^l}+u_{l,X^k}\right)\mathrm{d}\Gamma + \alpha \int\limits_{\Gamma_{su}^I} v_2 u_k\,\mathrm{d}\Gamma = \tag{5.23}$$

$$\int\limits_{\Omega_s^I} v_2\,b_k\,\mathrm{d}\Omega + \int\limits_{\Gamma_{st}^I} v_2\,\overline{t_k}\mathrm{d}\Gamma + \alpha \int\limits_{\Gamma_{su}^I} v_2\overline{u}_k\,\mathrm{d}\Gamma.$$

Since the highest-order derivatives appearing under the integrals are of the first order for both the test and trial functions, both of them have to be C^0 continuous functions, and therefore the last expression is sometimes called the local symmetric weak form (LSWF) [15].

5.3 Primal solid-shell MLPG approach and locking effects

Various pathological numerical phenomena commonly known as the locking effects usually plague the primal algorithms for the numerical analysis of shell-like structures. In FEM, these unwanted phenomena usually manifest as the overly stiff deformation response of the numerical model, or may cause the numerical instabilities during the solution procedure [3],[6],[63],[81],[86],[93],[102],[107]. Herein, the origins of Poisson's thickness locking and transversal shear locking are exposed by considering the behaviour of the solid-shell MLPG formulations in the bending state.

5.3.1 The Poisson's thickness locking effect

For the shell-like structures subjected to the pure bending state, the normal stress component σ^{33} in the thickness direction, i.e. in the direction θ^3, vanishes [3], [93],[138],[139]. However, in the primal numerical solid-shell approaches with the linear distribution of displacements in the thickness direction, the constant normal strain ε_{33} is predicted, which leads to the non-zero approximation of σ^{33} across the thickness. Consequently, the deformation response of the structure is too stiff. Such behaviour is called Poisson's thickness locking.

In order to better illustrate this unwanted numerical effect, the reasoning analogous to the one presented in [138] for the solid-shell finite elements is applied here. Consider a thin rectangular plate subjected to pure bending, according to Figure 5.2. The true stress state for such case is

$$\sigma_{12} = \sigma_{23} = \sigma_{13} = \sigma_{22} = \sigma_{33} = 0, \quad \sigma_{11} = \frac{12M}{h^3}X^3. \tag{5.24}$$

It is obvious from the above equation that the normal in-plane stress σ_{11} should be distributed linearly over the thickness. For the linear elastic isotropic material the corresponding true state of strains may be obtained by employing the constitutive relations (2.29), (2.34) and (2.35)

$$\varepsilon_{12} = \varepsilon_{23} = \varepsilon_{13} = 0,$$

$$\varepsilon_{11} = \frac{\sigma_{11}}{E}, \quad \varepsilon_{22} = -\frac{v}{E}\sigma_{11} = -v\varepsilon_{11}, \quad \varepsilon_{33} = -\frac{v}{E}\sigma_{11} = -v\varepsilon_{11}. \tag{5.25}$$

It is to note that, according to (5.25), the normal strains ε_{33} should be linear across the thickness, as shown in Figure 5.2 b). According to such distribution of ε_{33}, the total length of normal fibre remains the same, but on the one side of the plate middle surface, it becomes shorter, while on the opposite side it streches for the same amount of length.
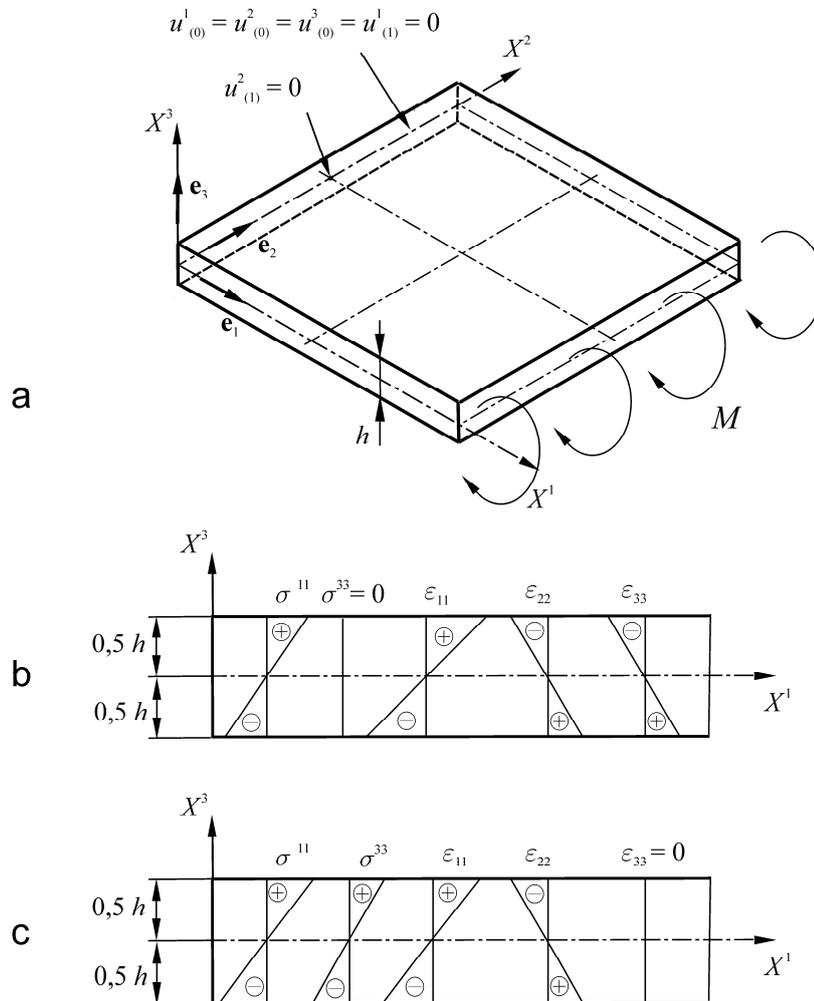
Figure 5.2 Rectangular plate subjected to pure bending: a) boundary condition b) true strain and stress states, c) predicted strain and stress states.

In the standard primal solid-shell approach the displacements are approximated linearly in the thickness direction, as in (2.20) or (2.21). Taking into account that for the rectangular plates $\theta^k = X^k$, the displacement field may be written as

$$\mathbf{u}\left(X^j\right) = \mathbf{u}_{(0)}\left(X^\alpha\right) + X^3\,\mathbf{u}_{(1)}\left(X^\alpha\right) \tag{5.26}$$

and corresponding strains are evaluated according to (2.27) as

$$\varepsilon_{ij}\left(X^k\right)=\frac{1}{2}\left(\frac{\partial u^i\left(X^k\right)}{\partial X^j}+\frac{\partial u^j\left(X^k\right)}{\partial X^i}\right)\qquad(5.27)$$

This leads to the following prediction for the normal strains

$$\varepsilon_{11}=\frac{\partial u^1\left(X^k\right)}{\partial X^1}=\left(\frac{\partial u_{(0)}^1\left(X^\gamma\right)}{\partial X^1}+X^3\frac{\partial u_{(1)}^1\left(X^\gamma\right)}{\partial X^1}\right),$$

$$\varepsilon_{22}=\frac{\partial u^2\left(X^k\right)}{\partial X^2}=\left(\frac{\partial u_{(0)}^2\left(X^\gamma\right)}{\partial X^2}+X^3\frac{\partial u_{(1)}^2\left(X^\gamma\right)}{\partial X^2}\right),\qquad(5.28)$$

$$\varepsilon_{33}=\frac{\partial u^3\left(X^k\right)}{\partial X^3}=\frac{\partial}{\partial X^3}\left(u_{(0)}^3\left(X^\gamma\right)+X^3u_{(1)}^3\left(X^\gamma\right)\right)=u_{(1)}^3\left(X^\gamma\right).$$

Employing the constitutive relations (2.29), (2.34) and (2.35), the normal stresses computed from the strains are

$$\sigma_{11}=\left(2G+\lambda\right)\varepsilon_{11}+\lambda\varepsilon_{22}+\lambda\varepsilon_{33},$$

$$\sigma_{22}=\lambda\varepsilon_{11}+\left(2G+\lambda\right)\varepsilon_{22}+\lambda\varepsilon_{33},\qquad(5.29)$$

$$\sigma_{33}=\lambda\varepsilon_{11}+\lambda\varepsilon_{22}+\left(2G+\lambda\right)\varepsilon_{33}.$$

It is clear from the first two expressions in (5.28) that the adequate linear distribution of ε_{11} and ε_{22} across the thickness may be predicted. However, ε_{33} may assume only constant values over the thickness. Therefore, it must hold that $\varepsilon_{33}=0$ if the total length of the normal fibre is to remain unchanged. Consequently, due to the coupling of ε_{33} with the linear in-plane components $\varepsilon_{\alpha\alpha}$ for $v\neq0$, the third expression in (5.29) yields σ_{33} that is linear in the thickness direction instead of being $\sigma_{33}=0$. This distribution of σ_{33} leads to the erroneous structure response, which is commonly called the Poisson's thickness locking effect. The analogous effect occurs in the curved shell structures, but then the more complicated metrics of such structures must be taken into account [93]. It is to note that Poisson's thickness locking arises only if $v\neq0$. It does not depend on the structure dimensions, and therefore it is present in both thin and thick shell-like structure.

Various ways to eliminate this unwanted numerical phenomenon are known in FEM [3], [93], [95]. However, not all of them are directly applicable in the MLPG

method. In this work, the hierarchical quadratic interpolation [93],[139] for the transversal displacement component u^3 in the thickness direction is implemented in the purely-displacement formulations, while the various novel approaches are developed for the mixed MLPG approach, as explained in details in Chapters 6 and 7.

5.4 Transversal shear locking effect

The transversal shear locking effect appears in the numerical formulations that are unable to satisfy the zero transversal shear strain condition in pure bending mode. As a result parasitic transversal shear strains appear, causing erroneous deformation response of the discretized numerical models. The intensity of this effect depends on the structure length-to-thickness ratio and increases as the structure becomes thinner.

The existence of the transversal shear locking effect has been detected in a number of meshless methods. In [103], Li and co-workers tried to reveal the origin of the shear locking effect in the primal MLPG solid-shell formulations from the theoretical point of view. By considering the MLS trial functions as polynomial functions in the neighbourhood of each point, they show that the shear locking appears because the displacement approximations are unable to fulfil the Kirchoff-Love assumptions in the thin plate limit. In this contribution, the problem of transversal shear locking is reviewed by partially reiterating the proof presented in [103], but without introducing any simplifications considering the MLS trial functions.
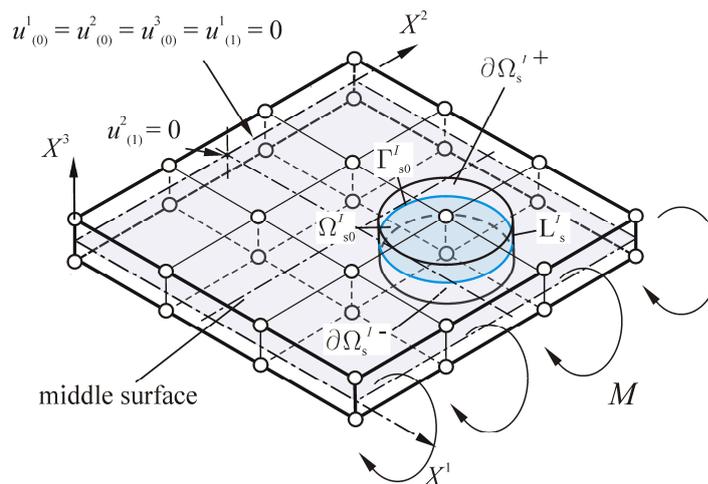
Figure 5.3 Rectangular plate subjected to pure bending. Local sub-domain for internal node *I*.

A rectangular plate subjected to the pure bending state as shown in Figure 5.3 is considered, where $\theta^k = X^k$. The global Cartesian coordinate system with the unit

vectors $\mathbf{e}_i$ is attached to the plate so that the plate middle surface coincides with the X^1, X^2-plane, while the coordinate axis X^3 is in the thickness direction.

For simplicity the following restrictions are introduced, which however do not cause any loss of generality:

▫ The value of the Poisson's coefficient is set to zero, i.e., $\nu = 0$, to avoid the Poisson's thickness effect.

▫ The displacement field is assumed in the form as in (2.21),

$$\mathbf{u}\left(X^{j}\right) = \mathbf{u}_{(0)}\left(X^{\alpha}\right) + X^{3}\,\mathbf{u}_{(1)}\left(X^{\alpha}\right), \tag{5.26}$$

where $\mathbf{u}_{(0)}$ and $\mathbf{u}_{(1)}$ are approximated by employing the same C^1 continuous MLS functions.

▫ In order to avoid the influence of the applied boundary conditions, the LWF for the internal node I, whose local sub-domain Ω_s^I does not intersect the plate side edges, is analyzed. According to (5.8), in such case it may be written that

$$\Gamma_{su}^{I} = \partial\Omega_s^I \cap \Gamma_u \in \varnothing, \tag{5.30}$$

Because the essential and non-zero natural BC are prescribed only on the side edges of the plate, on the upper and lower plate surface the prescribed surface tractions have zero values. Consequently, the following statement holds,

$$t_i = n_i\sigma_{ij} = \overline{t}_i = 0 \quad \text{on } \Gamma_{st}^I = \partial\Omega_s^I \cap \Gamma_t = \partial\Omega_s^{I+} \cup \partial\Omega_s^{I-}, \tag{5.31}$$

where $\partial\Omega_s^{I+}$ and $\partial\Omega_s^{I-}$ are the parts of $\partial\Omega_s^I$ that coincide with the upper and lower plate surface, respectively, as shown in Figure 5.3.

▫ Body forces are neglected, $b_i = 0$.

▫ The side surfaces of Ω_s^I, denoted here as L_s^I, are perpendicular to the X^1, X^2-plane, and it holds that $n_3 = 0$ for the outward unit normal vector on L_s^I.

▫ The test functions are defined by employing (5.15) and (5.16), leading to

$$v_1\left(X^k\right) = \begin{cases} 1, & X^{\alpha} \in \Omega_s^I \cup \partial\Omega_s^I \\ 0, & X^{\alpha} \notin \Omega_s^I \cup \partial\Omega_s^I \end{cases}, \quad v_2\left(X^k\right) = \begin{cases} X^3, & X^{\alpha} \in \Omega_s^I \cup \partial\Omega_s^I \\ 0, & X^{\alpha} \notin \Omega_s^I \cup \partial\Omega_s^I \end{cases}. \tag{5.32}$$

By employing the test functions (5.32) in LSWF (5.22) and (5.23), and taking into account the above mentioned assumptions, it may be easily proved that LWF for Ω_s^I associated with the internal node I assumes the following form

$$\int_{L_s^I} n_\gamma C_{i\gamma kl} \frac{1}{2}\left(u^k_{,X^l} + u^l_{,X^k}\right) d\Gamma = 0, \tag{5.33}$$

$$\int_{\Omega_s^I} X^3_{,X^j} C_{ijkl} \frac{1}{2}\left(u^k_{,X^l} + u^l_{,X^k}\right) d\Omega - \int_{L_s^I} X^3 n_j C_{ijkl} \frac{1}{2}\left(u^k_{,X^l} + u^l_{,X^k}\right) d\Gamma = 0. \tag{5.34}$$

By recalling the constitutive relations (5.21), and by noting that the integration over the thickness may be performed separately, expressions (5.33) and (5.34) may be written as

$$\int_{L_s^I} n_\gamma \sigma_{i\gamma} d\Gamma = \int_{-\frac{h}{2}}^{\frac{h}{2}} \int_{L_{s0}^I} n_\gamma C_{i\gamma kl} \frac{1}{2}\left(u^k_{,X^l} + u^l_{,X^k}\right) d\Gamma_0\, dX^3 = 0, \tag{5.35}$$

$$\int_{L_s^I} X^3 n_\gamma \sigma_{i\gamma} d\Gamma - \int_{\Omega_s^I} \sigma_{i3} d\Omega = \int_{-\frac{h}{2}}^{\frac{h}{2}} \int_{L_{s0}^I} X^3 n_\gamma C_{i\gamma kl} \frac{1}{2}\left(u^k_{,X^l} + u^l_{,X^k}\right) d\Gamma_0\, dX^3 -$$

$$\int_{-\frac{h}{2}}^{\frac{h}{2}} \int_{\Omega_{s0}^I} C_{i3kl} \frac{1}{2}\left(u^k_{,X^l} + u^l_{,X^k}\right) d\Omega_0\, dX^3 = 0, \tag{5.36}$$

where $\int_{\Omega_{s0}^I} (\ ) d\Omega_0$ denotes the integral over the intersection between Ω_s^I and the X^1, X^2-plane, i.e., $\Omega_{s0}^I = \Omega_s^I \cap X^1, X^2$-plane, while $\int_{L_{s0}^I} (\ ) d\Gamma_0$ is the integral over the intersection between $\partial\Omega_s^I$ and the X^1, X^2-plane, i.e., $L_{s0}^I = \partial\Omega_s^I \cap X^1, X^2$-plane. The intersections L_{s0}^I and Ω_{s0}^I are illustrated in Figure 5.3. Inserting the displacement approximation (5.26) into (5.35) and (5.36), and after integrating over the thickness, the following expressions may be easily obtained

$$h \int_{L_{s0}^I} n_\gamma \left[C_{i\gamma\alpha\beta} \frac{1}{2}\left(u^\alpha_{(0),X^\beta} + u^\beta_{(0),X^\alpha}\right) + C_{i\gamma\alpha 3}\left(u^\alpha_{(1)} + u^3_{(0),X^\alpha}\right) + C_{i\gamma 33} u^3_{(1)} \right] d\Gamma_0 = 0, \tag{5.37}$$

$$\frac{h^3}{12} \int_{L_{s0}^I} n_\gamma \left[C_{i\gamma\alpha\beta} \frac{1}{2} \left(u_{(1),X^\beta}^\alpha + u_{(1),X^\alpha}^\beta \right) + C_{i\gamma\alpha3} \frac{1}{2} u_{(1),X^\alpha}^3 \right] d\Gamma_0 -$$

$$h \int_{\Omega_{s0}^I} \left[C_{i3\alpha\beta} \frac{1}{2} \left(u_{(0),X^\beta}^\alpha + u_{(0),X^\alpha}^\beta \right) + C_{i3\alpha3} \left(u_{(0),X^\alpha}^3 + u_{(1)}^\alpha \right) + C_{i333} u_{(1)}^3 \right] d\Omega_0 = 0. \tag{5.38}$$

According to (2.34) and (2.35), in the material tensor for the linear isotropic Hookean material only the terms C_{1111}, C_{2222}, C_{3333}, $C_{1212} = C_{2112} = C_{1221}$, $C_{1313} = C_{3113} = C_{1331}$ and $C_{2323} = C_{2332} = C_{3223}$ will be the non-zero terms if $\nu = 0$. After expansion with respect to free index i, the relations (5.37) and (5.38) then yield the following set of equations

$$\text{for } i = 1: \quad h \int_{L_{s0}^I} n_\gamma \left[C_{1\gamma\alpha\beta} \frac{1}{2} \left(u_{(0),X^\beta}^\alpha + u_{(0),X^\alpha}^\beta \right) \right] d\Gamma_0 = 0,$$

$$\text{for } i = 2: \quad h \int_{L_{s0}^I} n_\gamma \left[C_{2\gamma\alpha\beta} \frac{1}{2} \left(u_{(0),X^\beta}^\alpha + u_{(0),X^\alpha}^\beta \right) \right] d\Gamma_0 = 0, \tag{5.39}$$

$$\text{for } i = 3: \quad h \int_{L_{s0}^I} n_\gamma \left[C_{3\gamma\alpha3} \left(u_{(1)}^\alpha + u_{(0),X^\alpha}^3 \right) \right] d\Gamma_0 = 0,$$

$$\text{for } i = 1: \quad \frac{h^3}{12} \int_{L_{s0}^I} n_\gamma \left[C_{1\gamma\alpha\beta} \frac{1}{2} \left(u_{(1),X^\beta}^\alpha + u_{(1),X^\alpha}^\beta \right) \right] d\Gamma_0 -$$
$$h \int_{\Omega_{s0}^I} \left[C_{1313} \left(u_{(0),X^1}^3 + u_{(1)}^1 \right) \right] = 0,$$

$$\text{for } i = 2: \quad \frac{h^3}{12} \int_{L_{s0}^I} n_\gamma \left[C_{2\gamma\alpha\beta} \frac{1}{2} \left(u_{(1),X^\beta}^\alpha + u_{(1),X^\alpha}^\beta \right) \right] d\Gamma_0 - \tag{5.40}$$
$$h \int_{\Omega_{s0}^I} \left[C_{2323} \left(u_{(0),X^2}^3 + u_{(1)}^2 \right) \right] = 0,$$

$$\text{for } i = 3: \quad \frac{h^3}{12} \int_{L_{s0}^I} n_\gamma \left[C_{3\gamma\alpha3} \frac{1}{2} u_{(1),X^\alpha}^3 \right] d\Gamma_0 - h \int_{\Omega_{s0}^I} \left[C_{3333} u_{(1)}^3 \right] = 0.$$

By inspecting (5.35) it is obvious that (5.39) represents the weak form of the three equilibrium equations over the L_{s0}^I in the direction of the global Cartesian axes, which are written in terms of the plate stress resultant over $\partial\Omega_s^I$. On the other hand, from (5.36) it is clear that the first two equations in (5.40) may be interpreted as the moment equations in the directions of the global Cartesian axes. The first terms in these expressions represent the moments of the in-plane stresses over $\partial\Omega_s^I$ with respect to the

axes X^1 and X^2. From (5.40) it may be seen that these moments are caused by the bending strains $\varepsilon_{\alpha\beta}^{(b)}$, which are defined as

$$\varepsilon_{\alpha\beta}^{(b)} = \frac{1}{2}\left(u_{(1),X^\beta}^\alpha + u_{(1),X^\alpha}^\beta\right). \tag{5.41}$$

The second integral terms in the first two equations in (5.40) are the contributions from the transversal shear stress components over Ω_s^I. The third relation in (5.40) may be perceived as just another independent equilibrium equation in the thickness direction, which takes into account the effect of the transversal normal component σ_{33} over Ω_s^I. For the case considered, this equation may be decoupled from the equation set (5.39) and (5.40), and be solved separately for $u_{(1)}^3$.

Obviously, the first integrands in relations (5.40) produce the terms of the type h^3, while the second terms are dependant on h. It means that the contribution of the in-plane stresses in the moment equations will weaken very quickly if $h \to 0$, while at the same time the influence of the transversal shear stresses will be more pronounced. In other words, the inner mechanism inside Ω_s^I for resisting the bending surface traction moments acting over $\partial\Omega_s^I$ is driven by transversal shear strains $\sigma_{\alpha 3}$. It becomes too strong in the thin structures and causes the overly stiff bending response.

As already mentioned, in the case of pure bending the transversal shear strains should be zero. From (5.40) it is clear that the zero transversal shear stress condition will surely be exactly satisfied only if

$$u_{(1)}^\alpha = -u_{(0),X^\alpha}^3 \tag{5.42}$$

everywhere in Ω_s^I. As $u_{(1)}^\alpha$ describes the rotations, according to (2.22), relation (5.42) represents the Kirchhoff-Love plate theory hypothesis.

The first two equations in (5.40) may be rewritten as

$$\int_{L_{s0}^I} n_\gamma \left[C_{1\gamma\alpha\beta} \frac{1}{2}\left(u_{(1),X^\beta}^\alpha + u_{(1),X^\alpha}^\beta\right) \right] d\Gamma_0 - \frac{12}{h^2}\int_{\Omega_{s0}^I}\left[C_{1313}\left(u_{(0),X^1}^3 + u_{(1)}^1\right)\right] = 0,$$
$$\int_{L_{s0}^I} n_\gamma \left[C_{2\gamma\alpha\beta} \frac{1}{2}\left(u_{(1),X^\beta}^\alpha + u_{(1),X^\alpha}^\beta\right) \right] d\Gamma_0 - \frac{12}{h^2}\int_{\Omega_{s0}^I}\left[C_{2323}\left(u_{(0),X^2}^3 + u_{(1)}^2\right)\right] = 0. \tag{5.43}$$

In the thin limit, i.e., $h \to 0$ and consequently $1/h^2 \to 0$. In that case, the terms in the global stiffness coefficient matrix that arise from the second integrals in (5.43) may become much bigger than those stemming from the first integrals if the transversal shear strains are not zero. This causes the ill-conditioning of the global stiffness matrix, as confirmed by numerical experiments. If the transversal shear strains, and consequently the second integrands in (5.43), are not zero, then one way to avoid such problems is to set the bending strains to zero,

$$\varepsilon_{\alpha\beta}^{(b)} = \frac{1}{2}\left(u_{(1),X^\beta}^\alpha + u_{(1),X^\alpha}^\beta\right) = 0, \tag{5.44}$$

which is of course contrary to what happens in the bending dominated cases. As noticed in [103], the condition from (5.44) could be achieved by letting $u_{(1),X^\beta}^\alpha \to 0$ when $h \to 0$. However, this means the constant rotations over Ω_s^I, which is not the case in the bending state.

From the above discussion, it is to conclude that the purely-displacement solid-shell MLPG formulation will suffer from transversal shear locking unless the condition (5.42) is met in the thin plate limit. However, since meshless approximations are complicated non-polynomial functions, it seems that it is not possible to satisfy this condition exactly if both $u_{(1)}^\alpha$ and $u_{(0)}^3$ are approximated directly.

Nevertheless, it is known from the available literature that one simple way to alleviate transversal shear locking in the primal meshless algorithms is the raising of the order of the trial functions, and therefore such approach is applied in this work. Another strategy for eliminating this unwanted numerical phenomenon is by devising appropriate mixed formulations, as presented in Chapter 7.

6 Primal MLPG formulations for thick plates and shells

In the purely displacement-based or primal numerical approximations, only the displacements appear as the independent variables. In this chapter, two different primal MLPG solid-shell formulations are presented. As shown in Section 5.3, the primal MLPG formulations are plagued by different locking phenomena. The Poisson's thickness locking effect, which appears regardless of the structure dimensions, is circumvented in the proposed algorithms by means of the hierarchical quadratic interpolation scheme described in Section 6.1. The first formulation outlined in Section 6.3 employs collocation procedures beside the local weak forms, as proposed in [140],[141]. In the second formulation, exposed in Section 6.4, the closed system of governing equation in the weak form is obtained by applying the test functions that are quadratic in the thickness direction, as in [142]. Due to their sensitivity to transversal shear locking, the proposed formulations are suitable mainly for the analysis of thick plates and shells.

6.1 Elimination of Poisson's thickness locking effect in primal MLPG formulations

By assuming the quadratic hierarchical distribution over the thickness for the transversal displacement component u'^3, as proposed in [93], the displacement vector is written in the local curvilinear coordinates associated with the middle surface as

$$\mathbf{u}'\left(\theta^j\right) = u'^k \mathbf{A}_k = \mathbf{u}'_{(0)}\left(\theta^\alpha\right) + \theta^3\, \mathbf{u}'_{(1)}\left(\theta^\alpha\right) + \begin{bmatrix} 0 \\ 0 \\ \gamma\left(\theta^3\right) \end{bmatrix} \lambda\left(\theta^\delta\right). \tag{6.1}$$

Herein $\mathbf{u}'_{(0)} = u'^{\,k}_{(0)} \mathbf{A}_k$ and $\mathbf{u}'_{(1)} = u'^{\,k}_{(1)} \mathbf{A}_k$ are the displacement parameters associated with the shell middle surface and defined analogously to (2.22). Metric vectors $\mathbf{A}_k = \mathbf{G}_k\left(\theta^3 = 0\right)$ are illustrated in Figure 6.1 and may be calculated from (2.5) and

81

(2.7). The function $\gamma(\theta^3)$ describes the quadratic hierarchical interpolation of the transversal displacement component u'^3 as illustrated in Figure 6.1 and is defined by

$$\gamma(\theta^3) = \frac{1}{2}\left[1 - \left(\frac{\theta^3}{0.5h}\right)^2\right], \tag{6.2}$$

while $\lambda(\theta^\delta)$ is the scalar parameter associated with the quadratic term $\gamma(\theta^3)$.
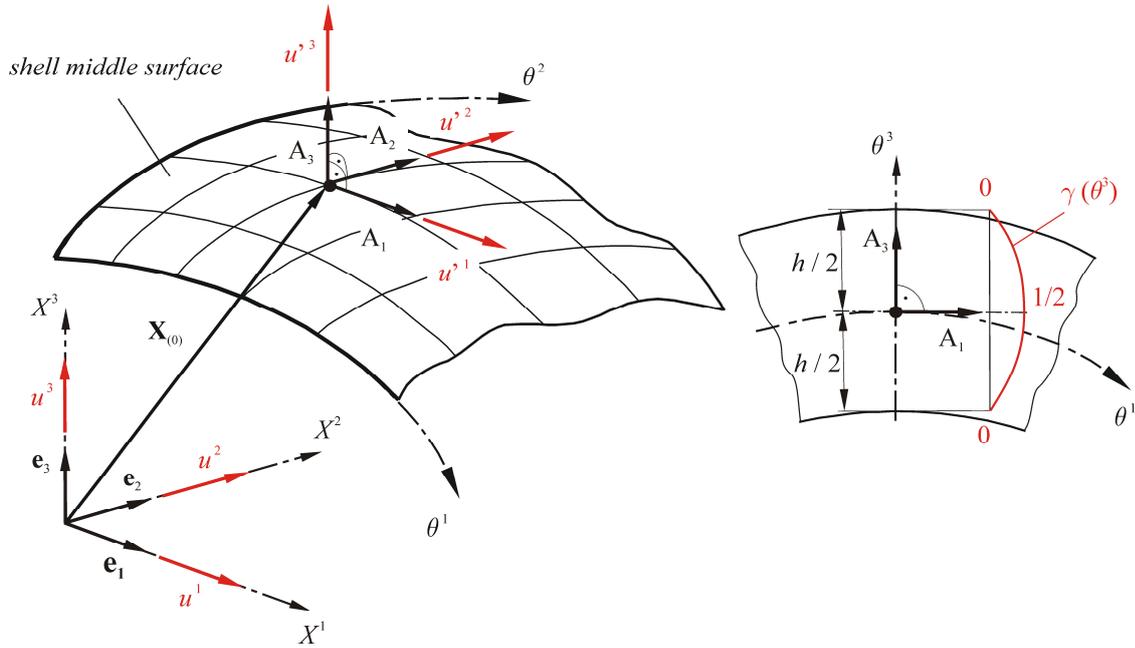
Figure 6.1 Hierarchical quadratic interpolation for transversal displacement component.

From (2.23) it is clear that the quadratic interpolation of u'^3 yields the linear distribution of the normal transversal strain component ε_{33} across the thickness, which is necessary for the elimination of the Poisson's thickness locking effect. By applying the vector transformation rules (2.16) and after some additional manipulation, the displacement field in the global Cartesian coordinate system assumes the following matrix from

$$\mathbf{u}(\theta^i) = u^k\mathbf{e}_k = \mathbf{T}(\theta^\delta)\mathbf{\Psi}(\theta^3)\begin{bmatrix} \mathbf{T}^{-1}(\theta^\delta) & \mathbf{0} & \mathbf{0} \\ \mathbf{0} & \mathbf{T}^{-1}(\theta^\delta) & \mathbf{0} \\ \mathbf{0} & \mathbf{0} & 1 \end{bmatrix}\begin{bmatrix} \mathbf{u}^{(0)}(\theta^\delta) \\ \mathbf{u}^{(1)}(\theta^\delta) \\ \lambda(\theta^\delta) \end{bmatrix}, \tag{6.3}$$

where $\mathbf{u}_{(0)} = u_{(0)}^k \mathbf{e}_k = \left(\mathbf{u}_{(u)} + \mathbf{u}_{(l)} \right)/2$ and $\mathbf{u}_{(1)} = u_{(1)}^k \mathbf{e}_k = \left(\mathbf{u}_{(u)} - \mathbf{u}_{(l)} \right)/h$ according to (2.22).

Herein $\mathbf{u}_{(u)} = u_{(u)}^k \mathbf{e}_k$ and $\mathbf{u}_{(l)} = u_{(l)}^k \mathbf{e}_k$ are the displacement vectors on the upper and lower surfaces, respectively. The matrix $\mathbf{\Psi}\left(\theta^3\right)$ describes the displacement interpolation in the shell thickness direction as

$$\mathbf{\Psi}\left(\theta^3\right) = \begin{bmatrix} 1 & 0 & 0 & \theta^3 & 0 & 0 & 0 \\ 0 & 1 & 0 & 0 & \theta^3 & 0 & 0 \\ 0 & 0 & 1 & 0 & 0 & \theta^3 & \gamma\left(\theta^3\right) \end{bmatrix}. \tag{6.4}$$

The matrix $\mathbf{T}\left(\theta^\delta\right) = \mathbf{J}\left(\theta^\delta, \theta^3 = 0\right)$, where $\mathbf{J}$ is the Jacobian matrix defined as to (2.14), stands for the transformation matrix from the curvilinear coordinates associated with the middle surface to the global Cartesian coordinate system. According to relation (6.3), the interpolation over the thickness is performed separately from the approximations in the in-plane directions θ^α.

6.2 Discretization and approximation of field variables

The continuum is discretized in the parametric coordinate space by the node couples, as explained in Section 5.1. In order to construct the local weak forms, the local sub-domain that has the cylindrical shape in the parametric space is defined around each node couple, as shown in Figure 6.2.
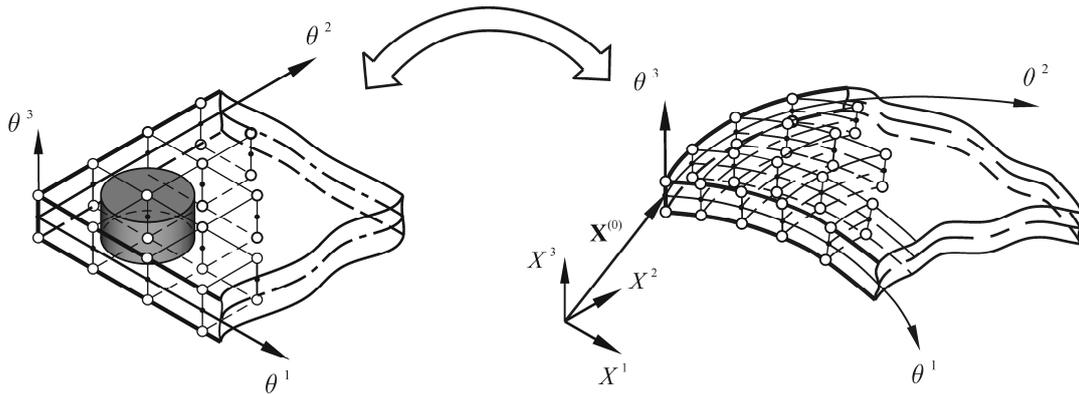

Figure 6.2 Discretization of shell continuum for primal MLPG formulations

The variables $\mathbf{u}_{(0)}$, $\mathbf{u}_{(1)}$ and λ are approximated in the in-plane directions θ^α by employing the same MLS functions, where the 4th-order spline from (3.20) is used as the weight function. The discretized forms for $\mathbf{u}_{(0)}$, $\mathbf{u}_{(1)}$ and λ are

$$\mathbf{u}_{(0)}\left(\theta^{\delta}\right)=\sum_{J=1}^{n}\phi_{J}\left(\theta^{\delta}\right)\hat{\mathbf{u}}_{(0)J}\,,\quad\mathbf{u}_{(1)}\left(\theta^{\delta}\right)=\sum_{J=1}^{n}\phi_{J}\left(\theta^{\delta}\right)\hat{\mathbf{u}}_{(1)J}\,,\quad\lambda\left(\theta^{\delta}\right)=\sum_{J=1}^{n}\phi_{J}\left(\theta^{\delta}\right)\hat{\lambda}_{J}\,,\quad(6.5)$$

where $\phi_{J}\left(\theta^{\delta}\right),J=1,2,...,n$ stands for the MLS shape functions associated with the nodes positioned inside the domain of definition of the sample point θ^{δ}, denoted as $\Omega_{\theta^{\alpha}}$, and $\hat{\mathbf{u}}_{(0)J}$, $\hat{\mathbf{u}}_{(1)J}$ and $\hat{\lambda}_{J}$ are the corresponding fictitious nodal values. n is the total number of nodes in $\Omega_{\theta^{\alpha}}$. The shape function $\phi_{J}\left(\theta^{\delta}\right)$ is calculated according to procedures in Chapter 3 by employing the parametric coordinates θ^{δ} instead of X^{δ}. The more detailed description of this scheme is available in [142].

By using the approximation (6.5), the displacement field (6.3) may be expressed as

$$\mathbf{u}\left(\theta^{i}\right)=\sum_{J=1}^{n}\boldsymbol{\Phi}_{J}(\theta^{i})\,\hat{\mathbf{u}}_{J}\,.\tag{6.6}$$

Herein $\boldsymbol{\Phi}_{J}(\theta^{i})$ describes the 3-D nodal shape functions associated with the Jth node in $\Omega_{\theta^{\alpha}}$, and has the following form

$$\boldsymbol{\Phi}_{J}(\theta^{i})=\phi_{J}\left(\theta^{\delta}\right)\mathbf{T}\left(\theta^{\delta}\right)\boldsymbol{\Psi}(\theta^{3})\begin{bmatrix}\mathbf{T}^{-1}\left(\theta^{\delta}\right)&\mathbf{0}&\mathbf{0}\\\mathbf{0}&\mathbf{T}^{-1}\left(\theta^{\delta}\right)&\mathbf{0}\\\mathbf{0}&\mathbf{0}&1\end{bmatrix}.\tag{6.7}$$

The vector $\hat{\mathbf{u}}_{J}$ is the vector of the nodal unknown parameters, defined as

$$\hat{\mathbf{u}}_{J}^{\text{T}}=\left[\left(\hat{\mathbf{u}}_{(0)J}\right)^{\text{T}}\quad\left(\hat{\mathbf{u}}_{(1)J}\right)^{\text{T}}\quad\hat{\lambda}_{J}\right]=\left[\hat{u}_{(0)J}^{1}\quad\hat{u}_{(0)J}^{2}\quad\hat{u}_{(0)J}^{3}\quad\hat{u}_{(1)J}^{1}\quad\hat{u}_{(1)J}^{2}\quad\hat{u}_{(1)J}^{3}\quad\hat{\lambda}_{J}\right].\,(6.8)$$

It should be noted that the applied MLS shape functions do not possess the Kronecker Delta property, meaning that $\hat{\mathbf{u}}_{J}$ in (6.8) are the fictitious and not the true nodal values of the trial function $\mathbf{u}\left(\theta^{i}\right)$.

By employing the discretized displacements (6.6) to calculate the strain components according to (2.27), the complete discretized 3-D strain tensor may be written in the matrix form as

$$\boldsymbol{\varepsilon} = \mathbf{D}_k \, \mathbf{u} = \mathbf{D}_k \sum_{J=1}^{n} \boldsymbol{\Phi}_J \, \hat{\mathbf{u}}_J = \sum_{J=1}^{n} \mathbf{B}_J \, \hat{\mathbf{u}}_J , \tag{6.9}$$

where $\boldsymbol{\varepsilon}$ and $\mathbf{D}_k$ stand for the 3-D strain vector and the 3-D kinematic differential operator in the global Cartesian system, respectively, and are defined analogously to the general matrix forms given in (2.24) to (2.26). The matrix $\mathbf{B}_J$ represents the strain-displacement matrix, written in detail as

$$\mathbf{B}_J = \mathbf{D}_k \boldsymbol{\Phi}_J =$$

$$\begin{bmatrix}
\phi_{J,\theta^p} J_{p1}^{-1} & 0 & 0 & \left(\theta^3 \phi_J\right)_{,\theta^p} J_{p1}^{-1} & 0 \\
0 & \phi_{J,\theta^p} J_{p2}^{-1} & 0 & 0 & \left(\theta^3 \phi_J\right)_{,\theta^p} J_{p2}^{-1} \\
0 & 0 & \phi_{J,\theta^p} J_{p3}^{-1} & 0 & 0 \\
\phi_{J,\theta^p} J_{p2}^{-1} & \phi_{J,\theta^p} J_{p1}^{-1} & 0 & \left(\theta^3 \phi_J\right)_{,\theta^p} J_{p2}^{-1} & \left(\theta^3 \phi_J\right)_{,\theta^p} J_{p1}^{-1} & \cdots \\
0 & \phi_{J,\theta^p} J_{p3}^{-1} & \phi_{J,\theta^p} J_{p2}^{-1} & 0 & \left(\theta^3 \phi_J\right)_{,\theta^p} J_{p3}^{-1} \\
\phi_{J,\theta^p} J_{p3}^{-1} & 0 & \phi_{J,\theta^p} J_{p1}^{-1} & \left(\theta^3 \phi_J\right)_{,\theta^p} J_{p3}^{-1} & 0 \\
\end{bmatrix}$$

$$\begin{matrix}
0 & \left(X_{(1)}^1 \gamma \phi_J\right)_{,\theta^p} J_{p1}^{-1} \\
0 & \left(X_{(1)}^2 \gamma \phi_J\right)_{,\theta^p} J_{p2}^{-1} \\
\left(\theta^3 \phi_J\right)_{,\theta^p} J_{p3}^{-1} & \left(X_{(1)}^3 \gamma \phi_J\right)_{,\theta^p} J_{p3}^{-1} \\
0 & \left(X_{(1)}^1 \gamma \phi_J\right)_{,\theta^p} J_{p2}^{-1} + \left(X_{(1)}^2 \gamma \phi_J\right)_{,\theta^p} J_{p1}^{-1} \\
\left(\theta^3 \phi_J\right)_{,\theta^p} J_{p2}^{-1} & \left(X_{(1)}^2 \gamma \phi_J\right)_{,\theta^p} J_{p3}^{-1} + \left(X_{(1)}^3 \gamma \phi_J\right)_{,\theta^p} J_{p2}^{-1} \\
\left(\theta^3 \phi_J\right)_{,\theta^p} J_{p1}^{-1} & \left(X_{(1)}^1 \gamma \phi_J\right)_{,\theta^p} J_{p3}^{-1} + \left(X_{(1)}^3 \gamma \phi_J\right)_{,\theta^p} J_{p1}^{-1} \\
\end{matrix} \tag{6.10}$$

Herein J_{pi}^{-1} denotes the terms of the inverse Jacobian matrix from (2.15), while $X_{(1)}^k$ stands for the components of the shell director $\mathbf{X}_{(1)} = \mathbf{G}_3$.

Using the generalized Hooke's law for the isotropic linear elastic material, defined by relations (2.29), (2.34) and (2.35), the stress tensor components may be expressed as

$$\boldsymbol{\sigma} = \mathbf{D}\boldsymbol{\varepsilon} = \mathbf{D}\sum_{J=1}^{n} \mathbf{B}_J \, \hat{\mathbf{u}}_J = \sum_{J=1}^{n} \mathbf{D}\mathbf{B}_J \hat{\mathbf{u}}_J \tag{6.11}$$

with $\mathbf{D}$ as the 3-D stress-strain matrix in the global Cartesian coordinate system defined as explained in Section 2.2. Relation (2.39) yields the surface traction vector $\mathbf{t} = t^k \mathbf{e}_k$ over the local boundary $\partial \Omega_s^I$ as

$$\mathbf{t} = \mathbf{N}\boldsymbol{\sigma} = \mathbf{N}\sum_{J=1}^{n}\mathbf{D}\mathbf{B}_J\hat{\mathbf{u}}_J = \sum_{J=1}^{n}\mathbf{N}\mathbf{D}\mathbf{B}_J\hat{\mathbf{u}}_J, \qquad (6.12)$$

where $\mathbf{N}$ represents the matrix from (2.40) that contains the components of the outward unit normal vector $\mathbf{n} = n_i\,\mathbf{e}_i$ to $\partial\Omega_s^I$.

It is important to note that the deformation responses over the shell thickness are described by seven independent variables, including $u_{(0)}^k$, $u_{(1)}^k$ and λ, according to relations (6.1)-(6.3). Consequently, after performing the discretization of the field variables, seven unknown nodal parameters associated with each node couple appear, as shown by (6.8). However, LSWF (5.22)-(5.23) contains only six equations per local sub-domain, which result in an undetermined system of equations on the global level. In the next two sections, two different ways for obtaining the closed systems of equations are presented. The first one employs the collocation approach at the nodes to obtain the additional necessary equations, while in the second one, the test functions that are quadratic in the thickness direction are applied in LWF (5.10).

6.3 Collocation approach

In order to obtain the discretized set of equations, LSWF (5.22)-(5.23) are derived over the cylindrical local sub-domains $\Omega_s^I, I = 1, 2, \ldots, N$ that surround the node couples $I, I = 1, 2, \ldots, N$ by performing the procedure presented in Section 5.2.1.1. Herein N is the total number of the nodes used for the discretization of the shell continuum. For each Ω_s^I, the test functions v_1 and v_2 with the circular support domains in the $\theta^1\theta^2$-plane of the parametric space are constructed by using (5.15) and (5.16) as

$$v_1\left(\theta^k\right) = \begin{cases} 1, & 0 \le d_I \le R_{tI} \\ 0, & d_I \ge R_{tI} \end{cases}, \qquad v_2\left(\theta^k\right) = \begin{cases} \theta^3, & 0 \le d_I \le R_{tI} \\ 0, & d_I \ge R_{tI} \end{cases}. \qquad (6.13)$$

where R_{tI} is the radius of the test function support domain, and $d_I = \left|\theta^\delta - \theta_I^\delta\right|$ is the distance between the node I and the sample point θ^δ calculated in the parametric space.

Employing the test functions (6.13) in (5.22) and (5.23) leads to the following LSWF for each Ω_s^I

$$-\int_{L_s^I} n_j C_{ijkl} \frac{1}{2}\left(u_{k,X^l}+u_{l,X^k}\right)\mathrm{d}\Gamma - \int_{\Gamma_{su}^I} n_j C_{ijkl}\frac{1}{2}\left(u_{k,X^l}+u_{l,X^k}\right)\mathrm{d}\Gamma + \alpha\int_{\Gamma_{su}^I} u_k\,\mathrm{d}\Gamma =$$

$$\int_{\Omega_s^I} b_k\,\mathrm{d}\Omega + \int_{\Gamma_{st}^I}\overline{t}_k\mathrm{d}\Gamma + \alpha\int_{\Gamma_{su}^I}\overline{u}_k\,\mathrm{d}\Gamma, \tag{6.14}$$

$$\int_{\Omega_s^I}\theta^3{}_{,X^j} C_{ijkl}\frac{1}{2}\left(u_{k,X^l}+u_{l,X^k}\right)\mathrm{d}\Omega - \int_{L_s^I}\theta^3 n_j C_{ijkl}\frac{1}{2}\left(u_{k,X^l}+u_{l,X^k}\right)\mathrm{d}\Gamma -$$

$$-\int_{\Gamma_{su}^I}\theta^3 n_j C_{ijkl}\frac{1}{2}\left(u_{k,X^l}+u_{l,X^k}\right)\mathrm{d}\Gamma + \alpha\int_{\Gamma_{su}^I}\theta^3 u_k\,\mathrm{d}\Gamma = \tag{6.15}$$

$$\int_{\Omega_s^I}\theta^3 b_k\,\mathrm{d}\Omega + \int_{\Gamma_{st}^I}\theta^3\,\overline{t}_k\mathrm{d}\Gamma + \alpha\int_{\Gamma_{su}^I}\theta^3\overline{u}_k\,\mathrm{d}\Gamma.$$

To obtain the additional equation for each node couple, the equilibrium is enforced at the points $\mathbf{X}_{(0)}^I = \mathbf{X}\left(\theta_I^1,\theta_I^2,0\right), I=1,2,\ldots,N$. These points are located on the middle surface between the nodes that form a node couple, as shown in Figure 6.3.
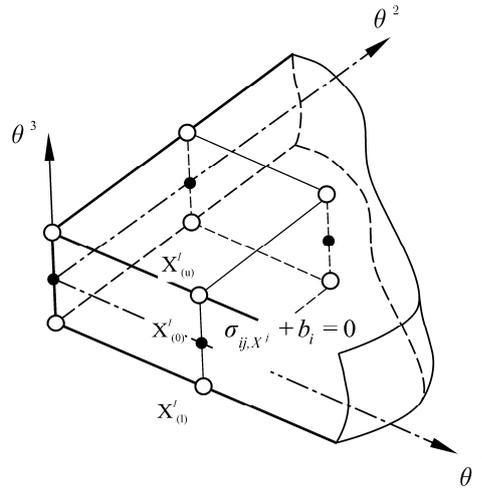
Figure 6.3 Collocation points for primal MLPG formulation

For that purpose, the collocation procedure is employed by using the Dirac's delta function $\delta\left(\mathbf{X}-\mathbf{X}_{(0)}^I\right)$ as the test function in LWF (5.3), which leads to

$$\sigma_{ij,X^j}\left(\mathbf{X}_{(0)}^I\right)+b_i\left(\mathbf{X}_{(0)}^I\right)=0. \tag{6.16}$$

The three equilibrium equations (6.16) are then summed up in order to form one additional equation per local sub-domain as

$$\sum_{i=1}^3\left[\sigma_{ij,X^j}\left(\mathbf{X}_{(0)}^I\right)+b_i\left(\mathbf{X}_{(0)}^I\right)\right]=0,\ I=1,2,\ldots,N. \tag{6.17}$$

Note that the essential BC are not enforced explicitly in the above expression, because the collocation point may always be moved away from the boundary with the prescribed displacements for some very small distance.

Relations (6.14), (6.15) and (6.17) together represent a system of seven governing equations for each nodal couple, which yields a closed system of equations on the global level.

By means of (6.6), (6.9), (6.11) and (6.12), the governing equations (6.14), (6.15) and (6.17) may be transformed into the following discretized set of linear equations

$$
\sum_{J=1}^{N_I}\left[-\int_{L_s^I} \mathbf{N}\,\mathbf{D}\,\mathbf{B}_J \, \mathrm{d}\Gamma - \int_{\Gamma_{su}^I} \mathbf{N}\,\mathbf{D}\,\mathbf{B}_J \, \mathrm{d}\Gamma + \alpha \int_{\Gamma_{su}^I} \boldsymbol{\Phi}_J \, \mathrm{d}\Gamma \right] \hat{\mathbf{u}}_J =
$$
$$
\int_{\Omega_s^I} \mathbf{b}\, \mathrm{d}\Omega + \int_{\Gamma_{st}^I} \overline{\mathbf{t}}\, \mathrm{d}\Gamma + \alpha \int_{\Gamma_{su}^I} \overline{\mathbf{u}}\, \mathrm{d}\Gamma, \tag{6.18}
$$

$$
\sum_{J=1}^{N_I}\left[\int_{\Omega_s^I} \nabla\mathbf{d}^{\mathrm{T}}\,\mathbf{D}\,\mathbf{B}_J \, \mathrm{d}\Omega - \int_{L_s^I} \theta^3\,\mathbf{N}\,\mathbf{D}\,\mathbf{B}_J \, \mathrm{d}\Gamma - \int_{\Gamma_{su}^I} \theta^3\,\mathbf{N}\,\mathbf{D}\,\mathbf{B}_J \, \mathrm{d}\Gamma + \alpha \int_{\Gamma_{su}^I} \theta^3\,\boldsymbol{\Phi}_J \, \mathrm{d}\Gamma \right] \hat{\mathbf{u}}_J =
$$
$$
\int_{\Omega_s^I} \theta^3\mathbf{b}\, \mathrm{d}\Omega + \int_{\Gamma_{st}^I} \theta^3\, \overline{\mathbf{t}}\, \mathrm{d}\Gamma + \alpha \int_{\Gamma_{su}^I} \theta^3\, \overline{\mathbf{u}}\, \mathrm{d}\Gamma, \tag{6.19}
$$

$$
\boldsymbol{\mathscr{D}}^{\mathrm{T}} \sum_{J=1}^{\tilde{n}_I} \boldsymbol{\mathscr{B}}_J \, \hat{\mathbf{u}}_J = -\sum_{i=1}^{3} b_i\left(\mathbf{X}_{(0)}^I\right), \quad I = 1, 2, \ldots, N \, . \tag{6.20}
$$

Herein N_I and $\tilde{n}_I$ denote the total numbers of the node couples in the domain of influence Ω_{inf}^I and the domain of definition Ω_{X_I}, respectively, both associated with the node I. The vector $\hat{\mathbf{u}}_J$ contains the unknown DOF associated to the Jth node couple inside Ω_{inf}^I or Ω_{X_I}. Thereby both Ω_{inf}^I and Ω_{X_I} are defined as described in Section 4.1. The matrix $\nabla\mathbf{d}^{\mathrm{T}}$ contains the derivatives of θ^3

$$
\nabla\mathbf{d}^{\,\mathrm{T}} = \begin{bmatrix} \theta^3_{,X^1} & 0 & 0 & \theta^3_{,X^2} & 0 & \theta^3_{,X^3} \\ 0 & \theta^3_{,X^2} & 0 & \theta^3_{,X^1} & \theta^3_{,X^3} & 0 \\ 0 & 0 & \theta^3_{,X^3} & 0 & \theta^3_{,X^2} & \theta^3_{,X^1} \end{bmatrix}, \tag{6.21}
$$

while the vector $\boldsymbol{\mathscr{D}}$ is defined by

$$
\boldsymbol{\mathscr{D}}^{\mathrm{T}} = \left[\left(\mathbf{D}_1^{\,T} + \mathbf{D}_4^{\,T} + \mathbf{D}_6^{\,T}\right) \quad \left(\mathbf{D}_4^{\,T} + \mathbf{D}_2^{\,T} + \mathbf{D}_5^{\,T}\right) \quad \left(\mathbf{D}_6^{\,T} + \mathbf{D}_5^{\,T} + \mathbf{D}_3^{\,T}\right) \right], \tag{6.22}
$$

where $\mathbf{D}_i$, $i = 1, 2, \ldots, 6$, are the rows of the standard 3-D elasticity matrix from (2.36) in the global Cartesian coordinate system. The matrix $\boldsymbol{\mathcal{B}}_J$ contains the derivatives of the strain-displacement matrix (6.10) calculated at $\mathbf{X}_{(0)}^I$

$$\boldsymbol{\mathcal{B}}_J = \begin{bmatrix} \mathbf{B}_J\left(\mathbf{X}_{(0)}^I\right)_{,X^1} \\ \mathbf{B}_J\left(\mathbf{X}_{(0)}^I\right)_{,X^2} \\ \mathbf{B}_J\left(\mathbf{X}_{(0)}^I\right)_{,X^3} \end{bmatrix}. \tag{6.23}$$

Very often, the body forces may be neglected in engineering computations, and therefore, the terms containing the body force vector $\mathbf{b}$ can be omitted. The global system of equations may now be derived by forming the discretized equations (6.18)-(6.20) for each node couple in the so-called "node-by-node" fashion, without having to resort to the classical assembly process of the global stiffness matrix as in FEM.

As evident, no integration is needed in relation (6.20), which is convenient with respect to the total required computational time. On the other hand, it is necessary to calculate the second derivatives of the MLS functions, which complicates the algorithm and demands significant additional computational effort in the case of curved shell structures. Therefore, this approach is especially convenient for the analysis of plate structures. It is interesting that in some problems involving plate structures, it is sufficient to employ only the equilibrium equation in the thickness direction to form the additional equations [103],[143].

6.4 Quadratic test function

A shell continuum is first discretized by a set of N node couples, and the cylindrical local sub-domains Ω_s^I, $I = 1, 2, \ldots, N$ are defined around each node couple in the parametric space, as in the formulation presented in the previous section. In order to derive the local weak forms of the 3-D equilibrium equations (2.42), the test function that is quadratic across the shell thickness is now assumed as

$$v\left(\theta^j\right) = c_0 + c_1\theta^3 + c_2\left(\theta^3\right)^2, \ c_0, c_1, c_2 \in \mathbb{R} \tag{6.24}$$

with c_0, c_1 and c_2 as arbitrary real constants. After inserting the test function (6.24) into LWF (5.12), LSWF for each $\Omega_s^I, I = 1, 2, \ldots, N$ may be written as

$$
c_0 \left[-\int\limits_{L_s^I} n_j \sigma_{kj} \, \mathrm{d}\Gamma - \int\limits_{\Gamma_{su}^I} n_j \sigma_{kj} \, \mathrm{d}\Gamma + \alpha \int\limits_{\Gamma_{su}^I} u_k \, \mathrm{d}\Gamma - \int\limits_{\Omega_s^I} b_k \, \mathrm{d}\Omega - \int\limits_{\Gamma_{st}^I} \overline{t}_k \, \mathrm{d}\Gamma - \alpha \int\limits_{\Gamma_{su}^I} \overline{u}_k \, \mathrm{d}\Gamma \right] +
$$

$$
+ c_1 \left[\int\limits_{\Omega_s^I} \left(\theta^3 \right)_{,X^j} \sigma_{kj} \, \mathrm{d}\Omega - \int\limits_{L_s^I} \theta^3 \, n_j \sigma_{kj} \, \mathrm{d}\Gamma - \int\limits_{\Gamma_{su}^I} \theta^3 \, n_j \sigma_{kj} \, \mathrm{d}\Gamma + \alpha \int\limits_{\Gamma_{su}^I} \theta^3 \, u_k \, \mathrm{d}\Gamma - \right.
$$

$$
\left. - \int\limits_{\Omega_s^I} \theta^3 \, b_k \, \mathrm{d}\Omega - \int\limits_{\Gamma_{st}^I} \theta^3 \, \overline{t}_k \, \mathrm{d}\Gamma - \alpha \int\limits_{\Gamma_{su}^I} \theta^3 \, \overline{u}_k \, \mathrm{d}\Gamma \right] + \tag{6.25}
$$

$$
c_2 \left[\int\limits_{\Omega_s^I} \left(\theta^3 \right)_{,X^j}^2 \sigma_{kj} \, \mathrm{d}\Omega - \int\limits_{L_s^I} \left(\theta^3 \right)^2 n_j \sigma_{kj} \, \mathrm{d}\Gamma - \int\limits_{\Gamma_{su}^I} \left(\theta^3 \right)^2 n_j \sigma_{kj} \, \mathrm{d}\Gamma + \alpha \int\limits_{\Gamma_{su}^I} \left(\theta^3 \right)^2 u_k \, \mathrm{d}\Gamma - \right.
$$

$$
\left. - \int\limits_{\Omega_s^I} \left(\theta^3 \right)^2 b_k \, \mathrm{d}\Omega - \int\limits_{\Gamma_{st}^I} \left(\theta^3 \right)^2 \overline{t}_k \, \mathrm{d}\Gamma - \alpha \int\limits_{\Gamma_{su}^I} \left(\theta^3 \right)^2 \overline{u}_k \, \mathrm{d}\Gamma \right] = 0.
$$

Since relation (6.25) has to hold for all choices of c_0, c_1 and c_2, it yields the following system of governing equations for Ω_s^I

$$
-\int\limits_{L_s^I} n_j \sigma_{kj} \, \mathrm{d}\Gamma - \int\limits_{\Gamma_{su}^I} n_j \sigma_{kj} \, \mathrm{d}\Gamma + \alpha \int\limits_{\Gamma_{su}^I} u_k \, \mathrm{d}\Gamma - \int\limits_{\Omega_s^I} b_k \, \mathrm{d}\Omega - \int\limits_{\Gamma_{st}^I} \overline{t}_k \, \mathrm{d}\Gamma - \alpha \int\limits_{\Gamma_{su}^I} \overline{u}_k \, \mathrm{d}\Gamma = 0 \tag{6.26}
$$

$$
\int\limits_{\Omega_s^I} \left(\theta^3 \right)_{,X^j} \sigma_{kj} \, \mathrm{d}\Omega - \int\limits_{L_s^I} \theta^3 \, n_j \sigma_{kj} \, \mathrm{d}\Gamma - \int\limits_{\Gamma_{su}^I} \theta^3 \, n_j \sigma_{kj} \, \mathrm{d}\Gamma + \alpha \int\limits_{\Gamma_{su}^I} \theta^3 \, u_k \, \mathrm{d}\Gamma -
$$

$$
- \int\limits_{\Omega_s^I} \theta^3 \, b_k \, \mathrm{d}\Omega - \int\limits_{\Gamma_{st}^I} \theta^3 \, \overline{t}_k \, \mathrm{d}\Gamma - \alpha \int\limits_{\Gamma_{su}^I} \theta^3 \, \overline{u}_k \, \mathrm{d}\Gamma = 0 \tag{6.27}
$$

$$
\int\limits_{\Omega_s^I} \left(\theta^3 \right)_{,X^j}^2 \sigma_{kj} \, \mathrm{d}\Omega - \int\limits_{L_s^I} \left(\theta^3 \right)^2 n_j \sigma_{kj} \, \mathrm{d}\Gamma - \int\limits_{\Gamma_{su}^I} \left(\theta^3 \right)^2 n_j \sigma_{kj} \, \mathrm{d}\Gamma + \alpha \int\limits_{\Gamma_{su}^I} \left(\theta^3 \right)^2 u_k \, \mathrm{d}\Gamma -
$$

$$
- \int\limits_{\Omega_s^I} \left(\theta^3 \right)^2 b_k \, \mathrm{d}\Omega - \int\limits_{\Gamma_{st}^I} \left(\theta^3 \right)^2 \overline{t}_k \, \mathrm{d}\Gamma - \alpha \int\limits_{\Gamma_{su}^I} \left(\theta^3 \right)^2 \overline{u}_k \, \mathrm{d}\Gamma = 0. \tag{6.28}
$$

Obviously, equations (6.26)-(6.28) represent a set of nine equations for Ω_s^I. However, according to (6.1)-(6.3), the deformation responses of the shell continuum are described with seven variables through the thickness, including $\mathbf{u}_{(0)}$, $\mathbf{u}_{(1)}$ and λ. Consequently, only seven equations per local sub-domain are required for the solution

of the boundary value problem. Therefore, three equations represented by (6.28) are summed up as

$$\sum_{k=1}^{3}\left[\int_{\Omega_s^I}\left(\theta^3\right)^2_{,X^j}\sigma_{kj}\,d\Omega-\int_{L_s^I}\left(\theta^3\right)^2 n_j\sigma_{kj}d\Gamma-\int_{\Gamma_{su}^I}\left(\theta^3\right)^2 n_j\sigma_{kj}d\Gamma+\alpha\int_{\Gamma_{su}^I}\left(\theta^3\right)^2 u_k\,d\Gamma-\right.$$

$$\left.-\int_{\Omega_s^I}\left(\theta^3\right)^2 b_k\,d\Omega-\int_{\Gamma_{st}^I}\left(\theta^3\right)^2\overline{t}_k d\Gamma-\alpha\int_{\Gamma_{su}^I}\left(\theta^3\right)^2\overline{u}_k\,d\Gamma\right]=0, \tag{6.29}$$

which together with LSWF (6.26) and (6.27) forms a system of seven governing equations for each $\Omega_s^I, I=1,2,\ldots,N$.

By using (6.6) to approximate the displacements, and after computing strains, stresses, and surface traction vectors according to relations (6.9), (6.11) and (6.12), the governing equations (6.26), (6.27) and (6.29) for the node couple I may be transformed into the following discretized set of linear equations

$$\sum_{J=1}^{N_I}-\left[\int_{L_s^I}\mathbf{N}\mathbf{D}\mathbf{B}_J\,d\Gamma-\int_{\Gamma_{su}^I}\mathbf{N}\mathbf{D}\mathbf{B}_J\,d\Gamma+\alpha\int_{\Gamma_{su}^I}\mathbf{\Phi}_J\,d\Gamma\right]\hat{\mathbf{u}}_J=$$

$$=\int_{\Omega_s^I}\mathbf{b}\,d\Omega+\int_{\Gamma_{st}^I}\overline{\mathbf{t}}\,d\Gamma+\alpha\int_{\Gamma_{su}^I}\overline{\mathbf{u}}\,d\Gamma, \tag{6.30}$$

$$\sum_{J=1}^{N_I}\left[\int_{\Omega_s^I}\nabla\mathbf{d}^T\mathbf{D}\mathbf{B}_J\,d\Omega-\int_{L_s^I}\theta^3\mathbf{N}\mathbf{D}\mathbf{B}_J\,d\Gamma-\int_{\Gamma_{su}^I}\theta^3\mathbf{N}\mathbf{D}\mathbf{B}_J\,d\Gamma+\right.$$

$$\left.+\alpha\int_{\Gamma_{su}^I}\theta^3\mathbf{\Phi}_J\,d\Gamma\right]\hat{\mathbf{u}}_J=\int_{\Omega_s^I}\theta^3\mathbf{b}\,d\Omega+\int_{\Gamma_{st}^I}\theta^3\overline{\mathbf{t}}\,d\Gamma+\alpha\int_{\Gamma_{su}^I}\theta^3\overline{\mathbf{u}}\,d\Gamma, \tag{6.31}$$

$$\sum_{J=1}^{N_I}\left[\int_{\Omega_s^I}\nabla\mathbf{d}_2^{\ T}\mathbf{D}\mathbf{B}_J\,d\Omega-\int_{L_s^I}\mathbf{v}_2^T\mathbf{N}\mathbf{D}\mathbf{B}_J\,d\Gamma-\int_{\Gamma_{su}^I}\mathbf{v}_2^T\mathbf{N}\mathbf{D}\mathbf{B}_J\,d\Gamma+\right.$$

$$\left.\alpha\int_{\Gamma_{su}^I}\mathbf{v}_2^T\mathbf{\Phi}_J\,d\Gamma\right]\hat{\mathbf{u}}_J=\int_{\Omega_s^I}\mathbf{v}_2^T\mathbf{b}\,d\Omega+\int_{\Gamma_{st}^I}\mathbf{v}_2^T\overline{\mathbf{t}}\,d\Gamma+\alpha\int_{\Gamma_{su}^I}\mathbf{v}_2^T\overline{\mathbf{u}}\,d\Gamma \tag{6.32}$$

with

$$\mathbf{v}_2^T\left(\theta^i\right)=\left[\begin{array}{ccc}\left(\theta^3\right)^2 & \left(\theta^3\right)^2 & \left(\theta^3\right)^2\end{array}\right], \tag{6.33}$$

$$\nabla \mathbf{d}_2^T = \left[\left(\theta^3 \right)_{,X^1}^2 \quad \left(\theta^3 \right)_{,X^2}^2 \quad \left(\theta^3 \right)_{,X^3}^2 \right.$$

$$\left. \left(\theta^3 \right)_{,X^2}^2 + \left(\theta^3 \right)_{,X^1}^2 \quad \left(\theta^3 \right)_{,X^3}^2 + \left(\theta^3 \right)_{,X^2}^2 \quad \left(\theta^3 \right)_{,X^3}^2 + \left(\theta^3 \right)_{,X^1}^2 \right].$$

$$(6.34)$$

Herein N_I stands for the total number of node couples in the domain of influence associated with the node I, Ω_{inf}^I, and $\hat{\mathbf{u}}_J$ contains the unknown DOF associated with the Jth node couple inside Ω_{inf}^I. If the body forces are neglected, then all domain integrals involving the body force vector $\mathbf{b}$ vanish from the discredited equations.

The expressions (6.30) and (6.31) are identical to LWF (6.18) and (6.19), used in the previous formulation in Section 6.3. However, the calculation of (6.32) involves numerical integration, which is influenced by all nodes in Ω_{inf}^I. Consequently, the global stiffness matrix has more non-zero terms than it is the case in the formulation employing the collocation approach, wherein only the nodes positioned inside the domain of definition Ω_{X_I} of the node I produce the non-zero couplings with the node I in the global stiffness matrix. Consequently, somewhat greater computational effort and time are needed for solving the final system obtained by using the quadratic test function. In addition, further additional computational costs arise due to the matrix manipulation needed for establishing the sub-integral functions in (6.32) at each integration point. On the other hand, here it is not necessary to compute the second derivatives of the MLS equations, which is computationally costly and may contribute to the numerical inaccuracies. The integral approach is also simpler and more straightforward than the collocation procedure in the case of curved shells. Furthermore, the continuity requirement for the trial functions is lower, and therefore, any C^0 continuous function is admissible as the trial function.

6.5 Numerical examples

The results of several numerical experiments involving plates and shells are presented hereafter to illustrate the performance of the proposed displacement-based MLPG approach. First, thick rectangular plates as well as thick cylindrical and spherical shells with various boundary conditions were considered by comparing the results with the FEM available analytical solutions. Next, some classical benchmark problems

involving thin shells revealed the behaviour of the developed formulations in the thin structure limit and the sensitivity to the shear locking effect.

In the following, the formulation that employs the collocation, presented in Section 6.3, is denoted as MLPG-COLL, while the algorithm that uses the quadratic test function, as explained in Section 6.4, is labelled as MLPG-QTS. For the purpose of comparison, hexahedral solid finite elements from the MSC.Nastran program package [87],[144] were used. These elements employ the reduced integration for the alleviation of shear locking. In addition, in the 8-noded element the Poisson's thickness locking is circumvented by means of bubble functions.

For facilitation, structures were discretized by uniform grids of node couples, and the local sub-domains with circular cylindrical shapes in the parametric space were applied, as explained in Section 6.2. The integration was performed by employing the simple Legendre-Gaussian numerical integration scheme over the entire local sub-domain, as described in Section 4.4.

The MLS functions with complete polynomial bases of different order were used to approximate the displacements in the in-plane directions. They are labelled as MLSX, where $X = 1, 2, 3, ..., 6$ denotes the order of the applied complete polynomial basis. For all calculations, the MLS weight functions were the 4th-order spline functions with circular support domains, given by relation (3.20). The radii R_t define the sizes of the support domains of the nodal test functions Ω_t, while R_{tr} stands for the radii of the support domains of the nodal trial MLS shape functions Ω_{tr}. Due to the uniform discretization, the radii R_{tr} of all support domains Ω_{tr} in the model were equal. The same applies to the radii R_t of the local sub-domains Ω_t.

Since the utilized MLS functions do not posses the Kronecker delta property, the essential boundary conditions (BC) are enforced by means of the penalty method in the proposed meshless formulations, as explained in Chapter 6. The parametric analyses showed that the value of the penalty parameter hardly affects the solution accuracy in the considered problems if it is in the range $\alpha = 10^5 - 10^{12}$. Consequently, in all examples the value of the penalty parameter was $\alpha = 10^9$.

6.5.1 Thick rectangular plates

6.5.1.1   Clamped square plate

A clamped square plate subjected to the uniformly distributed load over the upper surface was considered. The plate configuration is presented in Figure 6.4. The plate thickness to span ratio is $h/a = 0.1$. The material data are Young's modulus $E = 10.92 \cdot 10^5 \, \text{N/mm}^2$ and Poisson's ratio $\nu = 0.3$.
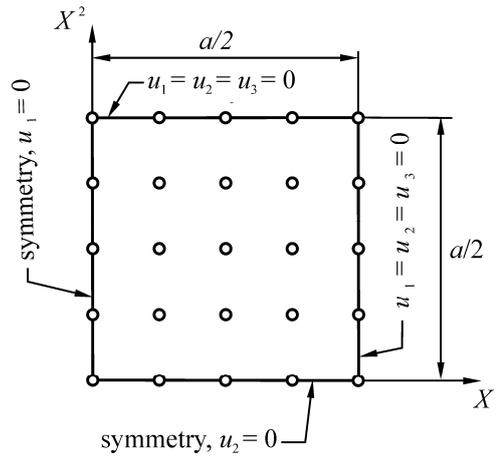

Figure 6.4 Clamped thick square plate. Discretization and applied essential BCs.

All calculations were performed by using the complete MLS basis of the 2nd order (MLS2) and results were normalized by using the exact analytic solution from Srinivas and Rao [145], denoted here as w_{ca}. Due to symmetry, only one quarter of the plate was discretized by uniformly distributed grids of nodes positioned on the upper and lower plate surfaces.

The quality of the solution generally depends on the size of the local sub-domains Ω_t, defined here by the value of R_t. Figure 6.5 depicts the influence of R_t on the accuracy of the solution for the plate central deflection w_c. The calculations were performed by using the MLPG-QTS formulation. Therein, the results for three different values of R_t, defined by the ratios $R_t / h_m = 0.75, 0.8, 0.85$, are displayed for the discretization pattern consisting of 289 node couples. Herein, h_m denotes the distance between nodes in the direction of coordinate axes X^α. Although it is obvious from Figure 6.5 that there are some discrepancies in the solutions for different values of R_t / h_m, it should be noted that the differences are always in the range $\approx \le 1\%$. Similar conclusions are valid for the MLPG-COLL formulation. Therefore, all results presented

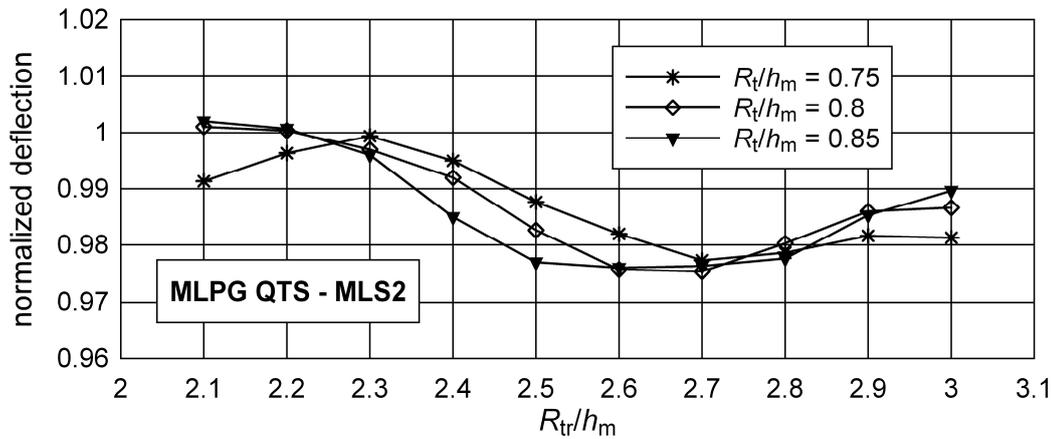in the following sections were obtained using the value $R_t / h_m = 0.8$, unless specified otherwise.

Figure 6.5 Clamped thick square plate. Influence of R_{tr} on solution accuracy for MLPG-QTS formulation.

The influence of the radius R_{tr} on the solution for w_c was investigated for different discretization patterns. The dependency of the plate central deflection on the ratio R_{tr} / h_m is plotted in Figure 6.6 and Figure 6.7 for the MLPG-COLL and MLPG-QTS formulations, respectively.
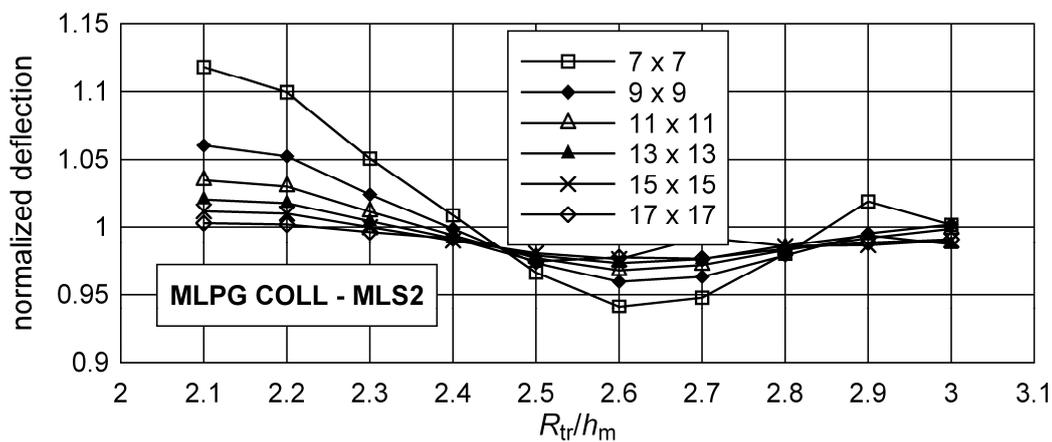
Figure 6.6 Clamped thick square plate. Influence of R_{tr} on solution accuracy for MLPG-COLL formulation.

Although the value of R_{tr} significantly affects the numerical error, this effect diminishes with increasing the number of nodes. However, it is to note that for both

formulations the solutions always oscillate around the analytical value w_{ca} in the interval $R_{tr}/h_m \approx 2.3 - 2.5$.

Next, the convergence of central deflection was tested for various values of R_{tr}/h_m by using the MLPG-QTS formulation. The results are given in Figure 6.8. The curves converge to the similar value for all tested values of R_{tr}/h_m, although the exact deflection w_{ca} is slightly underestimated in all cases. Nevertheless, it may be concluded that the proposed formulations were able to converge regardless of the value of R_{tr}.
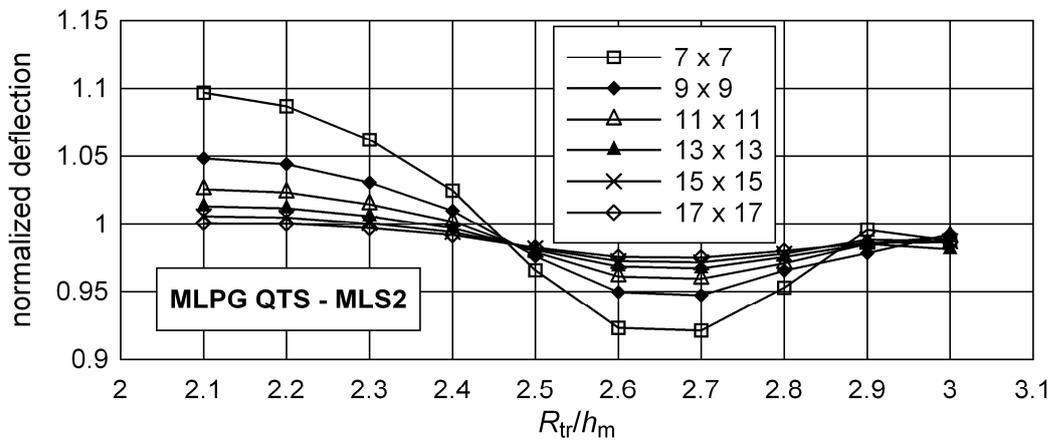

Figure 6.7 Clamped thick square plate. Influence of R_{tr} on solution accuracy for MLPG-QTS formulation.
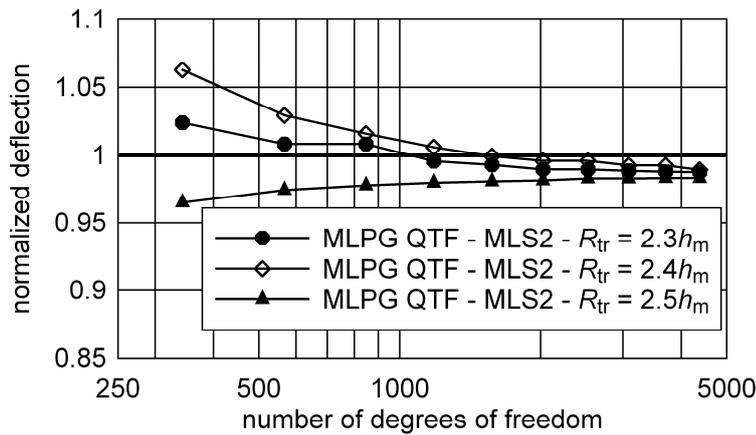

Figure 6.8 Clamped thick square plate. Convergence of w_{ca} for various values of R_{tr}/h obtained by using the MLPG-QTS formulation.

The convergence of the central deflection w_c, obtained by using the $R_{tr}/h_m = 2.5$, is compared with the values obtained by the algorithm from Sorić et al. [146] in Figure

6.9. The linear distribution of the transversal displacement u_3 in the plate thickness direction is assumed in the applied primal MLPG formulation. The convergence is plotted in dependence on the number of node couples along the side edges of the plate. The results show that the algorithm employing the linear interpolation for u_3 suffers from thickness locking, which is not the case with the MLPG-QTS and MLPG-COLL formulations, where the hierarchical quadratic interpolation for u_3 is used.
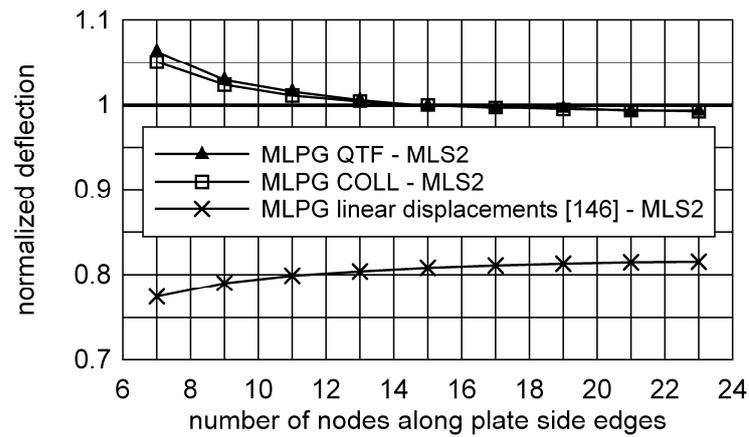

Figure 6.9 Clamped chick square plate. Convergence of central deflection for various displacement-based MLPG formulations.
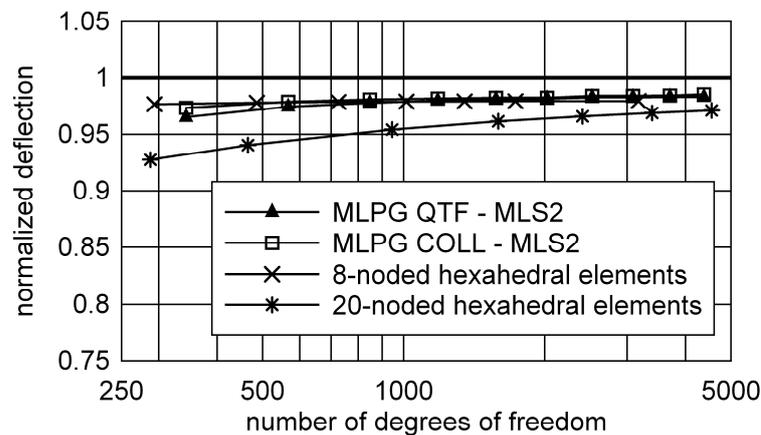

Figure 6.10 Clamped thick square plate. Convergence of MLPG COLL and MLPG QTS formulations in comparison with finite element solutions.

Figure 6.10 shows the comparison of the convergences of the proposed formulations with the FE solutions obtained by using the 3-D brick-type elements from the program package MSC.Nastran. This time, the ratio w_c / w_{ca} is plotted versus the total number of DOF plotted on logarithmic scale. The presented meshless formulations yield very

similar convergences, which are comparable to the FE solutions. It is also to note that all the tested methods slightly underestimate the applied analytical value.

6.5.1.2 Simply supported square plate

The second example is the simply supported square plate with the same geometry and material data as in the previous example, subjected to a uniformly distributed load over the upper surface. Here, only the transversal displacements are suppressed along the simply supported boundary, according to Figure 6.11.
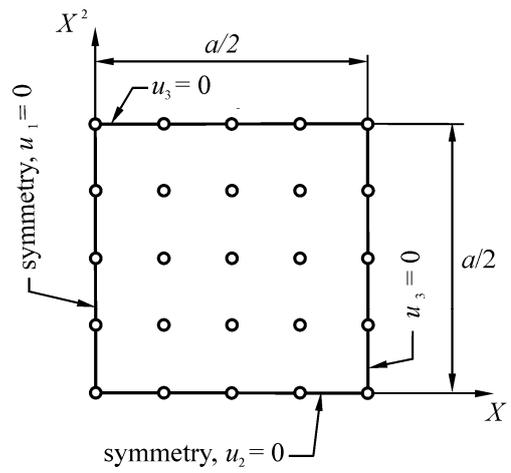

Figure 6.11 Simply supported thick square plate. Discretization and applied essential BCs.

As in the first example, the influence of the radius R_{tr} on the plate central deflection w_c was investigated, and the results of the performed parametric analyses are plotted in Figure 6.12 and Figure 6.13. Conclusions similar to those in the previous example may be drawn. The convergence for the central deflection is presented in Figure 6.14, which shows the comparison with the FE solutions obtained by using hexahedral finite elements form the MSC.Nastran program package. The analytical value used for the normalization is again available in Srinivas and Rao [145]. As in the case considering the clamped plate, both formulations exhibit practically the same convergences. They are again very similar to those obtained by using the 8-noded brick finite elements, while for this case the 20-noded brick elements converge faster than other tested algorithms. As before, all results converge to the value slightly lower than the analytical solution.
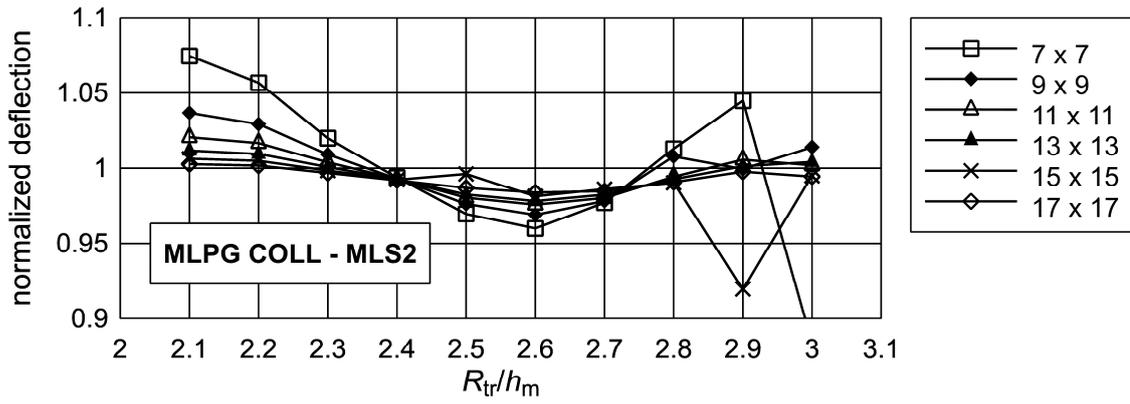
Figure 6.12 Simply supported thick square plate. Influence of R_{tr} on solution accuracy for MLPG-COLL formulation.
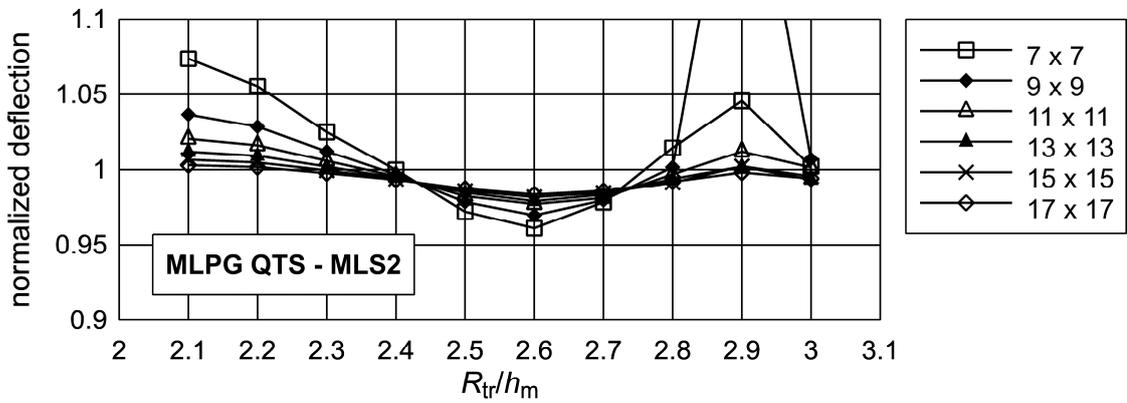

Figure 6.13 Simply supported thick square plate. Influence of R_{tr} on solution accuracy for MLPG-QTS formulation.
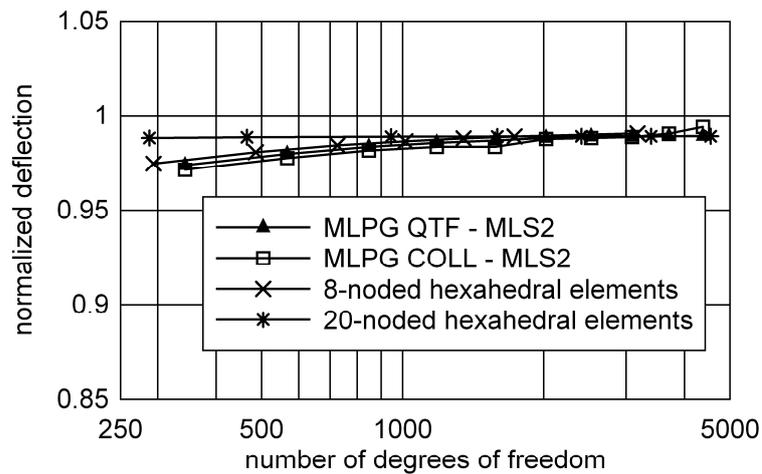

Figure 6.14 Simply supported thick square plate. Convergence of MLPG-COLL and MLPG-QTS formulations in comparison with finite element solutions.

6.5.2 Thick shells

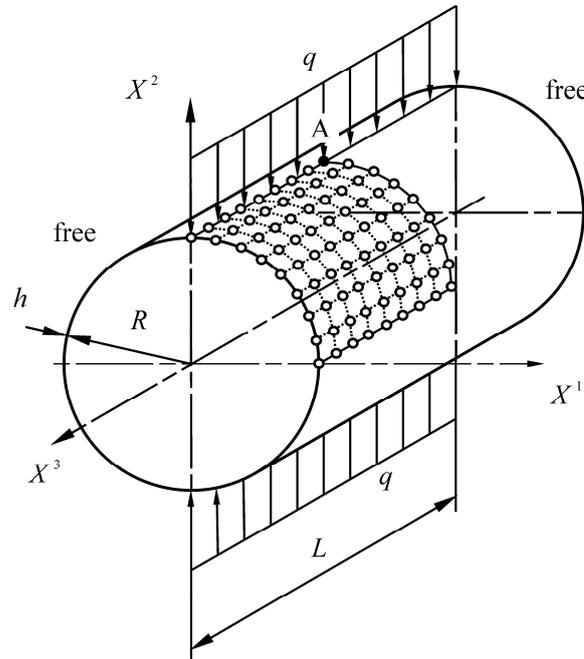#### 6.5.2.1   Thick cylindrical shell subjected to line load

Figure 6.15 Thick cylindrical shell. Geometry and discretization.

The results for a thick horizontal cylindrical shell shown in Figure 6.15 are given in this section. The shell is subjected to the uniform line load of $q = 1 \text{N/mm}$ along the upper and lower generatrix, while the far ends of the cylinder are free. The shell thickness is $h = 9 \text{mm}$ with a radius to thickness ratio of $R/h = 10$ and the length of the cylinder is $L = 300 \text{mm}$. The material data are Young's modulus $E = 210000 \text{N/mm}^2$ and Poisson's ratio $\nu = 0.3$. Due to symmetry, only one octant of the shell was modelled.

The convergence of the vertical displacement at the central point A, positioned under the line load, was analyzed. In Figure 6.16, the results are compared to the FE solutions obtained by using the hexahedral finite elements from the MSC.Nastran package. The calculations were performed by employing the MLS2 functions and by setting $R_t = 0.8 h_{\text{m}}$ to define the sizes of the local sub-domains, where h_{m} is the minimal distance between node couples in the directions of the parametric coordinates.
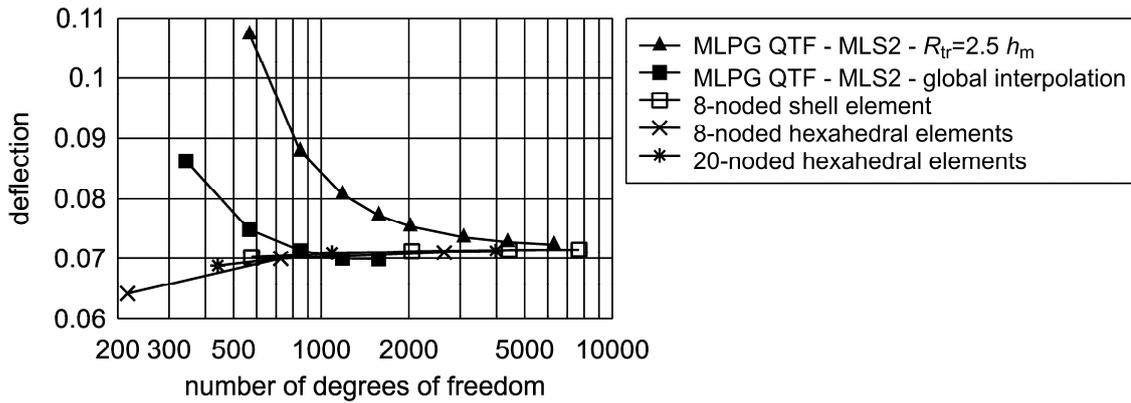
Figure 6.16 Thick cylindrical shell. Convergence at point A for MLPG-QTS formulation in comparison with FE solutions.

In Figure 6.16, the curves representing the convergence of the MLPG-QTS formulation were obtained by employing two different values of R_{tr}. First, the value $R_{tr} = 2.5 h_\mathrm{m}$ was used, as in the previous example. However, for this problem the convergence is significantly worse than those obtained by the applied finite elements. Furthermore, it was found that the essential BC were not satisfied as accurately as in the previous examples. The possible causes for such deterioration may be the inaccurate numerical integration, arising due to the reasons explained in Section 4.4. The numerical experiments proved that these negative phenomena could be reduced significantly by performing the global MLS interpolation. Therefore, the value of R_{tr} was adjusted so that the support domain of the MLS shape function of each node couple covered the entire global domain. It is evident from Figure 6.16 that the convergence considerably improved by using the described strategy. However, it is important to note that such an approach is not practical because it demands prohibitively large computational costs for computing the MLS shape functions. Furthermore, the coefficient matrix in the resulting final algebraic system of equations becomes a fully populated matrix, which additionally increases the total computational costs.

The convergence of the vertical displacement at point A, depending on the order of the in-plane MLS basis, is displayed in Figure 6.17 for the global MLS approximation strategy. It is obvious that the convergence improves considerably if the sixth-order MLS basis is used.
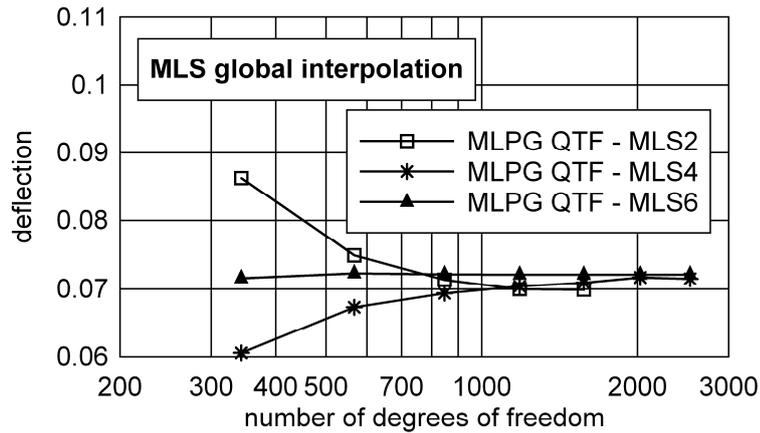
Figure 6.17 Thick cylindrical shell. Convergence at point A for MLPG-QTS formulation obtained by employing different orders of MLS bases.

6.5.2.2   Clamped thick hemispherical shell under line load

A thick hemispherical shell with a central opening, representing a doubly curved thin-walled structure, is considered in this section. The shell is clamped along the bottom edge and subjected to the uniform line load of $q = 10\,\text{N/mm}$ on the upper edge, according to Figure 6.18. The shell thickness is $h = 9\,\text{mm}$, the radius of the shell is $R = 90\,\text{mm}$ and the central opening is defined by $\alpha = 60^0$. The material data are Young's modulus $E = 210000\,\text{N/mm}^2$ and Poisson's ratio $v = 0.3$. Due to symmetry, only one quadrant was modelled by uniform grids of node couples.

The convergence of point A, positioned at the corner of the upper edge, as shown in Figure 6.18, was analyzed - the results are presented in Figure 6.19. The calculations were performed by employing the MLS2 functions, and by using $R_t = 0.8 h_\text{m}$ and $R_{tr} = 2.5 h_\text{m}$, where h_m is the distance between node couples in the direction of the parametric coordinate axes θ^α. Because no analytical solution to this problem exists in the literature, the results were compared to the FE solutions from MSC.Nastran program package. Thereby, the 8-noded shell elements [144] were used besides the hexahedral elements to double-check the validity of the converged values. The shear locking effects are suppressed by using the reduced integration in these elements. It can be seen that, similarly to the examples involving the rectangular plates, the meshless formulation converge in to the value that is close to those obtained by the finite elements.
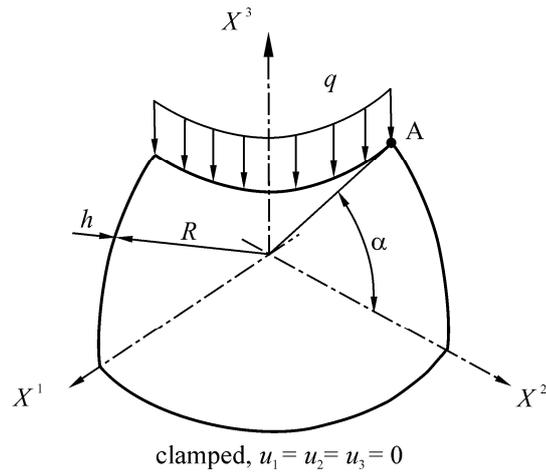
Figure 6.18 Clamped thick hemispherical shell. Geometry and boundary conditions.
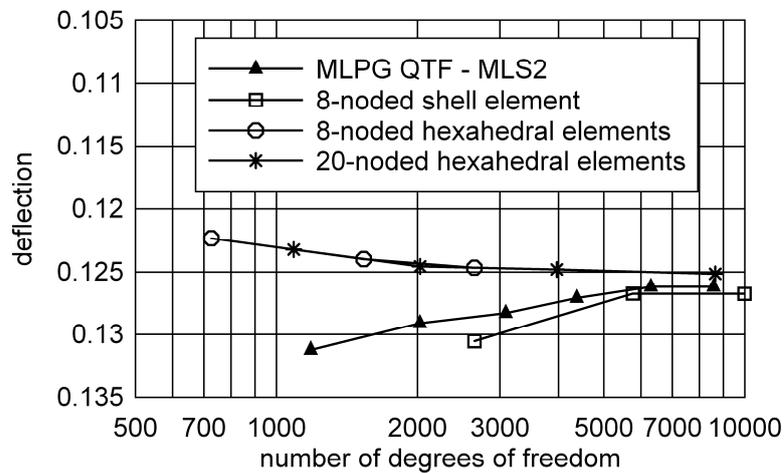
Figure 6.19 Clamped thick hemispherical shell. Convergence of MLPG-QTS formulation in comparison with finite element solutions.

6.5.3 Thin shells

This section contains the results for some typical benchmark tests dealing with the numerical formulations for the analysis of thin shell-like structures. By performing such numerical experiments, it is possible to test the performance of new algorithms in the thin structure limit where various locking phenomena, such as transversal or membrane locking, may significantly affect the quality of solutions. In order to gain better insight into the behaviour of the proposed meshless algorithms with respect to locking, all calculations were performed by utilizing the global MLS approximations in the shell in-plane directions, as explained in Section 6.5.2.1.

6.5.3.1 Scordelis-Lo shell roof

The problem considered in this section is the Scordelis-Lo shell roof, a well-known standard benchmark for testing FE formulations regarding the resistance to shear locking. In this problem, the membrane response of the shell is as important as the bending response, so this test is used in FEM to check whether a formulation is free of membrane, as well as transversal shear locking [6]. Material data for this benchmark test are Young's modulus $E = 2.0684 \times 10^4 \, \text{N/mm}^2$ and Poisson's ratio $\nu = 0.0$. The radius and length of the roof are $R = 7.62\,\text{m}$ and $L = 15.24\,\text{m}$, respectively, and the radius to thickness ratio is $R/h = 100$. The shell is subjected to the uniform vertical load of $q = 4.302 \times 10^{-3} \, \text{N/mm}^2$. It is assumed that the two longitudinal edges are free and the two circular edges are supported by diaphragms. Owing to symmetry, only one quarter of the shell was modelled by applying uniform grids and appropriate symmetry conditions, as shown in Figure 6.20.
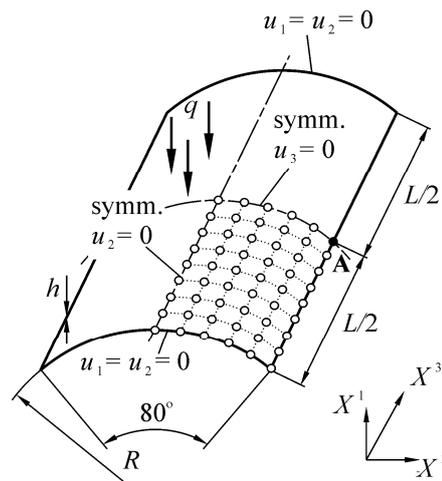
Figure 6.20 Scordelis-Lo shell roof. Geometry and discretization of the shell.

Figure 6.21 displays the convergence of the vertical displacement at point A, positioned on the shell middle surface, for different MLS basis functions. The results are normalized by the analytical value available in [152]. As expected, the convergence improves by increasing the order of the MLS basis function. It also demonstrates that the shear locking effect is sufficiently suppressed by using the sixth-order basis function. The deformed shape of the structure is presented in Figure 6.23.
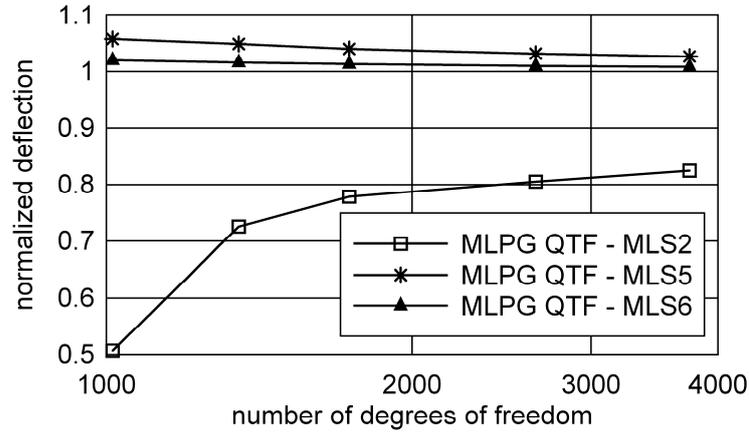
Figure 6.21 Scordelis-Lo shell roof. Convergence at the point A for MLPG-QTS formulation obtained by employing different orders of MLS bases.
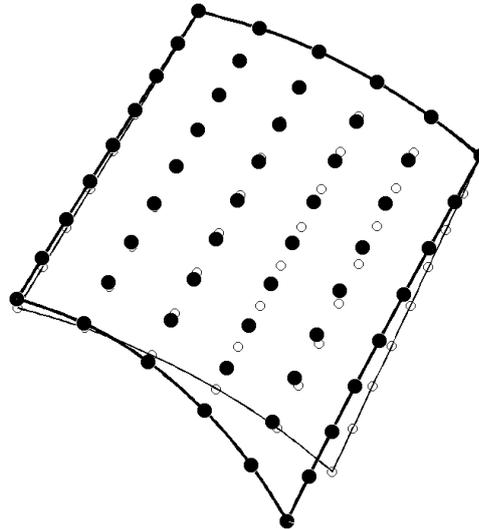
Figure 6.22 Scordelis-Lo shell roof. Deformed shape of one quarter of shell.

6.5.3.2 Pinched cylinder

The next typical benchmark test analyzed here is a thin cylinder pinched by two radial forces $P = 4.482$ N in the middle of the structure and bounded by two rigid diaphragms. In this problem, transversal shear locking is more significant than membrane locking due to the acting of the concentrated forces. The geometry, boundary conditions, and the discretization of the shell are presented in Figure 6.23. Young's modulus of the material is $E = 2.0684 \times 10^5$ N/mm^2 and Poisson's ratio is $\nu = 0.3$. The radius to thickness ratio is $R/h = 100$ with the shell thickness $h = 76.2$ mm. The length

of the shell is $L = 15.24$ mm. Due to the symmetry, only one octant of the shell was modelled.
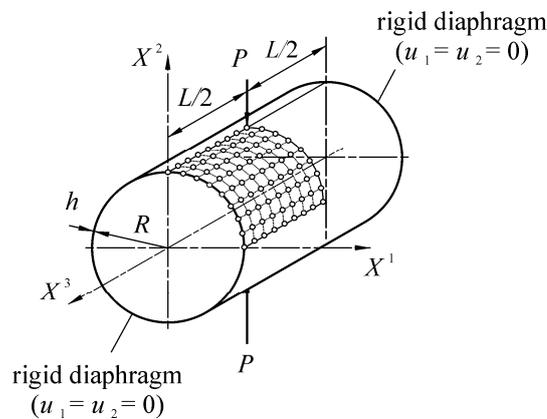
Figure 6.23 Pinched cylinder. Geometry, boundary conditions, and discretization.

The convergence of the normalized vertical displacement under the point load was studied and results are plotted in Figure 6.24. The exact solution used for the normalization is available in [6]. The convergence rate again improves with increasing the order of the MLS basis. However, because of severe shear locking, the sixth-order MLS basis is necessary for the solution to converge to the analytical value at all in this problem.
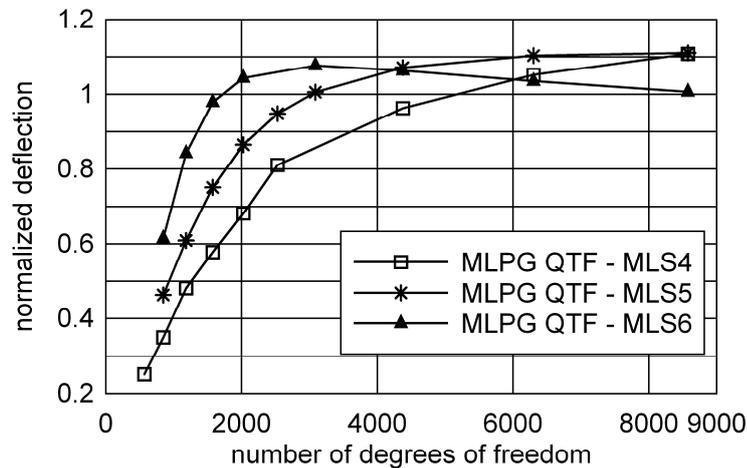
Figure 6.24 Pinched cylinder. Convergence of vertical displacement under point load obtained by MLPG-QTS formulation

7 Mixed MLPG solid-shell formulations

The solid-shell formulations presented in this chapter are based on the mixed approach originally presented by Atluri et al. in [40]. In contrast to the primal MLPG formulations, in the mixed MLPG strategy some additional field variables, such as strain or stress components, are approximated separately from displacements. In Section 7.1, the formulation for the analysis of plate structures, first proposed in [147], and later described and analyzed in details in [148], is presented. Section 7.2 contains the description of the formulation for curved shell structures, originally proposed in [149]. Therein the theoretical estimates of the computational costs for both the mixed and primal MLPG solid-shell approaches are given. Finally, Section 7.3 comprises of some numerical tests that demonstrate the performance of the developed mixed formulations.

7.1 Mixed MLPG formulation for the analysis of plates

7.1.1 Governing equations

In order to derive the governing equations for the proposed formulation, a homogeneous rectangular plate of uniform thickness is considered. The 3-D Cartesian co-ordinate system is used to define the equilibrium equations, as shown in Figure 7.1.

Figure 7.1 Discretization of plate continuum

The plate continuum is represented by a set consisting of N node couples, where the nodes are positioned on the upper and lower plate surfaces. A local sub-domain

$\Omega_s^I, I = 1, 2, ..., N$, is defined around each node couple $\mathbf{X}_I, I = 1, 2, ..., N$, as explained in Section 5.1.

By following the procedure described in details in Section 5.2, the equilibrium equations (2.42) are written in LWF (5.19)-(5.20) over each Ω_s^I as

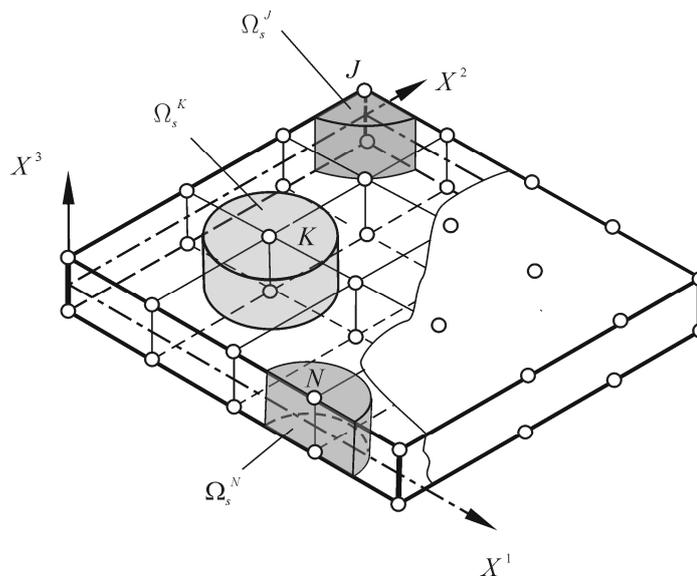$$\int_{\Omega_s^I} v_{1,X^j} \sigma_{kj} d\Omega - \int_{L_s^I} v_1 n_j \sigma_{kj} d\Gamma - \int_{\Gamma_{su}^I} v_1 n_j \sigma_{kj} d\Gamma + \alpha \int_{\Gamma_{su}^I} v_1 u_k d\Gamma =$$
$$\int_{\Omega_s^I} v_1 b_k d\Omega + \int_{\Gamma_{st}^I} v_1 \overline{t}_k d\Gamma + \alpha \int_{\Gamma_{su}^I} v_1 \overline{u}_k d\Gamma, \tag{7.1}$$

$$\int_{\Omega_s^I} v_{2,X^j} \sigma_{kj} d\Omega - \int_{L_s^I} v_2 n_j \sigma_{kj} d\Gamma - \int_{\Gamma_{su}^I} v_2 n_j \sigma_{kj} d\Gamma + \alpha \int_{\Gamma_{su}^I} v_2 u_k d\Gamma =$$
$$\int_{\Omega_s^I} v_2 b_k d\Omega + \int_{\Gamma_{st}^I} v_2 \overline{t}_k d\Gamma + \alpha \int_{\Gamma_{su}^I} v_2 \overline{u}_k d\Gamma. \tag{7.2}$$

Herein, all variables are defined in the global Cartesian system shown in Figure 7.1, e.g., $\boldsymbol{\sigma} = \sigma_{ij} \mathbf{e}_i \otimes \mathbf{e}_j$, etc. Using (5.16) and the Heaviside function (5.15) with the circular support domain in the in-plane directions X^α, the test functions v_1 and v_2 may be written like in (5.32)

$$v_1\left(X^k\right) = \begin{cases} 1, & X^\alpha \in \Omega_s^I \cup \partial\Omega_s^I \\ 0, & X^\alpha \notin \Omega_s^I \cup \partial\Omega_s^I \end{cases}, \quad v_2\left(X^k\right) = \begin{cases} X^3, & X^\alpha \in \Omega_s^I \cup \partial\Omega_s^I \\ 0, & X^\alpha \notin \Omega_s^I \cup \partial\Omega_s^I \end{cases}. \tag{7.3}$$

Inserting (5.32) into (7.1) and (7.2), and after employing the constitutive relations from (2.29), (2.34) and (2.35), LWF is transformed to

$$-\int_{L_S^I} C_{ijkl} \varepsilon_{kl}^{(h)} n_j d\Gamma - \int_{\Gamma_{Su}^I} C_{ijkl} \varepsilon_{kl}^{(h)} n_j d\Gamma + \alpha \int_{\Gamma_{su}^I} u_i^{(h)} d\Gamma =$$
$$= \int_{L_{St}^I} \overline{t}_i d\Gamma + \int_{\Omega_s^I} b_i d\Omega + \alpha \int_{\Gamma_{su}^I} \overline{u}_i d\Gamma, \tag{7.4}$$

$$\int_{\Omega_s^I} \left(X^3\right)_{,X^j} C_{ijkl} \varepsilon_{kl}^{(h)} d\Omega - \int_{L_S^I} X^3 C_{ijkl} \varepsilon_{kl}^{(h)} n_j d\Gamma - \int_{\Gamma_{Su}^I} X^3 C_{ijkl} \varepsilon_{kl}^{(h)} n_j d\Gamma$$
$$+\alpha \int_{\Gamma_{su}^I} X^3 u_i^{(h)} d\Gamma = \int_{L_{St}^I} X^3 \overline{t}_i d\Gamma + \int_{\Omega_s^I} X^3 b_i d\Omega + \alpha \int_{\Gamma_{su}^I} X^3 \overline{u}_i d\Gamma, \tag{7.5}$$

where both the strains $\varepsilon_{kl} = \varepsilon_{kl}^{(h)}$ and the displacements $u_i = u_i^{(h)}$ are considered as independent variables.

Linear distribution over the plate thickness is assumed for all displacement and strain components as

$$u_i^{(h)}\left(X^k\right)=\psi^1\left(X^3\right)u_{i(u)}^{(h)}\left(X^\alpha\right)+\psi^2\left(X^3\right)u_{i(l)}^{(h)}\left(X^\alpha\right), \tag{7.6}$$

$$\varepsilon_{ij}^{(h)}\left(X^k\right)=\psi^1\left(X^3\right)\varepsilon_{ij(u)}^{(h)}\left(X^\alpha\right)+\psi^2\left(X^3\right)\varepsilon_{ij(l)}^{(h)}\left(X^\alpha\right), \tag{7.7}$$

where functions ψ^1 and ψ^2, defined analogously to (2.2), describe the linear distribution of variables over the thickness, while $\varepsilon_{ij(u)}^{(h)}$, $\varepsilon_{ij(l)}^{(h)}$ and $u_{i(u)}^{(h)}$, $u_{i(l)}^{(h)}$ denote the strains and displacements on the upper and lower plate surface, respectively. h stands for the plate thickness.

It is to note that equations (7.4) and (7.5) represent a system of six equations for each local sub-domain Ω_s^I, while in the approximated fields (7.6) and (7.7) there are altogether 18 unknown variables, including $\varepsilon_{ij(u)}^{(h)}$, $\varepsilon_{ij(l)}^{(h)}$, $u_{i(u)}^{(h)}$ and $u_{i(l)}^{(h)}$. Therefore, in order to derive a closed system of equations on the structural level, the following 3-D kinematics constraints are imposed for each $\Omega_s^I, I = 1, 2, ..., N$, written here in a general local weak form as

$$\int_{\Omega_S^I} v_{(ij\varepsilon)}\left[\varepsilon_{ij}^{(h)}\left(X^k\right)-\varepsilon_{ij}^{(c)}\left(X^k\right)\right]d\Omega=0 . \tag{7.8}$$

Herein $\varepsilon_{ij}^{(c)}$ stands for the strains that are compatible with the approximated displacements. From the 3-D strain-displacement relations (2.27) it follows that

$$\varepsilon_{ij}^{(c)}\left(X^k\right)=\frac{1}{2}\left[u_{i,X^j}^{(h)}\left(X^k\right)+u_{j,X^i}^{(h)}\left(X^k\right)\right], \tag{7.9}$$

while $v_{(ij\varepsilon)}$ are some admissible test functions. By suitably choosing $v_{(ij\varepsilon)}$, it is possible to obtain the additional twelve equations for each , which are necessary for closing the global system of equations.

7.1.2 Numerical implementation

The displacements and strains associated with the upper and lower plate surfaces are approximated by employing the same MLS shape functions in the in-plane directions X^α for all strain and displacement components, which leads to

$$u_{i(u)}^{(h)}\left(X^{\delta}\right)=\sum_{J=1}^{n}\phi^{J}\left(X^{\delta}\right)\hat{u}_{i(u)}^{J}, \quad u_{i(l)}^{(h)}\left(X^{\delta}\right)=\sum_{J=1}^{n}\phi^{J}\left(X^{\delta}\right)\hat{u}_{i(l)}^{J}, \tag{7.10}$$

$$\varepsilon_{ij(u)}^{(h)}\left(X^{\delta}\right)=\sum_{J=1}^{n}\phi^{J}\left(X^{\delta}\right)\hat{\varepsilon}_{ij(u)}^{J}, \quad \varepsilon_{ij(l)}^{(h)}\left(X^{\delta}\right)=\sum_{J=1}^{n}\phi^{J}\left(X^{\delta}\right)\hat{\varepsilon}_{ij(l)}^{J}. \tag{7.11}$$

Herein $\phi^{J}\left(X^{\delta}\right)$ is the in-plane MLS shape function associated with the Jth node couple positioned inside the domain of definition $\Omega_{X^{\delta}}$ of the sample point X^{δ}, and n stands for the total number of node couples inside $\Omega_{X^{\delta}}$. The shape function $\phi^{J}\left(X^{\delta}\right)$ is calculated by employing local normalized coordinates, according to the procedure given in Section 3.4.1. More details about the applied approximation scheme may be found in [148].

Employing (7.10) and (7.11), the displacement and strain fields (7.6) and (7.7) may be written in the discretized forms as

$$\mathbf{u}^{(h)}=\sum_{J=1}^{n}\mathbf{\Phi}_{u}^{J}\,\hat{\mathbf{u}}^{J}, \tag{7.12}$$

$$\boldsymbol{\varepsilon}^{(h)}=\sum_{J=1}^{n}\mathbf{\Phi}_{\varepsilon}^{J}\,\hat{\boldsymbol{\varepsilon}}^{J}. \tag{7.13}$$

The matrices $\mathbf{\Phi}_{u}^{J}$ and $\mathbf{\Phi}_{\varepsilon}^{J}$ describe the 3-D displacement and strain nodal shape functions, respectively, and they are defined by

$$\mathbf{\Phi}_{u}^{J}=\phi^{J}\left[\psi^{1}\,\mathbf{I}_{3} \quad \psi^{2}\,\mathbf{I}_{3}\right], \tag{7.14}$$

$$\mathbf{\Phi}_{\varepsilon}^{J}=\phi^{J}\left[\psi^{1}\,\mathbf{I}_{6} \quad \psi^{2}\,\mathbf{I}_{6}\right]. \tag{7.15}$$

In the above relations, $\mathbf{I}_{3}$ and $\mathbf{I}_{6}$ stand for the 3x3 and 6x6 identity matrices, respectively. The vector $\hat{\mathbf{u}}^{J}$ contains the unknown fictitious nodal displacement values

$$\left(\hat{\mathbf{u}}^{J}\right)^{T}=\left[\left(\hat{\mathbf{u}}_{(u)}^{J}\right)^{T} \quad \left(\hat{\mathbf{u}}_{(l)}^{J}\right)^{T}\right], \tag{7.16}$$

while $\hat{\boldsymbol{\varepsilon}}^{J}$ are the vectors of the corresponding unknown fictitious nodal strain values,

$$\left(\hat{\boldsymbol{\varepsilon}}^{J}\right)^{T}=\left[\left(\hat{\boldsymbol{\varepsilon}}_{(u)}^{J}\right)^{T} \quad \left(\hat{\boldsymbol{\varepsilon}}_{(l)}^{J}\right)^{T}\right]. \tag{7.17}$$

Herein $\hat{\mathbf{u}}_{(u)}^{J}$, $\hat{\mathbf{u}}_{(l)}^{J}$, $\hat{\boldsymbol{\varepsilon}}_{(u)}^{J}$ and $\hat{\boldsymbol{\varepsilon}}_{(l)}^{J}$ are the vectors of the nodal displacements and strains associated with the upper and lower nodes, respectively, and they are defined as

$$\hat{\mathbf{u}}_{(u)}^{J} = \begin{bmatrix} \hat{u}_{1(u)}^{J} & \hat{u}_{2(u)}^{J} & \hat{u}_{3(u)}^{J} \end{bmatrix}^{T}, \quad \hat{\mathbf{u}}_{(l)}^{J} = \begin{bmatrix} \hat{u}_{1(l)}^{J} & \hat{u}_{2(l)}^{J} & \hat{u}_{3(l)}^{J} \end{bmatrix}^{T},$$

$$\hat{\boldsymbol{\varepsilon}}_{(u)}^{J} = \begin{bmatrix} \hat{\varepsilon}_{11(u)}^{J} & \hat{\varepsilon}_{22(u)}^{J} & \hat{\varepsilon}_{33(u)}^{J} & 2\hat{\varepsilon}_{12(u)}^{J} & 2\hat{\varepsilon}_{23(u)}^{J} & 2\hat{\varepsilon}_{13(u)}^{J} \end{bmatrix}^{T}, \tag{7.18}$$

$$\hat{\boldsymbol{\varepsilon}}_{(l)}^{J} = \begin{bmatrix} \hat{\varepsilon}_{11(l)}^{J} & \hat{\varepsilon}_{22(l)}^{J} & \hat{\varepsilon}_{33(l)}^{J} & 2\hat{\varepsilon}_{12(l)}^{J} & 2\hat{\varepsilon}_{23(l)}^{J} & 2\hat{\varepsilon}_{13(l)}^{J} \end{bmatrix}^{T}.$$

Employing the strain field approximation (7.13), and the constitutive relations (2.36) and (2.37), the stress vector from (2.31) may be calculated in terms of the nodal strains as

$$\boldsymbol{\sigma} = \mathbf{D} \sum_{J=1}^{n} \boldsymbol{\Phi}_{\varepsilon}^{J} \, \hat{\boldsymbol{\varepsilon}}^{J}. \tag{7.19}$$

The traction surface vector $\mathbf{t} = t_i \, \mathbf{e}_i$ is obtained by inserting the discretized stresses (7.19) into (2.39)

$$\mathbf{t} = \mathbf{N} \mathbf{D} \sum_{J=1}^{n} \boldsymbol{\Phi}_{\varepsilon}^{J} \, \hat{\boldsymbol{\varepsilon}}^{J}, \tag{7.20}$$

where the matrix $\mathbf{N}$ contains the components of the unit normal vector to the local boundary $\partial \Omega_s^I$, $\mathbf{n} = n_i \, \mathbf{e}_i$, according to (2.40).

By means of relations (7.12), (7.13), (7.19) and (7.20), LWF (7.4) and (7.5) of each node couple are transformed into the following discretized form

$$\sum_{J=1}^{N_I} \left[-\int_{L_S^I} \mathbf{N} \mathbf{D} \boldsymbol{\Phi}_{\varepsilon}^{J} d\Gamma - \int_{\Gamma_{Su}^I} \mathbf{N} \mathbf{D} \boldsymbol{\Phi}_{\varepsilon}^{J} d\Gamma \right] \hat{\boldsymbol{\varepsilon}}^{J} + \alpha \sum_{J=1}^{N_I} \left[\int_{\Gamma_{su}^I} \boldsymbol{\Phi}_{u}^{J} d\Gamma \right] \hat{\mathbf{u}}^{J} =$$
$$= \int_{\Gamma_{St}^I} \bar{\mathbf{t}} \, d\Gamma + \int_{\Omega_s^I} \mathbf{b} \, d\Omega + \alpha \int_{\Gamma_{su}^I} \bar{\mathbf{u}} \, d\Gamma, \tag{7.21}$$

$$\sum_{J=1}^{N_I}\left[\int_{\Omega_s^I}\nabla\mathbf{d}^T\mathbf{D}\,\mathbf{\Phi}_\varepsilon^J\mathrm{d}\Omega-\int_{L_S^I}X^3\mathbf{N}\,\mathbf{D}\,\mathbf{\Phi}_\varepsilon^J\,\mathrm{d}\Gamma-\int_{\Gamma_{Su}^I}X^3\mathbf{N}\,\mathbf{D}\,\mathbf{\Phi}_\varepsilon^J\mathrm{d}\Gamma\right]\hat{\mathbf{\varepsilon}}^J+$$

$$+\alpha\sum_{J=1}^{N_I}\left[\int_{\Gamma_{su}^I}X^3\,\mathbf{\Phi}_u^J\,\mathrm{d}\Gamma\right]\hat{\mathbf{u}}^J=\int_{\Gamma_{St}^I}X^3\,\mathbf{t}\,\mathrm{d}\Gamma+\int_{\Omega_s^I}X^3\,\mathbf{b}\,\mathrm{d}\Omega+\alpha\int_{\Gamma_{su}^I}X^3\,\overline{\mathbf{u}}\,\mathrm{d}\Gamma. \tag{7.22}$$

The above relations represent a system of six linear equations on the level of the domain of influence Ω_{inf}^I, which is related to the Ith node couple. Herein N_I denotes the total number of nodes inside Ω_{inf}^I and $\nabla\mathbf{d}^T$ describes the gradient of the linear part of the test function

$$\nabla\mathbf{d}^{\,T}=\begin{bmatrix}X^3_{,X^1}&0&0&X^3_{,X^2}&0&X^3_{,X^3}\\0&X^3_{,X^2}&0&X^3_{,X^1}&X^3_{,X^3}&0\\0&0&X^3_{,X^3}&0&X^3_{,X^2}&X^3_{,X^1}\end{bmatrix}=\begin{bmatrix}0&0&0&0&0&1\\0&0&0&0&1&0\\0&0&1&0&0&0\end{bmatrix}.\tag{7.23}$$

The additional kinematics constraints (7.8) are derived by means of the collocation approach at the nodes located on the upper and lower plate surfaces. Using the Dirac delta functions $\delta\left(\mathbf{X}-\mathbf{X}_{I(u)}\right)$ and $\delta\left(\mathbf{X}-\mathbf{X}_{I(l)}\right)$ as the test functions $v_{(ij\varepsilon)}$ in (7.8), the 3-D kinematics relations (7.9) are imposed directly at the upper and lower nodes of the node couple I as

$$\varepsilon_{ij}^{(h)}\left(\mathbf{X}_{(u)}^I\right)\approx\hat{\varepsilon}_{ij(u)}^I=\frac{1}{2}\left[u_{i,X^j}\left(\mathbf{X}_{I(u)}\right)+u_{j,X^i}\left(\mathbf{X}_{I(u)}\right)\right],$$

$$\varepsilon_{ij}^{(h)}\left(\mathbf{X}_{(l)}^I\right)\approx\hat{\varepsilon}_{ij(l)}^I=\frac{1}{2}\left[u_{i,X^j}\left(\mathbf{X}_{I(l)}\right)+u_{j,X^i}\left(\mathbf{X}_{I(l)}\right)\right] \tag{7.24}$$

with $\mathbf{X}_{I(u)}=\begin{bmatrix}X_I^1&X_I^2&X^3=0,5h\end{bmatrix}^T$ and $\mathbf{X}_{I(l)}=\begin{bmatrix}X_I^1&X_I^2&X^3=-0,5h\end{bmatrix}^T$ as the global Cartesian coordinates of the upper and lower nodes that form the Ith node couple, respectively, as shown in Figure 7.2. In (7.24) it is assumed that the nodal strain values $\hat{\varepsilon}_{ij(u)}^I$ and $\hat{\varepsilon}_{ij(l)}^I$ are exactly interpolated by the strain approximation (7.13).
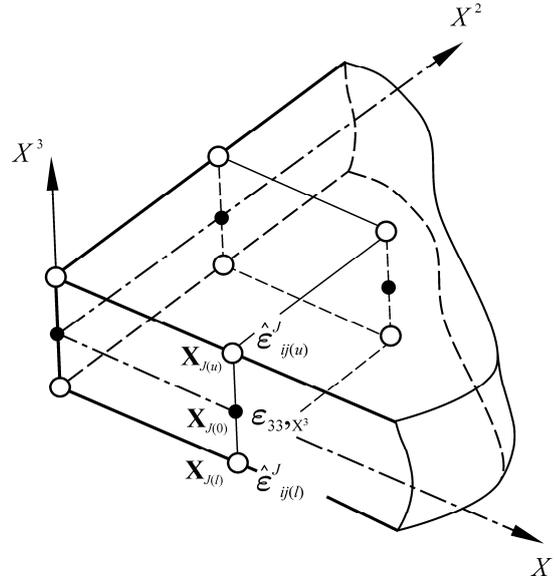
Figure 7.2 Collocation points for mixed MLPG plate formulation

Applying the displacement interpolation (7.12) in (7.24), it is possible to express the nodal strain components in terms of the displacement components in the following matrix form

$$\hat{\boldsymbol{\varepsilon}}_{(u)}^{I} = \sum_{J=1}^{n_I} \mathbf{B}_{(u)}^{JI} \hat{\mathbf{u}}^{J}, \qquad \hat{\boldsymbol{\varepsilon}}_{(l)}^{I} = \sum_{J=1}^{n_I} \mathbf{B}_{(l)}^{JI} \hat{\mathbf{u}}^{J}. \tag{7.25}$$

Herein, $\mathbf{B}_{(u)}^{JI} = \mathbf{B}^{J}\left(\mathbf{X}_{I(u)}\right)$ and $\mathbf{B}_{(l)}^{JI} = \mathbf{B}^{J}\left(\mathbf{X}_{I(l)}\right)$ stand for the 3-D strain-displacement matrix, calculated at the upper and lower node of the Jth node couple that is positioned inside Ω_{X^I}, i.e., the MLS domain of definition of the Ith node couple. n_I is the total number of the nodes in Ω_{X^I}, and the matrix $\mathbf{B}^{J}$ is defined by

$$\mathbf{B}^{J} = \begin{bmatrix} \psi^1 \phi_{,X^1}^{J} & 0 & 0 & \psi^2 \phi_{,X^1}^{J} & 0 & 0 \\ 0 & \psi^1 \phi_{,X^2}^{J} & 0 & 0 & \psi^2 \phi_{,X^2}^{J} & 0 \\ 0 & 0 & \psi_{,X^3}^{1} \phi^{J} & 0 & 0 & \psi_{,X^3}^{2} \phi^{J} \\ \psi^1 \phi_{,X^2}^{J} & \psi^1 \phi_{,X^1}^{J} & 0 & \psi^2 \phi_{,X^2}^{J} & \psi^2 \phi_{,X^1}^{J} & 0 \\ 0 & \psi_{,X^3}^{1} \phi^{J} & \psi^1 \phi_{,X^2}^{J} & 0 & \psi_{,X^3}^{2} \phi^{J} & \psi^2 \phi_{,X^2}^{J} \\ \psi_{,X^3}^{1} \phi^{J} & 0 & \psi^1 \phi_{,X^1}^{J} & \psi_{,X^3}^{2} \phi^{J} & 0 & \psi^2 \phi_{,X^1}^{J} \end{bmatrix}. \tag{7.26}$$

As evident, the employment of the above-described collocation approach avoids the numerical integration in equations (7.8), resulting in the significant reduction of computational time.

7.1.3 Elimination of Poisson's thickness locking effect by modifying transversal strain nodal values

In the proposed formulation, the normal transversal strain component ε_{33} is initially assumed linear through the thickness according to (7.7). Nevertheless, by using relations (7.25) and (7.26), it follows that

$$\hat{\varepsilon}_{33(u)}^I = \hat{\varepsilon}_{33(l)}^I = \frac{1}{h}\sum_{J=1}^{n_I} \phi^{JI} \hat{u}_{3(u)}^K - \frac{1}{h}\sum_{J=1}^{n_I} \phi^{JI} \hat{u}_{3(l)}^J \neq f\left(X^3\right), \ I = 1, 2, ..., N, \qquad (7.27)$$

where $\phi^{JI} = \phi^J\left(X_I^\alpha\right)$ denotes the in-plane MLS nodal shape functions evaluated at the location of the Ith node couple. It is clear that employing $\hat{\varepsilon}_{33(u)}^I$ and $\hat{\varepsilon}_{33(l)}^I$ from (7.27) in the discretized strain field (7.13) results in the constant distribution of $\varepsilon_{33}^{(h)}$ over the thickness and thickness locking appears if the Poisson's ratio is different from zero, as explained in Section 5.3.1. Therefore, it follows that the condition $\hat{\varepsilon}_{33(u)}^I \neq \hat{\varepsilon}_{33(l)}^I$ has to be fulfilled in order to avoid the Poisson's thickness locking phenomenon.

A new procedure based on the modification of the nodal strain component values $\hat{\varepsilon}_{33(u)}^I$ and $\hat{\varepsilon}_{33(l)}^I$ has been developed to avoid the Poisson's thickness locking effect. These new nodal values may be obtained by rewriting the assumed distribution for ε_{33} from (7.7) as

$$\varepsilon_{33}^{(h)}\left(X^\alpha\right) = \varepsilon_{33(0)}^{(h)}\left(X^\alpha\right) + X^3\, \varepsilon_{33(1)}^{(h)}\left(X^\alpha\right), \qquad (7.28)$$

where $\varepsilon_{33(0)}^{(h)}$ and $\varepsilon_{33(1)}^{(h)}$ are the variables associated with the plate middle surface. They are defined by

$$
\begin{aligned}
\varepsilon_{33(0)}^{(h)}\left(X^\alpha\right) &= \frac{\varepsilon_{33(u)}^{(h)}\left(X^\alpha\right) + \varepsilon_{33(l)}^{(h)}\left(X^\alpha\right)}{2}, \\
\varepsilon_{33(1)}^{(h)}\left(X^\alpha\right) &= \frac{\varepsilon_{33(u)}^{(h)}\left(X^\alpha\right) - \varepsilon_{33(l)}^{(h)}\left(X^\alpha\right)}{h} = \varepsilon_{33,X^3}^{(h)}\left(X^\alpha\right).
\end{aligned}
\qquad (7.29)
$$

By taking into account that $\varepsilon_{33}^{(h)}$ is linear over the thickness, it is clear from the second expression in (7.29) that $\varepsilon_{33(1)}^{(h)}$ is identical to the derivative of $\varepsilon_{33}^{(h)}$ with respect to X^3,

i.e., $\varepsilon_{33(1)}^{(h)} = \varepsilon_{33,X^3}^{(h)}$. Moreover, it follows from (7.28) and (7.29) that both $\varepsilon_{33(0)}^{(h)}$ and $\varepsilon_{33,X^3}^{(h)}$ should be constant through the thickness and should have non-zero values if $\varepsilon_{33}^{(h)}$ is to be linear across the plate thickness.

By using (7.28) and (7.29), and by assuming that the strain approximation functions exactly interpolate the nodal values, similarly as in (7.24), it is possible to express the nodal values of ε_{33} at the nodes $\mathbf{X}_{I(u)}$ and $\mathbf{X}_{I(l)}$ that belong to the node couple I as

$$\hat{\bar{\varepsilon}}_{33(u)}^I \approx \varepsilon_{33}^{(h)}\left(\mathbf{X}_{I(u)}\right) = \varepsilon_{33(0)}^I + \frac{h}{2}\varepsilon_{33(1)}^I, \quad \hat{\bar{\varepsilon}}_{33(l)}^I \approx \varepsilon_{33}^{(h)}\left(\mathbf{X}_{I(l)}\right) = \varepsilon_{33(0)}^I - \frac{h}{2}\varepsilon_{33(1)}^I, \quad (7.30)$$

where $\hat{\bar{\varepsilon}}_{33(u)}^I$ and $\hat{\bar{\varepsilon}}_{33(l)}^I$ are the new modified nodal values that are not kinematically compatible with the displacement field (7.6). The parameters $\varepsilon_{33(0)}^I = \varepsilon_{33(0)}^{(h)}\left(\mathbf{X}_{I(0)}\right)$ and $\varepsilon_{33(1)}^I = \varepsilon_{33(1)}^{(h)}\left(\mathbf{X}_{I(0)}\right) = \varepsilon_{33,X^3}^{(h)}\left(\mathbf{X}_{I(0)}\right)$ are computed at the point $\mathbf{X}_{I(0)} = \begin{bmatrix} X_I^1 & X_I^2 & 0 \end{bmatrix}^T$ located on the plate middle surface between the nodes of the Ith node couple, as shown in Figure 7.2. The constant term $\varepsilon_{33(0)}^I$ is calculated directly from the approximated displacements as in (7.27), leading to the following identity

$$\varepsilon_{33(0)}^I = u_{3,X^3}^{(h)}\left(\mathbf{X}_{I(0)}\right) = \hat{\bar{\varepsilon}}_{33(u)}^I = \hat{\bar{\varepsilon}}_{33(l)}^I. \quad (7.31)$$

In order to obtain the derivative $\varepsilon_{33(1)}^I = \varepsilon_{33,X^3}^{(h)}\left(\mathbf{X}_{I(0)}\right)$, the additional equilibrium equation in the middle surface normal direction is enforced at the mid-point $\mathbf{X}_{I(0)}$ as

$$\sigma_{3j,X^j}\left(\mathbf{X}_{I(0)}\right) + b_3\left(\mathbf{X}_{I(0)}\right) = 0. \quad (7.32)$$

Inserting the constitutive equations (2.29), (2.34) and (2.35) into (7.32), it follows that

$$\begin{aligned} \varepsilon_{33(1)}^I = \varepsilon_{33,X^3}^{(h)}\left(\mathbf{X}_{I(0)}\right) = \\ -\frac{1}{C_{3333}}\left[b_3 + C_{3311}\varepsilon_{11,X^3}^{(h)} + C_{3322}\varepsilon_{22,X^3}^{(h)} + C_{1313}2\varepsilon_{13,X^1}^{(h)} + C_{2323}2\varepsilon_{23,X^2}^{(h)}\right]_{\mathbf{X}=\mathbf{X}_{I(0)}} \end{aligned} \quad (7.33)$$

By means of the strain approximation (7.13), the derivatives of the strain components on the right-hand side of relation (7.33) may be written in their discretized forms as

$$\varepsilon_{11,X^3}^{(h)}\left(\mathbf{X}_{I(0)}\right)=\sum_{J=1}^{n_I}\left[\frac{1}{h}\phi^{JI}\ \hat{\varepsilon}_{11(u)}^{J}-\frac{1}{h}\phi^{JI}\ \hat{\varepsilon}_{11(l)}^{J}\right],$$

$$\varepsilon_{22,X^3}^{(h)}\left(\mathbf{X}_{I(0)}\right)=\sum_{J=1}^{n_I}\left[\frac{1}{h}\phi^{JI}\ \hat{\varepsilon}_{22(u)}^{J}-\frac{1}{h}\phi^{JI}\ \hat{\varepsilon}_{22(l)}^{J}\right],$$

$$\varepsilon_{13,X^1}^{(h)}\left(\mathbf{X}_{I(0)}\right)=\frac{1}{2}\sum_{J=1}^{n_I}\left[\phi_{,X^1}^{JI}\hat{\varepsilon}_{13(u)}^{J}+\phi_{,X^1}^{JI}\ \hat{\varepsilon}_{13(l)}^{J}\right],$$

$$\varepsilon_{23,X^2}^{(h)}\left(\mathbf{X}_{I(0)}\right)=\frac{1}{2}\sum_{J=1}^{n_I}\left[\phi_{,X^2}^{JI}\hat{\varepsilon}_{23(u)}^{J}+\phi_{,X^2}^{JI}\ \hat{\varepsilon}_{23(l)}^{J}\right] \tag{7.34}$$

with $\phi^{JI}=\phi^{J}\left(X_I^{\alpha}\right)$ and $\phi_{,X^{\alpha}}^{JI}=\phi_{,X^{\alpha}}^{J}\left(X_I^{\alpha}\right)$. After inserting (7.34) into (7.33), by neglecting the body forces, and by means of (7.31), the nodal values $\hat{\varepsilon}_{33(u)}^{I}$ and $\hat{\varepsilon}_{33(l)}^{I}$ are expressed in terms of the nodal strains as

$$\hat{\varepsilon}_{33(u)}^{I}=\hat{\varepsilon}_{33(u)}^{I}+\frac{h}{2}\sum_{J=1}^{n_I}\boldsymbol{\Psi}_{(0)}^{JI}\hat{\boldsymbol{\varepsilon}}^{J}\ ,\quad \hat{\varepsilon}_{33(l)}^{I}=\hat{\varepsilon}_{33(l)}^{I}-\frac{h}{2}\sum_{J=1}^{n_I}\boldsymbol{\Psi}_{(0)}^{JI}\hat{\boldsymbol{\varepsilon}}^{J}\ . \tag{7.35}$$

Herein the vector $\boldsymbol{\Psi}_{(0)}^{JI}$ is defined by

$$\boldsymbol{\Psi}_{(0)}^{JI}=-\frac{1}{C_{3333}}\left[\frac{1}{h}C_{3311}\phi^{JI}\quad \frac{1}{h}C_{3322}\phi^{JI}\quad 0\quad 0\quad \frac{1}{2}C_{2323}\phi_{,X^2}^{JI}\quad \frac{1}{2}C_{1313}\phi_{,X^1}^{JI}\quad \cdots\right.$$
$$\left.\cdots\quad -\frac{1}{h}C_{3311}\phi^{JI}\quad -\frac{1}{h}C_{3322}\phi^{JI}\quad 0\quad 0\quad \frac{1}{2}C_{2323}\phi_{,X^2}^{JI}\quad \frac{1}{2}C_{1313}\phi_{,X^1}^{JI}\right], \tag{7.36}$$

and the vector $\hat{\boldsymbol{\varepsilon}}^{J}$, defined as in (7.17), contains the nodal strains associated with the Jth node couple in the domain of definition Ω_{X^I} of the Ith node couple.

After employing (7.25) in relation (7.35) to evaluate $\hat{\varepsilon}_{33(u)}^{I}$ and $\hat{\varepsilon}_{33(l)}^{I}$, the modified nodal values $\hat{\varepsilon}_{33(u)}^{I}$ and $\hat{\varepsilon}_{33(l)}^{I}$ are expressed in dependence of the nodal displacements as

$$\hat{\varepsilon}_{33(u)}^{I}=\sum_{J=1}^{n_I}\mathbf{B}_{3(0)}^{JI}\hat{\mathbf{u}}^{J}+\frac{h}{2}\sum_{J=1}^{n_I}\left[\boldsymbol{\Psi}_{(0)}^{JI}\sum_{K=1}^{n_J}\mathbf{B}^{KJ}\hat{\mathbf{u}}^{K}\right],$$

$$\hat{\varepsilon}_{33(l)}^{I}=\sum_{J=1}^{n_I}\mathbf{B}_{3(0)}^{JI}\hat{\mathbf{u}}^{J}-\frac{h}{2}\sum_{J=1}^{n_I}\left[\boldsymbol{\Psi}_{(0)}^{JI}\sum_{K=1}^{n_J}\mathbf{B}^{KJ}\hat{\mathbf{u}}^{K}\right], \tag{7.37}$$

where $\mathbf{B}_{3(0)}^{JI}$ and $\mathbf{B}^{KJ}$ are calculated by using the 3-D strain-displacement matrix $\mathbf{B}^J$ from (7.26). $\mathbf{B}_{3(0)}^{JI}$ is the third row of the 3-D strain-displacement matrix calculated at the point $\mathbf{X}_{I(0)}$, and the matrix $\mathbf{B}^{KJ}$ is defined as $\left(\mathbf{B}^{KJ}\right)^T = \left[\left(\mathbf{B}_{(u)}^{KJ}\right)^T \quad \left(\mathbf{B}_{(l)}^{KJ}\right)^T\right]$ with $\mathbf{B}_{(u)}^{KJ} = \mathbf{B}^K\left(\mathbf{X}_{J(u)}\right)$ and $\mathbf{B}_{(l)}^{KJ} = \mathbf{B}^K\left(\mathbf{X}_{J(l)}\right)$. The nodal strain vector may now be rewritten into the following "classical" matrix strain-displacement form as

$$\hat{\tilde{\boldsymbol{\varepsilon}}}^I = \sum_{M=1}^{\tilde{n}_I} \tilde{\mathbf{B}}^{MI}\, \hat{\mathbf{u}}^M, \quad I = 1, 2, ..., N. \tag{7.38}$$

Herein $\hat{\tilde{\boldsymbol{\varepsilon}}}^I$ is defined according to relations (7.17) and (7.18), with $\hat{\tilde{\varepsilon}}_{33(u)}^I$ and $\hat{\tilde{\varepsilon}}_{33(l)}^I$ replacing compatible nodal values $\hat{\varepsilon}_{33(u)}^I$ and $\hat{\varepsilon}_{33(l)}^I$. $\tilde{n}_I$ stands for the total number of the node couples that influence the nodal strain values $\hat{\tilde{\varepsilon}}_{33(u)}^I$ and $\hat{\tilde{\varepsilon}}_{33(l)}^I$, and $\tilde{\mathbf{B}}^{MI}$ are the 3-D strain-displacement matrices calculated at $\mathbf{X}_{I(0)}$ using (7.26), except for the terms associated with ε_{33}, which are derived from the right-hand side of (7.37).

After inserting (7.38) into the discretized LWF of equilibrium equations (7.21) and (7.22), the following system of algebraic equations, which contains only the nodal displacements as unknown variables, is obtained for $\Omega_s^I, I = 1, 2, ..., N,$

$$\sum_{J=1}^{N_I}\left[-\int_{L_S^I} \mathbf{N}\,\mathbf{D}\boldsymbol{\Phi}_\varepsilon^J\mathrm{d}\Gamma - \int_{\Gamma_{Su}^I} \mathbf{N}\,\mathbf{D}\boldsymbol{\Phi}_\varepsilon^J\mathrm{d}\Gamma\right]\sum_{M=1}^{\tilde{n}_J} \tilde{\mathbf{B}}^{MJ}\,\hat{\mathbf{u}}^M + \alpha\sum_{J=1}^{n_I}\left(\int_{\Gamma_{su}^I} \boldsymbol{\Phi}_u^J\,\mathrm{d}\Gamma\right)\hat{\mathbf{u}}^J =$$
$$= \int_{L_{St}^I} \mathbf{t}\,\mathrm{d}\Gamma + \int_{\Omega_s^I} \mathbf{b}\,\mathrm{d}\Omega + \alpha\int_{\Gamma_{su}^I} \bar{\mathbf{u}}\,\mathrm{d}\Gamma, \tag{7.39}$$

$$\sum_{J=1}^{N_I}\left[\int_{\Omega_s^I} \nabla\mathbf{d}^T\,\mathbf{D}\boldsymbol{\Phi}_\varepsilon^J\mathrm{d}\Omega - \int_{L_S^I} X^3\mathbf{N}\,\mathbf{D}\boldsymbol{\Phi}_\varepsilon^J\,\mathrm{d}\Gamma - \int_{\Gamma_{Su}^I} X^3\mathbf{N}\,\mathbf{D}\boldsymbol{\Phi}_\varepsilon^J\mathrm{d}\Gamma\right]\sum_{M=1}^{\tilde{n}_J} \tilde{\mathbf{B}}^{MJ}\,\hat{\mathbf{u}}^M +$$
$$+\alpha\sum_{J=1}^{n_I}\left(\int_{\Gamma_{su}^I} X^3\,\boldsymbol{\Phi}_u^J\,\mathrm{d}\Gamma\right)\hat{\mathbf{u}}^J = \int_{L_{St}^I} X^3\,\mathbf{t}\,\mathrm{d}\Gamma + \int_{\Omega_s^I} X^3\,\mathbf{b}\,\mathrm{d}\Omega + \alpha\int_{\Gamma_{su}^I} X^3\,\bar{\mathbf{u}}\,\mathrm{d}\Gamma. \tag{7.40}$$

As already mentioned, the global system of equations is derived by using a node-by-node numerical procedure, without having to perform the global stiffness matrix assemblage as in FEM.

The applied mixed concept possesses some remarkable advantages in comparison to the primal MLPG method. The numerical integration of the derivatives of the MLS functions in (7.39) and (7.40) is avoided, which contributes significantly to the numerical efficiency and accuracy of the proposed mixed formulation. Moreover, the requirements for the continuity of trial functions are lower by one degree. It is also to note that thickness locking is eliminated without increasing the total number of equations in the global system of equations, in contrast to the hierarchical quadratic concept. Finally, as demonstrated by the numerical experiments shown in Sections 7.3.1 and 7.3.2, the mixed approach successfully alleviates the transversal shear locking effect even if the low-order MLS functions are used. However, the procedure for the elimination of the Poisson's thickness locking effect is complicated, especially in case of curved shells, and becomes impracticable if extended t geometrically non-linear problems.

7.2 Mixed MLPG formulation for the analysis of shell structures

7.2.1 Local weak form of the equilibrium equations

Similarly to the other formulations presented in this thesis, the local weak forms of the governing equations are derived according to the general instructions for the solid-shell concept given in Section 5.1.

The strong form of the governing equations are the 3-D equilibrium equations (2.42), whose solutions have to comply with the boundary conditions (5.1) and (5.2). The shell is mapped into the parametric space $\left(\xi^1, \xi^2, \xi^3\right)$, where its middle surface is transformed to the 2-D unit square in the ξ^1, ξ^2-plane, as explained in details in Section 2.1.1 and illustrated in Figure 7.3. Node couples are then generated uniformly over the upper and lower shell surfaces in the parametric space. The interpolations of all variables are performed in the parametric coordinates ξ^i by means of the MLS or IMLS functions, as described in Section 3.2.3. According to the local Petrov-Galerkin approach, the prismatic or cylindrical local sub-domain Ω_s^I is defined around the Ith node couple, as shown in Figure 7.3.
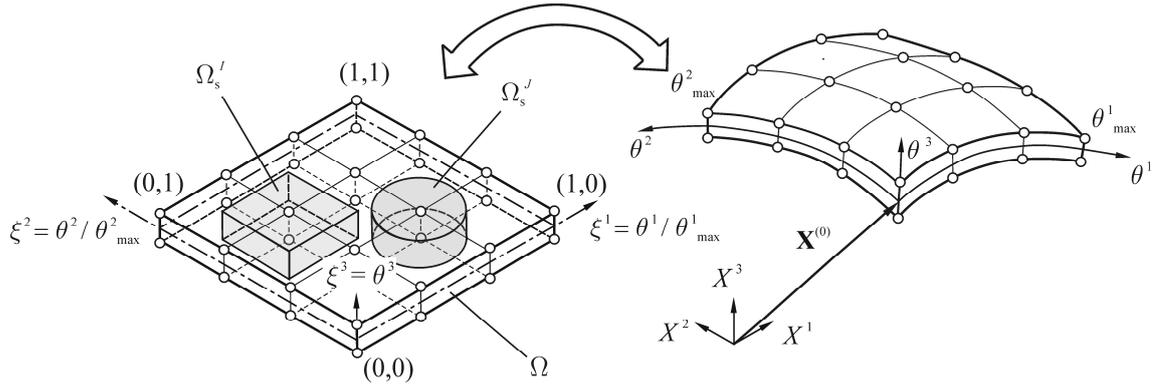
Figure 7.3 Parametric representation and discretization of shell geometry for mixed MLPG formulation

The local weak form (LWF) (5.12) of the equilibrium equations (2.42) is derived over Ω_s^I, $I = 1, 2, ..., N$, by following the procedure given in Section 5.2 as

$$
\int_{\Omega_s^I} v_{,X^j} \sigma_{kj} d\Omega - \int_{L_s^I} v n_j \sigma_{kj} d\Gamma - \int_{\Gamma_{su}^I} v n_j \sigma_{kj} d\Gamma + \alpha \int_{\Gamma_{su}^I} v u_k \, d\Gamma -
$$
$$
- \int_{\Omega_s^I} v b_k \, d\Omega - \int_{\Gamma_{st}^I} v \overline{t_k} d\Gamma - \alpha \int_{\Gamma_{su}^I} v \overline{u}_k \, d\Gamma = 0. \tag{7.41}
$$

where N is the total number of the node couples used for the discretization of the shell-like continuum. Here all tensor and vector components are defined in the Cartesian coordinates, i.e., $\boldsymbol{\sigma} = \sigma_{ij} \, \mathbf{e}_i \otimes \mathbf{e}_j$, $\mathbf{t} = t_i \, \mathbf{e}_i$, $\mathbf{n} = n_i \, \mathbf{e}_i$, $\mathbf{b} = b_i \, \mathbf{e}_i$ and $\mathbf{u} = u_i \, \mathbf{e}_i$. It is important to note that if the regularized function (3.24) is applied as the MLS weight function, the essential BC are imposed directly. For clarity reasons, the penalty terms are omitted in the following expressions in this section.

By employing the Heaviside function (5.15) in the ξ^1, ξ^2-plane and the linear functions according to (5.16) in the ξ^3 direction, the test function is defined according to expressions (5.13) and (5.14) as

$$
v\left(\xi^j\right) = \begin{cases} c_0 + c_1 \xi^3, & \xi^k \in \Omega_s^I \cup \partial\Omega_s^I \\ 0, & \xi^k \notin \Omega_s^I \cup \partial\Omega_s^I \end{cases} \tag{7.42}
$$

with c_0 and c_1 as arbitrary chosen real constants.

Applying (7.42) in (7.41), and using the derivation procedure described in Section 5.2.1, LWF may be transformed to the following form

$$
- \int_{L_s^I} n_j \sigma_{ij} d\Gamma - \int_{\Gamma_{su}^I} n_j \sigma_{ij} d\Gamma = \int_{\Gamma_{st}^I} \overline{t}_i d\Gamma + \int_{\Omega_s^I} b_i \, d\Omega, \tag{7.43}
$$

$$\int_{\Omega_s^I} \left(\xi^3\right)_{,X^j} \sigma_{ij} \, d\Omega - \int_{L_s^I} \xi^3 n_j \sigma_{ij} \, d\Gamma - \int_{\Gamma_{su}^I} \xi^3 n_j \sigma_{ij} \, d\Gamma = \int_{L_s^I} \xi^3 \, \overline{t_i} \, d\Gamma + \int_{\Omega_s^I} \xi^3 \, b_i \, d\Omega . \quad (7.44)$$

As explained in Section 5.1, integration is performed in the parametric coordinates, and the shell continuum kinematics is then mapped back to the global Cartesian coordinate system by means of the metric covariant vectors $\widehat{\mathbf{G}}_i$ defined by (2.18).

7.2.2 Elimination of locking effects

As mentioned before, in order to suppress the transversal shear locking phenomenon, strains should be approximated separately from displacements. As shown in Section 7.1.3, the Poisson's thickness locking effect nevertheless remains present. To avoid that locking effect, the transversal stress component σ^{33} is taken here as the independent variable instead of the transversal normal strain component ε_{33}. This switch of independent variables is performed by employing the well-known 3-D constitutive equations (2.29), written here in the parametric coordinate system as

$$\sigma^{ij} = C^{ijkl} \, \varepsilon_{kl} \quad (7.45)$$

with σ^{ij} and ε_{kl} as the components of the stress tensor $\boldsymbol{\sigma} = \sigma^{ij} \widehat{\mathbf{G}}_i \otimes \widehat{\mathbf{G}}_j$ and strain tensor $\boldsymbol{\varepsilon} = \varepsilon_{ij} \widehat{\mathbf{G}}^i \otimes \widehat{\mathbf{G}}^j$, respectively. C^{ijkl} are the components of the elasticity tensor for linear isotropic materials $\mathbf{C} = C^{ijkl} \widehat{\mathbf{G}}_i \otimes \widehat{\mathbf{G}}_j \otimes \widehat{\mathbf{G}}_k \otimes \widehat{\mathbf{G}}_l$, defined as in (2.33) and (2.34). The component ε_{33} is expressed from the equation for σ^{33} from the set (2.29) as

$$\varepsilon_{33} = \frac{-1}{C^{3333}} \left(C^{33\alpha\beta} \, \varepsilon_{\alpha\beta} + C^{33\alpha3} \, \varepsilon_{\alpha3} + C^{333\alpha} \, \varepsilon_{3\alpha} - \sigma^{33} \right). \quad (7.46)$$

After back-substituting (7.46) into (2.29), the stress tensor relation may be rewritten as

$$\sigma^{ij} = \left(C^{ij\alpha\beta} - C^{ij33} \frac{C^{33\alpha\beta}}{C^{3333}} \right) \varepsilon_{\alpha\beta} + \left(C^{ij\alpha3} - C^{ij33} \frac{C^{33\alpha3}}{C^{3333}} \right) \varepsilon_{\alpha3} +$$
$$+ \left(C^{ij3\alpha} - C^{ij33} \frac{C^{333\alpha}}{C^{3333}} \right) \varepsilon_{3\alpha} + \frac{C^{ij33}}{C^{3333}} \sigma^{33} . \quad (7.47)$$

Now the new set of independent field variables includes $u_i, \varepsilon_{\alpha\beta}, \varepsilon_{\alpha3}$ and σ^{33}. By approximating σ^{33} directly, it is possible to describe the zero distribution for σ^{33} in the

pure bending state, which is necessary for avoiding the Poisson's thickness locking effect, as discussed in Section 5.3.1. The linear distribution over the thickness for ε_{33} can be obtained subsequently from relation (7.46).

The matrix form of relation (7.47) is

$$\hat{\boldsymbol{\sigma}} = \tilde{\mathbf{C}} \boldsymbol{\omega}, \tag{7.48}$$

where $\hat{\boldsymbol{\sigma}}$ is the vector of the contravariant components of the stress tensor

$$\hat{\boldsymbol{\sigma}}^T = \begin{bmatrix} \sigma^{11} & \sigma^{22} & \sigma^{33} & \sigma^{12} & \sigma^{23} & \sigma^{13} \end{bmatrix}, \tag{7.49}$$

the vector $\boldsymbol{\omega}$ contains the independent strain and stress variables as

$$\boldsymbol{\omega}^T = \begin{bmatrix} \varepsilon_{11} & \varepsilon_{22} & 2\varepsilon_{12} & 2\varepsilon_{23} & 2\varepsilon_{13} & \sigma^{33} \end{bmatrix}, \tag{7.50}$$

and $\tilde{\mathbf{C}}$ denotes the modified material matrix that has the following form

$$\tilde{\mathbf{C}} = \begin{bmatrix} C^{1111} - \dfrac{C^{1133}C^{3311}}{C^{3333}} & C^{1122} - \dfrac{C^{1133}C^{3322}}{C^{3333}} & 0 & 0 & 0 & \dfrac{C^{1133}}{C^{3333}} \\ C^{2211} - \dfrac{C^{2233}C^{3311}}{C^{3333}} & C^{2222} - \dfrac{C^{2233}C^{3322}}{C^{3333}} & 0 & 0 & 0 & \dfrac{C^{2233}}{C^{3333}} \\ 0 & 0 & 0 & 0 & 0 & 1 \\ 0 & 0 & C^{1212} & 0 & 0 & 0 \\ 0 & 0 & 0 & C^{2323} & 0 & 0 \\ 0 & 0 & 0 & 0 & C^{1313} & 0 \end{bmatrix}. \tag{7.51}$$

Similarly to the mixed MLPG plate formulation, the linear distribution over the thickness is assumed for all displacement and in-plane strain components as

$$u_i^{(h)}\left(\xi^k\right) = \psi^1\left(\xi^3\right) u_{i(u)}^{(h)}\left(\xi^\gamma\right) + \psi^2\left(\xi^3\right) u_{i(l)}^{(h)}\left(\xi^\gamma\right), \tag{7.52}$$

$$\varepsilon_{\alpha\beta}^{(h)}\left(\xi^k\right) = \psi^1\left(\xi^3\right) \varepsilon_{\alpha\beta(u)}^{(h)}\left(\xi^\gamma\right) + \psi^2\left(\xi^3\right) \varepsilon_{\alpha\beta(l)}^{(h)}\left(\xi^\gamma\right). \tag{7.53}$$

Herein $\psi^1\left(\xi^3\right)$ and $\psi^2\left(\xi^3\right)$ are the linear functions defined according to (2.2), $u_{i(u)}^{(h)}$ and $u_{i(l)}^{(h)}$ are the displacement components on the upper and lower shell surface, respectively, while $\varepsilon_{\alpha\beta(u)}\left(\xi^\gamma\right)$ and $\varepsilon_{\alpha\beta(l)}\left(\xi^\gamma\right)$ denote the corresponding strain

components. It is further assumed that the transversal shear strain and transversal normal stress components are constant over the thickness

$$\varepsilon_{\alpha 3}^{(h)}\left(\xi^k\right)=\varepsilon_{\alpha 3}^{(h)}\left(\xi^\gamma\right),\tag{7.54}$$

$$\sigma^{33(h)}\left(\xi^k\right)=\sigma^{33(h)}\left(\xi^\gamma\right).\tag{7.55}$$

In relations (7.52)-(7.55), the displacement components are written in the directions of the global Cartesian coordinates, $\mathbf{u}=u_i\,\mathbf{e}_i$, while the strain and stress tensor components are expressed in the parametric space, i.e., $\boldsymbol{\varepsilon}=\varepsilon_{ij}\widehat{\mathbf{G}}^i\otimes\widehat{\mathbf{G}}^j$ and $\boldsymbol{\sigma}=\sigma^{ij}\widehat{\mathbf{G}}_i\otimes\widehat{\mathbf{G}}_j$. It is obvious that 15 variables, including $u_{i(u)}^{(h)}$, $u_{i(l)}^{(h)}$, $\varepsilon_{\alpha\beta(u)}$, $\varepsilon_{\alpha\beta(l)}$, $\varepsilon_{\alpha 3}^{(h)}$ and $\sigma^{33(h)}$, have be approximated separately to describe the deformation response of the shell. On the other hand, LWF (7.43) and (7.44) yield only six equations per each Ω_s^I, and therefore, additional equations are needed to obtain the closed global system of equations.

7.2.3 Additional kinematic constraints

In order to close the system of equations on the global level, the additional 3-D kinematical constraints for $\varepsilon_{\alpha 3}$ and σ^{33}, written here in generalized weak forms, are imposed for each $\Omega_s^I, I=1,2,...,N$, as

$$\begin{aligned}
&\int_{\Omega_s^I} v_{(\varepsilon\alpha\beta)}\left(\varepsilon_{\alpha\beta}^{(h)}-\varepsilon_{\alpha\beta}^{(c)}\right)\mathrm{d}\Omega=0,\\
&\int_{\Omega_s^I} v_{(\varepsilon\alpha 3)}\left(\varepsilon_{\alpha 3}^{(h)}-\varepsilon_{\alpha 3}^{(c)}\right)\mathrm{d}\Omega=0,\\
&\int_{\Omega_s^I} v_{(\sigma 33)}\left(\sigma^{33(h)}-\sigma^{33(c)}\right)\mathrm{d}\Omega=0.
\end{aligned}\tag{7.56}$$

Herein $\varepsilon_{\alpha\beta}^{(c)}$, $\varepsilon_{\alpha 3}^{(c)}$ and $\sigma^{33(c)}$ stand for the values to be calculated from approximated displacements (7.52), while $v_{(\varepsilon\alpha\beta)}$, $v_{(\varepsilon\alpha 3)}$ and $v_{(\sigma 33)}$ are some kinematically admissible test functions. The test functions have to be chosen in a way which should result in additional nine equations for each Ω_s^I needed for closing the system of equations.

In order to avoid numerical integration, the additional kinematics constraints (7.56) are imposed by means of the collocations at the points presented in Figure 7.4.
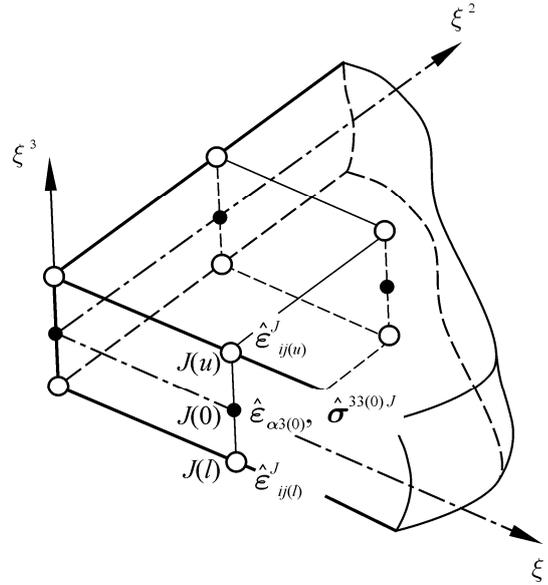
Figure 7.4 Collocation points for mixed MLPG formulation for curved shell structures

For the in-plane strain components $\varepsilon_{\alpha\beta}$ the collocation is performed at the upper nodes $J(u)$ and the lower nodes $J(l)$ with the coordinates $\mathbf{X}_{J(u)} = \mathbf{X}\left(\xi^k_{J(u)}\right)$ and $\mathbf{X}_{J(u)} = \mathbf{X}\left(\xi^k_{J(l)}\right)$, respectively. Herein $\xi^k_{J(u)} = \left(\xi^1_J, \xi^2_J, 0,5h\right)$ and $\xi^k_{J(l)} = \left(\xi^1_J, \xi^2_J, -0,5h\right)$ are the parametric coordinates of the nodes. Using the Dirac delta functions $\delta\left(\mathbf{X} - \mathbf{X}_{J(u)}\right)$ and $\delta\left(\mathbf{X} - \mathbf{X}_{J(l)}\right)$ successively as the test functions $v_{(\varepsilon\alpha\beta)}$ in the first relation in (7.56), the following conditions for the in-plane strain components are enforced at the nodal points

$$\varepsilon^{(h)}_{\alpha\beta}\left(\xi^k_{J(u)}\right) = \varepsilon^{(c)}_{\alpha\beta}\left(\xi^k_{J(u)}\right), \quad \varepsilon^{(h)}_{\alpha\beta}\left(\xi^k_{J(l)}\right) = \varepsilon^{(c)}_{\alpha\beta}\left(\xi^k_{J(l)}\right). \qquad (7.57)$$

In the second and third relations in (7.56), the collocation is performed at the points $\mathbf{X}^k_{J(0)} = \mathbf{X}\left(\xi^1_J, \xi^2_J, 0\right)$, positioned on the middle surface right between the nodes of the Jth node couple, as presented in Figure 7.3. Applying the Dirac test function $\delta\left(\mathbf{X}^k - \mathbf{X}^k_{J(0)}\right)$, the following expressions hold for the transversal shear strain and the transversal normal stress components

$$\varepsilon^{(h)}_{\alpha3}\left(\xi^k_{J(0)}\right) = \varepsilon^{(c)}_{\alpha3}\left(\xi^k_{J(0)}\right), \quad \sigma^{33(h)}\left(\xi^k_{J(0)}\right) = \sigma^{33(c)}\left(\xi^k_{J(0)}\right). \qquad (7.58)$$

Equations (7.57) and (7.58), together with LWF (7.43)-(7.44), yield the closed global system of equations.

7.2.4 Discretization of the equations

The approximation of all unknown variables in (7.52)-(7.55) is performed by using the same MLS or IMLS functions

$$u_{i(u)}^{(h)}\left(\xi^{\gamma}\right)=\sum_{J=1}^{n}\phi^{J}\left(\xi^{\gamma}\right)\hat{u}_{i(u)}^{J}, \qquad u_{i(l)}^{(h)}\left(\xi^{\gamma}\right)=\sum_{J=1}^{n}\phi^{J}\left(\xi^{\gamma}\right)\hat{u}_{i(l)}^{J},$$

$$\varepsilon_{\alpha\beta(u)}^{(h)}\left(\xi^{\gamma}\right)=\sum_{J=1}^{n}\phi^{J}\left(\xi^{\gamma}\right)\hat{\varepsilon}_{\alpha\beta(u)}^{J}, \quad \varepsilon_{\alpha\beta(l)}^{(h)}\left(\xi^{\gamma}\right)=\sum_{J=1}^{n}\phi^{J}\left(\xi^{\gamma}\right)\hat{\varepsilon}_{\alpha\beta(l)}^{J}, \qquad (7.59)$$

$$\varepsilon_{\alpha3}^{(h)}\left(\xi^{\gamma}\right)=\sum_{J=1}^{n}\phi^{J}\left(\xi^{\gamma}\right)\hat{\varepsilon}_{\alpha3(0)}^{J}, \qquad \sigma^{33(h)}\left(\xi^{\gamma}\right)=\sum_{J=1}^{n}\phi^{J}\left(\xi^{\gamma}\right)\hat{\sigma}_{(0)}^{33J}.$$

Herein $\phi^{J}\left(\xi^{\gamma}\right)$ is the in-plane shape function associated with the Jth node couple inside the domain of definition $\Omega_{\xi^{\gamma}}$ of the current point ξ^{γ}. n stands for the total number of node couples inside $\Omega_{\xi^{\gamma}}$. $\hat{u}_{i(u)}^{J}$ and $\hat{\varepsilon}_{\alpha\beta(u)}^{J}$ are the nodal values on the upper surface, $\hat{u}_{i(l)}^{J}$ and $\hat{\varepsilon}_{\alpha\beta(l)}^{J}$ are associated with the lower surface, while $\hat{\varepsilon}_{\alpha3(0)}^{J}$ and $\hat{\sigma}_{(0)}^{33J}$ refer to the middle surface.

The nodal shape function $\phi^{J}\left(\xi^{\gamma}\right)$ is calculated in the parametric $\xi^{1}\xi^{2}$-plane by employing either the 4th-order spline from (3.20) or the regularized weight function (3.24), according to the procedures given in Section 3. An articulate description of the approximation scheme that employs the IMLS functions is also available in [149].

After employing the approximations (7.59) in (7.52), the approximated displacement vector may be written in the following matrix form as

$$\mathbf{u}=\sum_{J=1}^{n}\mathbf{\Phi}_{u}^{J}\left(\xi^{i}\right)\hat{\mathbf{u}}^{J}. \qquad (7.60)$$

Herein the shape function matrix $\mathbf{\Phi}_{J}^{u}\left(\xi^{i}\right)$ is given by

$$\mathbf{\Phi}_{u}^{J}\left(\xi^{i}\right)=\phi_{J}\left(\xi^{\delta}\right)\left[\psi^{1}\left(\xi^{3}\right)\mathbf{I}_{3} \quad \psi^{2}\left(\xi^{3}\right)\mathbf{I}_{3}\right] \qquad (7.61)$$

with $\mathbf{I}_{3}$ as the identity matrix of third order. The vector of the unknown displacements $\hat{\mathbf{u}}^{J}$ is

$$\hat{\mathbf{u}}_{J}^{T}=\left[\hat{u}_{1(u)}^{J} \quad \hat{u}_{2(u)}^{J} \quad \hat{u}_{3(u)}^{J} \quad \hat{u}_{1(l)}^{J} \quad \hat{u}_{2(l)}^{J} \quad \hat{u}_{3(l)}^{J}\right], \qquad (7.62)$$

where $\hat{u}_{i(u)}^J$ and $\hat{u}_{i(l)}^J$ are the nodal displacement components in the directions of the global Cartesian coordinates at the upper and lower surface, respectively. The vector $\boldsymbol{\omega}$ from (7.50) may be written in the similar discretized form as

$$\boldsymbol{\omega}\left(\xi^i\right) = \sum_{J=1}^n \boldsymbol{\Phi}_\omega^J\left(\xi^i\right)\hat{\boldsymbol{\omega}}^J \tag{7.63}$$

with $\boldsymbol{\Phi}_\omega^J\left(\xi^i\right)$ as the matrix of the 3-D shape functions

$$\boldsymbol{\Phi}_\omega^J\left(\xi^i\right) = \phi^J\left(\xi^\delta\right)\begin{bmatrix} \psi^1\left(\xi^3\right)\mathbf{I}_3 & \psi^2\left(\xi^3\right)\mathbf{I}_3 & \mathbf{0} \\ \mathbf{0} & \mathbf{0} & \mathbf{I}_3 \end{bmatrix}, \tag{7.64}$$

The vector $\hat{\boldsymbol{\omega}}^J$ contains the nodal unknown strain and stress variables

$$\hat{\boldsymbol{\omega}}^J = \begin{bmatrix} \hat{\varepsilon}_{11(u)}^J & \hat{\varepsilon}_{22(u)}^J & 2\hat{\varepsilon}_{12(u)}^J & \hat{\varepsilon}_{11(l)}^J & \hat{\varepsilon}_{22(l)}^J & 2\hat{\varepsilon}_{12(l)}^J & 2\hat{\varepsilon}_{23(0)}^J & 2\hat{\varepsilon}_{13(0)}^J & \hat{\sigma}_{(0)}^{33J} \end{bmatrix}^T. \tag{7.65}$$

Inserting the expression for $\boldsymbol{\omega}$ from (7.63) into equation (7.48) gives the approximation of the stress vector $\hat{\boldsymbol{\sigma}}$ from (7.49), which contains the components σ^{ij} defined in curvilinear coordinate system as

$$\hat{\boldsymbol{\sigma}} = \tilde{\mathbf{C}}\sum_{J=1}^n \boldsymbol{\Phi}_\omega^J\hat{\boldsymbol{\omega}}^J. \tag{7.66}$$

However, since LWF of the equilibrium equations (7.43) and (7.44) is written in the global Cartesian system, the stress vector (7.66) should be transformed from the convective to the global Cartesian coordinate system according to the transformation rule (2.17), written here in the matrix form as

$$\boldsymbol{\sigma} = \mathbf{T}^\sigma\,\hat{\boldsymbol{\sigma}} = \mathbf{T}^\sigma\tilde{\mathbf{C}}\sum_{J=1}^n \boldsymbol{\Phi}_\omega^J\hat{\boldsymbol{\omega}}^J. \tag{7.67}$$

Herein $\mathbf{T}^\sigma$ is the transformation matrix

$$
\mathbf{T}^{\sigma} = \begin{bmatrix}
J_{11}{}^{2} & J_{12}{}^{2} & J_{13}{}^{2} & 2J_{11}J_{12} & 2J_{12}J_{13} & 2J_{11}J_{13} \\
J_{21}{}^{2} & J_{22}{}^{2} & J_{23}{}^{2} & 2J_{21}J_{22} & 2J_{22}J_{23} & 2J_{21}J_{23} \\
J_{31}{}^{2} & J_{32}{}^{2} & J_{33}{}^{2} & 2J_{31}J_{32} & 2J_{32}J_{33} & 2J_{31}J_{33} \\
J_{11}J_{21} & J_{12}J_{22} & J_{13}J_{23} & J_{11}J_{22}+J_{12}J_{21} & J_{12}J_{23}+J_{13}J_{22} & J_{11}J_{23}+J_{13}J_{21} \\
J_{21}J_{31} & J_{22}J_{32} & J_{23}J_{33} & J_{21}J_{32}+J_{22}J_{31} & J_{22}J_{33}+J_{23}J_{32} & J_{21}J_{33}+J_{23}J_{31} \\
J_{11}J_{31} & J_{12}J_{32} & J_{13}J_{33} & J_{11}J_{32}+J_{12}J_{31} & J_{12}J_{33}+J_{13}J_{32} & J_{11}J_{33}+J_{13}J_{31}
\end{bmatrix}, \quad (7.68)
$$

with $J_{ij} = \mathbf{e}_i \cdot \widehat{\mathbf{G}}_j$ as the elements of the Jacobian matrix defined as in (2.14). The vector $\boldsymbol{\sigma}$ is defined analogously to (2.31) and contains the components of the stress tensor defined in the global Cartesian system, i.e., $\boldsymbol{\sigma} = \sigma^{ij}\mathbf{e}_i \otimes \mathbf{e}_j$.

Substituting $\boldsymbol{\sigma}$ from (7.67) into LWF (7.43) and (7.44), the discretized equilibrium equations for the local sub-domain Ω_s^I surrounding the Ith node couple are obtained, and are written in the matrix form as

$$
\sum_{J=1}^{N_I}\left[-\int_{L_s^I}\mathbf{N}\mathbf{T}^{\sigma}\tilde{\mathbf{C}}\boldsymbol{\Phi}_J^{\omega}\,\mathrm{d}\Gamma - \int_{\Gamma_{su}^I}\mathbf{N}\mathbf{T}^{\sigma}\tilde{\mathbf{C}}\boldsymbol{\Phi}_J^{\omega}\mathrm{d}\Gamma \right]\hat{\boldsymbol{\omega}}_J = \int_{L_{st}^I}\overline{\mathbf{t}}\,\mathrm{d}\Gamma + \int_{\Omega_s^I}\mathbf{b}\,\mathrm{d}\Omega \qquad (7.69)
$$

$$
\sum_{J=1}^{N_I}\left[\int_{\Omega_s^I}(\nabla\mathbf{d})^{T}\mathbf{T}^{\sigma}\tilde{\mathbf{C}}\boldsymbol{\Phi}_J^{\omega}\,\mathrm{d}\Omega - \int_{L_s^I}\xi^3\mathbf{N}\mathbf{T}^{\sigma}\,\tilde{\mathbf{C}}\boldsymbol{\Phi}_J^{\omega}\,\mathrm{d}\Gamma - \int_{\Gamma_{su}^I}\xi^3\mathbf{N}\mathbf{T}^{\sigma}\tilde{\mathbf{C}}\boldsymbol{\Phi}_J^{\omega}\mathrm{d}\Gamma \right]\hat{\boldsymbol{\omega}}_J =
$$

$$
= \int_{L_{st}^I}\xi^3\,\overline{\mathbf{t}}\,\mathrm{d}\Gamma + \int_{\Omega_s^I}\xi^3\,\mathbf{b}\,\mathrm{d}\Omega, \qquad (7.70)
$$

where $\mathbf{N}$ as the matrix of the components of the outward unit normal vector $\mathbf{n} = n_i\,\mathbf{e}_i$ to $\partial\Omega_s^I$, as defined in (2.40), and $(\nabla\mathbf{d})^{T}$ expressed as

$$
(\nabla\mathbf{d})^{T} = \begin{bmatrix}
\xi^3_{,X^1} & 0 & 0 & \xi^3_{,X^2} & 0 & \xi^3_{,X^3} \\
0 & \xi^3_{,X^2} & 0 & \xi^3_{,X^1} & \xi^3_{,X^3} & 0 \\
0 & 0 & \xi^3_{,X^3} & 0 & \xi^3_{,X^2} & \xi^3_{,X^1}
\end{bmatrix}. \qquad (7.71)
$$

N_I denotes the total number of the node couples inside the domain of influence Ω_{X_I} associated with the Ith node couple, as explained in Chapter 4.1

The additional relations (7.57) and (7.58) are discretized under the assumption that the applied approximation functions for the strain and stress components interpolate the nodal values exactly, i.e.,

$$\varepsilon_{\alpha\beta}^{(h)}\left(\xi_{J(u)}^k\right) \approx \hat{\varepsilon}_{\alpha\beta(u)}^J = \varepsilon_{\alpha\beta}^{(c)}\left(\xi_{J(u)}^k\right), \qquad \varepsilon_{\alpha\beta}^{(h)}\left(\xi_{J(l)}^k\right) \approx \hat{\varepsilon}_{\alpha\beta(l)}^J = \varepsilon_{\alpha\beta}^{(c)}\left(\xi_{J(l)}^k\right),$$

$$\varepsilon_{\alpha3}^{(h)}\left(\xi_{J(0)}^k\right) \approx \hat{\varepsilon}_{\alpha3(0)}^J = \varepsilon_{\alpha3}^{(c)}\left(\xi_{J(0)}^k\right), \qquad \sigma^{33(h)}\left(\xi_{J(0)}^k\right) \approx \hat{\sigma}_{(0)}^{33J} = \sigma^{33(c)}\left(\xi_{J(0)}^k\right).$$

(7.72)

For facilitation, the variables associated with the shell middle surface on the right-hand sides in (7.72) are expressed by the values computed on the upper and lower surfaces using the relations

$$\varepsilon_{\alpha3}^{(c)}\left(\xi_{J(0)}^k\right) = \frac{\varepsilon_{\alpha3}^{(c)}\left(\xi_{J(u)}^k\right) + \varepsilon_{\alpha3}^{(c)}\left(\xi_{J(l)}^k\right)}{2},$$

$$\sigma^{33(c)}\left(\xi_{J(0)}^k\right) = \frac{\sigma^{33(c)}\left(\xi_{J(u)}^k\right) + \sigma^{33(c)}\left(\xi_{J(l)}^k\right)}{2}.$$

(7.73)

The strain values $\varepsilon_{\alpha\beta}^{(c)}$ and $\varepsilon_{\alpha3}^{(c)}$ in (7.72) and (7.73) are computed from the displacement components by means of the 3-D kinematics relation (2.23) as

$$\varepsilon_{ij}^{(c)} = \frac{1}{2}\left(\hat{\mathbf{G}}_i \cdot \mathbf{u}_{,\xi^j}^{(h)} + \hat{\mathbf{G}}_j \cdot \mathbf{u}_{,\xi^i}^{(h)}\right)$$

(7.74)

where $\mathbf{u}^{(h)}$ denotes the approximated displacement vector from (7.60). $\sigma^{33(c)}$ is evaluated in terms of $\hat{\mathbf{u}}^J$ by using the standard constitutive relation from (2.29)

$$\sigma^{33(c)} = C^{33kl}\varepsilon_{kl}^{(c)}.$$

(7.75)

Herein C^{33kl} are the components of the material tensor obtained from (2.33) and (2.34), and $\varepsilon_{kl}^{(c)}$ are the compatible strain components computed by (7.74) .

Finally, the vector $\hat{\boldsymbol{\omega}}_J$ from (7.63) may be expressed in terms of the nodal displacement components by applying (7.72)-(7.75) as

$$\hat{\boldsymbol{\omega}}^J = \sum_{K=1}^{\tilde{n}_J} \tilde{\mathbf{B}}^{KJ}\hat{\mathbf{u}}^K,$$

(7.76)

where the matrix $\tilde{\mathbf{B}}^{KJ}$ contains the derivatives of the displacement 3-D shape functions from $\boldsymbol{\Phi}_J^u\left(\xi^i\right)$, which is given by (7.61). The matrix $\tilde{\mathbf{B}}^{KJ}$ is analogous to the standard 3-D strain-displacement matrix. $\tilde{n}_J$ denotes the number of the nodes influencing the

IMLS approximation at the position of the node couple J, i.e., it is the total number of the nodes positioned inside the domain of definition associated with the node couple J.

After inserting equation (7.76) into discretized LWF (7.69) and (7.70), the following discretized equations are obtained for each local sub-domain Ω_s^I

$$\sum_{J=1}^{N_I}\left[\int_{L_S^I}-\mathbf{N}\,\mathbf{T}^\sigma\tilde{\mathbf{C}}\,\mathbf{\Phi}_J^\omega\,\mathrm{d}\Gamma-\int_{\Gamma_{Su}^I}\mathbf{N}\,\mathbf{T}^\sigma\tilde{\mathbf{C}}\,\mathbf{\Phi}_J^\omega\mathrm{d}\Gamma\right]\sum_{K=1}^{\tilde{n}_J}\tilde{\mathbf{B}}^{KJ}\hat{\mathbf{u}}^K=\int_{L_{St}^I}\overline{\mathbf{t}}\,\mathrm{d}\Gamma+\int_{\Omega_s^I}\mathbf{b}\,\mathrm{d}\Omega,\qquad(7.77)$$

$$\sum_{J=1}^{N_I}\left[\int_{\Omega_s^I}\nabla\mathbf{d}^T\mathbf{T}^\sigma\tilde{\mathbf{C}}\,\mathbf{\Phi}_J^\omega\mathrm{d}\Omega-\int_{L_S^I}\xi^3\mathbf{N}\,\mathbf{T}^\sigma\tilde{\mathbf{C}}\,\mathbf{\Phi}_J^\varepsilon\,\mathrm{d}\Gamma-\int_{\Gamma_{Su}^I}\xi^3\mathbf{N}\,\mathbf{T}^\sigma\,\tilde{\mathbf{C}}\,\mathbf{\Phi}_J^\omega\mathrm{d}\Gamma\right]\sum_{K=1}^{\tilde{n}_J}\tilde{\mathbf{B}}^{KJ}\hat{\mathbf{u}}^K=$$

$$=\int_{L_{St}^I}\xi^3\,\overline{\mathbf{t}}\,\mathrm{d}\Gamma+\int_{\Omega_s^I}\xi^3\,\mathbf{b}\,\mathrm{d}\Omega.\qquad(7.78)$$

Obviously, only the nodal displacements appear as the unknown variables in the above equations. If the non-interpolating MLS functions are used for the approximation of displacements, then the penalty terms have to be added to enforce the essential BC, as in the mixed formulation for plate structures presented in Section 7.1. All terms containing the body force vector $\mathbf{b}$ may again be omitted. The closed global system of equations on the structural level is derived by using the well-known point-by-point numerical procedure.

7.2.5 Estimate of the computational costs

From the presented formulation, it is clear that, in contrast to the primal MLPG formulations considered in Chapter 6, the differentiation of the MLS interpolation functions at each integration point in a local sub-domain is avoided. Therefore, less quadrature points are required to perform the integration accurately in comparison to the purely displacement approach, and consequently, the computational costs associated with the numerical integration are reduced. At the same time, the costs needed for the evaluation of the nodal strains and stresses are minimal due to the collocation procedures applied only at the nodes. In addition, the size of the support domains of trial functions does not influence the solution accuracy so significantly, as demonstrated in [148]. However, some additional computational effort is necessary for the elimination of the nodal stress/strain values from the discretized system of equations (7.77) and (7.78) by employing (7.76). A rough estimate of the computational costs for the mixed

formulation in comparison with the primal MLPG approach from Section 6.4 is given here.

The concept for the computational costs assessment together with the notations of variables has been taken from [150]. Accordingly, the $\boldsymbol{O}$-notation to imply the upper bound of the given functions is adopted. In addition, the variables associated with the primal and mixed formulation are denoted by superscripts d and m, respectively. Here, only the costs of forming the global stiffness matrix and of solving the global system of equations are taken into account. All other additional costs, such as the costs associated with the computational implementation, are neglected.

7.2.5.1 Primal MLPG formulation

The computation time needed for the assembling of the global stiffness matrix in the primal MLPG method with $d\,N$ non-zero rows and $d\,M$ non-zero columns per row is estimated according to the procedures given in [150] as

$$T_K^d = \boldsymbol{O}(d\,N^d d\,M^d\,T_e^d)\,,\qquad\qquad(7.79)$$

where N^d is the total number of node couples used for discretization, and M^d stands for the average number of nodes influencing the interpolation in each local sub-domain. The number of degrees of freedom (DOF) per node is denoted by d, i.e. $d = 7$. The variable T_e^d represents the computational time required for the calculation of a single term in the stiffness matrix, which may be assessed as

$$T_e^d = \boldsymbol{O}\left(n_g^d\,K\,T_h\right).\qquad\qquad(7.80)$$

Herein, n_g^d is the number of Gaussian points per local sub-domain and T_h represents the computational time needed for the evaluation of the MLS shape function in an integration point. For the purpose of comparison with the mixed approach, factor $K > 1$ is introduced to take into account additional costs required for the calculation of derivatives of the MLS shape functions at a given point. The variable T_h may be expressed as

$$T_h = \boldsymbol{O}\left(\left(m^d\right)^2 M^d t_w\right)\qquad\qquad(7.81)$$

with m^d being the number of monomial terms in the MLS basis vector **p**, while t_w is the computational time needed for the calculation of the MLS weight function at a given evaluation point. Accordingly, the computational time for the global stiffness matrix in the primal MLPG method may be estimated as

$$T_K^d = \boldsymbol{O}\left(49 N^d \left(M^d\right)^2 n_g^d \left(m^d\right)^2 K t_w\right). \tag{7.82}$$

7.2.5.2   Mixed MLPG formulation

The overall computational cost of assembling the global stiffness matrix of the proposed mixed MLPG formulation can be broken into three major parts as

$$T_K^m = T_{K\varepsilon} + T_\omega + T_{mlt}. \tag{7.83}$$

Herein $T_{K\varepsilon}$ is the computational cost of the non-zero terms for which integration has to be performed in the discretized LWF of the equilibrium equations (7.43)-(7.44) and T_ω is the cost of evaluating the nodal stress and strain values in $\hat{\boldsymbol{\omega}}^J$ from (7.76). The variable T_{mlt} stands for the cost of the matrix multiplication needed for replacing the nodal strain and stress values by the nodal displacement components, as shown in (7.77) and (7.78).

Analogously to T_K^d in (7.79), $T_{K\varepsilon}$ may be estimated as

$$T_{K\varepsilon} = \boldsymbol{O}(k \, N^m \, l \, M^m \, T_e^m), \tag{7.84}$$

where $k = 6$ stands for the number of equations per node couple and $l = 9$ is the number of independent stress and strain variables per node couple. Since there is no need to calculate the derivatives of the shape functions in each Gaussian point, the computation cost of a single non-zero term in LWF (7.43)-(7.44) can be estimated as

$$T_e^m = \boldsymbol{O}(n_g^m T_h) = \boldsymbol{O}\left(n_g^m \left(m^m\right)^2 M^m t_w\right). \tag{7.85}$$

By means of (7.85), $T_{K\varepsilon}$ may be modelled as

$$T_{K\varepsilon} = \boldsymbol{O}\left(54 N^m \left(M^m\right)^2 n_g^m \left(m^m\right)^2 t_w\right). \tag{7.86}$$

The cost of forming relation (7.76) may be assessed by taking into account that it is sufficient to compute the nodal stress or strain values from the displacements for each node in the discretization scheme just once during calculations. Therefore, T_ω may be expressed as

$$T_\omega = O(N^m \, l \, k \, M^m \, K \, T_h) = O\left(54 N^m \left(M^m\right)^2 \left(m^m\right)^2 K \, t_w\right).$$ (7.87)

Here, it is assumed that $\tilde{\mathbf{B}}^{KJ}$ in (7.76) contains only non-zero terms, and that $n_J \sim M$. Furthermore, the computational costs for the derivatives of the MLS shape functions at a node are included by employing the factor K, similarly as in (7.80).

By inspection of dimensions of matrices in (7.77) and (7.78), it may be concluded that the overall cost of the matrix multiplication required for the elimination of $\hat{\boldsymbol{\omega}}^J$ from the equation system may be assessed as

$$T_{mlt} = O\left(324 N^m \left(M^m\right)^2\right).$$ (7.88)

By means of (7.86)-(7.88) and after some modification of (7.83), the computational cost of assembling the stiffness matrix for the mixed MLPG formulation may be estimated as

$$T_K^m = T_{K\varepsilon}\left(1 + \frac{T_\omega}{T_{K\varepsilon}} + \frac{T_{mlt}}{T_{K\varepsilon}}\right) \approx T_{K\varepsilon}\left(1 + O\left(\frac{K}{n_g^m}\right) + O\left(\frac{6}{n_g^m \left(m^m\right)^2 t_w}\right)\right).$$ (7.89)

By analyzing this equation, it can be concluded that T_K^m is strongly governed by $T_{K\varepsilon}$ because the influence of T_ω and T_{mlt} on the overall computational cost is at least one order of the magnitude lower than that of $T_{K\varepsilon}$. Therefore, it is safe to write that

$$T_K^m = C \, T_{K\varepsilon}, \quad 1 < C < 2.$$ (7.90)

To compare the computational time estimations expressed by (7.82) and (7.90), it can be written that

$$\frac{T_K^d}{T_K^m} \approx \frac{T_K^d}{C\,T_{K\varepsilon}} \approx \boldsymbol{O}\left(\frac{49K\,N^d\left(M^d\right)^2 n_g^d\left(m^d\right)^2 t_w}{54\,C\,N^m\left(M^m\right)^2 n_g^m\left(m^m\right)^2 t_w} \right). \tag{7.91}$$

As evident from (7.91), the values of T_K^d and T_K^m might be comparable in magnitude in the case when $N^d = N^m$, $M^d = M^m$, $n_g^d = n_g^m$ and $m^d = m^m$, as it was confirmed by the numerical experiments. However, it has been noticed in [148] that $n_g^d > n_g^m$ in order to achieve the same order of accuracy in numerical integration. Furthermore, as evident from the presented numerical examples, in the cases involving the appearance of shear and membrane locking effects, the MLS functions of lower order may be used in the mixed MLPG formulation, and consequently $m^d > m^m$ and $M^d > M^m$. Moreover, $N^d > N^m$ is usually needed in order to obtain the same order of accuracy. Therefore, it may be concluded that $T_K^d \gg T_K^m$. The numerical experiments have shown that T_K^m is about one order of magnitude lower than T_K^d. Accordingly, it may be estimated that the mixed MLPG formulation is computationally more efficient than the fully displacement approach.

7.2.5.3   Costs of solving the global algebraic system of equations

Generally, the MLPG method produces the global systems of equations with the unsymmetrical coefficient matrices, solving of which is computationally expensive. In the most general case, the cost of solving such systems could be estimated as $T_S = \boldsymbol{O}\left(N^3\right)$. Herein, T_S is the solution time and N stands for the number of the node couples used for discretization. However, since the equation system matrices are sparse and banded the solution costs may be reduced to $\boldsymbol{O}(N)$ by applying appropriate solvers supporting a sparse matrix storage format [151]. As mentioned above, $m^d > m^m$ and $N^d > N^m$ is needed for obtaining the same level of accuracy in both the primal and mixed formulations. It results in $T_S^d > T_S^m$, which further contributes to increasing the numerical superiority of the mixed MLPG approach.

7.3 Numerical examples

This section contains various numerical examples that demonstrate the efficiency of the presented mixed formulations. First, an example dealing with a thick rectangular plate points to the numerical advantages, such as those associated with the numerical integration of the LWF, of the presented mixed approach over the primal MLPG algorithms presented in Chapter 6. Next, examples involving thin plates and shells demonstrate the successful elimination of shear locking by means of the adopted mixed concept, where strains are approximated separately from displacements.

Since the solutions obtained by means of two or more different meshless formulations are given, the following nomenclature is used for naming different algorithms in order to avoid confusion in interpreting the results. A label consisting of four sets of data, whose meaning is given in Table 7.1, defines each meshless formulation.

For facilitation, uniform grids of node couples were used for the discretization of analyzed structures. LWF were calculated over either the cylindrical or the parallelepipedic local sub-domains, as explained in Sections 7.1.1 and 7.2.1. Due to the uniform discretization, the sizes of all local sub-domains were identical. The shapes of the local sub-domains were either the circular cylinders or parallelepipeds with the square in-plane bases in the parametric space, as shown in Figure 6.2 and Figure 7.1, respectively. In the following presentation of results, the local sub-domains are denoted as Ω_t, r_T denotes the value of the radii of the cylindrical local sub-domains, while $2d_T$ is the length of the sides of the square in-plane bases of the parallelepipedic local sub-domains.

The MLS functions with complete polynomial bases of different order were used to approximate unknown field variables in the in-plane directions. They are labelled either as MLSX, if the MLS weight functions are the 4th-order spline functions given by relation (3.20), or as IMLSX, in the case of the regularized MLS weight functions defined by (3.24). In both cases, $X = 1, 2, 3, ..., 6$ denotes the order of the applied complete polynomial basis. In the following sections, the support domains of the nodal MLS shape functions is denoted as Ω_{tr}, while R_{tr} stands for their radii. Similarly to Ω_t, identical values of R_{tr} was assigned to all Ω_{tr} during computations. In the cases when the non-interpolation MLS functions were used for the approximation of

displacements, the essential BC were enforced by means of the penalty method with the value of the penalty parameter of $\alpha=10^9$.

LABEL: "FORMULATION" – "APPROX" "ORDER" – "LOCSUB"		
FORMULATION - defines the formulation by indicating some details, such as the set of independent variables or the order of approximation in the thickness direction.		
PRM-MLPG-U1	the primal formulation for shells that employs the linear distribution over the thickness for all displacement components [153]	
PRM-MLPG-QTS	the primal formulation for shells that implements the hierarchical quadratic interpolation for the transversal normal displacement u_3 by means of the quadratic test function (Section 6.4)	
MXD-MLPG-E0	the mixed MLPG formulation for plates, where all strain components are approximated directly, and their nodal values $\hat{\varepsilon}_{ij}$ are calculated from displacements by using relation (7.25), according to the procedures given in Section 7.1.2.	
MXD-MLPG-E1	the mixed MLPG formulation for plates presented in Section 7.1, where the nodal values for the transversal normal strain component $\hat{\varepsilon}_{33}$ is modified according to the procedure given in Section 7.1.3 in order to eliminate the thickness locking effect	
MXD-MLPG-S	the mixed MLPG formulation for shells presented in Section 7.2, where the thickness locking effect is circumvented by using the switch of independent variables according to the procedure given in Section 7.2.2	
APPROX – defines the type of MLS functions applied, i.e. the MLS weight function		
MLS	the MLS weight function is the 4th order spline from (3.20)	
IMLS	the MLS weight function is the regularized function from (3.24)	
ORDER – defines the order of the MLS function, i.e. the order of the MLS basis		
LOCSUB – defines the shape of the local sub-domains		
CYL	the cylindrical local sub-domain with the circular support in the in-plane directions of the parametric space	
REC	the parallelepipedic local sub-domain with the square support in the in-plane directions of the parametric space	
Example: MXD-MLPG-S – MLS2 – REC designates the mixed MLPG formulation for the analysis of shell structures which employs the non-interpolation MLS functions of the 2nd order with the spline-type weight functions for the approximation of unknown field variables and the parallelepipedic local sub-domains to integrate weak forms		

Table 7.1 Labels used for different meshless formulations

As in Section 6.5, the meshless results were again compared with the solutions obtained by the hexahedral solid elements from the MSC.Nastran program package, where the reduced integration is applied for the elimination of shear locking, while the Poisson's thickness locking in the 8-noded elements is circumvented by means of bubble functions [87],[144].

7.3.1 Clamped thick square plate under uniform continuous load

In order to expose numerical features of the proposed mixed approach, such as the efficiency of the numerical integration of the LWF or the absence of the Poisson's thickness locking effect, deformation responses of a clamped thick square plate were investigated. In addition, the following numerical experiments should demonstrate the numerical superiority of the presented mixed formulations over the primal MLPG method. Since the primal MLPG formulations are sensitive to transversal shear locking in the thin plate limit, a thick plate was analyzed to circumvent the difficulties associated with the shear locking phenomena.

The plate considered in this example has the same geometry and BC as the one presented in the Section 6.5.1.1. The Young's modulus of the material is $E = 10.92 \cdot 10^5$ N/mm^2. Due to symmetry, again only one quarter of the plate was discretized by uniform grids, as shown in Figure 6.4.

7.3.1.1 Numerical integration of LWF

Numerical integration is one of the most problematic issues in meshless methods. Therefore, the numerical cubature of LWF in the proposed mixed approach was inspected first. In order to avoid the appearance of the Poisson's thickness locking effect, the Poisson's ratio of the material is set to zero, $v = 0$. Therefore, the exact solution may be obtained by the developed meshless formulations without employing any procedures for the elimination of the Poisson's thickness locking effect. Consequently, for comparison we used the mixed formulation labelled as MXD-MLPG-E0 and the primal formulation denoted as PRM-MLPG-U1. More details on the applied algorithms are available in Table 7.1, and the references contained within.

The accuracy of the solution for the plate central deflection w_c was checked for different numbers of integration points. In both the mixed and primal formulations, the cylindrical local sub-domains were applied. Two models, consisting of 81 (9x9 grid) and 289 (17x17 grid) nodes, were used. The integration was performed by employing the simple Legendre-Gaussian numerical integration scheme over the entire local sub-domain, as described in Section 4.4. The numbers of integration points in the circular and radial direction of the local sub-domain are labelled as n_c and n_r, respectively. Two integration points were applied to compute the integrals over the thickness.
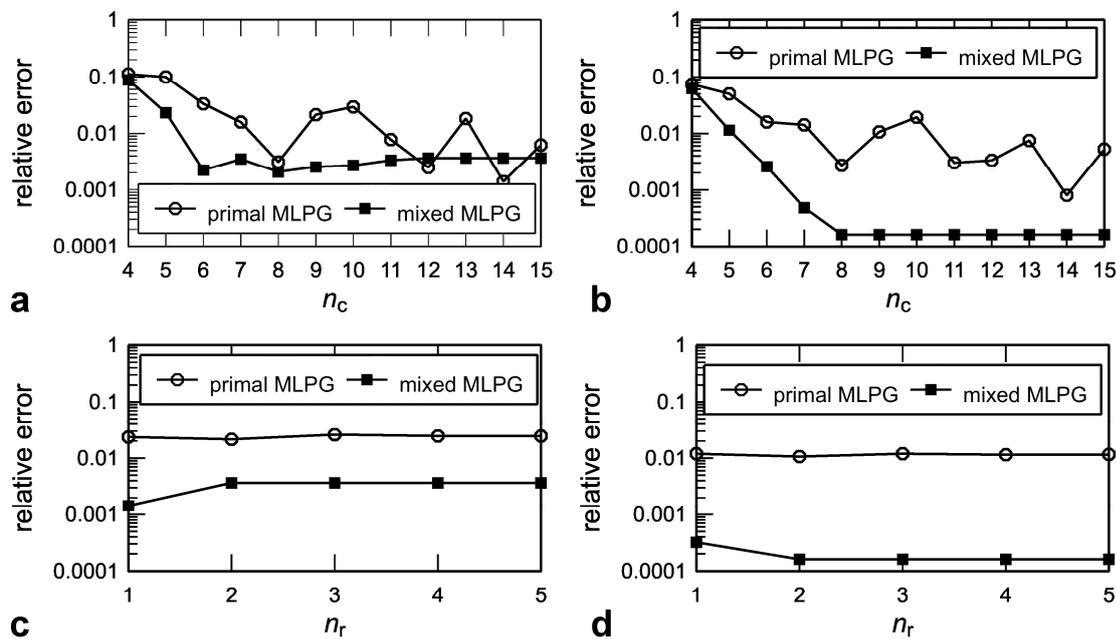
Figure 7.5 Clamped thick square plate with $v = 0.0$. Influence of number of integration points on solution accuracy: a) influence of n_c for $n_r = 2$ (81 nodes), b) influence of n_c for $n_r = 2$ (289 nodes), c) influence of n_r for $n_c = 9$ (81 nodes), d) influence of n_r for n_r (289 nodes).

Figure 7.5 shows the results of the tests. The relative error is defined as $(w_c - w_{cr})/w_{cr}$, where w_c is a meshless solution obtained for some particular choice of n_c and n_r, and w_{cr} is a referent value calculated by using sufficiently large values for n_c and n_r, $n_c = n_r = 20$. It is obvious from Figure 7.5a) and b) that in the primal method the value of n_c affects the stability of the solution more severely than in the proposed mixed algorithm. The oscillation of the solution values is clearly visible, and the solution accuracy does not significantly improve when more nodes are used. On the other hand, in the mixed approach $n_c = 7$ provides acceptable solution accuracy and the

results are stable for $n_c > 7$. It is clear from Figure 7.5 c) and d) that in both approaches the solution does not depend significantly on n_r and that two quadrature points in the radial direction are sufficient for obtaining stable results. The mixed algorithm clearly achieves higher accuracy.

7.3.1.2 Effects of sizes of Ω_t and Ω_{tr} on solution accuracy

The sizes of the support domains of the nodal test and trial shape functions, labelled as Ω_t and Ω_{tr}, may significantly affect the solution accuracy in the MLPG method. Hence, the influences of these parameters on the solution for the plate central deflection w_c were investigated. The results are plotted in Figure 7.6 and Figure 7.7.

Again, discretization was performed by using 81 (9x9) and 289 (17x17) node couples. All results were obtained by applying nine quadrature points in the circular direction, $n_c = 9$, and two points in the radial direction, $n_r = 2$, in each cylindrical local sub-domain. Furthermore, the Poisson's ratio was set to zero, $v = 0$, and the MXD-MLPG-E0 and PRM-MLPG-U1 formulations were employed. In Figure 7.6 and Figure 7.7, the radii R_t and R_{tr} are normalized with the nodal distance in the direction of the coordinate axes, denoted as h_m.
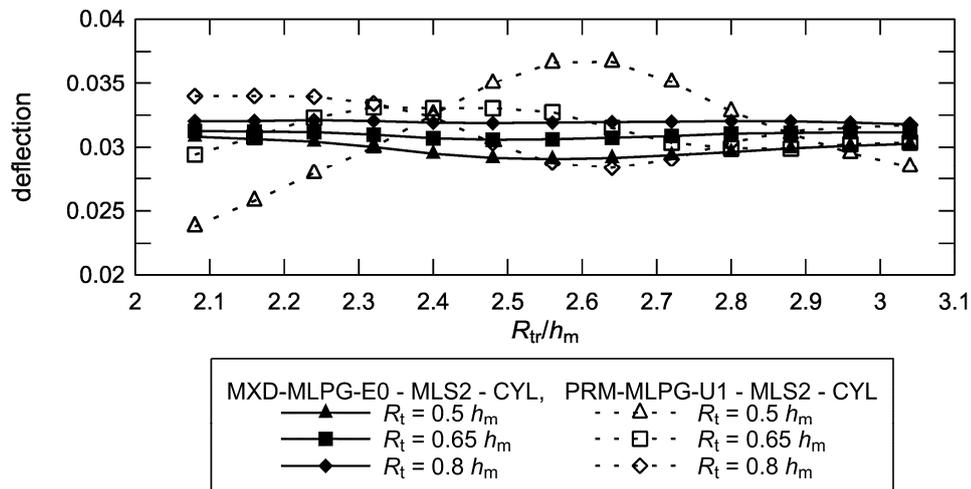
Figure 7.6 Clamped thick square plate with $v = 0.0$. Influence of sizes of Ω_t and Ω_{tr} on solution accuracy for 81 node couples.
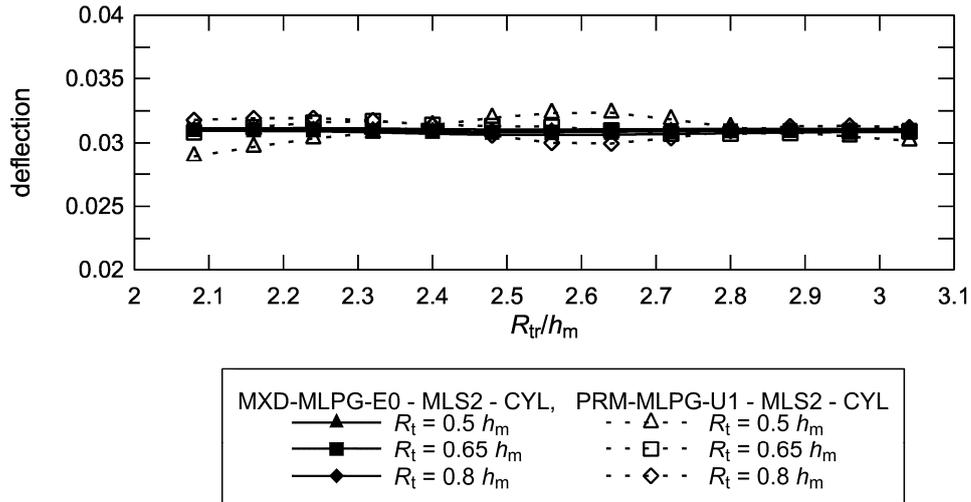
Figure 7.7 Clamped thick square plate with $\nu = 0.0$. Influence of sizes of Ω_t and Ω_{tr} on solution accuracy for 289 node couples.

Evidently, in the mixed approach the influence of R_{tr} on the accuracy of the solution is not as pronounced as in the primal MLPG formulation and it becomes almost negligible if more nodes are used. Therefore, the values that are close to the minimum admissible value of R_{tr} may be chosen in order to increase numerical efficiency. The value of R_t affects the solution accuracy more significantly, although less so than in the primal MLPG method. Nevertheless, this effect again diminishes if more nodes are applied for discretization.

7.3.1.3 Poisson's thickness locking effect

In order to demonstrate the efficiency of the procedures for the elimination of the Poisson's thickness locking effect, the Poisson's ratio was set to $\nu = 0.3$, and the same problem was computed by means of the mixed MXD-MLPG-E1 and MXD-MLPG-S formulations. For this example, all calculations involving the mixed algorithms were performed by using two quadrature points in the radial direction, $n_r = 2$, while in the circular direction seven integration points were used, $n_c = 7$. The test domain radius was $R_t = 0.65 h_m$, while the support domain radius was set to $R_{tr} = 1.25 h_m$ and $R_{tr} = 2.15 h_m$ for the MLS1 and MLS2 functions, respectively. Herein h_m stands for the distance between nodes in the direction of the coordinate axes X^α.

Figure 7.8 shows the convergence of the solutions for the central deflection w_c obtained by means of various mixed meshless formulations. The values are normalized by the analytical solution w_{ca}, which is obtained from [145]. The algorithms MXD-MLPG-E1 and MXD-MLPG-S achieve the convergence to a value close to w_{ca}, indicating the absence of the Poisson's thickness locking phenomenon. On the other hand, the formulation MXD-MLPG-E0 obviously suffers from the thickness locking effect, because therein the distribution of the transversal normal strain component ε_{33} is constant through the thickness, as proved by relation (7.27). It is also noteworthy that the formulations MXD-MLPG-E1 and MXD-MLPG-S yield almost identical results. Therefore, from now on, only the results for the algorithm MXD-MLPG-E1 will be considered for this example unless specified otherwise.
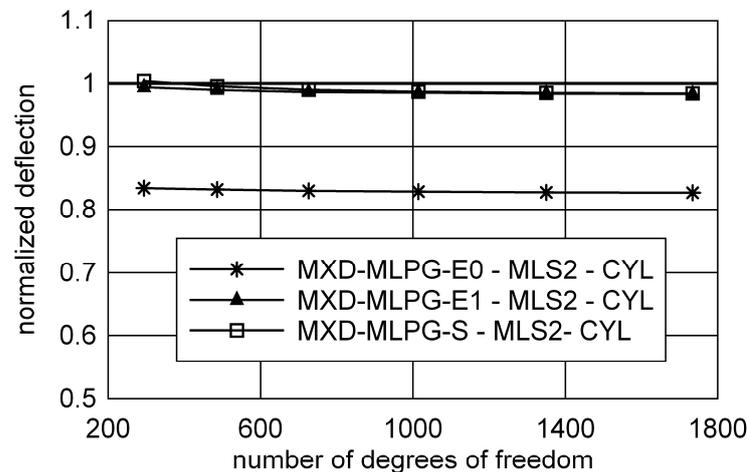
Figure 7.8 Clamped thick square plate with $\nu = 0.3$. Comparison of convergences of plate central deflection for various mixed MLPG formulations.

In addition, the convergence of the mixed formulation MXD-MLPG-E1 is compared with the results obtained by means of the primal formulation PRM-MLPG-QTS, as well as the hexahedral solid finite elements from the MSC.Nastran package in Figure 7.9. For the primal algorithm, the number of Gaussian points per local sub-domain were $n_r = 2$ and $n_c = 11$, and the values of $R_t = 0.8 h_m$ and $R_{tr} = 2.4 h_m$ were applied. It should be emphasized that only the MLS2 functions were used for the primal MLPG method because no convergence could be achieved for the MLS1 functions. On the other hand, the mixed formulation achieves satisfactory convergence even if the MLS1 functions are used. Moreover, the achieved

convergences are also better than that obtained by using the MSC.Nastran hexahedral 20-noded finite elements.
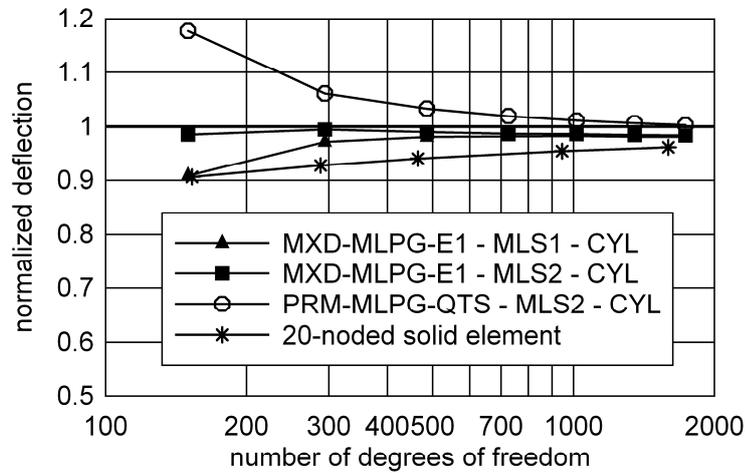

Figure 7.9 Clamped thick square plate with $\nu = 0.3$. Convergences of plate central deflection in comparison to primal MLG approach and solid finite elements.

7.3.2 Thin square plate subjected to constant continuous load

A clamped thin square plate with the thickness $h = 1\,\text{mm}$ and the side length $a = 100\,\text{mm}$ is subjected to the uniformly distributed load of $q = 0.1\,\text{N/mm}^2$ over the upper surface. The material data are the Poisson's ratio $\nu = 0.3$ and the Young's modulus $E = 10.92 \cdot 10^5\,\text{N/mm}^2$. Again, only one quadrant of the plate was modelled due to the symmetry conditions. The applied essential BC are shown in Figure 6.4 in Section 6.5.1.1.

For this example, both the cylindrical (CYL) and the parallelepipedic local sub-domains (REC), were used. First, only the application of the cylindrical local sub-domains is considered. After that, the non-interpolation (MLS) and interpolation Moving Least Square (IMLS) schemes are compared by employing the MXD-MLPG-S formulation. Finally, the parallelepipedic local sub-domains are applied in the MXD-MLPG-S formulation and a detailed analysis of the obtained results is presented.

Cylindrical local sub-domains

In this sub-section, the mixed formulations MXD-MLPG-E1 and MXD-MLPG-S employing the cylindrical local sub-domains and the non-interpolation MLS scheme are

considered. In both cases, the fourth-order spline function from (3.20) was used as the MLS weight function. First, we checked the influence of the radii of the local sub-domains R_t and the radii R_{tr} of the support domains of the nodal MLS shape functions on the solution accuracy. Figure 7.10 contains the results of the parametric analyses for the MLS1 and MLS2 functions.
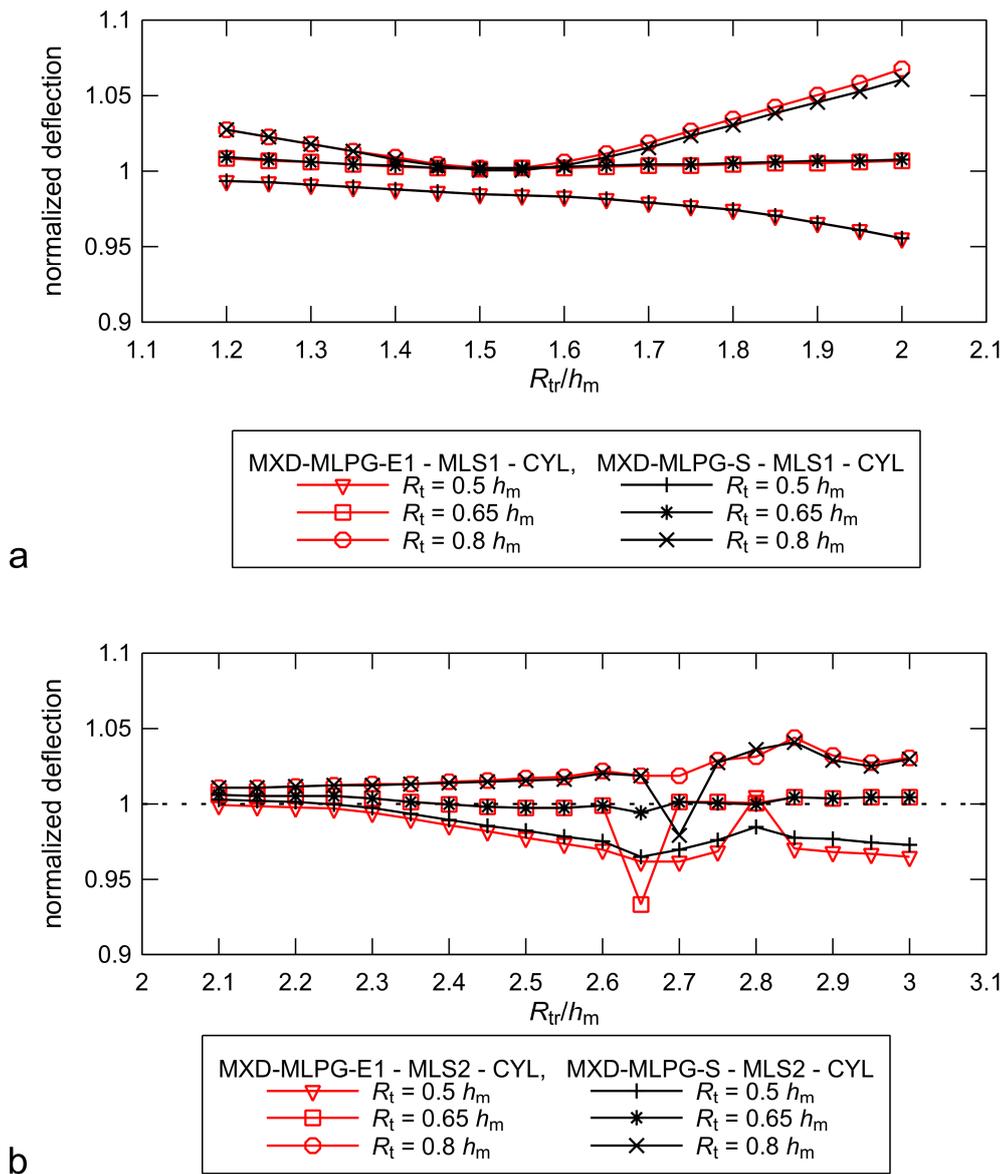

Figure 7.10 Clamped thin square plate subjected to constant continuous load. Influence of R_t and R_{tr} on solution accuracy for mixed formulations employing cylindrical local sub-domains for: a) MLS1 functions, b) MLS2 functions.

In the above figure, the numerical results for the deflection of the central plate point are normalized by using the analytic solution from [154]. The parameters R_{tr} and

R_t are again normalized by the nodal distance in the direction of coordinate axes, which is denoted as h_m. For discretization, 289 (17x17) node couples were employed. For all calculations, two Gaussian points were used in the radial direction of the local sub-domains, while nine integration points were applied in the circular direction, i.e., $n_r = 2$ and $n_c = 9$.

Considerable oscillations around the analytical value are clearly visible, particularly for the higher values of R_{tr}. However, for $R_t = 0.65 h_m$ the results are more accurate and do not depend significantly on the value of R_{tr}. Hence, the results of all subsequent numerical tests for this problem were obtained by using the support domain radii $R_{tr} = 1.25 h_m$ and $R_{tr} = 2.15 h_m$ for the MLS1 and MLS2 functions, respectively, and $R_t = 0.65 h_m$ for the local sub-domains. It is important to note that the chosen values for R_{tr} are close to the minimal admissible values, and that such a choice therefore increases numerical efficiency. As is evident from Figure 7.10, both formulations yield very similar results, especially for the low values of R_{tr}.
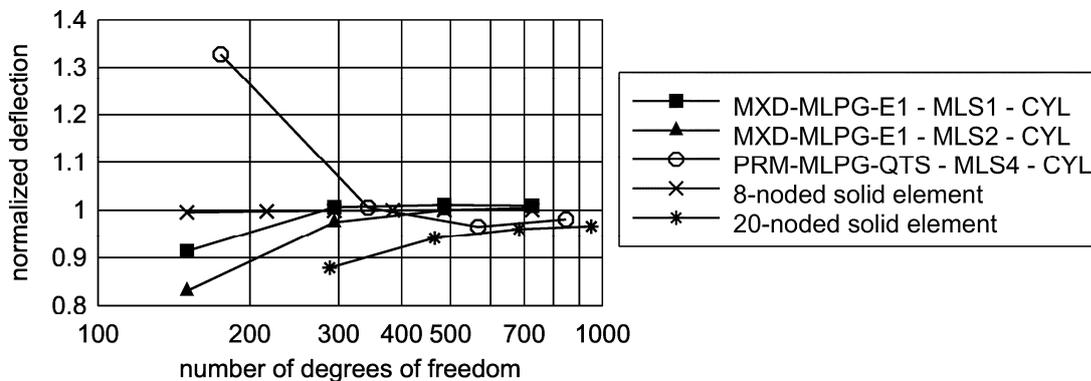
Figure 7.11 Clamped thin square plate subjected to constant continuous load. Convergences of plate central deflection for MXD-MLPG-E1 formulation compared to the finite elements solutions.

Figure 7.11 displays the convergence of the plate central deflection computed by the MXD-MLPG-E1 approach. The results are compared with the solutions obtained by the solid hexagonal finite elements and the displacement-based PRM-MLPG-QTS formulation. In the mixed algorithm, both the MLS1 and MLS2 functions were used, while only the MLS4 function was applied in the primal MLPG formulation. The mixed formulation achieves better accuracy and convergence than the 20-noded FE solutions even for the MLS1 functions, indicating that shear locking is efficiently overcome. Moreover, the convergence of the mixed approach is better than that of the primal

MLPG formulation even though the low-order MLS functions were used. It is important to note that the low order of the MLS functions allows the use of smaller values of R_{tr}, as well as fewer quadrature points, which further increases the numerical efficiency of the proposed mixed approach.

MLS vs. IMLS functions

To compare the performances of the MLS and IMLS approximation functions, the mixed MXD-MLPG-S formulation, exposed in Section 7.2, was used. In order to impose the essential BC when applying the MLS functions, the penalty method was implemented into the MXD-MLPG-S formulation. Figure 7.12 shows the influence of values R_t and R_{tr} on the solution accuracy. The complete second-order basis was applied for both the MLS and IMLS functions, and the model consisting of 289 (17x17) node couples was employed. As explained previously in detail, numerical integration was performed over the cylindrical local sub-domains.
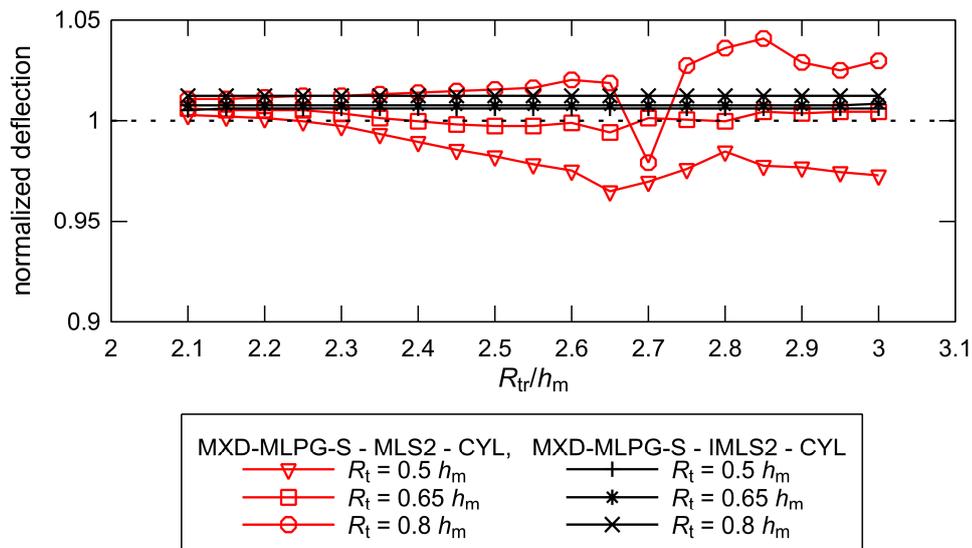
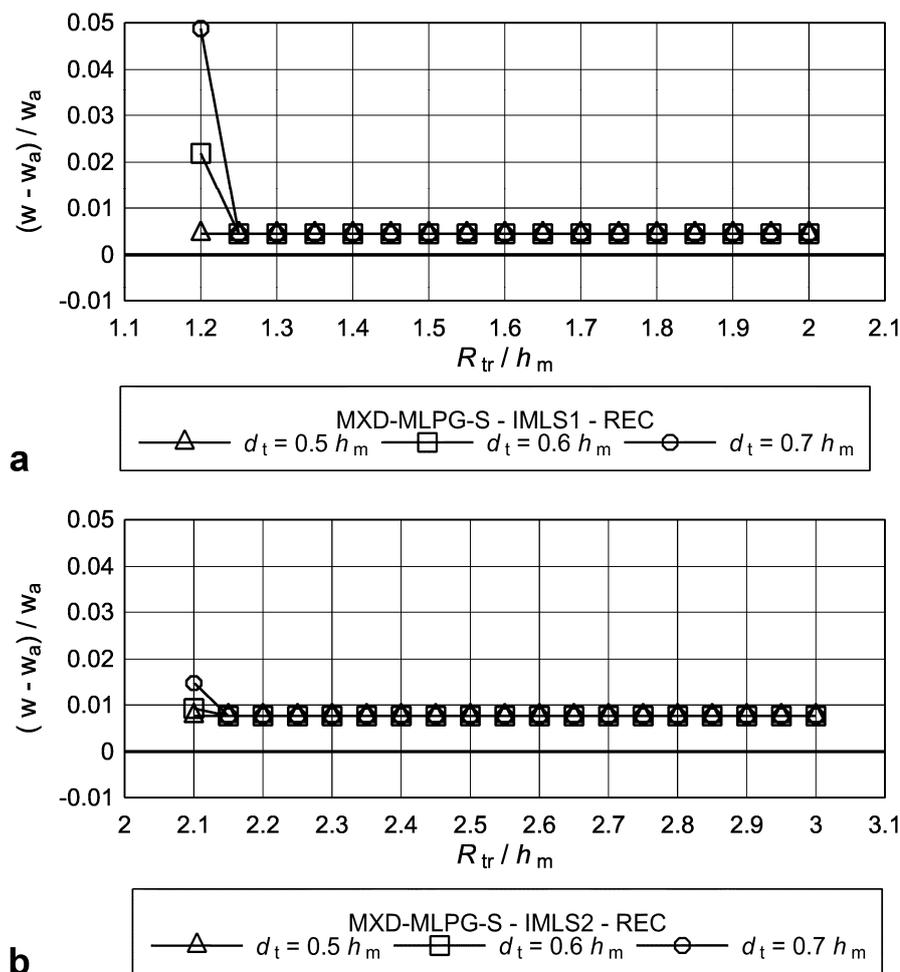

Figure 7.12 Clamped thin square plate subjected to constant continuous load. Influence of R_t and R_{tr} on the solution accuracy for MLS2 and IMLS2 functions.

Similarly to observations made in [117] and [128], the accuracy of the solution obtained by using IMLS functions is less influenced by the values of R_{tr} than the MLS functions. Therefore, for IMLS functions it is possible to employ small values that are close to the minimal admissible values of R_{tr} without having to perform the tedious parametric analyses prior to calculations. This is very convenient because using smaller local sub-domains also decreases the total computational costs.

Parallelepipedic local sub-domains

The MXD-MLPG-S formulation employing the parallelepipedic local sub-domains, which are shown in Figure 7.1, is considered next. The parallelepipedic local sub-domains are especially suitable for the analysis of curved shell structures, due to their metrics not involving trigonometric functions, which are necessary to describe the geometry of the cylindrical local sub-domains. This convenience has already been used for the analysis of thin shells and plates [13].

The results in the following section were obtained by using the IMLS functions. The MLS bases of the first and second order were applied. Numerical integration was performed by partitioning the local sub-domain into four equal quadrants in the parametric space, and by applying the simple 2-D Legendre-Gaussian formula with four (2x2) quadrature points in each quadrant.

Figure 7.13 Clamped thin square plate subjected to constant continuous load. The influence of the sizes of Ω_t and Ω_{tr} on the solution accuracy for the MXD-MLPG-S formulation employing parallelepipedic local sub-domains for: a) IMLS1 functions, b) IMLS2 functions.

Figure 7.13 displays the influence of the values of R_{tr} on the solution accuracy for different sizes of the local sub-domains Ω_s. The figure shows the relative error for the central plate deflection, defined as $(w - w_a)/w_a$ with w as a meshless solution and w_a as the referent analytical value from [154]. Therein d_t defines the size of the parallelepipedic local sub-domains as explained before, while R_{tr} denotes the radius of Ω_{tr}. Both parameters are normalized by the parameter h_m, which is the distance between the nodes in the direction of the in-plane axes θ^α. The calculations were performed on the model consisting of 289 (17x17) nodes. It may be concluded that for this problem the sizes of Ω_s and Ω_{tr} have negligible influence on the solution accuracy. However, it should be noted that the values for R_{tr} have to be large enough to ensure the adequate quality of approximations, i.e., $R_{tr} \geq 1.25 h_m$ and $R_{tr} \geq 2.15 h_m$ for the first-order and second-order MLS functions, respectively.
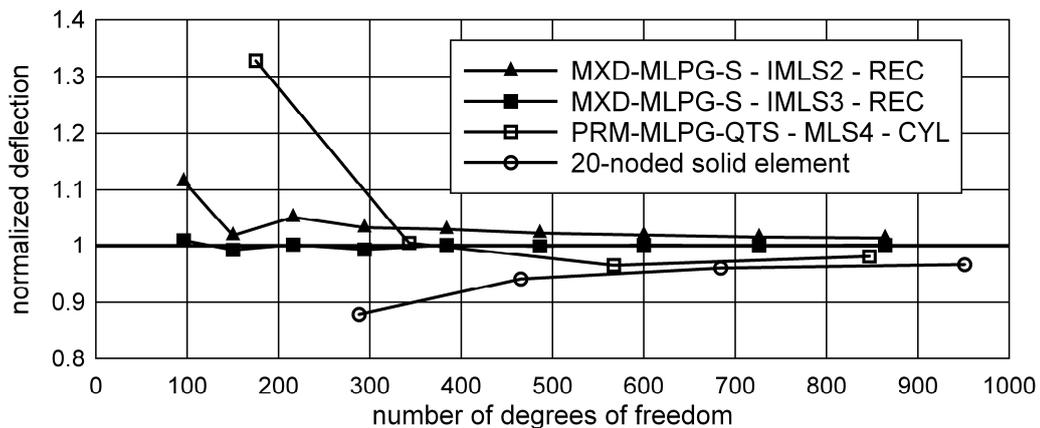
Figure 7.14 Clamped thin square plate subjected to constant continuous load. Convergence of central deflection for the MXD-MLPG-S – IMLS – REC algorithm

The convergence of the solution for the plate central deflection is compared with the values obtained by the PRM-MLPG-QTS formulation and with the solutions obtained by the 20-noded hexagonal 3-D elements from the MSC.Nastran program package [144] in Figure 7.14. The deflections were computed at the point positioned on the middle surface and normalized by using the exact analytical solution [154]. The second- and third-order complete polynomial bases were used in the mixed formulation. On the other hand, the MLS fourth-order basis is necessary in the PRM-MLPG-QTS formulation for achieving the convergence. Such a high basis requires relatively large

interpolation support domain and, consequently, large computation time, which decreases numerical efficiency. The mixed approach employing the third-order IMLS function produces accurate results even in the case of a coarse grid point distribution (5x5 nodes). Furthermore, it should be stressed that the accuracy of the applied finite elements is lower than that of the proposed mixed meshless computation strategy.

A more detailed convergence study has been performed by considering the L_2 norm of the relative error of deflection. The results were again compared with those computed by the purely displacement PRM-MLPG-QTS approach, as shown in Figure 7.15.
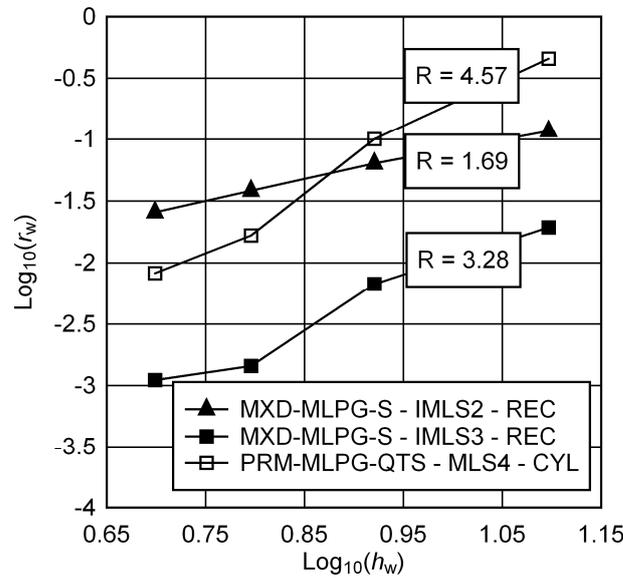
Figure 7.15 Clamped thin square plate subjected to constant continuous load. Relative errors and convergence rates for deflection

The L_2 norm is computed by the well-known relation

$$\|w\| = \left(\int_\Omega w^2 d\Omega \right)^{\frac{1}{2}} \tag{7.92}$$

and the relative error is defined as

$$r_w = \frac{\|w_n - w_e\|}{\|w_e\|} . \tag{7.93}$$

Herein w_n is the numerical solution obtained by the MLPG algorithms and w_e stands for the exact analytical solution [154]. The convergence rates are calculated approximately as the slopes of lines that are the least square fits to the numerical results

presented in Figure 7.15. The parameter h_w represents the nodal distance in the directions of the parametric in-plane axes θ^α. In the case of the mixed MLPG formulation, the measured convergence rates are $R = 1.68$ and $R = 3.28$ for the second- and third-order bases, respectively. The convergence rate of the primal PRM-MLPG-QTS formulation employing the fourth-order MLS functions is $R = 4.56$. Although the primal formulation yields considerably higher convergence rate, it is obvious from Figure 7.15 that the overall accuracy is approximately one order lower than that of the mixed formulation employing the third-order MLS functions.

Figure 7.16 contains the results for the convergence rate of the bending moments. The rates are defined analogously to the displacements as

$$r_M = \frac{\|\mathbf{M}_n - \mathbf{M}_e\|}{\|\mathbf{M}_e\|}, \tag{7.94}$$

where the L$_2$-norm for the moments is computed according to the following relation

$$\|\mathbf{M}\| = \left(\int_\Omega \mathbf{M} \cdot \mathbf{M} \, d\Omega \right)^{\frac{1}{2}}. \tag{7.95}$$

Herein, $\mathbf{M}^T = \begin{bmatrix} M_{11} & M_{22} & M_{12} \end{bmatrix}$ is the vector containing the bending moments M_{11} and M_{22}, as well as the twisting moment M_{12}, both calculated according to the general shell theory [120]. The analytical solutions $\mathbf{M}_e$ were again obtained from [154].

The measured convergence rates are $R = 2.28$ and $R = 4.5$ for the IMLS2 and IMLS3 functions, respectively. From Figure 7.15 and Figure 7.16, it is obvious that for the IMLS2 functions the convergence rate for the moments is higher than the convergence rate for displacements, while overall accuracy is close. Conversely, the IMLS3 functions yield lower convergence rates and accuracy than for the displacements.
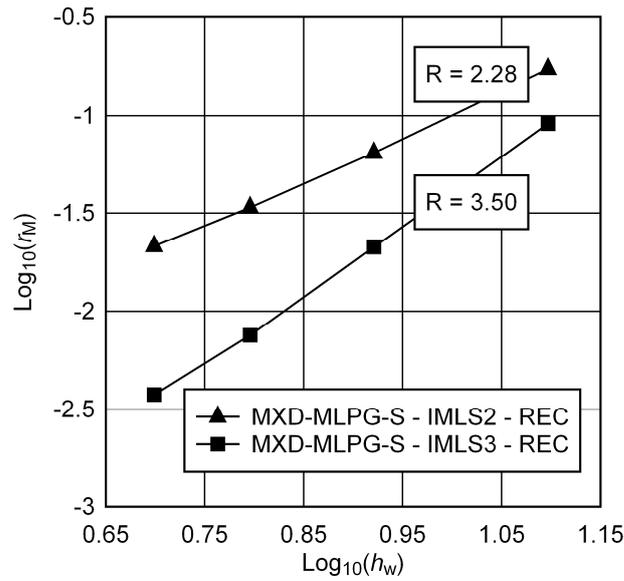
Figure 7.16 Clamped thin square plate subjected to constant continuous load. Relative errors and convergence rates for moments.
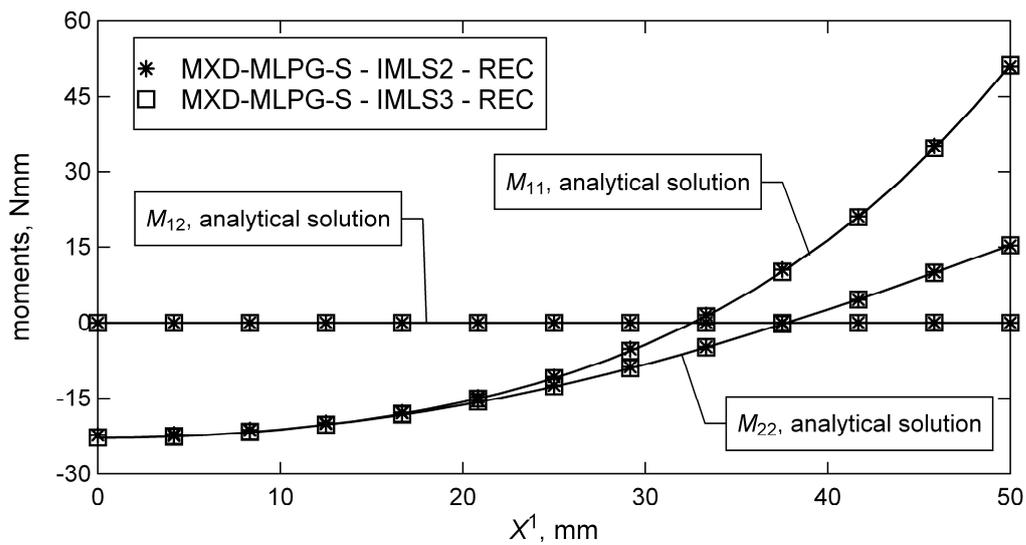

Figure 7.17 Clamped thin square plate subjected to constant continuous load. Distribution of bending and twisting moments along line $X^1 = 0$ (see Figure 6.4).

Figure 7.17 shows the distribution of the bending and twisting moments along the line $X^1 = 0$. The nodal values obtained using the meshless method are compared with the analytical solutions [154]. The calculations were performed by employing 81 nodes in the model with nine nodes along the inspected line. It is clear that the IMLS2 functions are sufficient to obtain excellent agreement with the analytical solutions.

The sensitivity of the proposed mixed approach on the shear locking effect was tested by increasing the plate span to the thickness ratio, as shown in Figure 7.18. The

second-order MLS polynomial basis was used. As evident, the accuracy does not deteriorate, even for very thin plates, which shows that the shear locking effect is successfully suppressed.
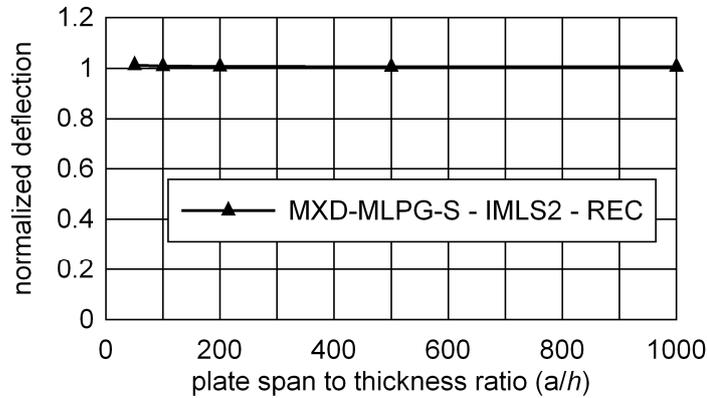

Figure 7.18 Clamped thin square plate subjected to constant continuous load. Central deflection vs. span-to-thickness ratio for clamped plate

7.3.3 Thin shell structures

The following sections deal with the application of the mixed MXD-MLPG-S algorithm on the analysis of thin shells. In order to test the performance of the proposed formulation, couple of typical benchmark problems for thin shells are considered.

Unless specified otherwise, the following setup was used in all calculations. The computations were performed by using the second- or third-order complete polynomial bases in the IMLS functions. The parallelepipedic local sub-domains were used, as explained in Section 7.2.1, and the sizes of the local sub-domains were defined by setting $d_t = 0.5 h_m$. The radii of the support functions of trial shape functions were $R_{tr} = 2.25 h_m$ and $R_{tr} = 3.25 h_m$ for the IMLS2 and IMLS3 functions, respectively. Numerical integration was again performed by partitioning the local sub-domains into four equal quadrants in the parametric space, and by using 3x3 2-D Legendre-Gaussian rule in each quadrant. The uniform grids of nodes were used for the discretization of all models. As before, the results obtained by the meshless approach were compared with the hexahedral solid finite elements from the MSC.Nastran program package [144].

7.3.3.1 Cylindrical shell subjected to uniform line load

A horizontal thin cylindrical shell subjected to the uniform line load along the upper and the lower generatrix was analyzed. The configuration of the shell, including

the material, geometrical and load data, is given in Figure 7.19. Due to symmetry, we modelled only one octant of the shell.

length, $L=300$ mm
radius, $R = 90$ mm
thickness, $h = 0.9$ mm
Young's modulus, $E = 210000$ N/mm^2
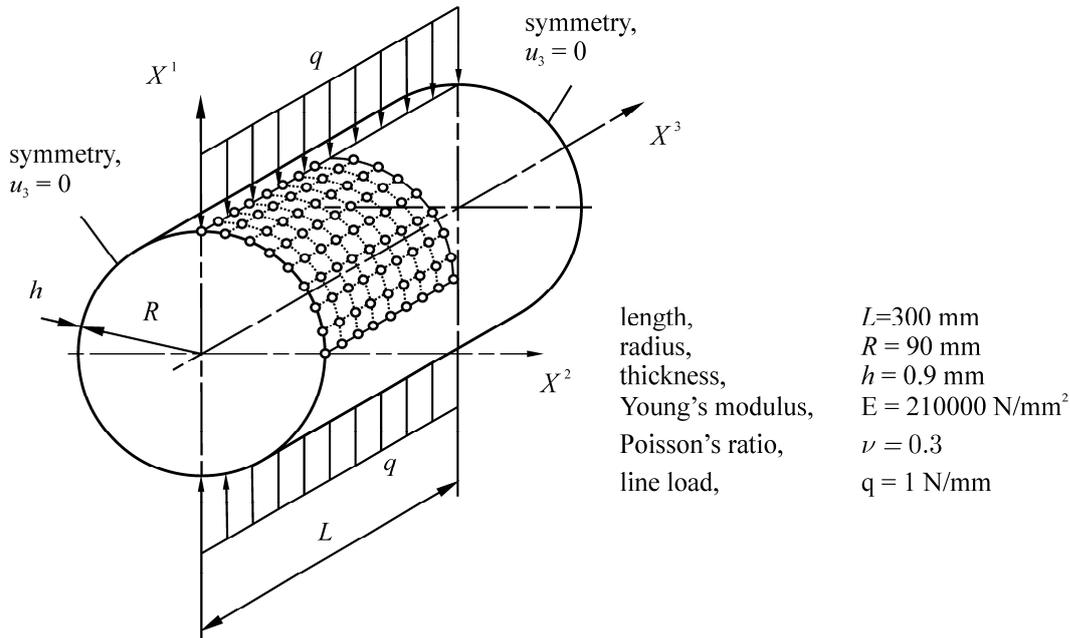Poisson's ratio, $\nu = 0.3$
line load, $q = 1$ N/mm

Figure 7.19 Thin cylindrical shell. Geometry, boundary conditions, and discretization.
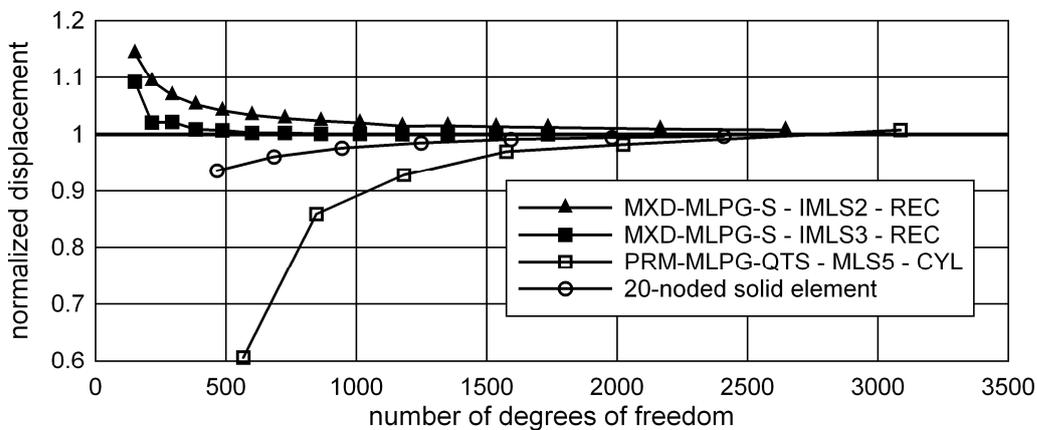
Figure 7.20 Thin cylindrical shell subjected to uniform line load. Convergence of vertical displacement under line load for MXD-MLPG-S formulation.

The convergence of the vertical displacement at the shell middle surface under the line load, normalized by the analytical solution from [155], is presented in Figure 7.20, where the results are again compared with the values obtained by the primal algorithm PRM-MLPG-QTS as well as with the 20-noded 3-D finite elements. As is clear from Figure 7.20, the mixed formulation is superior to the other tested formulations. The fifth-order basis function in the MLS approximation has to be used in the purely displacement approach in order to achieve the convergence, which significantly

decreases numerical efficiency. Furthermore, the computation by means of the third-order IMLS basis function in the mixed approach yields the exact displacement values, even for the relatively coarse discretization.

The relative errors of the displacements in the L_2 norm were again calculated. The results are compared with the values obtained by the purely displacement PRM-MLPG-QTS in Figure 7.21. The norm and relative error are defined analogously as in (7.92) and (7.93), while the parameter s represents the nodal distance in the circular direction. The analytical solution used for the normalization is available in [155].
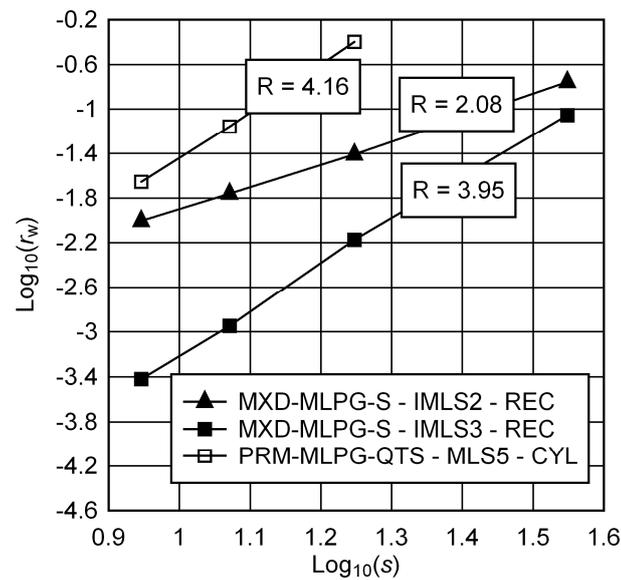
Figure 7.21 Thin cylindrical shell subjected to uniform line load. Relative errors and convergence rates for displacements.

The convergence rates of the mixed formulation are $R = 2.08$ and $R = 3.95$ for the IMLS2 and IMLS3 functions, while the convergence rate of the primal approach is $R = 4.16$. Although the primal method displays better convergence rates than the mixed formulation, the overall accuracy is almost two orders lower. It should also be noted that the convergence rates of the mixed formulation are higher than in the example involving the thin clamped plate subjected to the continuous load.

Figure 7.22 contains the results for the convergence rate studies for the bending moments, defined as in Figure 7.23. The moment rates are defined as

$$r_M = \frac{\|M_n - M_e\|}{\|M_e\|},\qquad(7.96)$$

where the L$_2$-norm for the moments is given by

$$\|M\| = \left(\int_\Omega M^2 d\Omega \right)^{\frac{1}{2}}. \tag{7.97}$$
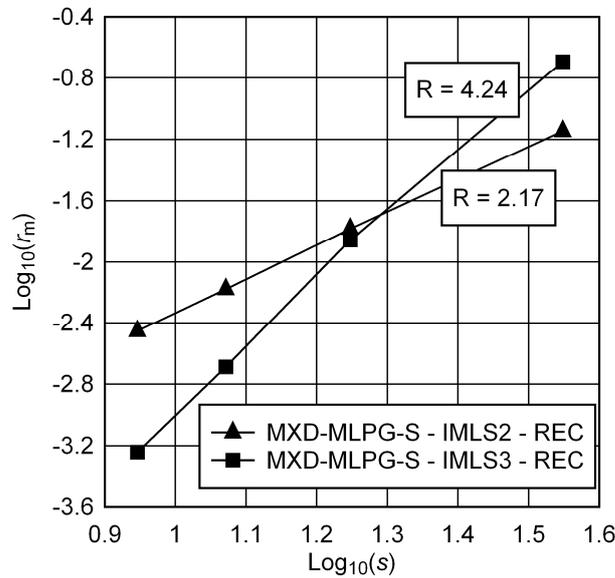

Figure 7.22 Thin cylindrical shell subjected to uniform line load. Relative errors and convergence rates of circular bending moments.

The measured convergence rates are $R = 2.17$ and $R = 4.24$ for the second- and third-order basis, respectively, which are higher than the rates obtained for displacements. It is noteworthy that the IMLS3 functions yield lower accuracy than the IMLS2 functions for coarser discretization, which may be attributed to the inaccuracies in the numerical integration of both the LWF and the L$_2$ norms.
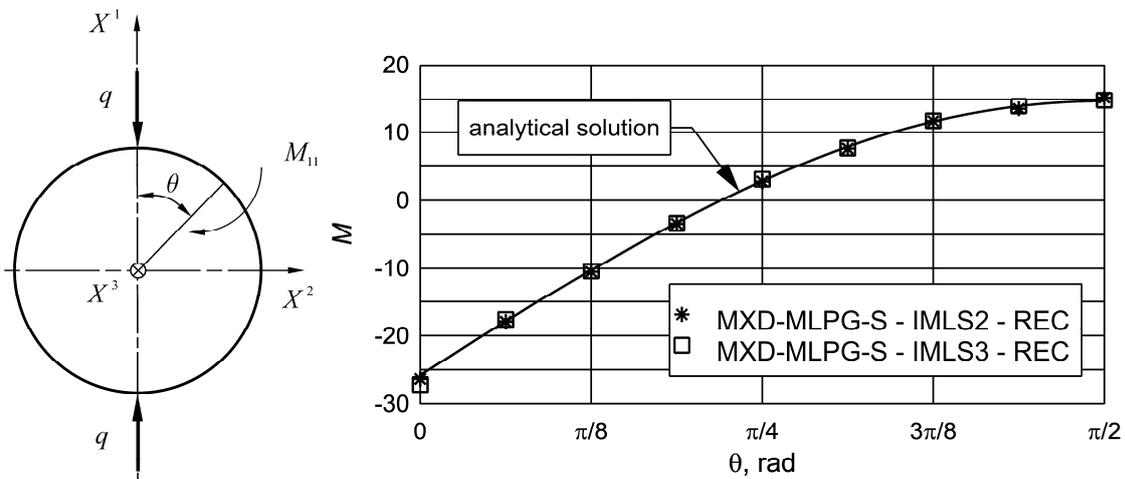

Figure 7.23 Thin cylindrical shell subjected to uniform line load. Distribution of bending moments along the shell circumference.

Figure 7.23 displays the distribution of the moments along the circumference of the cylinder for the discretization pattern containing nine nodes along the edges of the shell. It is to note that again excellent agreement with the analytical solution [155] is obtained.

The sensitivity of the mixed approach on transversal shear locking was tested by increasing the shell radius to thickness ratio and the results are shown in Figure 7.24. As evident, by using the IMLS2 functions, it is possible to eliminate shear locking even for very thin shells.
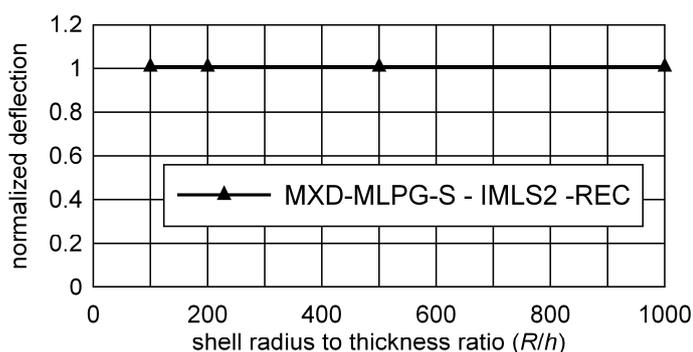

Figure 7.24 Thin cylindrical shell subjected to uniform line load. Vertical displacement under line load vs. radius-to-thickness ratio.

7.3.3.2 Scordelis-Lo shell roof

The benchmark test involving the Scordelis-Lo shell roof is revisited here by using the mixed MXD-MLPG-S algorithm. The data used in the calculations are given in Section 6.5.3.1 and the shell is depicted in Figure 6.20. Owing to symmetry, again only one quarter of the shell was modelled by using the uniform nodal grids.

Figure 7.25 and Figure 7.26 show the comparison of the convergence of the vertical displacement at the middle surface point A with the solutions obtained by the primal PRM-MLPG-QTS formulation and the 3-D solid hexahedral finite elements from the MSC.Nastran program package, respectively. Therein the numerical solutions are normalized by the analytical value [152]. The IMLS2 and IMLS3 functions were used in the mixed formulation. In the primal MLPG algorithm, the non-interpolation MLS functions of third and fourth order were applied, and numerical integration was done over cylindrical local sub-domains, as in earlier examples.
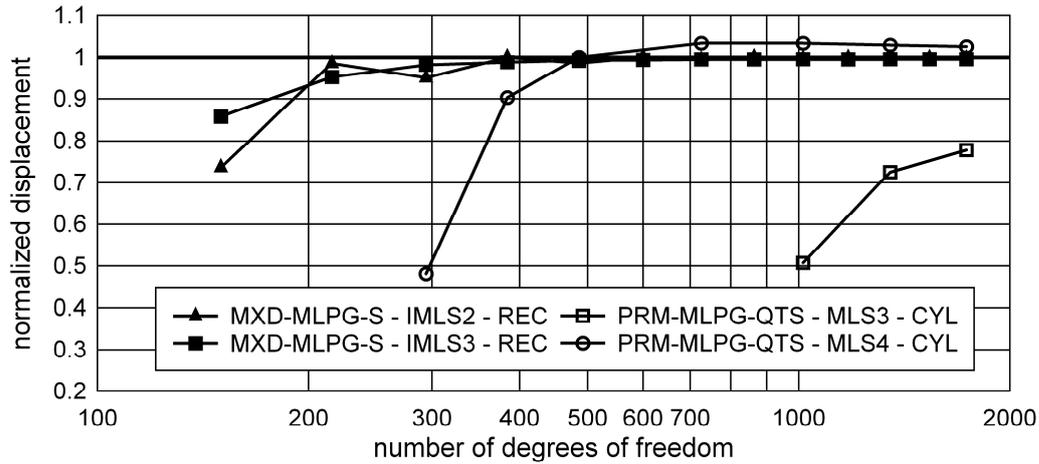
Figure 7.25 Scordelis-Lo shell roof. Convergence rates of vertical displacement at point A for MXD-MLPG-S and PRM-MLPG-QTS formulations.
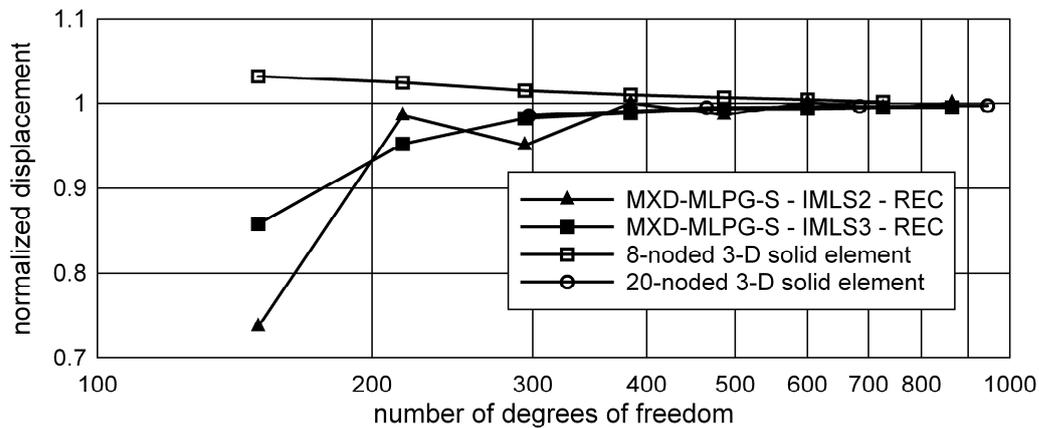

Figure 7.26 Scordelis-Lo shell roof. Convergence rate of vertical displacement at point A for MXD-MLPG-S algorithm in comparison to finite element solutions.

The results display the superiority of the mixed formulation over the primal MLPG approach. The mixed algorithm achieves satisfactory convergence even with the second-order IMLS function, while the fourth-order MLS function is necessary to obtain the convergence of the primal formulation. Moreover, it is clear from Figure 7.26 that the convergence of the MXD-MLPG-S algorithm is comparable to those obtained by using the applied 3-D solid elements. However, the convergence is non-uniform for the second-order IMLS functions, which may again be attributed to the inaccurate numerical integration.

7.3.3.3 Pinched cylinder

Similar to the previous example, the problem of the pinched cylinder is reviewed in this section by applying the MXD-MLPG-S formulation. The model data are given in Section 6.5.3.2 and the shell is shown in Figure 6.23.

The convergence was studied by applying the complete IMLS functions of the second, third and fourth order. The results are presented in Figure 7.27. Therein, the solutions for the vertical displacement under the point load are normalized by using the exact solution available in [6]. The rate of convergence for the considered point is similar for all applied functions, indicating that shear locking is suppressed even for the second-order MLS basis. From Figure 7.28 it is visible that the convergence of the mixed approach is better than those obtained by the applied 3-D solid elements. Once again, the performance of the proposed mixed approach is superior to the primal PRM-MLPG-QTS algorithm, where it was necessary to apply the MLS function of the sixth order to obtain plausible convergence.
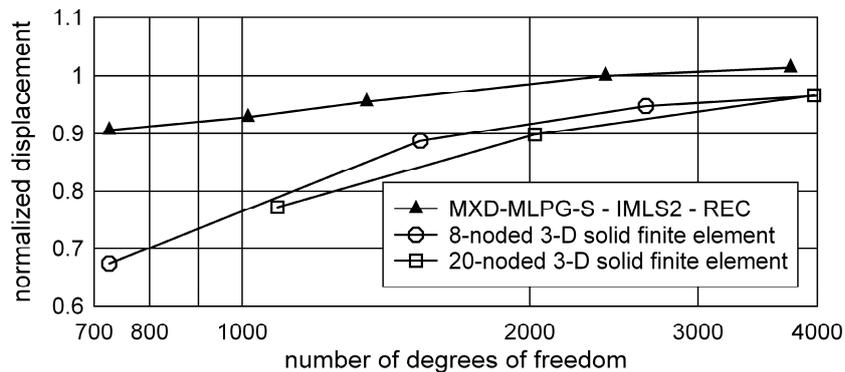

Figure 7.27 Pinched cylinder. Convergence of vertical displacement under line load obtained by MXD-MLPG-S formulation for different order of the MLS basis
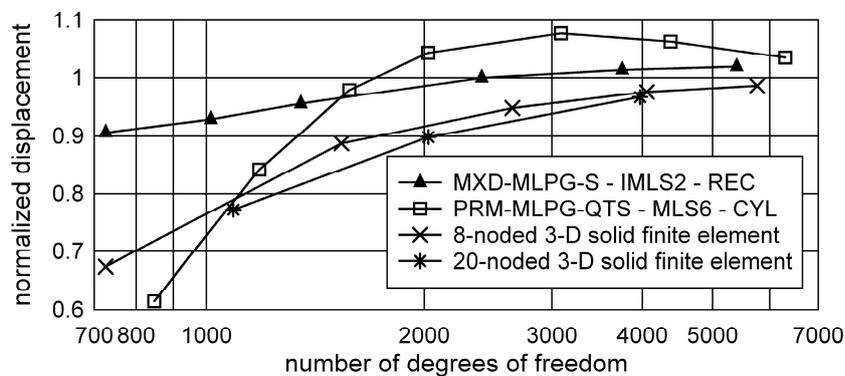

Figure 7.28 Pinched cylinder. Convergence rate of vertical displacement under line load obtained by MXD-MLPG-S algorithm in comparison to finite element solutions.

7.3.3.4 Clamped hemispherical shell

A thin hemispherical shell with a central opening, shown in Figure 7.29, is considered in this section. The shell is moderately thin, with the radius-to-thickness ratio $R/h = 100$. The material and geometrical data, together with the applied boundary conditions, are given in Figure 7.29. Again, only one quadrant of the shell was modelled by employing uniform grids, due to symmetry of the problem. The computations were performed using the mixed MXD-MLPG-S approach, and utilizing the IMLS functions of the second and third order.

radius, $R = 90$ mm
thickness, $h = 0.9$ mm
Young's modulus, $E = 210000$ N/mm^2
Poisson's ratio, $\nu = 0.3$
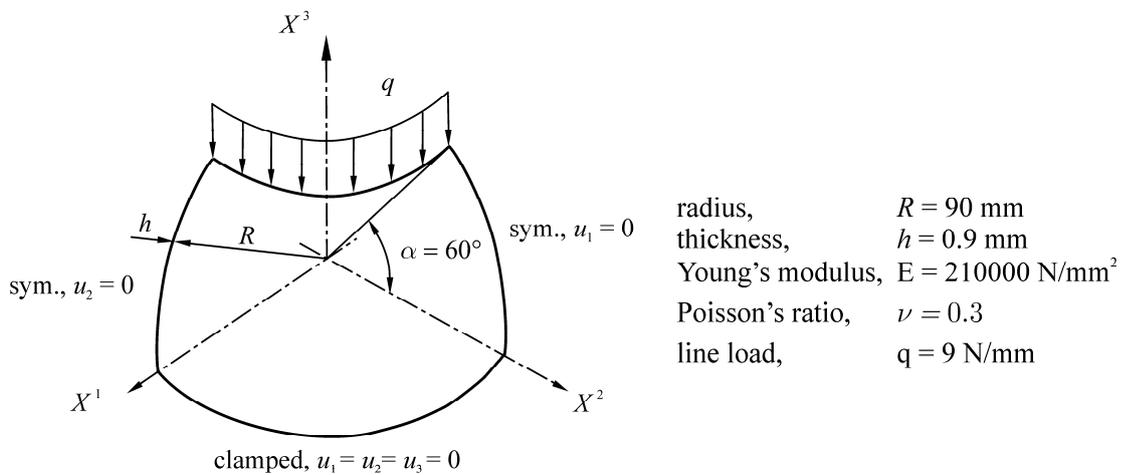line load,   q = 9 N/mm

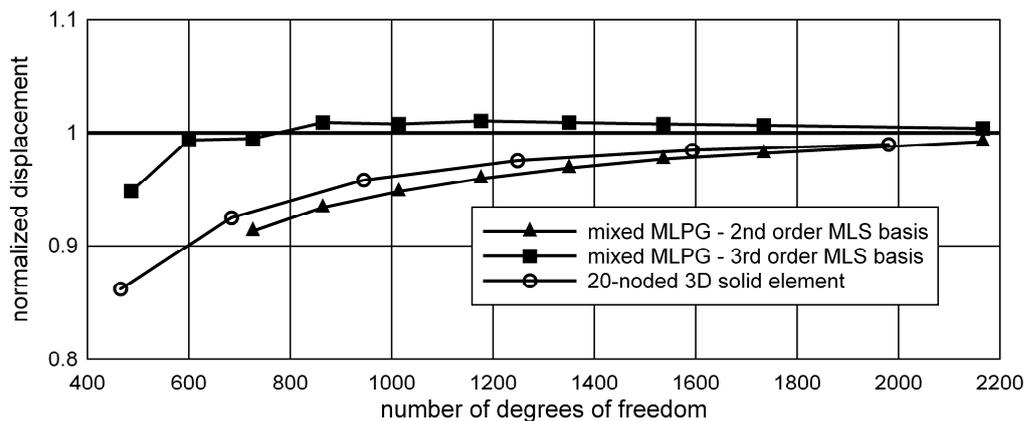Figure 7.29 Clamped hemispherical shell. Geometry and boundary conditions.

Figure 7.30 Clamped hemispherical shell. Convergence of vertical displacement under line load for MXD-MLPG-S formulation.

The convergence study, in comparison with the finite element solution, is displayed in Figure 7.30. It presents the curves of the normalized displacement at the middle surface under the line load versus the number of degrees of freedom. Normalization was

performed using the analytical solution from [156]. The meshless results, employing the second-order MLS basis, agree well with the finite element solutions, while the third-order IMLS function produces better accuracy and convergence at the observed point.

Sensitivity to shear locking was tested using both the second- and third-order IMLS functions. As Figure 7.31 clearly demonstrates, shear locking is again successfully suppressed. The plotted curves show that slightly better results are achieved if the third-order IMLS function is used.
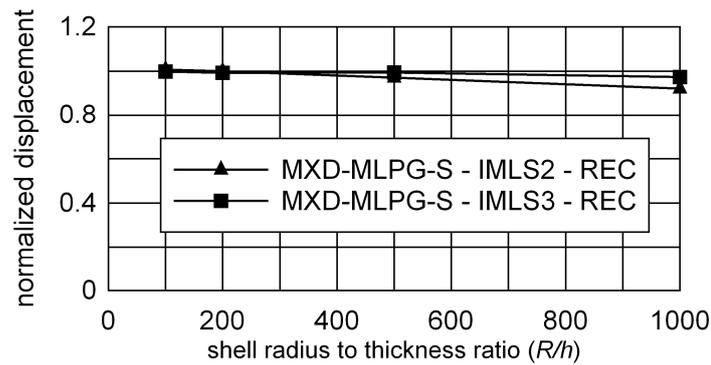
Figure 7.31 Clamped hemispherical shell. Vertical displacement under line load vs. radius-to-thickness ratio for MXD-MLPG-S formulation.

7.3.3.5 Pinched hemispherical shell

The analysis of the pinched hemispherical shell pinched by two concentrated forces, according to Figure 7.32, is one of the standard ways to test whether numerical formulations exhibit locking in the thin limit.

Figure 7.32 Pinched hemispherical shell. Geometry and boundary conditions of the model.

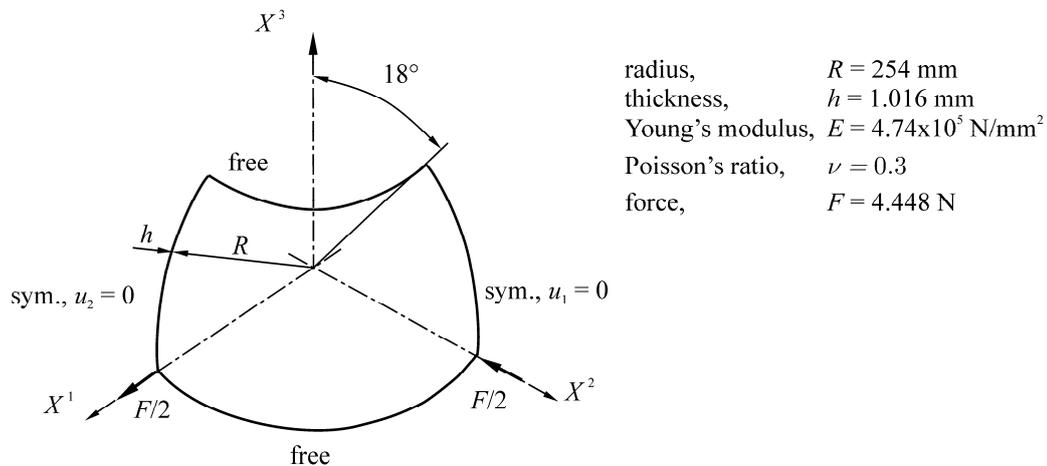Here, membrane locking is more critical than transversal shear locking because of the inextensional bending state appearing within the shell. The shell used in this test is very thin, with a radius-to-thickness ratio $R/h = 250$. The upper and lower edges of the shell are free, and the central opening of the shell is defined by the angle of $18°$. The material data and the value of forces are given in Figure 7.32.

Because of the symmetry of the problem, again only one quarter of the shell was modelled by applying the essential and natural BC as shown in Figure 7.32. Discretization was performed by using the uniform grids of node couples. The convergence of the solution for the radial displacements at the points under the load was tested for the MXD-MLPG-S formulation by employing the IMLS functions of the second, third, and fourth order. Figure 7.33 shows the results in comparison with the solutions obtained by the hexagonal 3-D finite elements. The analytical value used for the normalization of results is $2.3876\,mm$ [6].
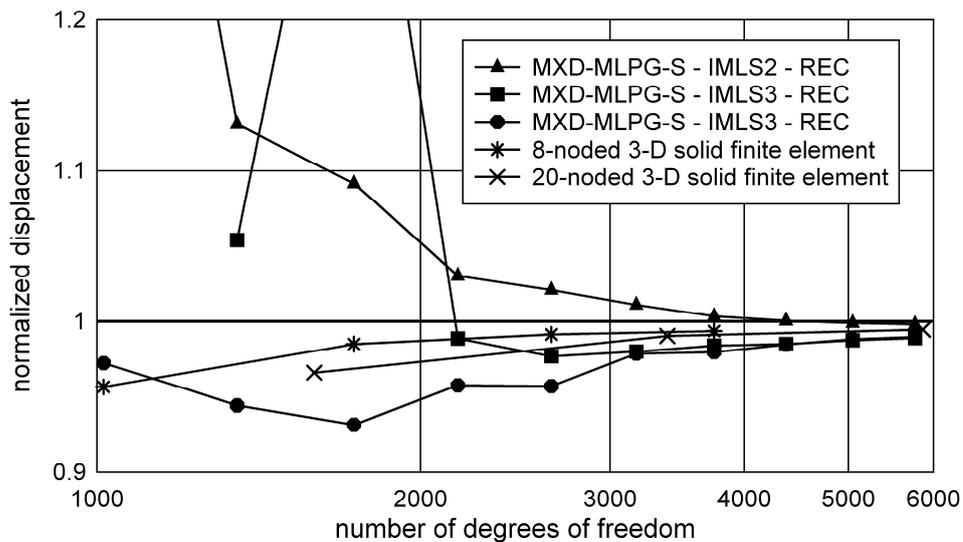
Figure 7.33 Pinched hemispherical shell. Convergence of solution for radial displacements at points under concentrated load (MXD-MLPG-S formulation).

Although the meshless solutions converge for all applied functions, it is clear that the convergence is non-uniform. Furthermore, the meshless results are poor and unreliable for the coarse grids if the IMLS functions of the lower order are used. This may be partly attributed to the sensitivity to the membrane locking effect. However, it bears mentioning that the sub-integral functions are more complicated here than in the problems involving cylindrical shells, because the functions that describe the geometry of a spherical surface are more complicated, as may be seen in Table 2.1. Depending on

the applied model, this may lead to a significant error in numerical integration, e.g., when using the model employing 13x13 nodes and the IMLS3 functions. It is possible that these errors additionally decrease the performance of the applied meshless formulation.

8 Conclusion

In this thesis, the novel meshless formulations for the analysis of shell and plate structures have been developed. This chapter contains an overview of the main results and contributions. The limitations of the presented formulations and procedures, as well as some directions about the future research, are also given.

The presented algorithms are based on the Meshless Local Petrov-Galerkin (MLPG) method, which is a truly meshless method because it does not employ the background cells either for the approximation of field variables or for the integration of governing equations. For the first time in meshless methods, a shell continuum was described by applying the solid-shell concept, which enabled the use of complete 3-D material models. The shell continuum was mapped to a parametric space, where the approximations of unknown field variables and the numerical integration of the local weak forms were performed. According to this approach, the couples of nodes positioned on the upper and lower shell surface were used to discretize the shell continuum. The governing equations were derived by defining a local sub-domain around each node couple, and by writing a local weak form (LWF) of the 3-D equilibrium equations over the local sub-domain. Thereby the Petrov-Galerkin method was applied, and accordingly, test and trial functions coming from distinctly different functional spaces were used. The test functions were chosen to be linear in the thickness direction. On the other hand, the trial functions for unknown field variables were constructed by using the meshless Moving Least Squares (MLS) functions in the in-plane directions, while simple polynomials were employed in the thickness direction.

The geometry of the shell continuum was defined by a mapping technique, where the middle surface of the shell was parameterized by using suitable curvilinear coordinates. Thereby, the geometry of the middle surface was described mathematically exactly in order to avoid the errors arising due to the approximate description of surfaces. Although straightforward and simple, the applied approach is not applicable for general shell geometries. Such shapes in general cannot be described mathematically exactly, and sometimes the middle surfaces cannot be parameterized in an unambiguous manner. Therefore, more advanced methods for describing shell geometries should be developed, which could be based on the existing CAD technology, or on splitting of the original surface into smaller manageable pieces.

161

Because, the solid-shell numerical models suffer from various locking phenomena, in this work a special attention has been devoted to the Poisson's thickness locking and the transversal shear locking effects. First, the theoretical origins of both locking effects were revealed by considering the problem of the rectangular plate subjected to the pure bending state, and thereafter the remedies for their elimination were proposed.

In the purely displacement algorithms, the hierarchical quadratic interpolation in the thickness direction was employed for the transversal displacement component to eliminate the Poisson's thickness locking effect, and two different MLPG formulations were developed. One algorithm employs the collocation of the equilibrium equations, and in the other, LWF were derived by applying the test functions quadratic in the thickness direction. The results obtained from the numerical examples considering thick shells and plates showed that both algorithms yield practically the same results and that the thickness locking phenomenon is successfully suppressed by applying the hierarchical interpolation approach. Furthermore, the obtained convergences are comparable to the applied 3-D solid finite elements. However, it should be stressed that the additional unknown variables associated with the quadratic terms in the hierarchical interpolation appear in the discretized equations. In contrast to the analogous FEM formulations, these variables cannot be eliminated on the local level by means of the static condensation, which leads to a larger global system of equations. The shear locking was alleviated by raising the order of the MLS basis and by using the global MLS approximation strategy, but as expected, the numerical experiments clearly demonstrated that such an approach is not capable of completely removing shear locking. Moreover, it is numerically inefficient due to the significant costs needed for the evaluation of approximation functions and for solving the global system of equations.

Because of the aforementioned reasons, new efficient mixed formulations thin shell structures have been researched. The mixed MLPG algorithm for plates was developed, where the shear tensor components were approximated separately from the displacements. LWF of the equilibrium equations was first written in terms of the approximated strains, and then the unknown nodal strain values were eliminated from the system of equations by employing the collocation of the 3-D kinematic relations at the nodes. It is to note that the applied procedure does not increase the total number of unknown parameters on the global level, in contrast to the hierarchical interpolation method used in the primal MLPG formulations. The Poisson's thickness locking was

eliminated by developing a novel procedure, which employs the modification of the nodal values of the transversal normal strain component. Therein, the independent term that is linear in the thickness direction was added to the constant nodal value calculated directly from displacements. The results showed that this procedure efficiently eliminates the thickness locking effect. It was also shown that the applied mixed concept is free of transversal shear locking in the plate thin limit. The proposed model is, however, not suitable for the application in the analysis of curved shells because of its complexity. Therefore, a mixed MLPG for the analysis of shell structures was proposed, which employs a simple switch of independent variables to eliminate thickness locking. Therein the transversal normal stress component was approximated instead of the transversal normal strain component. From the presented results, it is clear that both mixed formulations produce very close results if plate structures were considered. In addition, it is possible to suppress shear locking in very thin structures efficiently even by using the second-order MLS or IMLS functions. Moreover, in some cases the developed mixed MLPG algorithms yielded better results even than the applied finite elements, especially in the examples involving thin plate and cylindrical shell structures. It should be stressed that the considered locking effects were successfully removed even though all unknown variables were approximated by using the same approximation functions, which is not the case in the available FEM formulations. Nevertheless, the results obtained in the problems involving spherical shells suggest that future research should inevitably consider the existence of membrane locking in the proposed algorithms.

The mixed MLPG approach is superior in comparison to the primal MLPG formulations, as proved by the theoretical estimate of computational costs presented in Section 7.2.5.3, and confirmed by the performed numerical tests. The results indicated that fever Gaussian points are needed for accurate and stable numerical integration than in the primal MLPG formulations. Furthermore, the sizes of the support domains of the MLS shape functions affect the solution accuracy less intensely, and in many cases, it is possible to obtain excellent results by using the sizes that are close to the minimal admissible ones. In addition, it is to note that the direct approximation of the strain or stress variables in LWF separately from displacements decreases the continuity requirements for the trial functions. In addition, it is possible to suppress the shear locking effects in the shell thin limit efficiently by using the lower order of the MLS functions than in the primal MLPG method, which greatly reduces the costs of

calculating the MLS approximations. The numerical efficiency of the proposed mixed algorithms could be further improved by implementing simpler and numerically more efficient approximation schemes.

The local weak forms were integrated over the cylindrical or the parallelepipedic local sub-domains. For the cylindrical shapes, the LSW were integrated directly over the entire local sub-domain by means of the simple 2-D Gauss-Lagrange formula. On the other hand, the parallelepipedic local sub-domains were first partitioned into four equal quadrants in the parametric space, and LWF were integrated by applying 2-D Gauss-Lagrange formulas over each of these quadrants. Although both approaches yielded very similar results for plate structures, it was found out that the parallelepipedic local sub-domains produce more accurate in the analysis of curved shells, especially in the case of thin spherical shells. This can be attributed to the relatively complicated trigonometric functions used for the description of cylindrical geometrical shapes, which additionally increase the complexity of the sub-integral functions. This inconvenience could be alleviated by implementing different stratagems for numerical integration, such as the partitioning of the cylindrical local sub-domains. Moreover, new, more efficient methods for the numerical integration of LWF should also be explored.

Another difficulty in meshless methods is associated with the imposition of the essential BC. From the obtained results, it can be concluded that the penalty method performs well for flat plate structures, but that it might not be suitable for the application in curved structures. The causes for such behaviour should be explored in detail in future research. The interpolating MLS (IMLS) approximation scheme, where the interpolation condition at the nodes was imposed with a high accuracy by employing the regularized weight functions, was used in the mixed meshless formulations. It enables the enforcement of the essential BC in a simple and very efficient manner, similar to FEM. Furthermore, in comparison to the "classical" non-interpolation MLS functions, the influence of the sizes of the supporting domains of the nodal shape functions is further reduced. Because of the afore-mentioned reasons, it is concluded that the proposed solid-shell MLPG formulations are new useful tools for the analysis of shell-like structures by using meshless methods. Among them, the mixed MLPG approach for shell structures is the most attractive; it is theoretically straightforward, simple to implement, numerically efficient and most importantly, it is free of thickness and transversal shear locking. Consequently, it can serve as a basis for developing new

and efficient meshless algorithms for the non-linear numerical analysis of shell structures.

Finally, it is useful to condense the most important contributions of this thesis:

▫ Novel MLPG formulations for the analysis of plate and shell structures were developed, whereby the solid-shell concept was applied for the first time in meshless methods.

▫ In the purely displacement-based MLPG formulations, the Poisson's thickness locking effect was successfully eliminated by employing the hierarchical quadratic interpolation procedure. These algorithm are especially suitable for solving the problems dealing with thick plates structures, and with certain modifications and improvements, they could become applicable for solving practical engineering problems.

▫ The mixed MLPG approach was modified and extended to the analysis of shell and plate structures, which resulted in two novel mixed MLPG formulations. Two new and efficient procedures for the elimination of the Poisson's thickness locking effects were proposed for the developed mixed algorithms, and shear locking in the thin structural limit was removed in a simple and efficient manner by approximating the strain components separately from the displacements.

▫ It was proved theoretically and experimentally that the proposed mixed MLPG strategy is numerically far more efficient than the primal MLPG approach. In addition, by properly choosing the relevant parameters, the mixed formulations showed a potential to compete with the solid finite elements regarding accuracy and convergence.

Bibliography

[1] H.T.Y. Yang, S. Saigal, A. Masud and R.K. Kapania. A survey of recent shell finite elements, International Journal for Numerical Methods in Engineering, 2000, vol. 47: pp. 101-127.

[2] W.B.Kraetzig and D.Jun. On 'best' shell models – From classical shells, degenerated and multy-layered concepts to 3D. Archive of Applied Mechanics, 2003, vol. 73: pp. 1-25.

[3] K.Y. Sze. Three-dimensional continuum finite element models for plate/shell analysis. Prog. Struct. Engng. Mater., 2002, vol. 4: pp. 400-407.

[4] F. Koschnick. Geometrische Locking-Effecte bei Finiten Elementen und ein allgemeines Konzept zu iher Vermeidung. Ph.D. Thesis at TU Muenich, Munich, 2004.

[5] T.J.R. Hughes. The Finite Element Method. Prentice-Hall, Inc., New Yersey, 1987.

[6] R.H. MacNeal. Finite Elements: Their design and performance. Marcel-Dekker, Inc., New York, 1994.

[7] O.C. Zienkiewicz, R.L.Taylor, J.Z. Zhu. The Finite Element Method: Its Basis and Fundamentals, Sixth edition. Elsevier Butterworth-Heinemann, Oxford, 2005.

[8] P. Lancaster and K. Salkauskas. Curve and surface fitting: an introduction. Academic Press Ltd, London, 1986.

[9] H. Wenland. Scattered Data Approximation. Cambridge University Press, Cambridge, 2005.

[10] G.E. Fasshauer: Meshfree Approximation Methods with MATLAB. Singapore, World Scientific Publishing, 2007.

[11] W. Liu, S. Jun and Y. Zhang. Reproducing kernel particle method. International Journal for Numerical Methods in Fluids, 1995, vol. 20: pp. 1081-1106.

[12] I. Babuska and J.M.Melenk. The Partition of Unity method. Int. J. Num. Meth. Engrg., 1997, vol. 40: pp. 727-758.

[13] G.R. Liu: Mesh Free Methods: Moving beyond the Finite Element Method. CRC Press, Boca Raton, 2003.

[14] N. Sukumar, B. Moran and T. Belytschko. The Natural Element Method in Solid Mechanics. International Journal for Numerical Methods in Engineering, 1998, vol. 43: pp. 839-887.

[15] S.N. Atluri: The Meshless Method (MLPG) for Domain & BIE Discretization. Tech Science Press, Forsyth, 2004.

[16] N.Sukumar and R.W.Wright. Overview and construction of meshfree basis functions: From moving least squares to entropy approximants. Int. J. Numer. Meth. Engng., 2007, vol. 70: pp. 181-205.

[17] T. Belytschko, Y.Y. Lu and L. Gu. Element-free Galerkin Methods, International Journal for Numerical Methods in Engineering, 1994, vol. 37: pp. 229-256.

[18] G.R. Liu and M.B. Liu. Smoothed Particle Hydrodynamics − a meshfree particle method. World Scientific Publishing Co., Singapore, 2003.

[19] S. N. Atluri and T. Zhu: A new Meshless Local Petrov-Galerkin (MLPG) approach in computational mechanics. Computational Mechanics, 1998, vol. 22: pp. 117-127.

[20] T. Zhu, J.D. Zhang and S.N. Atluri, A Local Boundary Integral Equation (LBIE) Method in Computational Mechanics, and a Meshless Discretization Approach. Comput. Mech., 1998, vol. 21: pp. 223–235.

[21] S. De, K.J. Bathe. The method of finite spheres. Computational Mechanics, 2000, pp.329-345.

[22] E. Oñate, S. Idelsohn, O.C. Zienkiewicz and R.L.Taylor. A Finite Point Method in Computational Mechanics. Application to Convective Transport and Fluid Flow. Int. J. Num. Meth. Eng., 1996, vol. 39: pp. 3839–3866.

[23] E. Cueto, N. Sukumar, B. Calvo, J. Cegonino, M. Doblare. Overview and recent advances in natural neighbour Galerkin methods. Archives of Computational Methods in Engineering, 2003, vol. 10(4): pp. 307–384.

[24] X. Zhang, X-H Liu, K-Z Song and M-W Lu. Least-squares collocation meshless method. Int. J. Numer. Meth. Engng, 2001, vol. 51: pp. 1089-1100.

[25] S.N. Atluri, H.T. Liu and Z.D. Han. Meshless Local Petrov-Galerkin (MLPG) Mixed Finite Difference Method for Solid Mechanics. CMES: Computer Modeling in Engineering & Sciences, 2006, vol. 15: pp.1-16.

[26] S.N. Atluri, H.T. Liu and Z.D. Han. Meshless Local Petrov-Galerkin (MLPG) Mixed Collocation Method for Elasticity Problems. CMES: Computer Modeling in Engineering & Sciences, 2006, vol. 14: pp.141-152.

[27] S.-H. Park and S.-K. Youn. The least-squares meshfree method. Int. J. Numer. Meth. Engng., 2001, vol. 52: pp. 997-1012.

[28] D. Wang and J.-S. Chen: Locking-free stabilized conforming nodal integration for meshfree Mindlin-Reissner plate formulation. Comput. Methods. Appl. Mech. Engrg., vol. 193, 2004, pp. 1065-1083.

[29] J-S. Chen and D. Wang: A constrained reproducing kernel particle formulation for shear deformable shell in Cartesian coordinates. Int. J. Numer. Meth. Engng., 2006, vol. 68: pp. 151–172.

[30] N.H. Kim, K.K. Choi, J-S. Chen and M.E. Botkin: Meshfree analysis and design sensitivity analysis for shell structures. Int. J. Numer. Meth. Engng., 2002, vol. 53: pp. 2087–2116.

[31] K. Yi, K. K. Choi, N. H. Kim and M.E. Botkin. Continuum-based design sensitivity analysis and optimization of nonlinear shell structures using meshfree method. Int. J. Numer. Meth. Engng., 2006, vol. 68: pp. 231–266.

[32] N. Sukumar, A.Y. Semenov and V.V. Belikov. Natural Neighbour Galerkin methods. Int. J. Numer. Meth. Engng, 2001, vol. 50:1-27.

[33] S. Li and W.K.Liu. Meshfree and particle methods and their applications. Appl. Mech. Rev., 2002, vol. 55, no 1: pp. 1-34.

[34] G.R.Liu and Y.T.Gu. An Introduction to Meshfree Methods and Their Programming. Springer, Dordrecht, 2005.

[35] S.N. Atluri and S. Shen. Simulation of a 4th Order ODE: Illustration of Various Primal & Mixed MLPG Methods, CMES: Comput. Model. Eng. Sci., 2005, vol. 7: pp. 241-268.

[36] S.N. Atluri, H.-G. Kim and J.Y. Cho. A critical assessment of the truly Meshless Local Petrov-Galerkin (MLPG), and Local Boundary Integral Equation (LBIE) methods. Computational Mechanics, 1999, vol. 24: pp. 348-372.

[37] Y.T. Gu and G.R. Liu. A Local Point interpolation method for static and dynamic analysis of thin beams. Comput. Methods Appl. Mech. Engrg., 2001, vol. 190: pp. 5515-5528.

[38] G.R. Liu and Y.T. Gu. Comparisons of two meshfree local point interpolation methods for structural analyses. Computational Mechanics, 2002, vol. 29: pp. 107-121.

[39] G.R. Liu, L. Yan, J.G. Wang and Y.T. Gu. Point Interpolation method based on local residual formulation using radial basis functions. Structural Engineering and Mechanics, 2002, vol. 14: pp. 713-732.

[40] S.N. Atluri, Z.D. Han and M.J. Rajendran. A New Implementation of the Meshless Finite Volume Method, Through the MLPG "Mixed" Approach. CMES: Comput. Model. Eng. Sci., 2004, vol.6: pp. 491–513.

[41] S.N. Atluri and T. Zhu. New concepts in meshless methods. Int. J. Numer. Meth. Engng., 2000, vol. 47: pp. 537-556.

[42] S.N. Atluri and T.-L. Zhu. The meshless local Petrov-Galerkin (MLPG) approach for solving problems in elasto-statics. Computational Mechanics, 2000, vol. 25: pp. 169-179.

[43] J.R. Xiao. Local Heaviside weigthed MLPG meshless method for two-dimensional solids using compactly supported radial basis functions. Comput. Methods Appl. Mech. Engrg., 2004, vol. 193: pp. 117-138.

[44] K. Wang, S. Zhou and G. Shan. The natural neighbour Petrov-Galerkin method for elasto-statinc. Int. J. Numer. Meth. Engng., 2005, vol. 63: pp. 1126-1145.

[45] Z.D. Han and S.N: Atluri. Meshless Local Petrov-Galerkin (MLPG) approaches for solving 3D problems in elasto-statics. CMES: Comput. Model. Eng. Sci., 2004, vol. 6: pp. 169-188.

[46] Q. Li, S. Shen, Z.D: Han and S.N. atluri. Application of Meshless Local Petrov-Galerkin (MLPG) to Problems with Singularities, and Material Discontinuities, in 3-D Elasticity. CMES: Comput. Model. Eng. Sci., 2003, vol. 4: pp. 571-585.

[47] Y.T. Gu and G.R.Liu. A meshless local Petrov-Galerkin (MLPG) method for free and forced vibration analyses for solids. Computational Mechanics, 2001, vol. 27: pp. 188-198.

[48] S.Y. Long, K.Y. Liu and D.A. Hu. A new meshless method based on MLPG for elastic dynamic problems. Engineering analysis with Boundary Elements, 2006, vol. 30: pp. 43-48.

[49] J. Sladek, V. Sladek and R. Van Keer. Meshless local boundary integral equation method for 2D elastodynamic problems. Int. J. Numer. Meth. Engng., 2003, vol. 57: pp. 235-249.

[50] Z.D. Han and S.N. Atluri. A Meshless Local Petrov-Galerkin (MLPG) Approach for 3-Dimensional Elasto-dynamics. CMES: Comput. Model. Eng. Sci., 2004, vol. 1: pp. 129-140.

[51] S.N. Atluri and T.-L. Zhu. A New Meshless Local Petrov-Galerkin (MLPG) Approach to Nonlinear Problems in Computer Modeling and Simulation. Comput. Modeling Simulations in Engrg., 1998, vol. 3: pp. 187-196.

[52] T. Zhu, J. Zhang and S.N. Atluri. A meshless local boundary integral equation (LBIE) method for solving nonlinear problems. Computational Mechanics, 1998, vol. 22: pp. 174-186.

[53] T. Zhu, J. Zhang and S.N. Atluri. A meshless numerical method based on the local boundary integral equation (LBIE) to solve linear and non-linear boundary value problems. Engineering Analysis with Boundary value Elements, 1999, vol. 23: pp. 375-389.

[54] X. Zhang, Z. Yao and Z. Zhang. Application of MLPG in large deformation analysis. Acta Mechanica Sinica, 2006, vol. 22: pp. 331-340.

[55] Z. Yao, Z. Zhang and X. Zhang. Some Applications of MLPG in Large Deformation Analysis of Hyperelasto-Plastic Material. CMES: Comput. Model. Eng. Sci., 2007, vol. 3: pp. 133-138.

[56] J. Ma. Meshless Method for Modeling Large Deformation with Elastoplasticity. Ph.D. Thesis at Kansas State University, Manhattan, Kansas, 2007.

[57] Z.D. Han, A.M. Rajendran and S.N. Atluri. Meshless Local Petrov-Galerkin (MLPG) Approaches for Solving Nonlinear Problems with Large Deformations and Rotations. CMES: Computer Modeling in Engineering & Sciences, 2005, vol. 1: pp.1-12.

[58] Z.D. Han, H.T. Liu, A.M. Rajedran and S.N. Atluri. The applications of Meshless Local Petrov-Galerkin (MLPG) Approaches in High-Speed Impact, Penetration and Perforation Problems. CMES: Comput. Model. Eng. Sci., 2006, vol. 14: pp. 119-128.

[59] J.R. Xiao and M.A. McCarthy. Meshless analysis of the obstacle problem for beams by the MLPG method and subdomain variational formulations. European Journal of Mechanics A/Solid, 2003, vol. 22: pp. 385-399.

[60] J.R. Xiao, B.A. Gama, J.W. Gillespie Jr and E.J. Kansa. Meshless solutions of 2D contact problems by subdomain variational inequality and MLPG method with radial basis functions. Engineering Analysis with Boundary Elements, vol. 29: pp. 95-106.

[61] R.C. Batra, M Porfiri and D. Spinello. Treatment of material discontinuity in two meshless local Petrov-Galerkin (MLPG) formulations of axissymmetric transient heat conduction. Int. J. Numer. Meth. Engrg., 2004, vol. 61: pp. 2461-2479.

[62] L.F. Qian, R.C. Batra and L.M. Chen. Analysis of cylindrical bending thermoelastic deformations of functionally graded plates by a meshless local Petrov-Galerkin method. Computational Mechanics, 2004, vol. 33: pp. 263-273.

[63] J. Y. Cho and S.N. Atluri. Analysis of shear flexible beams, using the meshless local Petrov-Galerkin method, based on locking-free formulation. Engineering Computations, 2001, vol.18: pp. 215-240.

[64] S.N. Atluri, J.Y. Cho and H.-G. Kim. Analysis of thin beams, using the meshless local Petrov-Galerkin method, with generalized moving least squares interpolations. Computational Mechanics, 1999, vol. 24: pp. 334-347.

[65] I.S. Raju and D.R. Philllips. Furhter Developments in the MLPG Method for Beam Problems. CMES: Comput. Model. Eng. Sci., 2003, vol. 4: pp. 141-159.

[66] S. Long and S.N. Atluri: A Meshless Local Petrov-Galerkin Method for Solving the Bending Problem of a Thin Plate, CMES: Computer Modeling in Engineering & Sciences, 2002, vol. 3: pp. 53-63.

[67] J. Sladek, V. Sladek and M.A. Mang: Meshless formulations for simply supported and clamped plate problems. Int. J. Numer. Meth. Engng, 2002, vol. 55: pp. 359–375.

[68] S. Long and Q. Zhang. Analysis of thin plates by the local boundary integral equation (LBIE) method. Engineering Analysis with Boundary Elements, 2002, vol: pp. 707-718.

[69] J. Sladek, V. SLadek and H.A. Mang. Meshless local boundary integral equation method for simply supported and clamped plates resting on elastic foundation. Comput. Methods Appl. Mech. Engrg., 2002, vol 191: pp. 5943-5959.

[70] J. Sladek, V. Sladek, H.A. Mang. Meshless LBIE formulations for simply supported and clamped plates under dynamic load. Computer and Structures, 2003, vol 81: pp. 1643-1651.

[71] J. Sladek and V. Sladek. A meshless method for large deflection of plates. Computational Mechanics, 2003, vol 30: pp. 155-163.

[72] J. Sladek, V. Sladek, Ch. Zhang, J. Krivacek and P. H. Wen: Analysis of orthotropic thick plates by meshless local Petrov–Galerkin (MLPG) method. Int. J. Numer. Meth. Engng 2006, vol. 67: pp. 1830-1850.

[73] J. Sladek, V. Sladek, J. Krivacek, P.H. Wen and Ch. Zhang. Meshless local Petrov-Galerkin (MLPG) Method for Reissner-Mindlin plates under dynamic load. Comput. Methods Appl. Mech. Engrg., 2007, vol. 196: pp. 2681-2691.

[74] J. Sladek, V. Sladek, P. H. Wen and M.H. Aliabadi: Meshless Local Petrov-Galerkin (MLPG) Method for Shear Deformable Shells Analysis. CMES: Computer Modeling in Engineering & Sciences, 2006, vol.13, no.2, pp.103-117.

[75] J. Sladek, V. Sladek, J. Krivacek and M.H. Aliabadi: Local boundary integral equations for orthotropic shallow shells. International Journal of Solids and Structures, 2007, vol. 44: pp. 2285–2303.

[76] L.F. Qian, R.C. Batra, L.M. Chen: Elastostatic Deformations of a Thick Plate by using a Higher-Order Shear and Normal Deformable Plate Theory and two Meshless Local Petrov-Galerkin (MLPG) Methods, CMES: Computer Modeling in Engineering & Sciences, 2003, vol. 4, pp. 161-175.

[77] L.F. Qian, R.C. Batra, L.M. Chen: Static and dynamic deformations of thick functionally graded elastic plates by using higher-order shear and normal deformable plate theory and meshless local Petrov-Galerkin method, Composites, Composites: Part B, 2004, vol. 35, pp. 685–697.

[78] D.F. Gilhooley, R.C. Batra , J.R. Xiao, M.A. McCarthy, J.W. Gillespie Jr.: Analysis of thick functionally graded plates by using higher-order shear and normal deformable plate theory and MLPG method with radial basis functions. Composite Structures, 2007, vol. 80, pp. 539–552.

[79] D. Chapelle and K.J. Bathe. The Finite Element Analysis of Shells – Fundamentals. Springer-Verlag Berlin Heidelberg, 2003.

[80] P. Krystl and T. Belytschko: Analysis of Thin Plates by the Element-Free Galerkin Method. Computational Mechanics, 1985, vol. 16: pp.1-10.

[81] P. Krysl and T. Belytschko: Analysis of thin shells by the element-free Galerkin method. International Journal of Solids and Structures, 1996, vol. 33: pp. 3057-3080.

[82] L. Liu, G.R. Liu and V.B.C. Tan: Element free method for static and free vibration analysis of spatial thin shell structures. Comput. Methods Appl. Mech. Engrg., 2002, vol. 191: pp. 5923–5942.

[83] T. Rabczuk, P. M. A. Areias and T. Belytschko: A meshfree thin shell method for non-linear dynamic fracture, Int. J. Numer. Meth. Engng., 2007, vol. 72: pp. 524–548

[84] B.M. Donning and W.K. Liu: Meshless methods for shear-deformable beams and plates. Computer Methods in Applied Mechanics and Engineering, 1998, vol. 152: pp. 47-71.

[85] O. Garcia, E.A. Fancello, C.S. de Barcellos and C.A. Duarte: hp-Clouds in Mindlin's thick plate model. Int. J. Numer. Meth. Engng., 2000, vol. 47: pp. 1381-1400.

[86] H. Noguchi, T. Kawashima, T. Miyamura: Element free analyses of shell and spatial structures, Int. J. Numer. Meth. Engng., 2000, vol. 47: 1215-1240.

[87] MSC.Software Corporation, MSC.Nastran 2005 Linear Static Analysis Guide, MSC.Software Corporation, USA, 2005.

[88] ABAQUS, Analysis User's Manual, Dassault Systèmes, USA, 2007.

[89] A.J.M. Ferreira, C.M.C. Roque, P.A.L.S. Martins: Analysis of composite plates using higher-order shear deformation theory and a finite point formulation based on the multiquadric radial basis function method. Composites: Part B, vol. 34, 2003: pp. 627–636

[90] A.J.M. Ferreira, C.M.C. Roque, R.M.N. Jorge: Modelling cross-ply laminated elastic shells by a higher-order theory and multiquadrics. Computers and Structures, 2006, vol. 84: pp. 1288–1299.

[91] A.J.M. Ferreira, C.M.C. Roque, R.M.N. Jorge: Static and free vibration analysis of composite shells by radial basis functions. Engineering Analysis with Boundary Elements, 2006, vol. 30: pp.719–733.

[92] S. Li, W. Hao, W.K. Liu: Numerical simulations of large deformation of thin shell structures using meshfree method. Computational Mechanics, 2000, vol. 25: pp. 102–116.

[93] R. Hauptmann, K. Schweizerhof. A systematic development of solid-shell element formulations for linear and non-linear analyses employing only displacement degrees of freedom, Int. J. Numer. Meth. Engng, 1998, vol. 42: pp. 49-69.

[94] X.G. Tan and L. Vu-Quoc. Optimal solid shell element for large deformable composite structures with piezoelectric layers and active vibration control. Int. J. Numer. Mech. Engng., 2005, vol. 64: pp. 1981-2013.

[95] S. Klinkel, F. Grutmann and W. Wagner. A robust non-linear solid shell element based on a mixed variational formulation. Comput. Methods Appl. Mech. Engrg., 206, vol. 195: pp. 179-201.

[96] T. Zhu, S. N. Atluri: A modified collocation method and a penalty formulation for enforcing the essential boundary conditions in the element free Galerkin method. Computational Mechanics, 1998, vol. 21: pp. 211-222.

[97] J. Dolbow and T. Belytschko. Volumetric locking in the Element Free Galerkin Method. Int. J. Numer. Meth. Engn., 1999, vol. 46, pp. 925-942.

[98] L. Liu, L.P. Chua, D.N. Ghista: Element-free Galerkin method for static and dynamic analysis of spatial shell structures. Journal of Sound and Vibration, 2006, vol. 295: pp. 388-406.

[99] L. Liu, L.P. Chua, D.N. Ghista: Applications of point interpolation method for spatial genereal shell structures. Comput. Methods Appl. Mech. Engrg., 2007, vol. 196: pp. 1633-1647.

[100] W. Kanok-Nukulchai, W. Barry, K. Saran-Yasoontorn, P. H. Bouillard: On elimination of shear locking in the element-free Galerkin method. Int. J. Numer. Meth. Engng, 2001, vol. 52: pp. 705–725.

[101] C. Tiago and V. Leitão: On the procedures to eliminate shear locking in meshless methods. Proceedings of ECCOMAS Thematic Conference on Meshless Methods 2005. DM-IST, Portugal, 2005.

[102] C. Tiago and V. Leitão. Eliminating Shear-Locking in Meshless Methods: A Critical Overview and a New Framework for Structural Theories, in Advances in Meshfree Techniques, pp. 123-145. Springer, Dordrecht, 2007.

[103] Q. Li, J. Sorić, T. Jarak, S.N. Atluri. A locking-free meshless local Petrov-Galerkin formulation for thick and thin plates, Journal of Computational Physics, 2005, vol. 208: pp. 116-133.

[104] J.S. Chen, S.T. Yoon, S. Yoon and Y. You. A stabilized conforming nodal integration for Galerkin meshfree methods. Int. J. Numer. Methods Eng., 2001, vol. 50: pp. 435-466.

[105]K.-C. Kwon, S.-H. Park and S.-K. Youn. The support integration scheme in the least-squares mesh-free method. Finite Elements in Analysis and Desing, 2006, Vol. 43: pp. 127-144.

[106]S. De and K.J. Bathe. Displacement/pressure mixed interpolation in the method of finite spheres. Int. J. Numer. Methods Eng., 2001, vol. 51: pp. 275-292.

[107]S. M. BaniHani and S. De. On the evaluation of the method of finite spheres for the solution of Reissner-Mindlin plate problems using the numerical inf-sup test. Int. J. Numer. Meth. Engng., 2009, vol. 70: pp. 1366-1386.

[108]D.P.Recio, R.M. Natal Jorge and L.M.S. Dinis. Locking and hourglass phenomena in an element-free Galerkin context: the B-bar method with stabiization and an enhanced strain method. Int. J. Numer. Meth. Engng., 2006, vol. 68: pp. 1329-1357.

[109]G.R. Liu and Y.T. Gu. Meshless Local-Petrov (MLPG) method in combination with finite element and boundary element approaches. Computational Mechanics, 2000, vol. 26: pp. 536-546.

[110]T. Belytschko and M. Tabbara. Dynamic fracture using element-free Galerkin methods. Int. J. Numer. Meth. Engng., 1996, vol. 39: pp. 923-938.

[111]J.-S. Chen, C. Pan and C.-T. Wu. Large deformation analysis of rubber based on a reproducing kernel particle method. Compuatational Mechanics, 1997, vol. 19: pp. 211-237.

[112]J.Y. Cho, Y.M. Song and Y.H. Choi. Boundary locking induced by penalty enforcement of essential boundary conditons in mwesh-free methods. Comput. Methods Appl. Mech. Engrg., 2008, vol. 197: pp. 1167-1183.

[113]A. Huerta and S. Fernandez-Mendez. Enrichment and coupling of the finite element and meshless methods. Int. J. Numer. Meth. Engng., 2000, vol.48: pp. 1615-1636.

[114]Y.T. Gu and G.R. Liu. Meshless Methods Coupled with Other Numerical Methods. Tsinghua Science and Technology, 2005, vol. 10: pp. 8-15.

[115]H. Karutz and W.B. Kraetzig. A quadtree data structure for the coupled finite element-element-free Galerkin method. Int. J. Numer. Meth. Engng., 2002, vol.53: pp. 375-391.

[116]T. Chen and I.S. Raju. A coupled finite element and meshless local Petrov-Galerkin method for two-dimensional potential problems. Comput. Methods Appl. Mech. Engrg., 2003, vol. 192: pp. 4533-4550.

[117]T. Most and C. Bucher: A Moving Least Squares weighting function for the Element-free Galerkin Method which almost fulfills essential boundary conditions. Structural Engineering and Mechanics, 2005, vol. 21: pp. 315-332.

[118]T. Most, A natural neighbour-based moving least-squares approach for the element-free Galerkin method, Int. J. Numer. Meth. Engng., 2007, vol. 71: pp. 224-252.

[119]H. Parisch. A continuum-based shell theory for non-linear applications. Int. J. Numer. Meth. Engrg., 1995, vol. 38: pp. 1855-1883.

[120]Y. Basar and W.B. Krätzig. Theory of Shell Structures. VDI Verlag, 2001.

[121] I. Alfirević. Tenzorski račun I tenzorska mehanika. Golden Marketing – Tehnička knjiga, 2006.

[122]G.A. Holzapfel. Nonlinear solid mechanics. John Willey & Sons, Ltd, 2000.

[123]J. Fish and T. Belytschko. A First Course in Finite Elements, John Wiley & Sons Ltd., England, 2007.

[124]S. Skatulla. Computational aspects of generalized continua based on moving least square approximations. Phd Thesis, The University of Adelaide, 2006.

[125]T. Belytschko and M. Fleming. Smoothing, enrichment and contact in the element-free Galerkin method. Computers and -Structures, 1999, vol. 71: pp. 173-195.

[126]B.N. Rao and S. Rahman. An enriched meshless method for non-linear fracture mechanics. Int. Numer. Meth. Engng., 2004, vol. 59: pp. 197-223.

[127]I. Kaljević and S. Saigal. An improved element-free Galerkin formulation. Int. J. Numer. Meth. Engng., 1997, vol 40: pp. 2953-2974.

[128]T. Most. A natural neighbour-based moving least-squares approach for the element-free Galerkin approach. Int. J. Numer. Meth. Engng., 2001, vol. 71: pp. 224-252.

[129]T. Most and C. Bucher. New concepts for moving least squares: An interpolating non-singular weighting function and weighted nodal least squares. Engineering Analysis with Boundary Elements, 2008, vol. 32: pp. 461-470.

[130]M. Macri, S. De and M.S. Shepard. Hierarchical tree-based discretization for the method of finite spheres. Computers and Structures, 2003, vol. 81: pp. 798-803.

[131]T. Belytschko, Y. Krongauz, D. O, M. Fleming and P. Kryls. Meshless method: An overview and recent developments. Comput. Methods Appl. Mech. Eng., 1996, vol. 139: pp. 3-47.

[132] I. S. Raju and D.R. Phillips. A Local Coordinate Approach in the MLPG Method for Beam Problems. Technical memorandum NASA/TM-2002-211463, Langley Research Center, Hampton, 2002.

[133] W.-K. Liu, S. Li and T. Belytschko. Moving Least-square reproducing kernel methods (I) Methodology and convergence. Comput. Methods Appl. Mech. Engrg., 1997, vol. 143: pp. 113-154.

[134] S.N. Atluri and S. Shen. The Meshless Local Petrov-Galerkin (MLPG) Method: A Simple & Less-Costly Alternative to the Finite Element and Boundary Element Method. CMES: Comput. Model. Eng. Sci., 2002, vol. 3: pp. 11-51.

[135] S.N. Atluri and S. Shen. The Meshless Local Petrov-Galerkin (MLPG) Method. Tech Science Press, Forsyth, 2002.

[136] S. De and K.-J. Bathe. The method of finite spheres with improved numerical integration. Computers and Structures, 2001, vol. 79: pp. 2183-2196.

[137] A. Mazzia, M. Ferronato, G. Pini and G. Gambolati. A comparison of numerical integration rules for the meshless local Petrov-Galerkin method. Numer. Algor., 2007, DOI 10.1007/s11075-007-9110-6.

[138] S. Klinkel. Theorie und Numerik eines Volumen-Schalen-Elementes bei finiten elastischen und plastischen Verzerrungen. Ph.D. Thesis at TU Karlsruhe, Karlsruhe, 2000.

[139] R. Hauptmann. Structurangepasste geometrisch nichtlineare Finite Elemente fuer Flaechentragwerke. Ph.D. Thesis at TH Karlsruhe, Karlsruhe, 1997.

[140] T. Jarak, J. Sorić and J. Hoster. On Application of a Meshless Approach to Analysis of Shell-like Structures. Proceeding of the 2nd Eccomas Thematic Conference on Meshless Methods 2007, Porto, Portugal, 2007.

[141] T. Jarak, J. Sorić and J. Hoster. Robust Meshless Formulation for Numerical Analysis of Shell-like Structural Components. Proceedings of the 5th International Congress of Croatian Society of Mechanics, CD-ROM edition, Trogir, Croatia, 2006.

[142] T. Jarak, J. Sorić and J. Hoster. Analysis of shell deformation responses by the Meshless Local Petrov-Galerkin (MLPG) approach. CMES: Comput. Model. Eng. Sci., 2007, vol. 18: pp. 235-246.

[143] J. Sorić, Q. Li, T. Jarak and S.N. Atluri. Meshless Local Petrov-Galerkin (MLPG) formulation for analysis of thick plates. CMES: Comput. Model. Eng. Sci., 2004, vol. 6: pp. 349-357.

[144] MSC.Software Corporation. MSC.Nastran 2005 Quick Reference Guide. MSC.Software Corporation, USA, 2005.

[145] S. Srinivas, A.K. Rao. Flexure of Thick Rectangular Plates. J. Appl. Mech. ASME, 1973, vol. 40, pp. 298-299.

[146] J. Sorić, Q. Li, T. Jarak, T., S.N. Atluri. On the application of the meshless Local Petrov-Galerkin (MLPG) Method to the Analysis of Shear Deformable Plates. Proceedings of the 2004 International Conference on Computational & Experimental Engineering and Sciences, CD-ROM-Edition, Madeira, Portugal, 2004.

[147] J. Sorić and T. Jarak. Meshless Local Petrov-Galerkin (MLPG) Formulations for Analysis of Shell-Like Structures, in ECCOMAS Multidisciplinary Jubilee Symposium: New Computational Challenges in Material, Structures, and Fluids, Springer Netherlands, 2009, pp. 277-289.

[148] T. Jarak and J. Sorić. Analysis of rectangular square plates by the mixed Meshless Local Petrov-Galerkin (MLPG) approach. CMES: Comput. Model. Eng. Sci., 2008, vol. 38, pp. 231-261.

[149] J. Sorić and T. Jarak. Mixed Meshless formulation for analysis of shell-like structures. Comput. Methods Appl. Mech. Engrg., 2010, vol. 199: pp. 1153-1164.

[150] S. De and K.-J. Bathe. Towards an efficient meshless computational technique: the method of finite spheres. Engineering Computations, 2001, vol. 18: pp. 170-192.

[151] X.Zhang, Z. Yao and Z. Zhang. Application of MLPG in large deformation analysis. Acta Mechanica Sinica, 2006, vol. 22: pp. 331-340.

[152] ADINA Verification Manual, Adina R&C Inc., 2008.

[153] J. Sorić, T. Jarak, Q. Li and S.N. Atluri. Analysis of Plates and Shells by Meshless Local Petrov-Galerkin (MLPG) Method. In monography Advances in Meshless Methods, Tech Science Press, 2006, pp. 220-240.

[154] S. Timoshenko, S. Voinowsky-Krieger. Theory of Plates and Shells. McGraw-Hill, London, 1985.

[155] S. Timoshenko. Strenght of Materials, Part I, Elementary Theory and Problems, Third Edition. D. Van Nostrand Company, NewYork, 1955.

[156]V.V. Novozhilov. Thin Shell Theory. P. Noordhoff Ltd., Groningen, 1964.

ŽIVOTOPIS

Tomislav Jarak rođen je 11. siječnja 1977. u Čakovcu. Maturirao je na prirodoslovno-matematičkoj gimnaziji u Varaždinu 1995. godine. Nakon toga, upisao je studij strojarstva na Fakultetu strojarstva i brodogradnje u Zagrebu, gdje je diplomirao 2001. godine.

Od 2002. godine zaposlen je kao mlađi asistent na Zavodu za tehničku mehaniku na Fakultetu strojarstva i brodogradnje u Zagrebu, gdje je pohađao poslijediplomski studij, smjer Teorija konstrukcija. Kao istraživač sudjelovao je na četiri znanstvena i tehnološka projekta. Tijekom istraživanja, boravio je dva mjeseca na Centru za aeronautička istraživanja, Kalifornijsko sveučilište, Irvine, te tri mjeseca na Institutu za građevinsku statiku, Tehničko sveučilište u Karlsruheu. Uz istraživački rad, aktivno je sudjelovao u nastavi iz više kolegija dodiplomskog i diplomskog studija.

Autor je ukupno 29 znanstvenih članaka, od čega je pet objavljeno u cijenjenim CC znanstvenim časopisima. Član je Hrvatskog društva za mehaniku i Srednje-europskog udruženja za računalnu mehaniku.

CURRICULUM VITAE

Tomislav Jarak was born on January 11, 1977 in Čakovec, Croatia. He graduated at the grammar school in Varaždin, Croatia, in 1995. He then enrolled in the graduate study at the Faculty of Mechanical Engineering and Naval Architecture, University of Zagreb, where he received the Dipl.Ing. degree in mechanical engineering in 2001.

Since 2002, he has been employed as a junior researcher at the Department of Technical Mechanics at the Faculty of Mechanical Engineering and Naval Architecture, University of Zagreb, where he enrolled in the postgraduate study in Theory of Structures and Design. He has been working as a research assistant on four scientific projects. During his research, he stayed for two months at the Center for Aeronautical Research, University of California, Irvine, and for three months at the Institute for Structural Analysis, University of Karlsruhe, as a researcher. In addition, he has been involved in the teaching activities in a number of courses from the graduate study.

He is the author and co-author of 29 scientific publications, including five contributions published in the highly esteemed CC scientific journals. He is a member of the Croatian Society of Mechanics and the Central European Association for Computational Mechanics.